

Multiscale numerical model for the analysis of laminated glass structures exposed to static load

Grozdanić, Gabriјela

Doctoral thesis / Doktorski rad

2024

Degree Grantor / Ustanova koja je dodijelila akademski / stručni stupanj:

University of Split, Faculty of Civil Engineering, Architecture and Geodesy / Sveučilište u Splitu, Fakultet građevinarstva, arhitekture i geodezije

<https://doi.org/10.31534/DocT.059.GroG>

Permanent link / Trajna poveznica: <https://um.nsk.hr/um:nbn:hr:123:637483>

Rights / Prava: [In copyright](#) / [Zaštićeno autorskim pravom.](#)

Download date / Datum preuzimanja: **2024-11-24**



Repository / Repozitorij:

[FCEAG Repository - Repository of the Faculty of Civil Engineering, Architecture and Geodesy, University of Split](#)



UNIVERSITY OF SPLIT


DIGITALNI AKADEMSKI ARHIVI I REPOZITORIJI



**UNIVERSITY OF SPLIT, FACULTY OF CIVIL
ENGINEERING, ARCHITECTURE AND GEODESY**

**UNIVERSITÉ DE TECHNOLOGIE DE COMPIÈGNE
SORBONNE UNIVERSITÉS**

Gabrijela Grozdanić, mag.ing.aedif.

**MULTISCALE NUMERICAL MODEL
FOR THE ANALYSIS OF LAMINATED
GLASS STRUCTURES EXPOSED TO
STATIC LOAD**

D o c t o r a l t h e s i s

Split & Compiègne, 2024

Gabrijela Grozdanic, mag.ing.aedif.

Serial number: 059

This doctoral dissertation has been submitted for evaluation to Faculty of Civil Engineering, Architecture, and Geodesy of the University of Split, for the purpose of obtaining a doctoral degree in the field of Technical sciences, scientific field of Civil engineering

Mentors: Prof. Mirela Galic, PhD

Prof. Adnan Ibrahimbegovic, PhD

The committee for evaluation:

Assoc. Prof. Neno Toric, PhD, University of Split

Prof. Pierre Villon, PhD, UT Compiegne

Prof. Ivica Kozar, PhD, University of Rijeka

Prof. Damir Lazarevic, PhD, University of Zagreb

Asst. Prof. Ismar Imamovic, PhD, University of Sarajevo

Assoc. Prof. Chiara Bedon, PhD, University of Trieste

Asst. Prof. Sandra Jordão, PhD, University of Coimbra

The defence committee:

Assoc. Prof. Neno Toric, PhD, University of Split (Président)

Prof. Pierre Villon, PhD, UT Compiègne

Prof. Ivica Kozar, PhD, University of Rijeka (Rapporteur)

Asst. Prof. Ismar Imamovic, PhD, University of Sarajevo

Assoc. Prof. Chiara Bedon, PhD, University of Trieste

Prof. Mirela Galic, PhD, University of Split (Directeur de thèse)

Prof. Adnan Ibrahimbegovic, PhD, UT Compiègne (Directeur de thèse)

Asst. Prof. Sandra Jordão, PhD, University of Coimbra

The doctoral dissertation has been defended on 19th July, 2024.

Secretary:

Saša Delić, LL.M. (dipl. iur.)

This dissertation contains:

153 text pages

60 figures

21 tables

123 references

Acknowledgments

At the beginning, I would like to thank several people for their contributions and help during this entire process:

- * to my supervisors, **Professor Mirela Galic and Professor Adnan Ibrahimbegovic** who guided me throughout this journey and provided me with valuable knowledge that enabled me to complete this thesis successfully. They created ideas and visions for every step of this journey and guided me through new findings in the field of glass structures. My mentors invested a lot of knowledge, patience, and enthusiasm in helping me, for which I am very grateful.*
- * to my husband **Mislav** for his unconditional support, understanding, and optimism*
- * to my friend **Tomislav** who was always there for me, endlessly slapping me with sarcasm and fixing my grammar (except this thesis, thank you **Jagoda**)*
- * to my family for their unwavering support*
- * to my friends and colleagues for their help, compassion and for making this path pleasant and fun*

I would like to thank the reviewers of this thesis and committee members for evaluating and improving this work with comments, questions, and suggestions.

Additionally, I would like to thank the Faculty of Civil Engineering, Architecture and Geodesy in Split for their support and assistance.

This thesis has been supported by the Erasmus program, which was possible by the supportive and helpful people of the Erasmus office at the University of Split.

The used equipment was partially supported through project KK.01.1.1.02.0027, a project co-financed by the Croatian Government and the European Union through the European Regional Development Fund.

Gabrijela Grozdanic, mag.ing.aedif.

Multiscale numerical model for the analysis of laminated glass structures exposed to static load

Abstract:

This thesis presents a multiscale numerical model for the analysis of laminated glass structures exposed to static loads, and its validation with experimental tests and analytical calculations. The first part deals with the influence of atmospheric temperatures and load duration on laminated glass structures. The aim of this research is to analyse the stiffness degradation of laminated glass members exposed to different atmospheric temperatures and different load durations. The influence of these parameters is analysed through analytical calculations and numerical models. Analytical calculations include the effective thickness approach (ETA), and different expressions taken from the literature and regulations are used to define the effective thickness of the laminated glass elements. The accuracy of prediction for deflection and stress under applied loads was tested for each expression, by varying the temperature and load duration. The obtained results from the applied analytical expressions were compared and analysed. Numerical calculations were carried out using numerical models created in the ANSYS software. These numerical models were first validated by experimental tests conducted according to EN 1288-3. A four-point bending test was used so that the obtained results could be compared with available results from the literature. In the experiments, specimens were tested until fracture, while in the numerical analysis, the fracture was not simulated due to the lack of methods that could reliably describe the nonlinear behaviour of the glass part of the member. This issue arises in the simulation of the glass's nonlinear behaviour when exposed to static loads. Therefore, the analysis was conducted for a fixed load value (stress kept under nonlinear limits), but the temperature and load durations were varied. The results showed a significant influence of temperature and load durations, as well as the type and thickness of the interlayer, on the behaviour of laminated glass elements.

In the second part of this work, the focus is on solving the problem encountered in the numerical analysis from the previous step. There are not many numerical methods that can accurately predict the nonlinear behaviour of brittle materials exposed to static loads, and those that are capable usually require input to define an initial crack. Simulation of the initial crack

is not in the spirit of glass material because this type of analysis mostly observes the crack propagation, and an initial crack in glass elements implies the breakage of the whole element (especially in the case of tempered glass). The lack of methods for simulating the non-linear behaviour of laminated glass members exposed to static loads is solved here with a multiscale model that uses the embedded discontinuity method in simulations of nonlinear behaviour. The embedded discontinuity method is capable of simulating crack appearance in solids without the demand for initial cracks. By using the embedded discontinuity method, a multiscale model is developed, that can simulate the ultimate load for laminated glass elements without simulating detailed fracture pattern. The model consists of a micro model that simulates a real laminated glass cross-section and a macro model that represents a monolithic cross-section with assigned material behaviour according to the micro model. This model is further extended for plate structures using discrete Kirchhoff plate theory and a constitutive model for the principal directions of the internal forces/stresses. The basic micro model is also used to define the constitutive behaviour, but this time for the principal directions of macro plate elements.

In the third part of the research, in-plane loaded laminated glass elements are analysed using a combination of a simple numerical model and “Level 2” of interlayer modelling from regulations. The “Level 2” interlayer modelling proposes the simplified engineering approach (ETA) from regulations (and literature). This approach is analysed regarding the prediction of buckling forces for in-plane loaded laminated glass members. Two numerical models are used: one discretized with beam finite elements and the other with shell finite elements. The analysis was performed for several different geometries of laminated glass specimens, with different types of interlayers and different boundary conditions. The buckling force prediction is validated by comparing the results with experimental results from the literature for different geometries, interlayers, and boundary conditions. This work presents the analysis of laminated glass elements exposed to out-of-plane and in-plane static loading.

Keywords: laminated glass, numerical analysis, out-of-plane loading, in-plane loading, effective thickness approach

Gabrijela Grozdanic, mag.ing.aedif.

Višeskalni numerički model za analizu laminiranih staklenih konstrukcija izloženih statičkom opterećenju

Sažetak:

U ovom radu predložen je višeskalni numerički model za analizu laminiranih staklenih konstrukcija izloženih statičkom opterećenju potkrijepljen eksperimentalnim ispitivanjima i analitičkim proračunima. U prvom dijelu analizirani su laminirani stakleni elementi izloženi statičkom opterećenju i promjeni temperature. Prikazana je degradacija krutosti elemenata od laminiranog stakla izloženih različitim temperaturama, koje se nalaze unutar amplitude atmosferskih temperatura, te različitom trajanju opterećenja. Utjecaj ovih parametara analiziran je analitičkim proračunima i numeričkim modelima. Analitički proračuni podrazumijevaju tzv. pristup efektivne debljine – ETA gdje su korišteni različiti izrazi za definiranje efektivne debljine laminiranog staklenog elementa, preuzeti iz literature i propisa. Testirana je točnost predviđanja veličine progiba i naprezanja za primijenjeno opterećenje uz variranje temperature i trajanja opterećenja. Uspoređeni su i analizirani dobiveni rezultati primijenjenih analitičkih izraza. Numerički proračun je proveden kreiranim numeričkim modelima u programskom paketu ANSYS. Numerički modeli najprije su validirani eksperimentalnim ispitivanjima provedenima prema EN 1288-3 tako da se dobiveni rezultati mogu usporediti i s dostupnim rezultatima iz literature. U eksperimentima uzorci su ispitani do loma, dok se u numeričkoj analizi lom nije simulirao zbog ograničenja samog računalnog programa. Ovakav se problem javlja u simulaciji nelinearnog ponašanja stakla izloženog statičkom opterećenju. Stoga je analiza provedena za fiksnu vrijednost opterećenja (naprezanje se održava ispod granice nelinearnosti), uz variranje temperature, trajanja opterećenja i debljine slojeva. Analiza je pokazala utjecaj temperature i trajanja opterećenja, kao i vrste i debljine međusloja na ponašanje laminiranih staklenih elemenata, što je u radu potkrijepljeno dobivenim rezultatima.

U drugom dijelu rada fokus je na rješavanju problema koji se pojavio u prethodno opisanoj numeričkoj analizi. Numeričke metode koje se primjenjuju za simulaciju materijalne nelinearnosti krutih materijala pri statičkom opterećenju kao ulazni parametar zahtijevaju definiranje položaja inicijalne pukotine. Definiranje položaja inicijalne pukotine kao ulaznog parametra nije dobar pristup u analizi laminiranih staklenih konstrukcija zbog fizikalne prirode

stakla kao materijala jer se ovom vrstom analize uglavnom promatra propagacija već definirane početne pukotine. Početna pukotina u staklu uzrokovala bi lom cijelog elementa (posebno u slučaju kaljenog stakla) pa ovakav pristup nema fizikalno opravdanje. Nedostatak metoda za simulaciju nelinearnog ponašanja laminiranog stakla izloženog statičkom opterećenju ovdje je riješen modelom s više razmjera koji koristi metodu ugrađenog diskontinuiteta u simulacijama nelinearnog ponašanja. Metoda ugrađenog diskontinuiteta simulira pojavu pukotina u materijalu, bez potrebe za definiranjem položaja početne pukotine kao ulaznog parametra. Korištenjem metode ugrađenog diskontinuiteta razvijen je model u više razmjera koji može simulirati nosivost konstrukcije od laminiranog stakla bez simulacije detaljnog uzorka loma. Model se sastoji od mikromodela koji simulira stvarni poprečni presjek laminiranog stakla i makromodela koji ima monolitni presjek s konstitutivnim zakonom ponašanja materijala definiranim mikromodelom. Ovaj model je dalje proširen za analizu laminiranih staklenih konstrukcija pri diskretizaciji pločastim elementima, korištenjem diskretne Kirchhoffove teorije ploča. Osnovni mikro model se koristi za definiranje konstitutivnog zakona ponašanja, ali ovaj put za glavne smjerove momenata u makro elementu ploča.

U trećem dijelu istraživanja analiziraju se laminirani stakleni elementi opterećeni u ravnini i to kombinacijom numeričkog modela s „Razinom 2“ modeliranja međusloja prema tehničkim propisima. „Razina 2“ modeliranja međusloja podrazumijeva definiranje efektivne debljine elementa prema dostupnim analitičkim izrazima koji se koriste u numeričkom modelu za predviđanja sile izvijanja. Korištena su dva numerička modela, jedan koji primjenjuje diskretizaciju grednim elementima, a drugi elementima ljuske. Analiza je provedena za nekoliko različitih geometrija laminiranog stakla, s različitim vrstama međuslojeva i različitim rubnim uvjetima. Predviđanje sile izvijanja potvrđeno je usporedbom rezultata s eksperimentalnim rezultatima iz literature za različite slučajeve geometrije, međuslojeva i rubnih uvjeta. U sažetku, tri dijela ovoga rada prikazuju analizu laminiranih staklenih elemenata izloženih statičkom opterećenju izvan ravnine i u ravnini.

Keywords: laminirano staklo, numerička analiza, opterećenje izvan ravnine, opterećenje u ravnini, pristup efektivne debljine

Gabrijela Grozdanic, mag.ing.aedif.

Modèle numérique multi-échelle pour l'analyse de structures en verre feuilleté soumises à un chargement statique

Résumé:

Dans cette thèse, on propose un modèle numérique multi-échelle pour l'analyse des structures en verre feuilleté soumises à un chargement statique, et on le valide par des tests expérimentaux et des calculs analytiques. La première partie traite de l'influence des températures atmosphériques et de la durée des charges sur les structures en verre feuilleté. Le but de cette recherche est d'analyser la dégradation de la rigidité des éléments en verre feuilleté exposés à différentes températures atmosphériques et différentes durées de charge. L'influence de ces paramètres est analysée par des calculs analytiques et numériques. Les calculs analytiques incluent l'approche de l'épaisseur effective (ETA), et lors de l'analyse, différentes expressions tirées de la littérature et de la réglementation sont utilisées pour définir l'épaisseur effective des éléments en verre feuilleté. La précision de la prédiction de la flèche et de la contrainte pour la charge appliquée a été testée pour chaque expression, en faisant varier la température et la durée de la charge. Les résultats obtenus des expressions analytiques appliquées sont comparés et analysés. Le calcul numérique est réalisé à l'aide de modèles numériques créés dans le logiciel ANSYS. Les modèles numériques ont d'abord été validés par des tests expérimentaux réalisés selon la norme EN 1288-3. L'essai de flexion quatre points a été utilisé afin que les résultats obtenus puissent être comparés aux résultats disponibles dans la littérature. Dans les expériences, les échantillons sont testés jusqu'à la rupture, tandis que dans l'analyse numérique, la rupture n'est pas simulée en raison du manque de méthodes permettant de décrire de manière fiable le comportement non linéaire de la partie en verre de l'élément. Ce problème se produit dans la simulation du comportement non linéaire du verre lorsqu'il est exposé à des charges statiques. Par conséquent, l'analyse est effectuée pour une valeur de charge fixe, mais la température et les durées de charge ont varié. Les résultats montrent la grande influence de la température et des durées de charge, ainsi que du type et de l'épaisseur de l'intercalaire sur le comportement des éléments en verre feuilleté. La deuxième partie de ce travail concerne la résolution du problème apparu lors de l'analyse numérique en étape précédente. Il n'existe pas beaucoup de méthodes numériques capables de prédire avec précision le comportement non linéaire des matériaux fragiles exposés à un chargement

statique, et celles qui en sont capables ont généralement besoin de définir une fissure initiale. La simulation de la fissure initiale n'est pas dans l'esprit du matériau verrier car ce type d'analyse ne peut s'appliquer que pour la propagation de la fissure, et une fissure initiale dans les éléments en verre signifie la rupture de l'élément dans son ensemble (surtout dans le cas du verre trempé). Le manque de méthodes de simulation du comportement non linéaire des éléments en verre feuilleté exposés à un chargement statique est résolu ici avec un modèle multi-échelle qui utilise la méthode de discontinuité forte intégrée dans les simulations du comportement non linéaire. La méthode de discontinuité forte est capable de simuler l'apparition de fissures dans une structure, sans besoin de postuler une fissure initiale. En utilisant la méthode de discontinuité forte, un modèle multi-échelle est développé, capable de simuler la charge ultime pour les éléments en verre feuilleté sans simulation de modèle de fracture détaillé. Le modèle se compose d'un modèle micro qui simule une section transversale réelle de verre feuilleté et d'un modèle macro qui est une section transversale monolithique avec un comportement de matériau attribué selon le modèle micro. Ce modèle est encore étendu aux structures de type plaque, en utilisant la théorie des plaques discrètes de Kirchhoff et un modèle constitutif pour les directions principales des forces/contraintes internes. Le modèle micro de base est également utilisé pour définir le comportement constitutif, mais cette fois pour les directions principales de moments fléchissant calculés par un élément de plaque. Dans la troisième partie de la recherche, des éléments de verre feuilleté chargés dans le plan sont analysés et la combinaison d'un modèle numérique avec le « niveau 2 » de modélisation simplifiée d'interface entre couches issue de la réglementation (ETA) est utilisée dans l'analyse. Le « niveau 2 » implique de définir l'épaisseur effective de l'élément en fonction des expressions analytiques disponibles utilisées dans le modèle numérique pour prédire l'effort de flambement. Cette approche est utilisée pour calculer des charges critiques de flambement pour les éléments en verre feuilleté chargés dans le plan. Les deux modèles numériques sont utilisés, l'un construit des éléments finis de poutre et l'autre des éléments finis de coque. L'analyse a été réalisée pour plusieurs géométries différentes d'échantillons de verre feuilleté, avec différents types d'intercalaires et différentes conditions aux limites. La prédiction de la force de flambement est validée en comparant les résultats avec les résultats expérimentaux de la littérature pour différentes géométries, interfaces entre les couches et conditions aux limites. En somme, les trois parties du travail présentent l'analyse d'éléments en verre feuilleté soumis à des charges statiques appliquées hors plan et dans le plan.

Mots clés : verre feuilleté, analyse numérique, chargement hors plan, chargement dans le plan, approche de l'épaisseur effective

CONTENTS

- 1. INTRODUCTION 1**
 - 1.1. Motivation 2
 - 1.2. General Information About Glass, Types of Glass and Usage 2
 - 1.2.1. History and Production of Glass..... 2
 - 1.2.2. Glass Chemistry..... 3
 - 1.2.3. Glass as a Structural Material 4
 - 1.2.4. Laminated glass (LG) 6
 - 1.3. Overview of Standards and Regulations for Dimensioning 7
 - 1.4. Hypothesis of the Work and Main Goals 10
- 2. INFLUENCE OF TEMPERATURE AND LOAD DURATION ON THE BEHAVIOUR OF LAMINATED GLASS ELEMENTS LOADED OUT OF PLANE..... 13**
 - 2.1. Introduction 14
 - 2.2. Overview of the Research Area..... 14
 - 2.3. Experimental Tests on LG Specimens According to EN 1288-3 18
 - 2.4. Description of a Numerical Model for Analysing the Behaviour of LG Elements 22
 - 2.5. Model Results of a Parametric Study of Interlayer Properties Influence on the Bearing Capacity of LG Elements 24
 - 2.6. Effective Thickness Approaches in Cases of Different Temperatures and Load Durations 34
 - 2.6.1. Effective Thickness Approach (ETA) – Different Methods..... 34
 - 2.6.2. Effective Thickness Approach – Analytical Calculations for Different Temperatures and Load Durations..... 39
 - 2.7. Chapter Conclusions 49
- 3. MULTISCALE MODEL WITH EMBEDDED DISCONTINUITY FOR SIMULATION OF LAMINATED GLASS ELEMENTS EXPOSED TO OUT-OF-PLANE LOADING 51**
 - 3.1. Introduction 52
 - 3.2. Numerical Simulations of Glass Breakage and Fragmentation – Methods Used in Literature 52
 - 3.3. Embedded Discontinuity Method 55

3.4. Multiscale Model With Embedded Discontinuity	57
3.5. Mathematical Formulations of Fine-Scale Multilayer Model	58
3.5.1. Kinematic Equations for Fine-Scale Multilayer Model	58
3.5.2. Constitutive Laws for Glass and Polymer in Fine-Scale Multilayer Model.....	63
3.5.3. Equilibrium Equations for Fine-Scale Multilayer Model.....	66
3.6. Mathematical Formulations of the Coarse-Scale Macro Model With Beam Elements	67
3.6.1. Kinematic Equations for Coarse-Scale Macro Model (Macro Model 1)	68
3.6.2. Constitutive Laws For the Macro Model Elements.....	70
3.7. Application of Presented Mathematical Formulation in the Numerical Model.....	72
3.7.1. Layer Optimization for a Fine-Scale Multilayer Numerical Model	74
3.7.2. Mesh Objectivity Test for the Macro Numerical Model	74
3.7.3. Determination of Input Parameters for Coarse-Scale Macro Models	75
3.8. Numerical Simulation Four-Point Bending Tests in Multiscale Model .	77
3.8.1. Numerical Simulation of Tests 1, 2 and 3 in Macro Model 1	79
3.8.2. Numerical Simulation of Tests 4 and 5 in Macro Model 1	84
3.8.3. Numerical Simulation of Test 6 in Macro Model 1.....	86
3.9. Mathematical Formulations for the Coarse-Scale Macro Model 2 With Plate Elements	87
3.9.1. Kinematic Equations for Macro Model 2.....	88
3.9.2. Constitutive Equations for Macro Model 2.....	89
3.10. Chapter Conclusions.....	94
4. STABILITY OF LAMINATED GLASS ELEMENTS EXPOSED TO IN-PLANE LOADING	96
4.1. Introduction	97
4.2. Overview of the Research Area.....	97
4.2.1. Effective Thickness Approach in Buckling Analysis.....	101
4.3. Brief Model Description	104
4.4. Numerical Prediction of Critical Buckling Load for Laminated Glass Elements	105
4.4.1. Test 1 – Laminated Glass Elements (2-Ply and 3-Ply Cross-Section)	105
4.4.2. Test 2 – Laminated Glass Elements With Different Geometry.....	111
4.4.3. Test 3 – Laminated Glass Elements With Different Boundary Conditions.....	116

4.5. Chapter Conclusions	120
5. OVERVIEW OF RESEARCH RESULTS.....	123
5.1. Summary of all Conducted Research	124
5.2. Overview of Research Results	125
6. CONCLUSION AND FURTHER PERSPECTIVES.....	130
6.1. Conclusions Based on the Obtained Results.....	131
6.2. Future Perspectives	132
7. BIBLIOGRAPHY.....	134
7.1. Bibliography	135
7.2. List of Figures.....	142
7.3. List of Tables	146
7.4. List of Published Papers	148
7.5. List of Attended Conferences	149
APPEDIX A.....	150

1. INTRODUCTION

Contents

- 1.1. Motivation
 - 1.2. General Information About Glass, Types of Glass and Usage
 - 1.3. Overview of Standards and Regulations for Dimensioning
 - 1.4. Hypothesis of the Work and Main Goals
-

1.1. Motivation

The desire for unhindered contact with nature which arises from an imposed deficiency greatly influences the architectural design of buildings. This trend of bringing the interior spaces closer to the exterior with an emphasizing a connection with nature, is a logical progression guided by changes in everyday life. Historical buildings had minimal contact with the environment as a consequence of a lifestyle that involved spending most of the time outside. Today, when most work is carried out indoors, there is a strong urge to communicate with nature and minimize boundaries. This trend results in the design of more open buildings, achieved through the use of transparent outer envelopes that facilitate the desired interaction with the outside world. As boundaries continue to be pushed in today's world, transparent facades further develop into transparent structures.

This movement has led to the development of new and the rediscovery of already familiar transparent materials. Glass has taken a leading role, with its usage significantly increasing in the construction industry, evolving from a secondary material into a structural one. However, regulations have not kept pace with this transition, remaining in the development phase and not yet standardized at the European level. Current standards for glass [1][2][3] not cover all aspects of its structural use with the detailed and elaborated approach seen with other building materials. Many aspects remain unfamiliar, necessitating detailed research.

This situation explains the main motivation for this research which is to provide a better understanding of laminated glass behaviour and to define an appropriate approach to its modelling. This thesis presents several studies focused on identifying the essential aspects of designing glass structures and recognizing the pitfalls that occur in the design process. The general expected outcome is to bring engineers closer to using laminated glass as a constructive material and to make the design process more effective.

However, it is first necessary to be familiar with the basic characteristics and current knowledge. For that reason, basic information and current achievements are described in the next few sections.

1.2. General Information About Glass, Types of Glass and Usage

1.2.1. History and Production of Glass

Glass as a material has been known since 2000 years BC when the first elements of glass were created as accidental by-products of metal-working. Glass can also be found in nature in specific places containing silicate minerals where temperatures of over 1500 °C occur (such as

during lightning strikes and volcanic eruptions). Until the development of industrial production in the first part of the 20th century, glass was an inaccessible and expensive material. The complexity of the production method, which requires significant skill, was the leading cause of its high cost. Today, glass is produced in furnaces using the Float process, where part of glass ingredients are raw materials and another part is cullet, which lowers the melting point. The invention of the Float process is the most significant milestone in the recent history of glass, as it has greatly simplified the production of flat glass. The Float process scheme is shown in Figure 1.1. In the Float process, liquid glass is poured from the furnace into a bath of molten tin. Due to its lower density, the glass floats, forming a continuous strip that is then carried on small rollers and gradually cooled, allowing the release of residual stresses. The tin bath serves as a base for cooling and transporting the molten glass in the production process. Tin is commonly used because it has a higher density than glass and a low melting point while retaining its liquid form over a wide temperature range (232 °C to 2270 °C). By producing a flat surface that does not require any post-processing this invention made glass production more efficient and by that more affordable. [4] This simplified production method has significantly impacted glass usage, and today, glass is present in every aspect of life.

1.2.2. Glass Chemistry

According to ASTM, "Glass is an inorganic fusion product that has cooled to a solid state without crystallization." Molten glass is obtained by heating a mixture of silica, calcium oxide, and sodium oxide with additives at a temperature of about 1500 °C. While silicon dioxide alone is sufficient to make glass, the melting point of such a mixture is around 1700 °C. The addition of CaO and Na₂O reduces the melting temperature, thereby lowering the amount of energy required. [5] Sodium decreases the melting point of silicon dioxide but makes it soluble in water, so lime is added to counteract this effect. Depending on the elements added to the glass mixture, change of properties such as colour, increased heat resistance, and other can be achieved. Glass is formed by a cooling process that occurs at such a rate that crystallization does not happen. During cooling, the viscosity of the glass increases, which leads to an amorphous state that can be described as the "freezing" of liquid glass because the liquid structure is retained. Unlike a crystalline formation (e.g., quartz), glass does not have a strictly defined melting point, but exhibits the elasticity of crystalline substances during heating. [6] The most common glass in everyday use is sodium-calcium-silicate glass (SiO₂-Na₂O-CaO). The material characteristics of this type of glass, compared with borosilicate glass, are shown in Table 1.1.

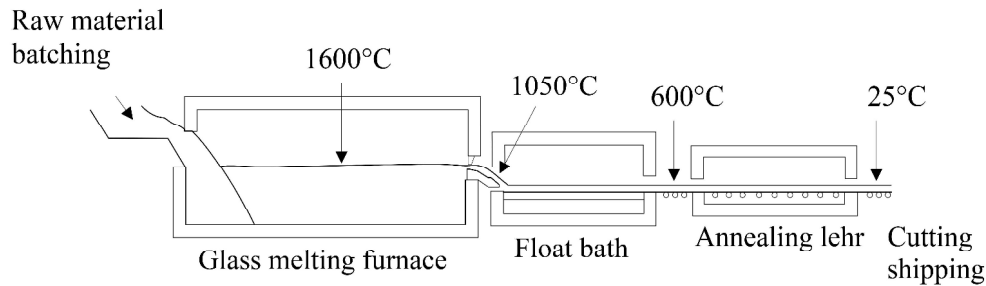


Figure 1.1. Float process scheme [7]

1.2.3. Glass as a Structural Material

In terms of mechanical characteristics, glass can be compared to primary building materials, in Figure 1.2. a comparison of stress-strain diagrams is presented. The theoretical failure stress of silica bonds is up to ≈ 30 GPa [8], but due to imperfections that occur in glass elements during production, it is impossible to achieve such strengths in practice. The brittle nature of glass, caused by inevitable networks of flaws, makes it a high-risk material for sudden loss of load-bearing capacity. [5] The macroscopic strength of glass depends on these imperfections, known in the field of linear elastic fracture mechanics as Griffith flaws. [9][10] Due to this unpredictability, macroscopic strength is usually determined using standard statistical distributions such as the Weibull and Gumbel distributions. [11] Typical structural glass is created from the basic glass product known as float glass. During production, float glass undergoes an annealing process (slow cooling) to release residual stress, resulting in basic non-treated glass called annealed glass. This type of glass can be used without any additional treatment if there are no specific demands for strength or safety, and it is widely used as a transparent, non-structural filling. Annealed glass can be further treated to induce compressive stresses on its surface, thereby increasing its load-bearing capacity. Glass processed in this way (tempered glass, heat-strengthened glass) has increased tensile strength and a different (smaller) fracture pattern compared to ordinary annealed glass. There are two methods to achieving tempering: chemical treatment or heating and rapidly cooling glass sheets. The difference between the fracture patterns of annealed and tempered glass is presented in Figure 1.3. Annealed glass produces large, sharp pieces upon fracture, while tempered glass breaks into small cubical pieces. Heat-strengthened glass is also tempered glass but with a lower level of prestressing. [12] The characteristic bending strength for differently treated glass according to prEN 13474:2009 [13] is presented in Table 1.2. The mechanical characteristics of glass are not influenced by temperature changes within ambient temperature intervals.

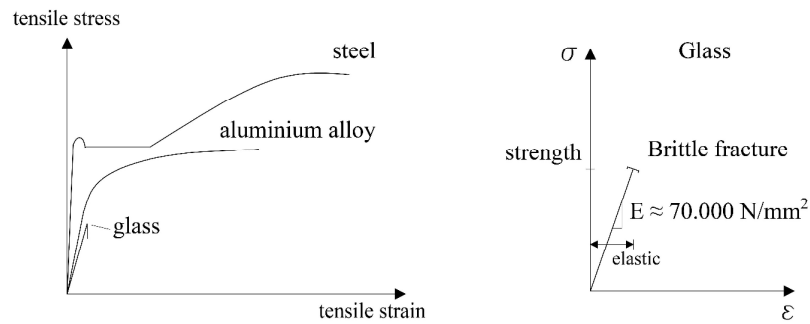


Figure 1.2. Stress-strain diagrams for structural materials [14]

Table 1.1. Physical properties of glass [4] [11]

Property	Label	Unit	Soda lime silica glass	Borosilicate glass
Density	ρ	kg/m ³	2500	2200 - 2500
Knoop hardness	$HK0.1/20$	GPa	6	4.5 - 6
Young's modulus	E	MPa	70000	60000 - 70000
Poisson's ratio	ν	-	0.23	0.2
Coef. of thermal expansion	a_t	10 ⁻⁶ K ⁻¹	9	4.0 - 6.0
Specific thermal capacity	c_p	Jkg ⁻¹ K ⁻¹	720	800
Thermal conductivity	λ	Wm ⁻¹ K ⁻¹	1	1
Average refractive index within the visible spectrum	n	-	1.52	1.5
Surface energy	γ	J m ⁻²	0.6	
Fracture toughness	K_{Ic}	MPa m ^{1/2}	0.75	
Stress corrosion threshold limit		MPa m ^{1/2}	0.25	

Table 1.2. Characteristic bending strength of each type of glass according to prEN 13474:2009 [13] and degree of surface prestressing

Annealed glass/Float glass	Heat-strengthened glass (HSG)	Thermally toughened glass (TTG)
45 N/mm ² (0 MPa)	70 N/mm ² (30 - 50 MPa)	120 N/mm ² (> 90 MPa)

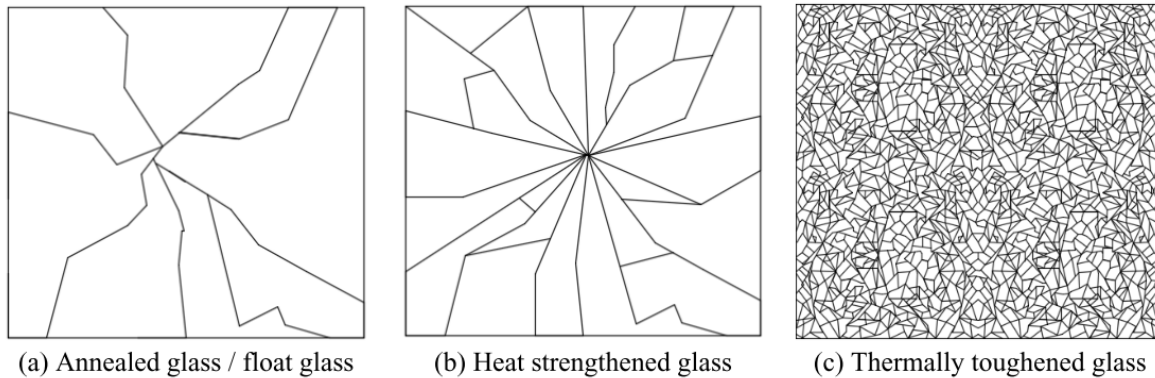


Figure 1.3. Breakage pattern for different types of glass [15]

1.2.4. Laminated Glass (LG)

Since glass is an extremely brittle material and therefore unpredictable in terms of safety, the basic requirement for structural elements made of glass is to ensure a certain load-bearing capacity after fracture in the post-fracture limit state (PFLS). Laminated glass is one form of intervention in glass constructions that provides additional load-bearing capacity after one or several plies breaks. It is a product created by joining two or more glass plies with polymer interlayers that ensure the integrity of the element and the transfer of shear stresses on the contact surfaces. The behaviour after fracture is mostly dependent on the type of glass from which the LG is made. Annealed and heat-strengthened glass provide a locking effect due to larger pieces of glass within the fracture pattern [16], while tempered glass (which has a significantly higher fracture limit load) does not ensure additional locking after the breakage of the whole pane occurs. More precisely, because of extremely small fragments and in combination with a soft interlayer, a phenomenon called the „wet blanket effect“ appears once the whole pane is broken. This is the exact opposite effect of the locking effect, causing a complete loss of stability, especially if the glass is not well attached to the supports. [17][18] In addition to the type of glass, the interlayers that connect the glass plies also have a significant impact on the load-bearing capacity of LG. The most common interlayers in the production of LG are PVB (polyvinyl butyral), EVA (ethylene vinyl acetate) and interlayers based on ionomer (ionoplast). There are many variations in the mechanical characteristics of the mentioned types of interlayers depending on the manufacturers and the used chemical compositions. The interlayers come in different thicknesses (and numbers of layers) depending on the type of material and requirements, and most often it is in the range of 0.36 mm - 2.28 mm. The bearing capacity of the interlayers depends significantly on the temperature and duration of the load [19][20][12]. The influence of interlayer on the bearing capacity of LG structures will be first presented in the literature overview in section 2.1., and further numerically tested in Chapter 2.

1.3. Overview of Standards and Regulations for Dimensioning

The design of glass structures is defined in three parts of the European glass standards which cover general terms related to glass and the design basis in the first part [1], glass elements loaded perpendicular to the plane (out of plane) in the second part [2], and in the third part [3] elements loaded in-plane. In the first part, basic concepts and categorization of glass elements are defined, along with different limit states and basis of design being presented. The regulation refers to the norm EN 1990 for basic rules and defines a few peculiarities regarding glass members. For environmental and climatic influences, the regulation refers to the norm EN 1991 and EN 1998, with additional demands regarding cavity pressure in insulating glass units (IGU). The main division regarding design stages is into the serviceability limit state (SLS), ultimate limit state (ULS), fracture limit state (FLS), and post-fracture limit state (PFLS). The demand to design glass structures in each of the listed states is defined with four (0-3) limit state scenarios. FLS is presented as “failsafe verification” that can be verified by experimental tests or appropriate theoretical assessment where all effects appearing during the fracture are simulated. PFLS is described as the capacity of a structure to provide residual resistance for a certain time after breakage; this state also can be verified by experimental tests or by theoretical assessment. Both the FLS and the PFLS are described as cases where accidental load combinations should be used. Furthermore, in the first part, all standards for the production of different types of glass and their basic mechanical characteristics are listed. There are special requirements regarding thermally treated glass (HSG and TTG) for increased safety related to damage and chemical composition control. For the interlayer, different aspects such as load duration, moisture, UV radiation, temperature thermal cycling, etc., are mentioned as important features in design but without a detailed description of their influence. Shear stiffness, as the most influential characteristic in the aspect of the load-bearing capability of LG elements, is proposed to be determined according to the EN 16613 [21] regulation, which describes experimental tests and analytical expression to determine interlayer properties and how to place them in appropriate stiffness family. It is emphasized that the mechanical properties of interlayer and all belonging influences are not yet standardized and will be updated in upcoming versions of standards. For stress determination in LG structures, the first part of the regulation defines a linear elastic material model without any ductility as appropriate for glass modelling and a non-linear material model for interlayer or other polymer-like material features. The consideration of shear interaction is divided into three stages, with the early mentioned material models (non-linear material model) in the form of numerical calculation being the third, most

detailed level of interlayer modelling. In the first level, a rather radical approach of neglecting any influence of the interlayer in case of a favourable effect and taking into consideration a full interaction in case of an unfavourable effect on the structure is proposed. The second level defines the usage of analytical models or simplified approaches that are proposed in the regulation but with proof of their validity. Further in the regulation [1], special attention is paid to substructures acting as glass supports and connections in glass structures to avoid local peaks and overcome initial and acquired geometric irregularities. Bending resistance is determined in Annex A and Annex B for monolithic glass by taking into consideration production details and compliance methods, as well as type of load and load duration. The first part of the regulations concludes with a short description of the main features that can cause thermal stress in monolithic panels and describes the factors that should be considered; this part is not related to the LG.

The second part of the regulations [2] is related to out-of-plane load and contains a brief introduction that recalls concepts presented in the first part of the regulation. The greatest focus in this part is on joints, connections, and supports of glass structures, and the simplified analytical approach known as the “effective thickness approach”. The focus here is on the analytical approach since this concept will be used in this research in several different analyses. The effective thickness approach (ETA) is designed as a simple solution for complex composite cross-sections where the layered cross-section, often consisting of different materials, is replaced with a homogenized (monolithic) cross-section with reduced height and unique material characteristics. In the observed second part of the newest draft version of the regulation, there are two effective thickness concepts proposed. The first is the concept proposed in the regulation in Annex A, as an informative option with the expression for deflection prediction (effective thickness $h_{eff,w}$) and stress prediction (effective thickness for i -th ply $h_{eff,\sigma,i}$). The second concept refers to the previous version of the regulation [22] with the expression for deflection prediction and stress prediction; these expressions are different but they have the same purpose. The expressions from older regulations (EN 16612) [22] are defined as appropriate for use in the case of linearly supported panes subjected to uniformly distributed loads. Each approach has coefficients that describe the shear coupling of glass panels provided by the interlayer. In the first concept (from CEN/TS 19100-2:2021 [2]) it is defined as η , the coupling coefficient that depends on the number and thickness of plies, the distance from the center of the pane, the shear modulus of the interlayer (G_{int}), and Young’s modulus of glass (E). In the second approach from older regulations (EN 16612) [22], the shear transfer

coefficient ω is defined and it takes values from the interval 1-0 in dependence on the achieved shear transfer. The value of ω is defined according to the stiffness families (that are not precisely defined) and by taking into consideration load durations and temperatures. In Annex A of regulation CEN/TS 19100-2:2021 [2] a liaison between the proposed expressions for the effective thickness approach from EN 16612 [22] is defined, and it is determined as a ratio between geometric properties. These expressions will be presented in detail in Chapter 2. Besides defining these simplified engineering approaches, the second part of regulation CEN/TS 19100-2:2021 [2] defines limits for deformation class 2 from [1] and minimum edge cover for glass components of class 3 as well as other recommendations regarding joints and natural frequencies which are not the main focus of this research and won't be detailed here. The third part of regulation CEN/TS 19100-3:2021[3] refers to glass elements loaded in-plane. Similar to out-of-plane loading from [2], this regulation recalls limit state scenarios including (SLS, ULS, FLS and PFLS). Since the dominant failure mode here is stability loss, the regulation proposes ensuring robustness and possibly a second load path for the observed elements. For laminated glass, the shear interaction is again defined through the three levels, starting from the first which neglects the favourable influence of the interlayer to the second which suggests analytical calculations (effective thickness approach) to the third where a detailed numerical model is proposed. To verify different limit state scenarios, there are additional demands such as for FLS where for elements loaded in-plane “*an additional energy intensive lateral impact perpendicular to the surface at the most unfavourable location may be necessary*” [3]. For determining the resistance of glass components subjected to in-plane compression, a geometrical non-linear theory is proposed, when relevant. Second-order effects should be considered when their impact on the structure influences structural behaviour, but they can be neglected when the ratio between critical buckling force and design load for the observed structure is greater than 10. It is defined that second order effects can be performed analytically or numerically, and that buckling curves can be used for simple geometries once those are proposed. Element imperfections (geometrical and material) are combined into equivalent geometrical imperfections which should be considered in ULS, FLS and PFLS. The value of basic imperfection e_0 depends on the type of load on the element: flexural buckling and plate buckling, lateral torsional buckling and, shear buckling. It is determined by expression (1.3.1) and for $e_{0,installation}$ it is allowed to use the measured value but not less than 3 mm.

$$e_0 = \sqrt{e_{0,length}^2 + e_{0,installation}^2} \quad (1.3.1)$$

FLS and PFLS bring additional imperfection due to lateral shift after fracturing of a ply and for tempered glass due to the expansion of bonded fragments. These values are proposed in the regulation. The appearance of slip between panels at the edge of elements prone to flexural buckling failure should be prevented by enclosing the edge. The regulation further recalls the procedure for the calculation of three limit states, where for ULS the element is observed as intact, and in FLS and PFLS some of the plies should be fractured. For this type of loading, it is necessary to conduct strength and stability checks. Since glass strength is significantly higher in compression than in tension, the regulation proposes adopting the tensile strength of the observed glass as compressive strength to provide more reliable and safer calculations. Special attention is paid to dynamic effects in the case of FLS. Regarding SLS, no special demands other than those defined in the first part of the regulation are specified. The focus then shifts to joints and connections for in-plane loaded element, concluding with annexes which define the calculation of critical buckling force and critical bending moment (Annex A), followed by Annex B where effective moments of inertia are presented and Annex C which again relates on joint calculations. In Annex A, the critical buckling force is proposed based on Euler theory (expression for critical buckling force) but with the usage of effective moment of inertia ($I_{z,eff}$) for simple supported laminated glass elements. The calculation of $I_{z,eff}$ is defined in Annex B, where the proposed shape of lateral deflection component is sinusoidal. A detailed description of all members and equations for critical buckling force determination is provided in Chapter 4. The presented regulations define basic frameworks for calculations of glass and laminated glass elements serving as guidance for engineers. However, there is room for advancement and resolution of some important issues. The accuracy of the proposed effective thickness approach for in-plane and out-of-plane loaded elements is not fully defined and tested under varying temperatures and load duration. Additionally, the limits of usage of the proposed simplified method are not determined from the aspect of the size of the structure, boundary conditions, and the element's geometry.

1.4. Hypothesis of the Work and Main Goals

Considering current shortcomings in the field of glass structures, this thesis addresses three areas of interest in laminated glass constructions. Each of these topics has resulted in published papers [12][23][15] where most of the results are presented.

The first theme, presented in Chapter 2, is an analysis of the influence of atmospheric temperatures and load duration on the bearing capacity of laminated glass structures. The research addresses a lack of detailed information regarding capacity loss due to temperature

loads within the range of atmospheric temperatures and expected load durations. The research is conducted with numerical models validated by experiments. Specimens are tested until fracture, and in numerical analysis, the fracture is not simulated due to a lack of methods that could reliably describe the nonlinear behaviour of glass elements. The chosen geometry for the test is defined according to regulation EN 1288-3 [24] ensuring comparability with other results from the literature. The analysis is extended to a simplified engineering approach (ETA) where the accuracy of predicting ultimate load and deflection for assigned load is tested, again within the range of atmospheric temperatures.

The second topic, presented in Chapter 3 of this thesis, addresses the lack of methods for simulating the non-linear behaviour of glass elements exposed to static loads. This shortcoming is not present in analyses of laminated glass structures exposed to short-term impact/dynamic loads because explicit numerical methods are employed, providing excellent predictability of the structural response and fracture pattern. For static loading, there are not many numerical methods that can accurately predict the nonlinear behaviour of brittle materials, and those capable of it require the definition of an initial crack. Simulation of the initial crack is not appropriate for glass because this type of analysis primarily observes the crack propagation, and an initial crack in glass elements means the breakage of the whole element (especially in the case of tempered glass) as the propagation of cracks is an instantaneous process. The solution to this problem is proposed by using an embedded discontinuity method capable of simulating crack appearance in solids without the need for initial cracks. Based on this method, a multiscale model is developed, capable of accurately simulating the ultimate load for laminated glass elements. The model consists of a micro model that simulates a real laminated glass cross-section and a macro model that is a homogenized (monolithic) cross-section with assigned material behaviour according to the micro model. The validity of the multiscale model is tested by comparing the results with experiments, and the effective thickness approach is also tested in combination with the multiscale model. This model is further developed for plate structures, using discrete Kirchhoff plate theory and constitutive model for principal directions of inner forces and stresses. Again the basic micro Timoshenko beam model is used to define the constitutive behaviour, but this time for principal directions of macro plate elements.

The third topic, presented in Chapter 4, relates to in-plane loaded laminated glass elements and the combination of a simple numerical model with Level 2 of interlayer modelling. According to the regulations, a simplified engineering approach analysis regarding the predictability of buckling forces for in-plane loaded laminated glass elements is presented.

In each of the further sections, first, an overview of the literature is presented with an emphasis on the theme of the Chapter, followed by the research setup and the obtained results, along with the conclusions. The structure of work is divided similarly to regulations (out-of-plane and in-plane loaded elements) and it can be seen that in all chapters, an analysis of a simplified engineering approach (the effective thickness approach) is tested, and the predictability of element capacity using this approach is compared with the obtained experimental and numerical results. In all chapters, the main focus is on predicting the bearing capacity in the phase before failure and during failure, and the post-breakage capacity is not analysed in the case of out-of-plane or in-plane static loading.

2. INFLUENCE OF TEMPERATURE AND LOAD DURATION ON THE BEHAVIOUR OF LAMINATED GLASS ELEMENTS LOADED OUT OF PLANE

Contents

- 2.1. Introduction
 - 2.2. Overview of the Research Area
 - 2.3. Experimental Tests on LG Specimens According to EN 1288-3
 - 2.4. Description of a Numerical Model for Analysing the Behaviour of LG Elements
 - 2.5. Model Results of a Parametric Study of Interlayer Properties Influence on the Bearing Capacity of LG Elements
 - 2.6. Effective Thickness Approaches in Cases of Different Temperatures and Load Durations
 - 2.7. Chapter Conclusions
-

2.1. Introduction

In the previous chapter, an overview of different approaches and methods from current and former regulations was presented. As mentioned, the instructions regarding the design of laminated glass elements exposed to thermal atmospheric amplitudes and standard load duration are not precisely defined, leaving the estimation of these influences to the user's experience with a few minor guidelines.

To test the influence of real annual temperature amplitudes for regions of Croatia on the behaviour of simple laminated glass structures, a numerical analysis for different temperatures and load durations was conducted. First, an experimental test at room temperature conditions was conducted to compare the reliability of the numerical model. Using the material characteristics of the interlayer provided by the manufacturer, the observed results were compared in terms of stress and deflections. Furthermore, with a validated model and for two types of interlayers, a numerical analysis for the same specimens exposed to different temperatures was conducted. Stress and deflection, as the main measures of structural behaviour, were observed and compared. The element was numerically tested using a load level lower than the limit for ULS. The results were compared with other results from the literature and presented in 3D plots. At the end of the chapter, an overview of the results and conclusions is presented.

The majority of the upcoming results within Chapter 2 are published in the paper [12], and here the research, results and conclusions will be presented, along with additional experiments and analysis regarding the effective thickness approach (ETA). The table with the exact values of all numerical results is presented in Appendix A, and also can be found in [12].

2.2. Overview of the Research Area

Laminated glass is primarily used in applications where post-breakage capacity is essential for glass structures. Interlayers in laminated glass serve a dual purpose: first is a structural performance where they ensure the coupled behaviour of two or more glass plies by transferring shear forces between the panels. Secondly, they provide safety and post-breakage capacity which occurs after the breakage of one or more plies [25][26][27][28][29]. The interlayer retains the adhering glass fragments, preventing injuries from those fragments while also providing additional load-bearing capacity. In the tensile zone, this adhesion does not ensure any specific advantages other than retaining weight. However, in the compression zone, the glass fragments can create additional load-bearing capacity by accomplishing contact and

2. Influence of temperature and load duration on the behaviour of laminated glass elements loaded out of plane

transferring forces through the contact. The coupling behaviour in laminated glass depends on the type of interlayer, geometrical properties, and atmospheric conditions. Interlayers in LG are transparent polymer materials with significant variations in mechanical properties that depend on temperature, load duration, and moisture, affecting both coupled behaviour and post breakage capacity. [30] The mechanical behaviour of LG elements falls between two limit behaviours: one where the influence of interlayers is neglected, treating the LG as separate glass plies without frictional interaction, and a monolithic behaviour where full shear transfer through the interlayer is accomplished on LG element. [31][32] These two limits are illustrated in Figure 2.1. The behaviour of LG members within these limits depends on the mechanical properties of the interlayer, the type of loading and load duration, and the type of boundary conditions. For example, at high-velocity loads (impact), the interlayer behaves very stiffly, and the LG member behaviour is closer to the monolithic limit, whereas at longer load durations (static and long-term) the influence of the viscoelastic nature of the interlayer is emphasized. There are various types of interlayers used in LG production, but the most commonly used types of interlayers in LG structures are PVB (polyvinyl butyral), EVA (ethylene vinyl acetate), and ionoplast interlayer. Each of these mentioned materials has specific benefits and disadvantages, making it important to understand their properties before making a choice. Since the mechanical properties of interlayers are primarily affected by temperature, moisture, and load duration, researchers in [33] [34] conducted experimental and numerical tests on specimens to define parameters describing the behaviour of those materials. It has been proven in [35] that the influence of temperature reduces the relaxation time of the polymers. Shear modulus degradation due to increased temperatures and for different load durations has been observed and confirmed in static shear experimental testing [36] and long-term testing [37].

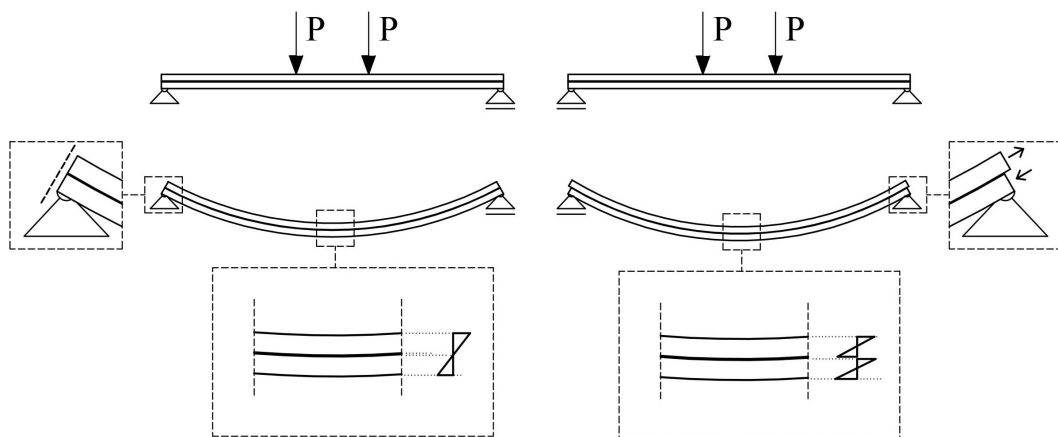


Figure 2.1. Representation of two limit states of the load capacity of LG [38]

2. Influence of temperature and load duration on the behaviour of laminated glass elements loaded out of plane

In numerical simulations of LG, different material models of interlayers are used with the chosen model depending largely on the type of loading. For the dynamic load, hyperelastic models [28] and rate-dependent hyperelastic models [29] are commonly used. For high strain rates, elastoplastic models are used [39], and for static loading, nonlinear elastic hardening models [40] are utilized.

For comparison, the material specifications of interlayers are shown in Table 2.1., and in Figure 2.2., graphs with Young's modulus taken from available technical sheets [41][42] are presented. The graph in Figure 2.2. illustrates the difference in behaviour between the ionoplast interlayer and PVB interlayer. For increasing the load duration (x axis), the slope of curves that present the degradation of Young's modulus of ionoplast interlayer (for different temperatures) is very small compared to PVB (dashed curves) which become steep for 30 min load at 20 °C, and for all load durations in case of temperatures over 30 °C. For both interlayers, the values of material characteristics decrease with higher temperatures and longer load durations, but the difference is more pronounced for the PVB interlayer. The thickness of an interlayer is standardized, with values depending on the type of interlayer. The thickness generally ranges from 0.36 mm to 2.28 mm, and the value is chosen depending on physical and structural requirements.

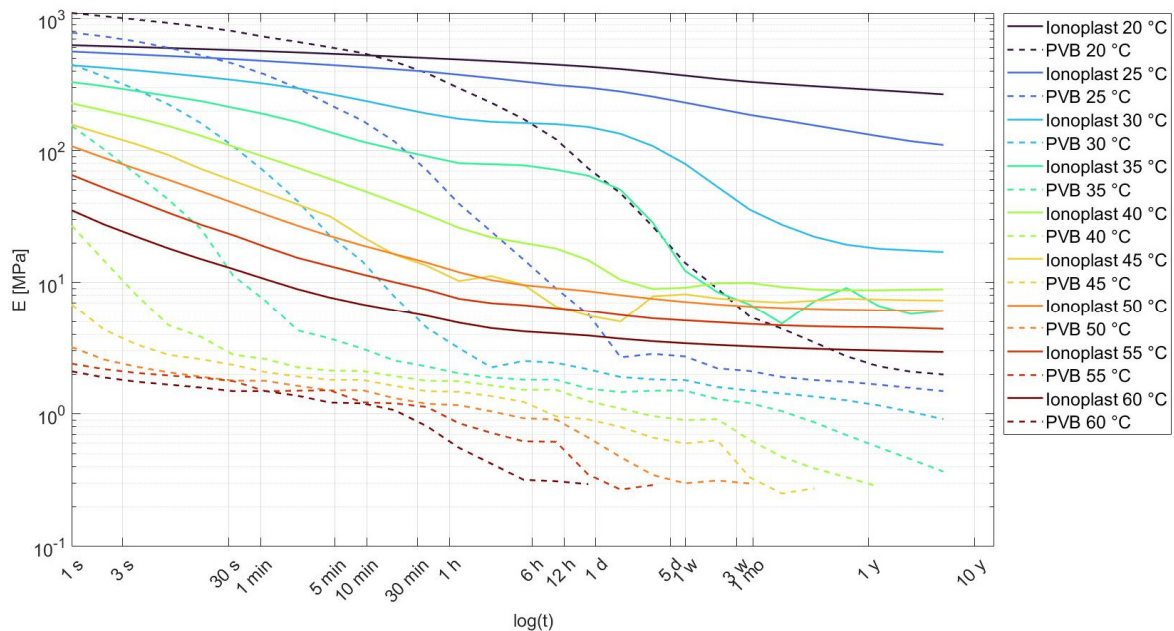


Figure 2.2. Comparison of degradation of Young modulus E (MPa), for the ionoplast and PVB interlayers due to load duration $\log(t)$ at different temperatures T (°C) [12]

2. Influence of temperature and load duration on the behaviour of laminated glass elements loaded out of plane

Table 2.1. Basic mechanical properties of the interlayers from [41][42][43][12]

	PVB (Structural)	EVA	Ionoplast
Density	1070 kg/m ³	970 kg/m ³	950 kg/m ³
Poisson's ratio	0.476	0.32	0.458
Glass transition temperature [43]	12–25 °C	–28 °C	55 °C

PVB - polyvinyl butyral - is a synthetic polymer from the polyvinyl acetate family, and is one of the most frequent materials used in LG members. The properties of PVB polymer show a dependence on moisture [44], temperature and load duration [39][45][46]. Depending on the primary purposes (acoustic, structural, and solar) different types of PVB interlayers are available each with distinct mechanical properties, resulting in varying stiffness and glass transition temperatures (T_g) [43]. It has been observed that the production process of LG with PVB causes changes in the mechanical characteristics of PVB. The mechanical properties, observed through shear modulus, show discrepancies when comparing specimens produced from raw PVB (before the autoclave process) and those embedded inside LG after the autoclave process [47]. The autoclave process, which provides heat and pressure to achieve coupling, affects the interlayer characteristics. PVB interlayers show a degradation of shear transfer between plies at increased temperatures, similar to EVA interlayers.

EVA - ethylene vinyl acetate - is a copolymer interlayer material, that is moisture resistant interlayer [44], often used for specific purposes, such as photovoltaic cells or a coloured designs. [12] EVA interlayers exhibit thermorheologically complex behaviour. [48][12] There is limited information about the material characteristics of EVA interlayers, except for those from the experiments such as humidity impact tests [49], which provide specific types of results. A dynamic single-lap shear test and dynamic torsion tests from [35] conducted on small-scale LG specimens with PVB and EVA interlayers, show differences between the two interlayers. Specimens tested at different temperatures and dynamic frequencies revealed that PVB has a stiffer response compared to EVA at temperatures below 40 °C. At a lower temperatures around -20 °C, where other interlayers have no ductility (almost brittle behaviour of interlayer occurs), EVA interlayers demonstrate better impact resistance (penetration resistance), due to their lower glass-transition temperatures. [43] However, in four-point bending tests conducted at room temperature from [50], elements with an EVA interlayer and PVB interlayer showed similar behaviour. The behaviour of samples of EVA interlayers tested in dynamic mechanical thermal analysis (DMTA), biaxial tests, and uniaxial tests [51] is described with two types of material models in dependence on the type of loading. For large deformations, where nonlinear

stress-strain behaviour occurs, the material behaviour is described with a hyperelastic model, while at small strains, EVA is described with time-dependent behaviour - linear viscoelasticity. The production of LG with EVA interlayer involves higher temperatures but does not require an autoclave process. [43]

In the literature, many studies compare different types of interlayers. In one study [20] authors tested specimens created from different types of EVA and PVB interlayers loaded in static single-lap shear tests with varying temperatures and strain rates. In another study [19] authors tested PVB specimens in double-lap long-term tests exposed to different humidity conditions and different temperatures. In both studies, it has been proven that the interlayer behaviour is highly dependent on temperature and only minimally sensitive to humidity. To simulate the behaviour of interlayers in an unfractured state of LG elements, these shear tests are more appropriate due to the realistic interlayer stress state. In uniaxial tests, the stress state is more appropriate for the simulation of PFLS. An overview of the commonly used methods for determining polymer thermos-viscoelastic behaviour is presented in [52], furthermore, the dynamic-torsion cyclic tests in rheometers on small samples of LG are described and the results are presented, which yielded similar conclusions regarding the viscous properties of interlayer material.

Ionoplast interlayer is the third most used type of interlayer, an ionomer-based material that provides the highest level of structural performance [44], but comes at highest cost. It is developed for hurricane-resistant building facades. [27] This interlayer is the best option when high strength and resistance of LG elements are necessary. [53] In static experimental tests [54], LG with an ionoplast interlayer, compared with LG with EVA and PVB interlayers, showed significantly higher ultimate load and better post-breakage capacity.

In all of the mentioned tests, some are performed on samples of interlayer materials only, and others are performed on coupled elements (with glass parts). In these observed geometries (very thin specimens) interlayers are not intended to be used as stand-only elements, and in LG panels, they are dominantly loaded in shear (not so much in the axial direction), and the tests on raw materials should always be validated with coupled real-size tests on LG specimens [12].

2.3. Experimental Tests on LG Specimens According to EN 1288-3

The experimental test on LG specimens is carried out in the Structural Laboratory of the Faculty of Civil Engineering, Architecture and Geodesy. These tests are conducted because the available data and the presented analyses showed unknowns regarding interlayer behaviour and

the impact of this behaviour on the capacity of LG members. Four-point bending tests are chosen as appropriate because it is possible to determine the real strength of the specimen regarding the known position of fracture occurrence and the exact value of internal forces. The three-point bending setup is not used because it is hard to achieve fracture origin exactly at the middle of the specimen where stress is calculated, which it could result in in apparently higher strength than the real one. In a four-point bending tests, the main requirement is to fracture to occur inside the load span. LG specimens are exposed to a four-point bending test at room temperature. The specimens are made of two tempered glass panels with a 6 mm thickness for each ply. The glass plies are connected with a 0.76 mm-thick Saflex DG41 PVB interlayer (EASTMAN, US; $E_{1min,25^{\circ}C} = 387MPa$; $G_{1min,25^{\circ}C} = 131MPa$; $\nu = 0.476$), where $E_{1min,25^{\circ}C}$ is Young's modulus at 25 °C, $G_{1min,25^{\circ}C}$ is shear modulus at 25 °C and ν is Poisson's coefficient. The test is conducted according to regulation EN 1288-3 [24] with some minor differences in span. The span is 950 mm, and the width and length of the specimen are 330 mm and 1000 mm, respectively. Testing device bearings are made of steel, and hard contact of the steel bearing and the glass specimen is prevented by using 0.1 mm-thick rubber protection. The specimens are exposed to bending with an increasing stress at a rate of $2.0N/mm^2.s$ until failure occurs. Tests are conducted at room temperature (25 °C) and controlled moisture conditions (50%). All specimens were produced approximately one year before the test and stored in the same conditions. [12]

The experiments are performed on a testing device CONTROLS Automax Multitest (CONTROLS, Italy). As mentioned, the samples are placed on cylindrical supports and separated with rubber protection. A QUANTUM MX840B from HBM (HBM, Germany) was employed for the data acquisition, with a sampling frequency of 300 Hz. Force and displacement are measured with the CONTROLS device implemented acquisition. The deflections are measured additionally with six linear variable displacement transducers (LVDTs), arranged symmetrically on the specimen: four at the bearings (two at each side) and two at the center. A CONTROLS device controlled the applied force at each step. [12]

A schematic view of the test setup is presented in Figure 2.3., and a photo of the test setup in Figure 2.4. Four strain gauges are used to measure upper and bottom glass ply strains at points A and B (Figure 2.3.). All tests are conducted until fractures occur on the bottom ply of the specimens, while the upper ply remains undamaged; see Figure 2.4.

2. Influence of temperature and load duration on the behaviour of laminated glass elements loaded out of plane

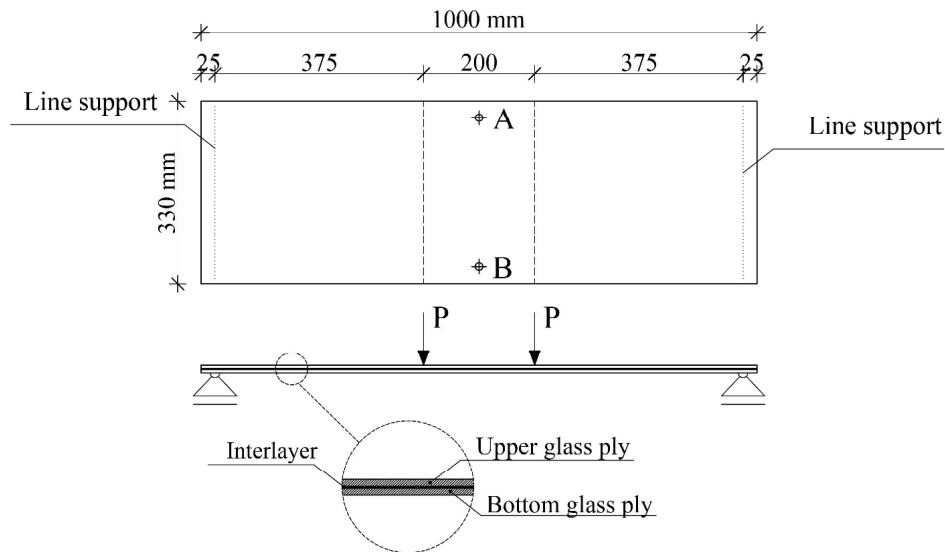


Figure 2.3. Schematic representation of test setup and loading [12]

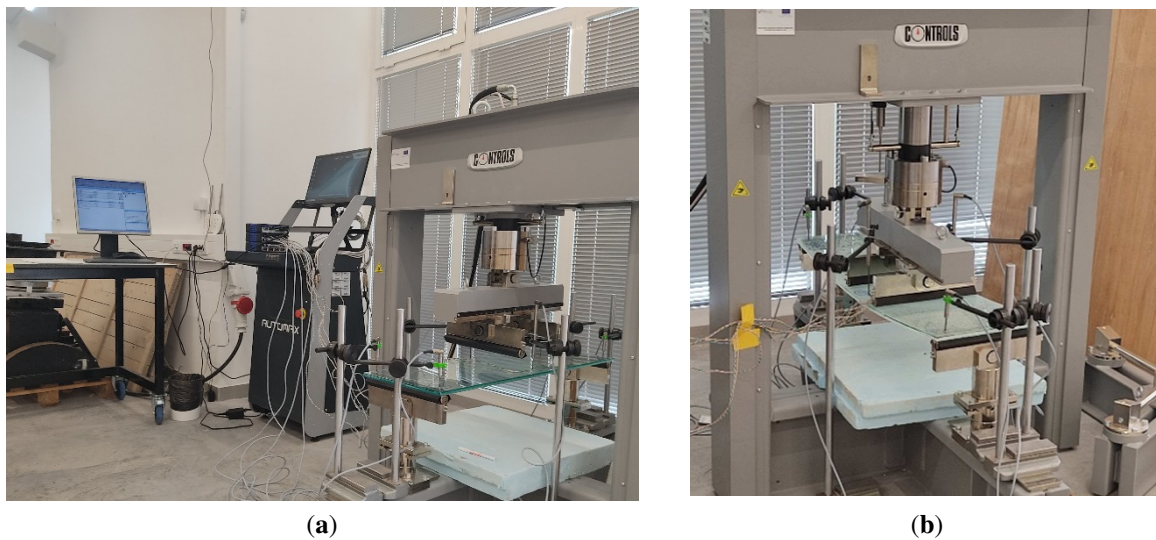


Figure 2.4. Photo of test setup: a) before loading; b) when breakage of bottom ply occurred

After the fracture of the bottom ply, which occurs in a manner that causes the whole ply to fragment, the load-bearing capacity is reduced. It is important to emphasize that these specimens are made of tempered glass, and that fracture initiation in one place results in the full fragmentation of the entire ply, as shown in Figure 2.5. With this kind of fragmentation, specimens lose transparency, but almost all fragments remain adhered to the polymer interlayer. In this phase, the polymer can provide the tensile force together with the lower part of the upper ply to withstand bending moments. [12] After the bottom ply fractures, the panel remains loaded

2. Influence of temperature and load duration on the behaviour of laminated glass elements loaded out of plane

with 1 kN of force without further increase in deflection, which is equivalent to 100 kg mass that the panel can withstand in its damaged state. This condition is the best indicator of the post-breakage capacity of the LG panel laminated with a PVB interlayer. Additionally, a permanent deformation in the direction of deflection of approximately 12 mm, remains after unloading. The permanent deformation is present even 6 months after the test, regardless of a slight tendency to straighten the panel caused by weight (the damaged specimens are placed on a flat surface with the broken glass ply facing upwards). The permanent deformation is a product of bulk volume increase in the tempered glass ply because cracks are filled with glass dust and small fragments. This volume increase is considered in the third part of regulation CEN/TS 19100-3:2021[3] as an additional imperfection for elements loaded in-plane. In all specimens exposed to four-point bending, fracture initiation occurred in the zone of the constant maximum moment (between the applied forces) on the tensile glass ply, which is typical for static loading.

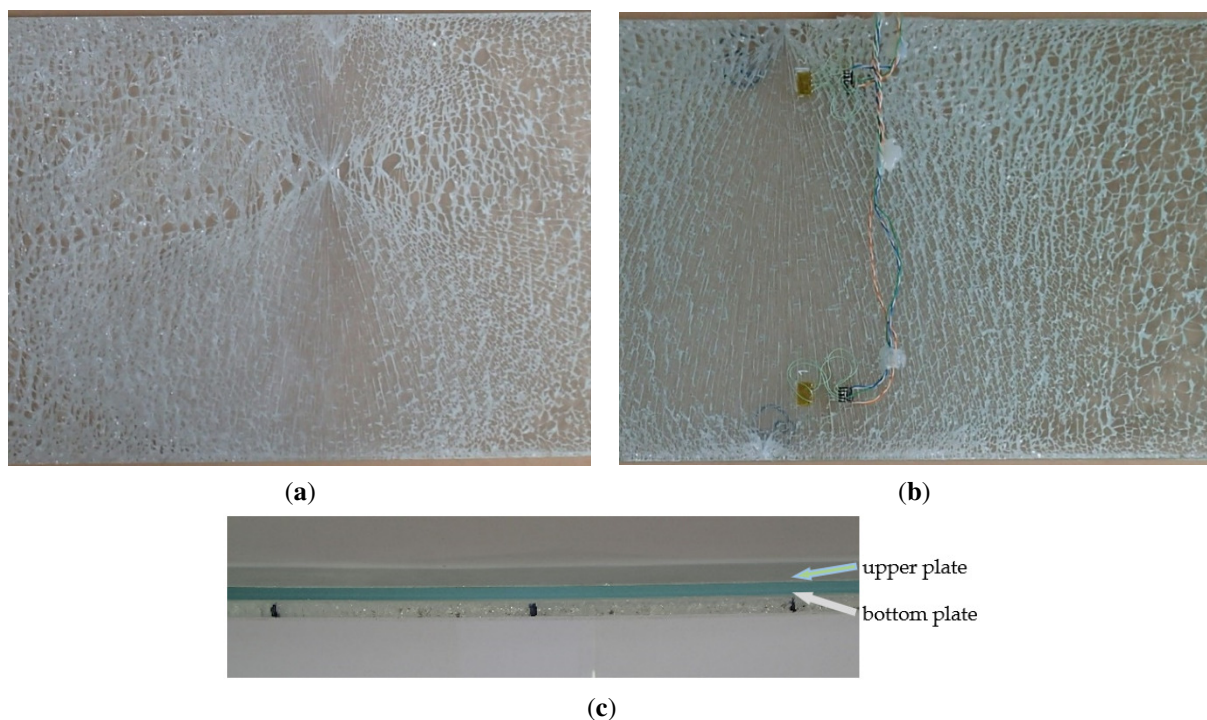


Figure 2.5. Photography of fracture patterns of specimens: (a) S1; (b) S3; and (c) side view on centre of LG pane [12]

The results for tested specimens are presented in the graph in Figure 2.6., deflections are compared to the four-point bending test results of Pankhardt and Balázs [30] and Serafinavicius et al.[27] where different types of interlayers are tested (PVB, EVA, SGP; EVA), with different thicknesses. In [27] the authors tested LG composed of two 6 mm plies with PVB (1.52 mm), EVA (0.89 mm), and SGP (1.52 mm) interlayers. All results are for room temperature, and it is

2. Influence of temperature and load duration on the behaviour of laminated glass elements loaded out of plane

visible that the value of ultimate force and deflection varies according to the interlayer type. At room temperature and different thicknesses (0.89 mm and 0.76 mm), the EVA [30] [27] and PVB interlayers have the lowest difference in ultimate force, with the mean value of PVB specimens $F_{mean,PVB\ 0.76} = 6.71\text{kN}$ and the ultimate force of EVA specimens $F_{mean,EVA\ 0.89} = 6.70\text{kN}$. However, specimens with EVA interlayer have greater deflection at fracture point ($w_{mean,PVB\ 0.76} = 30.32\text{mm}$ and $w_{mean,EVA\ 0.89} = 35.04\text{mm}$). The SentryGlas ionoplast interlayer, compared with the same thickness of the PVB interlayer, shows a much stiffer response, consequently increasing ultimate strength. It is expected that for increased temperatures, this discrepancy could be even higher due to lower stiffness of interlayers. Hence, the contribution of the interlayer to the global behaviour of the glass panels at room temperature is favourable because plies are coupled. [12]

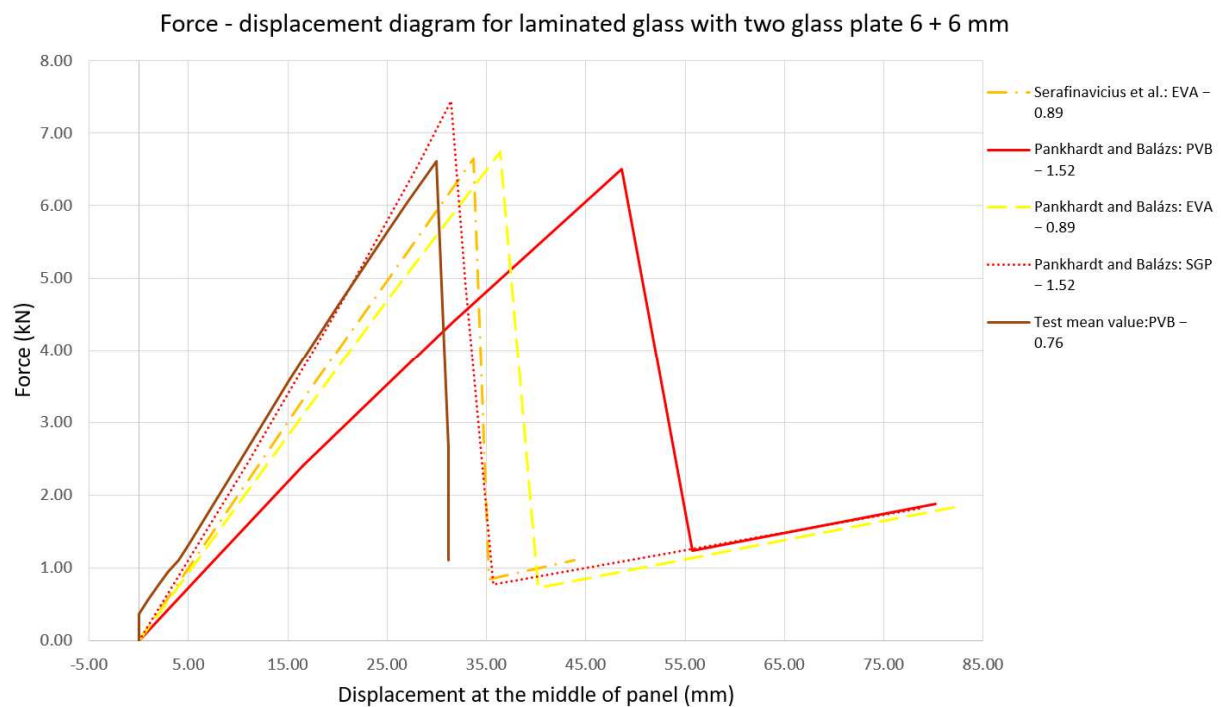


Figure 2.6. Results of four-point bending test compared with other similar tests [30] [27] from the literature [12]

2.4. Description of a Numerical Model for Analysing the Behaviour of LG Elements

The numerical model in ANSYS software is based on a four-point bending test and the presented geometry from the experimental tests. The model consists of two glass plies

connected with an interlayer. The model is discretized with 3D solid elements, with the element size ratio for the glass pane and interlayer not higher than 1.5 interlayer elements. Contact between the glass and interlayer is defined as an absolute bond, without any sliding. This is a typical case in modelling ULS because the interlayer-glass connection is not endangered until FLS and PFLS. For loading lower than the limit of ULS the contribution of the interlayer to the bearing capacity of the glass member appears mostly through its shear stiffness. The shear capacity of the interlayer offers a lower degree of resistance to deformation than the possible peel-off on the surface between the glass and the interlayer. The specimen (glass panel) has a total span of 950 mm and is supported on two ends with one sliding bearing (the panel is supported with rollers) and a fixed bearing that allows free rotation. The load is placed at the same positions as in the four-point bending test, 100 mm on each side from the mid-span, and it is modelled as line load. The adopted material characteristics for the glass, used for pre-calculation of expected force values and in numerical models, are those proposed in the regulation [1] and presented in Tables 1.1 and 1.2. Those for PVB are in Table 2.1., and Figure 2.2. For the validation of the numerical model, Young's modulus and Poisson's ratio of the interlayer are used according to the total test duration and test temperature (experiments) ($E_{1min,25^{\circ}C} = 387MPa$; $G_{1min,25^{\circ}C} = 131MPa$; $\nu = 0,476$). The shear modulus of the interlayer is determined in dependence to Young's modulus and Poisson's ratio, as proposed in producer's technical sheet. [12]

The accuracy of the numerical model (with PVB) is validated with the experimental results for the first loading stage (fracture of the bottom glass ply). In the model, stress is controlled and limited to the mean value of stress that occurred during the breakage of specimens - experimental fracture stress. The fracture simulation is not accomplished in the numerical model due to the lack of appropriate numerical methods for the simulation of fracturing brittle material exposed to static load, the calculation is interrupted by reaching the stress limit. The predicted deflection in the numerical model is compared with the experimental results, and the results are presented in the graph in Figure 2.7. A very good coincidence of numerical and experimental results can be seen regarding deflection for the assigned force. This result showed the good capability of the numerical prediction of the behaviour of specimens in aspects of stiffness and stress, without fracture simulation. In further analysis this model is used to provide a parametric analysis for different conditions regarding temperature, load duration and interlayers with different stiffness. The available data and the earlier mentioned analyses indicated the need for a parametric analysis of the influence of temperature change on the

2. Influence of temperature and load duration on the behaviour of laminated glass elements loaded out of plane

behaviour of LG members loaded out-of-plane. In further parametric analyses, for the PVB constitutive model, different values of Young's modulus (E) and the shear modulus (G), depending on the load duration ($\log(t)$) and temperature (T) are used. The pane is loaded under the fracture limit, and FLS and PFLS are not considered. In this type of loading (under the fracture limit), the interlayer is exposed only to small strains, lower than the failure strain of the glass ply in LG elements. [21] The failure strain of the glass ply is approximately 0.167%, for typical tempered glass with an ultimate strength of 120 MPa and an elastic modulus of approximately 70 GPa. In cross-section the interlayer is placed around the middle, and for dominant bending action, it is exposed to a very small strain in ULS. [12]

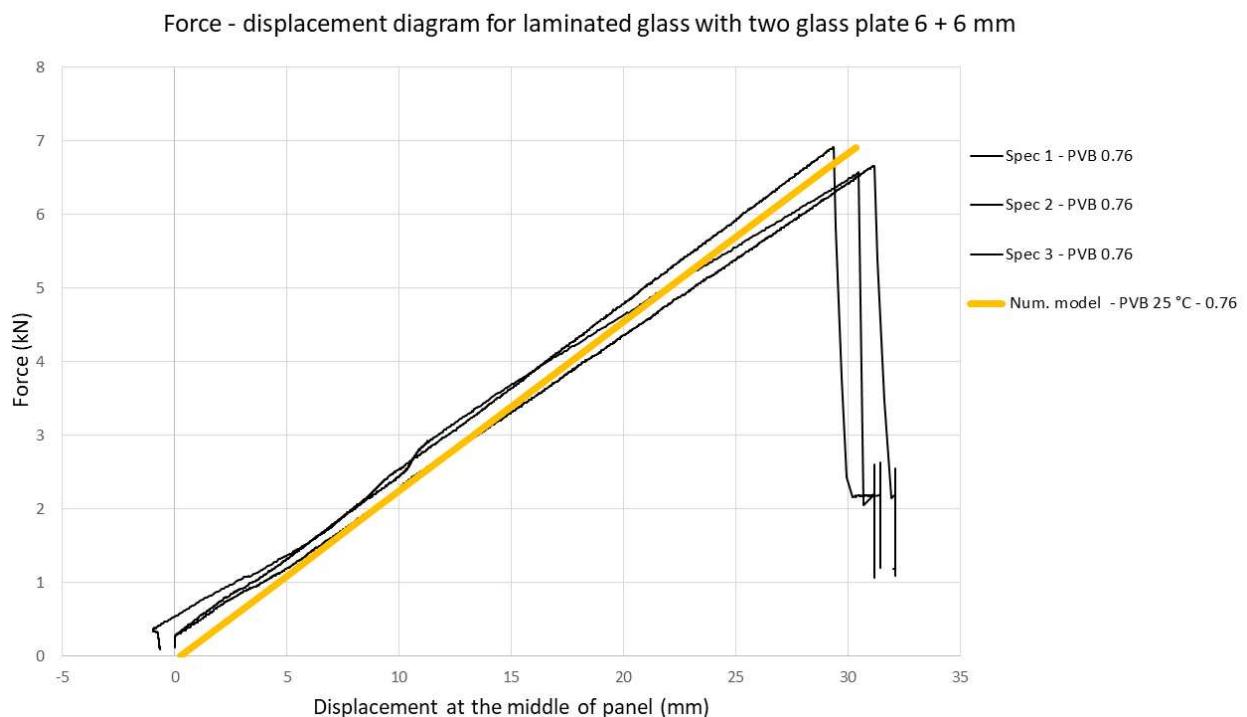


Figure 2.7. Force-displacement graph – comparison of the results of experimental test and numerical model [12]

By using this validated numerical model, other geometries with different thicknesses of the glass plies and interlayers are analysed, and these geometries are used in the parametric study.

2.5. Model Results of a Parametric Study of Interlayer Properties Influence on the Bearing Capacity of LG Elements

The parametric analysis is conducted for twelve geometries. The basic properties of the model, such as a span of 950 mm and a width of 330 mm, are kept the same. Uniform loading is

2. Influence of temperature and load duration on the behaviour of laminated glass elements loaded out of plane

adopted for all panels, with a total force of 1000N divided into two lines uniformly distributed as 15.151 N/cm'. For the interlayer, thicknesses of $t = 1.52$ mm and $t = 2.28$ mm for both PVB and ionoplast interlayers are used, and for lower thicknesses, PVB is used with a thickness of $t = 0.76$ mm and ionoplast with $t = 0.89$ mm according to production dimensions. For glass panes, two combinations of thickness are used, creating three dispositions: 6 + 10 mm, 10 + 6 mm, and 8 + 8 mm. The dispositions title and the geometry are presented in Table 2.2. As can be seen, the main goal is to use the same total thickness of the glass parts but with different dispositions. For all analyses, the force is kept fixed while the temperature, load duration and geometry are varied. As the main indicators of element behaviour and its stiffness the stresses on the bottom glass ply and total deflection are observed.

Table 2.2. The dispositions: title and the associated geometries

Disposition	Geometry	Interlayer type	Interlayer thickness
D1	6 mm + 10 mm	PVB + ionoplast	0.76(0.89) mm; 1.52 mm; 2.28 mm
D2	8 mm + 8 mm	PVB + ionoplast	0.76(0.89) mm; 1.52 mm; 2.28 mm
D3	10 mm + 6 mm	PVB + ionoplast	0.76(0.89) mm; 1.52 mm; 2.28 mm

To obtain the relationship between load duration, temperature, and geometry influence on pane deflection (as a measure of flexural stiffness) and tension stress in the bottom glass ply, an analytical polynomial of three independent variables with unknown coefficients is used. For these three variables (load duration, temperature, and thickness of the interlayer) each functional independence is defined by a second-order polynomial that generated a sixth total order polynomial:

$$\begin{aligned}
 P(x, y, z) = & F_1 + F_2 \cdot x + F_3 \cdot y + F_4 \cdot x^2 + F_5 \cdot Fx \cdot y + F_6 \cdot y^2 + F_7 \cdot x^2 \cdot y + F_8 \cdot x \cdot y^2 + F_9 \\
 & \cdot x^2 \cdot y^2 + F_{10} \cdot 0z + F_{11} \cdot 1x \cdot z + F_{12} \cdot y \cdot z + F_{13} \cdot x^2 \cdot xz + F_{14} \cdot x \cdot xy \cdot z \\
 & + F_{15} \cdot y^2 \cdot yz + F_{16} \cdot 6x^2 \cdot 6y \cdot z + F_{17} \cdot 7x \cdot y^2 \cdot z + F_{18} \cdot 8x^2 \cdot 8y^2 \cdot 8z + F_{19} \quad (2.5.1) \\
 & \cdot z^2 + F_{20} \cdot 0x \cdot z^2 + F_{21} \cdot 1y \cdot z^2 + F_{22} \cdot 2x^2 \cdot 2z^2 + F_{23} \cdot 3x \cdot y \cdot z^2 + F_{24} \cdot 4F^2 \\
 & \cdot 4F^2 + F_{25} \cdot x^2 \cdot y \cdot z^2 + F_{26} \cdot x \cdot y^2 \cdot z^2 + F_{26} \cdot 7^2 \cdot y^2 \cdot z^2
 \end{aligned}$$

where x, y, z are independent variables corresponding to the logarithm of load duration in seconds, the value of ambient temperature in °C, and the value of interlayer thickness in mm; the F_s are unknown coefficients. [12]

The unknown coefficients from the expression are solved iteratively by MATLAB [55]. The coefficients are calculated using a nonlinear least-squares estimation [56]. The solution successfully converged for all datasets. A detailed explanation of the fitting process and RMSE values is provided in [12].

2. Influence of temperature and load duration on the behaviour of laminated glass elements loaded out of plane

For easier comparison of all data, and after fitting with polynomial function isosurfaces are created, representing the dependence of the deflection and stress on the specified parameters. The isosurfaces are presented in Figures 2.8. to 2.13. In each figure, the results of deflection or stresses at the bottom panel are presented for two interlayers, PVB and ionoplast. They can be described as three – parameter representation of differences that occur in LG member behaviour at different interlayer thicknesses, temperatures and load durations. By comparing the different families of isosurfaces, the influence of dispositions and different types of interlayers along the described independent variables can be seen. As expected, from the slope of isosurface families belonging to ionoplast and PVB interlayers, higher flexural stiffness and better behaviour (lower deflections) are observed for ionoplast when temperatures over 20 °C and load durations over 24 h occur. PVB interlayers have a lower capacity for longer (permanent) loads, and the glass panes with PVB interlayers show higher deflection compared to ionoplast interlayers under the same conditions (thickness of the glass pane, load duration, and temperature). If the disposition D1 is observed in Figure 2.8., for the thickness $t=1.52$ mm of both interlayers, fixed loading, and load duration (24 h), in the interval from 10 °C to 25 °C, the decrease in moment of inertia for PVB specimen is approximately $\Delta_{I_{eff}} = 5.485 \text{ cm}^4$ ($I_{eff,10^\circ\text{C}} = 11.526 \text{ cm}^4$; $I_{eff,25^\circ\text{C}} = 6.041 \text{ cm}^4$), resulting in $\Delta_w = 1.886 \text{ mm}$ higher deflection and $\Delta_\sigma = 1.821 \text{ MPa}$ higher stress in the bottom tensile ply. For the same conditions and D1 disposition, the decrease in moment of inertia for ionoplast specimens is approximately $\Delta_{I_{eff}} = 0.202 \text{ cm}^4$ ($I_{eff,10^\circ\text{C}} = 12.99 \text{ cm}^4$; $I_{eff,25^\circ\text{C}} = 12.788 \text{ cm}^4$), resulting in $\Delta_w = 0.029 \text{ mm}$ higher deflection and $\Delta_\sigma = 0.04 \text{ MPa}$ higher stress in the bottom tensile ply, which is almost negligible. The stiffness and behaviour of elements for different conditions are visible in the slope change of isosurfaces when moving through each axis. If the stiffness decrease is observed as a percentage of monolithic limit (ML), calculated as the moment of inertia with the full height of the cross-section, then for the D1 disposition, the decrease in stiffness of panes with PVB interlayer is from 77.94% of ML for 10 °C and 24 h to 40.85% of ML for 25 °C and 24 h. For panes with ionoplast interlayer, the decrease for the same conditions is from 87.83% of ML to 86.47% of ML.

2. Influence of temperature and load duration on the behaviour of laminated glass elements loaded out of plane

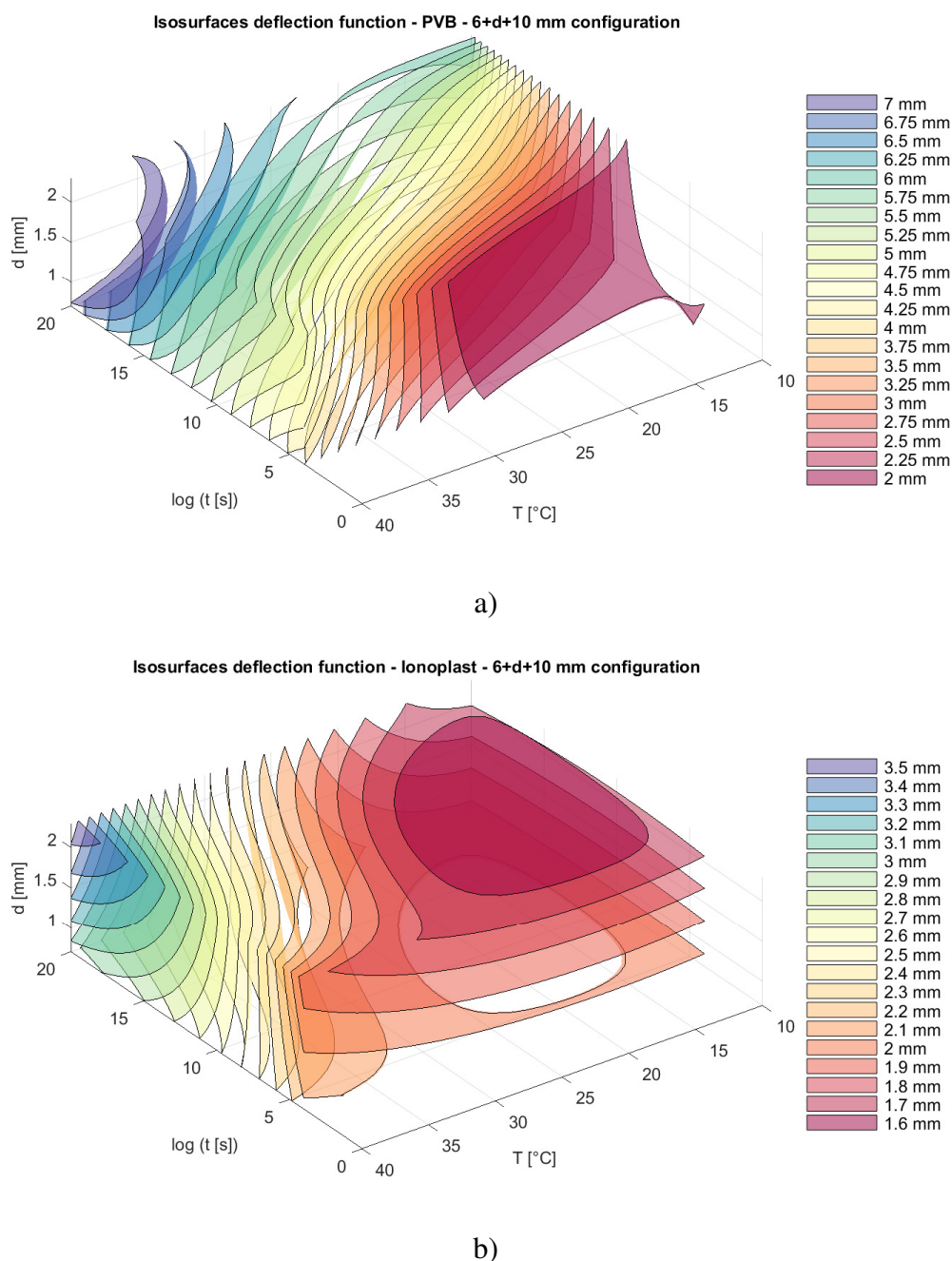


Figure 2.8. The deflection graph for disposition D1: (a) PVB interlayers; (b) ionoplast interlayers [12]

For disposition D2, presented in Figure 2.9. the stiffness decrease, observed as a percentage of monolithic limit (ML) in the case of panes with PVB interlayer is from 77.68% of ML at 10 °C and 24 h to 37.95% of ML at 25 °C and 24 h. For pane with an ionoplast interlayer, the decrease under the same conditions is from 88.89% of ML to 87.41% of ML.

2. Influence of temperature and load duration on the behaviour of laminated glass elements loaded out of plane

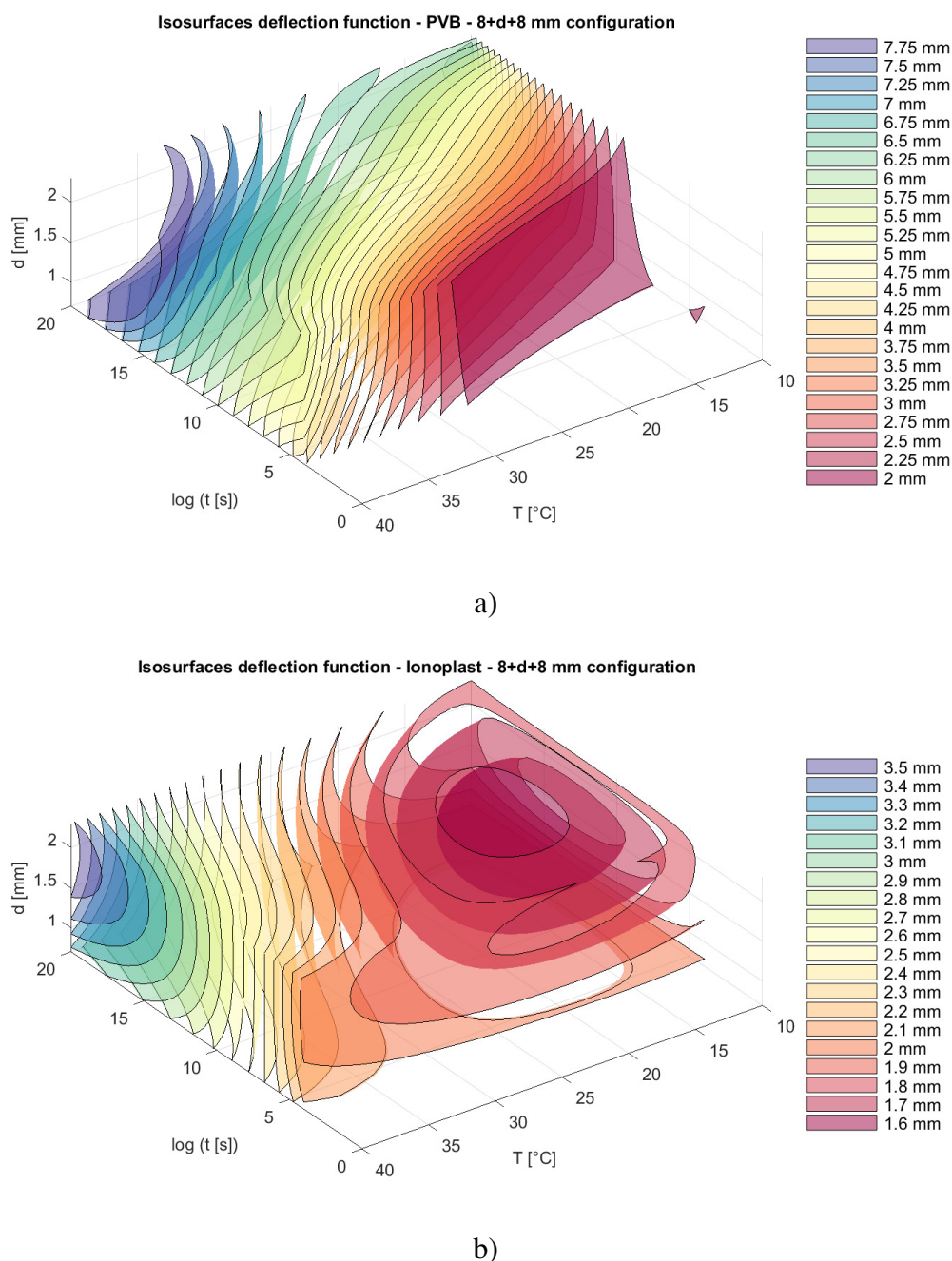


Figure 2.9. The deflection graph for disposition D2: (a) PVB interlayers; (b) ionoplast interlayers [12]

For disposition D3, presented in Figure 2.10. the stiffness decrease, observed as a percentage of monolithic limit (ML) in the case of panes with PVB interlayer is from 77.94% of ML at 10 °C and 24 h to 40.85% of ML at 25 °C and 24 h. For pane with an ionoplast interlayer, the decrease under the same conditions is from 87.84% of ML to 86.47% of ML. These results are equal to the results for disposition D1.

2. Influence of temperature and load duration on the behaviour of laminated glass elements loaded out of plane

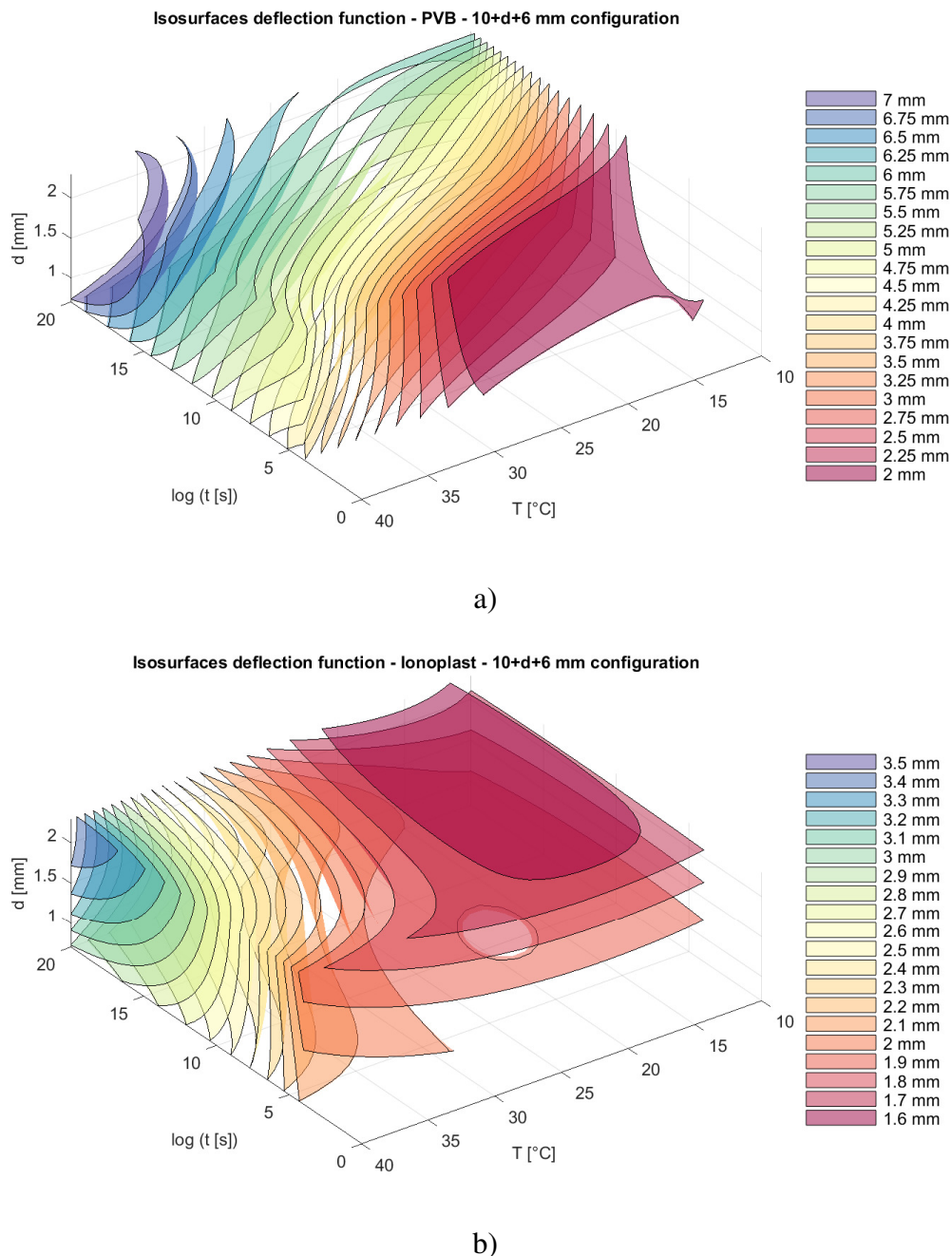


Figure 2.10. The deflection graph for disposition D3: (a) PVB interlayers; (b) ionoplast interlayers [12]

In Figures 2.11., 2.12., and 2.13., the stress on the bottom panel is presented for different conditions. If the stress behaviour pattern is observed, it can be seen that the highest stress occurs in disposition D1 for the case of panes with a PVB interlayer. The increase in stress for a fixed temperature (10 °C) and the same thickness of interlayer (1.52 mm) is 42.9% when the load duration increases from 24 h to 10 years. This ratio is the highest for D1 disposition and

2. Influence of temperature and load duration on the behaviour of laminated glass elements loaded out of plane

slightly lower for D2 (40.18%) and D3 (35.44%) dispositions. A similar pattern, but on a much lower scale, is observed for panes with an ionoplast interlayer, where under the same conditions, the increase in stress at the bottom ply is 0.45% for D1 disposition, 0.36% for D2 and 0.095% for D3 disposition (these values are also calculated for 10 °C). However, a slightly higher value of stress at the bottom ply for the ionoplast interlayer occurs in disposition D3.

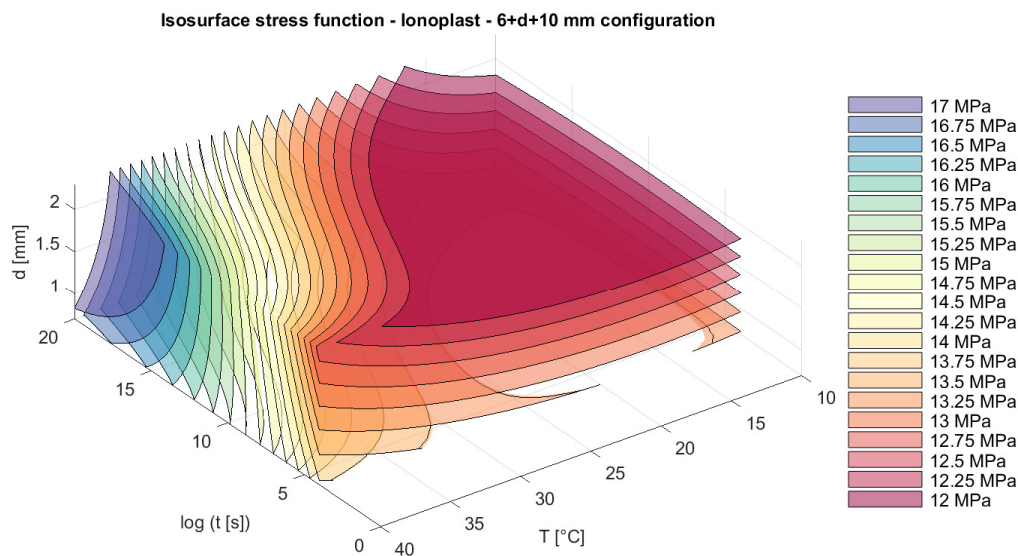
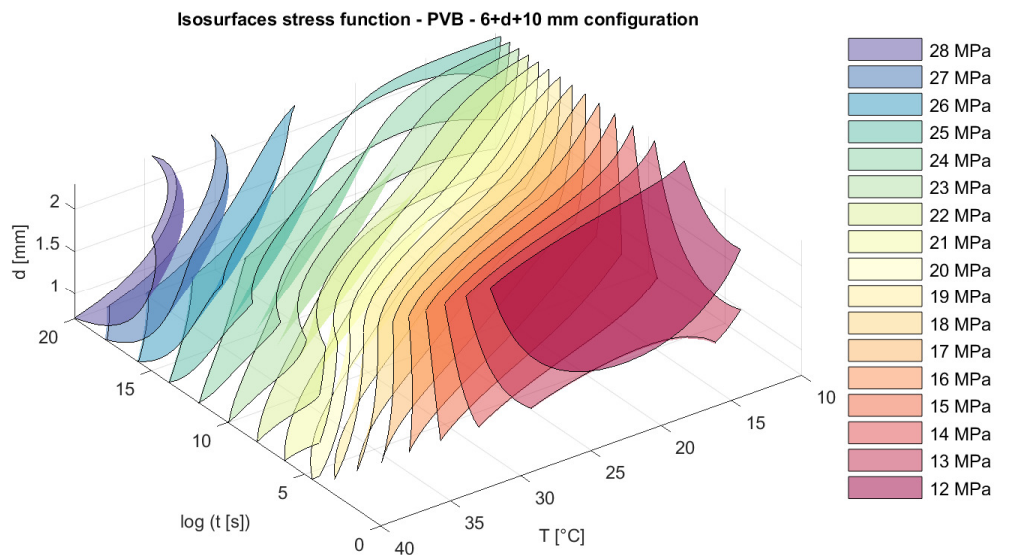


Figure 2.11. The stress graph for a disposition D1: (a) PVB interlayers; (b) ionoplast interlayers [12]

2. Influence of temperature and load duration on the behaviour of laminated glass elements loaded out of plane

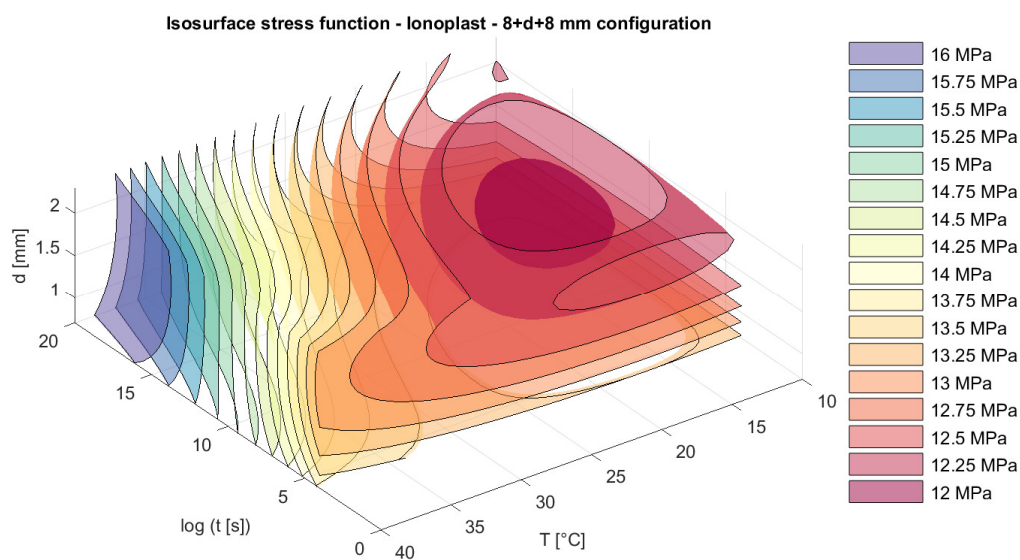
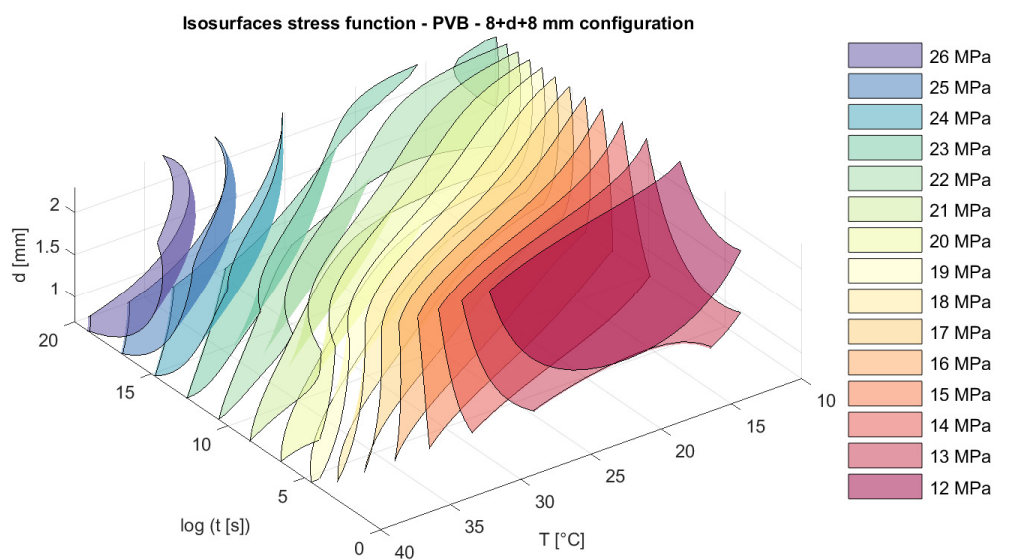


Figure 2.12. The stress graph for a disposition D2: (a) PVB interlayers; (b) ionoplast interlayers [12]

2. Influence of temperature and load duration on the behaviour of laminated glass elements loaded out of plane

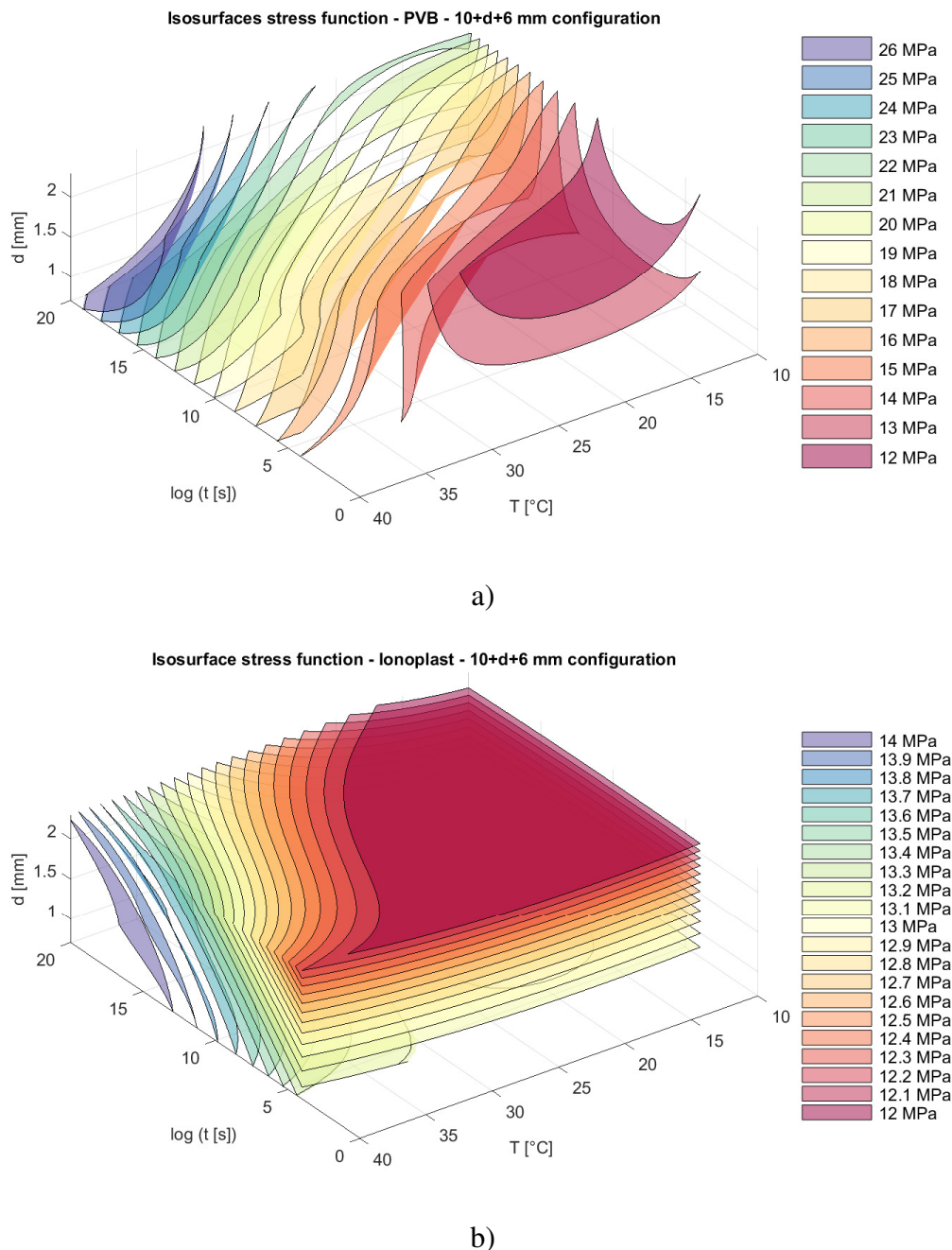


Figure 2.13. The stress graph for a disposition D3: (a) PVB interlayers; (b) ionoplast interlayers [12]

To observe the influence of specific parameters through the isosurfaces, the clearest insight is to “freeze” certain values and to follow the behaviour in that plane. Below, each parameter is described through its effects:

Influence of thickness dispositions - For non-symmetrical glass ply dispositions, and PVB interlayers dominantly, greater stress appears in cases where the thicker glass ply is on the

tension side – at the bottom (6 mm + 10 mm) for both types of interlayers. This behaviour is expected because the thicker panel has higher bending stiffness and can withstand higher loads, resulting in higher stresses in that part. The symmetrical disposition of glass plies (8 mm + 8 mm) shows stress values between the two presented disposition limits (6 mm + 10 mm and 10 mm + 6 mm). Regarding deflection, the non-symmetrical dispositions do not provide a significant deviation, and these values are slightly lower than those from symmetrical dispositions of plies (8 mm + 8 mm). The only factor influencing deflection size, when disposition is observed, is the total thickness of the pane.

Influence of different interlayer materials and their thickness – When observing deflections, LG panes with ionoplast interlayers generally provide higher stiffness than the same model with PVB (Saflex DG41) interlayer, with the difference increasing with higher temperatures and longer load durations. This behaviour is expected because an ionoplast interlayer provides the highest level of structural performance [44], which causes lower deflection. A different trend regarding the increase in interlayer thickness is visible in the model with PVB interlayers (vertical orientation of surfaces) than those with Ionoplast (horizontal orientation of surfaces with a tendency of verticalization as higher temperature and load duration occur). Namely, for PVB interlayers at temperatures up to 25 °C and shorter loadings (up to 24 h), an increase in interlayer thickness doesn't affect the deflection, and for longer loadings (>1 month), an increase in the thickness of PVB interlayers shows an unfavourable effect on pane deflection increase due to PVB's sensitivity to load duration and temperatures, which for increased thickness results only in higher shear deformations. On the other hand, an increase in ionoplast thickness decreases deflections (increased static height), and that effect diminishes with increasing load durations and temperatures (over 35 °C and 1 month).

Influence of load duration - For longer load durations and increased temperatures, PVB interlayers show unfavourable behaviour regarding bearing capacity (higher deflections) in comparison with ionoplast interlayers. These observations are also confirmed by other experimental tests in the literature [41]. The graphs show that increasing the height of the interlayer doesn't reduce the negative influence of load duration for PVB. At the same time, for ionoplast, there is some positive effect that slowly vanishes at load duration longer than $t = 1$ month.

Influence of interlayer thickness and temperature - For temperatures up to 25 °C, an increase in interlayer thickness in the ionoplast model shows a positive effect, resulting in lower deflection (increasing the pane stiffness). However, for temperatures above 35 °C, this effect

diminishes, and for long-term loading, the increase in interlayer thickness results in higher deflection of the pane when comparing an ionoplast interlayer thickness of 0.89 mm with 2.28 mm. A different trend is observed in the model with PVB (Saflex DG41) interlayers, where at lower temperatures and shorter load durations, the increased thickness of the interlayers does not provide any beneficial influence on deflection, and at higher temperatures, it only increases deflection. The increase in thickness for a softer interlayer only emphasizes the layered effect in LG structures.

2.6. Effective Thickness Approaches in Cases of Different Temperatures and Load Durations

2.6.1. Effective Thickness Approach (ETA) – Different Methods

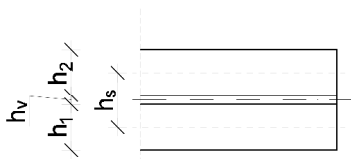
The effective thickness (ET) refers to a monolithic pane with a reduced thickness that behaves in the same way as the observed laminated glass pane under the same boundary and load conditions. Effective glass thicknesses are used for the calculation of deflection and stress due to different (out-of-plane and in-plane) loads according to the literature and regulations. Some of the expressions from the regulations are mentioned in the first chapter where a regulations overview is presented, and here it will be presented in detail. This simplified calculation for laminated glass can be used for laminated panes exposed to static and dynamic loads. With dynamic loading, due to the short time interval during which the load occurs, there is no significant activation of the unfavourable nonlinear behaviour of the polymer interface, and the element behaviour is close that of monolithic glass pane with a total thickness equal to the sum of the thicknesses of the glass plies in the element. The effective thickness in this case is usually very close to the monolithic limit due to the high shear modulus of the interlayer that occurs for short load durations. In the case of static loading, the influence of incomplete coupling (due to the deformation of the interlayer) cannot be ignored and it is emphasized with lower values of the effective thickness.

In the further text, the methods for ET and the differences between the approaches are observed. Equations for the calculation of deflection and stress are used. The presented expressions are proposed for beam elements, some with limitations in number of plies and types of boundary conditions. After the description, an analytical calculation is done for two different temperatures (25 °C and 40 °C) and three load durations (1 min; 24 h; 1 month). These values are chosen because they belong to frequent design situations for structures in normal conditions. The results (stress and deflection) are compared with results from numerical models.

2. Influence of temperature and load duration on the behaviour of laminated glass elements loaded out of plane

This concept was first established by Wölfel [57] for the calculation of sandwich panels with thick soft cores placed between stiff outer metal sheets. The first proposal for using this simplified method in laminated glass elements was made by Bennison and his research team [58], who adopted a method proposed by Wölfel [57] for determination of deflection and stress in layered structure. The equations from the work of Bennison and his research team [58] are presented in Table 2.3. (2.6.1 – 2.6.3). In the equation, a coefficient $\beta=9.6$ is used, for which in Wölfel's work [57], $\beta=12.0$ is proposed for loading with force in the middle of the span and $\beta=9.6$ for the distributed load.

Table 2.3. The expressions for the effective thickness approach according to Wölfel-Bennison

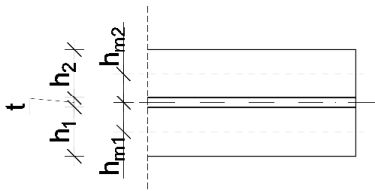
	$h_{ef,w} = \sqrt[3]{h_1^3 + h_2^3 + 12 \cdot \Gamma \cdot I_s}$	(2.6.1)
	$h_{ef,\sigma,j} = \sqrt{\frac{h_{ef,w}^3}{h_1 + 2 \cdot \Gamma \cdot h_{s,2}}}$	(2.6.2)
	$\Gamma = \frac{1}{1 + \beta \cdot \frac{E \cdot I_s \cdot h_v}{G \cdot h_s^2 \cdot a^2}}$	(2.6.3)
	<p>$h_{ef,w}$ - the effective thickness for calculating the deflection of any glass ply in the panel (mm)</p> <p>$h_{ef,\sigma,j}$ - the effective thickness for normal stress calculation of j-th glass ply (mm)</p> <p>h_v - interlayer thickness</p> <p>$h_{1,2}$ - ply thickness</p> <p>Γ - the shear transfer coefficient defined in (2.6.3)</p> <p>G - interlayer shear modulus</p> <p>E - Young's modulus for glass</p> <p>a - shortest bending direction - span</p> <p>$\beta = 9.6$</p>	
$I_s = h_1 \cdot h_{s,2}^2 + h_2 \cdot h_{s,1}^2 ; \mathbf{h}_{s,1} = \frac{h_s \cdot h_1}{h_1 + h_2} ; \mathbf{h}_{s,2} = \frac{h_s \cdot h_2}{h_1 + h_2} ; \mathbf{h}_s = 0.5 \cdot (h_1 + h_2) + h_v$		

The concept is further adopted in the scientific literature for laminated glass, and is present in all draft versions of the regulations presented through the years. The regulations (some still in use and other older versions): from 2009 prEN 13474-3 [13], design guidelines from 2014 [14], standard [59] from 2018, the latest standard EN 16612 [22] from 2019, and the unofficial draft

2. Influence of temperature and load duration on the behaviour of laminated glass elements loaded out of plane

version of the new European standard from 2021 CEN/TS 19100-2:2021 [2] have included simplified calculations according to the effective thickness approach with different equations. Two expressions that are still in use (from the regulations) are from EN 16612 [22] and the expressions from the draft version of regulation CEN/TS 19100-2:2021 [2]. The equations according to EN 16612 [22] are presented in Table 2.4., together with all the necessary ingredients. This approach is very similar to the Wölfel-Bennison approach, the only difference occurs in the determination of the shear transfer coefficient Γ/ω . The basis of both coefficients is same as they provide the amount of shear transfer / coupling of plies. The coefficients can take values from 0 (no shear transfer) to 1 (full shear transfer). The shear transfer coefficient Γ is determined based on geometry, boundary conditions, and material characteristics of interlayer (shear modulus) and glass (Young's modulus). On the other hand, the coefficient ω is determined based on the proposed "stiffness family" of the interlayer, taking into account the load duration, type of load, and interlayer characteristics as well as expected climatic conditions for the element's geographic position. This categorization is well thought out but not defined in detail and therefore difficult to use.

Table 2.4. The expressions for the effective thickness approach according to EN 16612 [22]

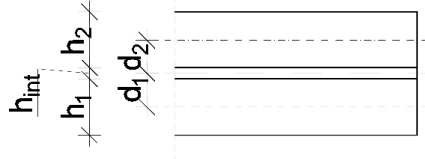
$h_{ef,w} = \sqrt[3]{\sum_k h_k^3 + 12\omega \left(\sum_k h_k h_{m,k}^2 \right)}$		(2.6.4)
$h_{ef,\sigma,j} = \sqrt{\frac{h_{ef,w}^3}{h_j + 2\omega h_{m,j}}}$		(2.6.5)
	<p>ω - the shear transfer coefficient depending on the type of interlayer that is used and the loading case</p> <p>$h_{ef,w}$ - the effective thickness for calculating the deflection of any glass ply in the panel (mm)</p> <p>$h_{ef,\sigma,j}$ - the effective thickness for normal stress calculation of j-th glass ply (mm)</p> <p>t - interlayer thickness</p> <p>h_k and h_j - the thicknesses of the individual glass plies (mm)</p> <p>$h_{m,k}$ and $h_{m,j}$ - the distances of the mid-plane of the k-th or j-th glass plies from the mid-plane of the laminated glass (mm)</p>	

The expressions for the ETA from the draft version of regulation CEN/TS 19100-2:2021 [2] are presented in Table 2.5. The expressions from Table 2.5. are valid for beams with n panels of the same thickness. The expression for beams with three plies of different thicknesses is also

2. Influence of temperature and load duration on the behaviour of laminated glass elements loaded out of plane

proposed in the regulation. The coupling parameter η from CEN/TS 19100-2:2021 [2] is dependent on geometry, load type, boundary conditions, and the change in the shear modulus of the interlayer.

Table 2.5. The expressions for the effective thickness approach according to CEN/TS 19100-2:2021 [2]

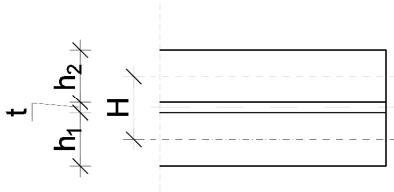
$h_{eff,w} = \sqrt[3]{\frac{1}{\frac{\eta}{\sum_i h_i^3 + 12 \sum_i (h_i \cdot d_i^2)} + \frac{1 - \eta}{\sum_i h_i^3}}} \quad (2.6.6)$	(2.6.6)
$h_{eff,\sigma,i} = \sqrt{\frac{1}{\frac{2 \cdot \eta \cdot d_i }{\sum_i h_i^3 + 12 \sum_i (h_i \cdot d_i^2)} + \frac{h_i}{h_{eff,w}^3}}} \quad (2.6.7)$	(2.6.7)
$\eta = \frac{1}{1 + \frac{h_{int} \cdot E \cdot n \cdot h^3 \cdot (n + 1) \cdot \Psi_B}{12 G_{int} \cdot h^2 + (h + h_{int})^2 \cdot (n^2 - 1)}} \quad (2.6.8)$	(2.6.8)
	<p>h_i/h - the thickness of the glass plies (mm) h_{int} - interlayer thickness η - the shear forces transfer factor depending on the shear stiffness of the interlayer, loading, and boundary conditions Ψ_B - boundary coefficient G_{int} - interlayer shear modulus E - Young's modulus for glass n - number of plies</p>

Another approach, presented by Galuppi and Royer-Carfagni [31] in 2012, is the approximation of the Generalized Newmark (energetic) approach - Enhanced Effective Thickness (EET) approach, presented in Table 2.6. This approach is similar to the one from the draft version of the European standard [2] (Table 2.5.), and since it was developed 10 years before the draft version of the standard, it can be concluded that it was a basis for that proposal. The equations are similar, and the biggest difference occurs in the definition of the coupling parameter / shear transfer coefficient η . This coefficient describes the coupling between glass plies and is equivalent to the shear transfer coefficient Γ from [58] and the shear transfer coefficient ω from [22]. The shear transfer coefficient η is defined separately for beams and plates. In this analysis,

2. Influence of temperature and load duration on the behaviour of laminated glass elements loaded out of plane

only the beams are observed, and the corresponding parameter is determined according to expressions 2.6.8 [2], and expression 2.6.12 [31].

Table 2.6. The expressions for the effective thickness approach according to Galuppi and Royer-Carfagni [31]

$h_{ef,w} = \frac{1}{\sqrt[3]{\frac{\eta}{h_1^3 + h_2^3 + 12I_s} + \frac{1-\eta}{h_1^3 + h_2^3}}}$		(2.6.9)
$h_{1,ef,\sigma} = \frac{1}{\sqrt[3]{\frac{2\eta h_{s,2}}{h_1^3 + h_2^3 + 12I_s} + \frac{h_1}{h_{ef,w}^3}}}$		(2.6.10)
$h_{2,ef,\sigma} = \frac{1}{\sqrt[3]{\frac{2\eta h_{s,1}}{h_1^3 + h_2^3 + 12I_s} + \frac{h_2}{h_{ef,w}^3}}}$		(2.6.11)
$\eta = \frac{1}{1 + \frac{I_1 + I_2}{\mu \cdot I_{tot}} \cdot \frac{A_1 \cdot A_2}{A_1 + A_2} \Psi}$		(2.6.12)
	<p>h_1 and h_2 - the thickness of the glass plies (mm) t - interlayer thickness I_s - the “bonding inertia” (mm³) η - the shear forces transfer factor depending on the shear stiffness of the interlayer, loading, and boundary conditions $h_{s,1}$ and $h_{s,2}$ - modified dimensions of the cross-section Ψ - coupling factor G - interlayer shear modulus E - Young’s modulus for glass</p>	
$\mu = \frac{Gb}{Et}; \quad I_{tot} = I_1 + I_2 + A^* \cdot H^2; \quad A^* = \frac{A_1 \cdot A_2}{A_1 + A_2}; \quad H = t + \frac{h_1 + h_2}{2}; \quad I_s = \frac{h_1 \cdot h_2}{h_1 + h_2} \cdot H^2$		

The coupling factor Ψ/Ψ_B should be determined according to the boundary conditions and load type, and for both expressions (2.6.8 and 2.6.12) it is proposed only for the most common types of loading and boundary conditions. The coupling factor Ψ/Ψ_B is not proposed for the case of four-point bending of a simply supported beam.

To observe a link between the approach according EN 16612 [22] and the one from CEN/TS 19100-2:2021 [2], an equal value of ω can be determined by using a liaison between the two proposed expressions for the effective thickness ([2] and [22]) approach defined in [2].

$$\omega_{EN 16612} = \frac{h_{ef,w,CEN/TS19100}^3 - \sum_i h_i^3}{12 \sum_i (h_i \cdot d_i^2)} \quad (2.6.13)$$

2.6.2. Effective Thickness Approach – Analytical Calculations for Different Temperatures and Load Durations

To test the accuracy of the presented methods, stress and deflection on a simply supported laminated glass pane are observed. The panes are loaded in four-point bending with the same geometry as the one presented in numerical tests in section 2.3. - 2.5.

A model with dimensions of 950 mm x 330 mm composed of two 8 mm thick glass plies with an interlayer of 0.76 mm thickness (PVB) is tested. The glass is defined as a linearly elastic material with a modulus of elasticity $E=70$ GPa, and the interlayer characteristics are taken from commercial manufacturers [41], as in the numerical tests. The shear modulus of the interlayer is presented in Table 2.7 for different temperatures and load durations.

Table 2.7. The values of shear modulus (G_{int}) of PVB interlayer [41]

Temperature / duration	1 min	24 h	1 month
25 °C	131 MPa	1.7 MPa	0.7 MPa
40 °C	0.9 MPa	0.4 MPa	0.2 MPa

The maximum deflections that occur due to the bending load (simulation of the four-point bending test) are first observed at room temperature (25 °C) and then at 40 °C. The total applied force on the element is 1000 N. The force is divided into two forces ($P = 500N$) at a distance of 200 mm apart. An analytical calculation is carried out, and the used expression for the deflection is determined through the elastic line of the beam:

$$w_{l/2} = \frac{1}{E \cdot I_{ef}} \cdot \left[\frac{P}{6} \cdot \left(-\left(\frac{l}{2}\right)^3 + \left(\frac{l}{2} - a\right)^3 \right) \right] + \left[\frac{P}{12} \cdot ((l)^3 - (l - a)^3 - (l - b)^3) \right] \quad (2.6.14)$$

where, the used values (P, l, a, b) are presented in Figure 2.14., and I_{ef} is the effective stiffness calculated using the effective thickness for each method.

2. Influence of temperature and load duration on the behaviour of laminated glass elements loaded out of plane

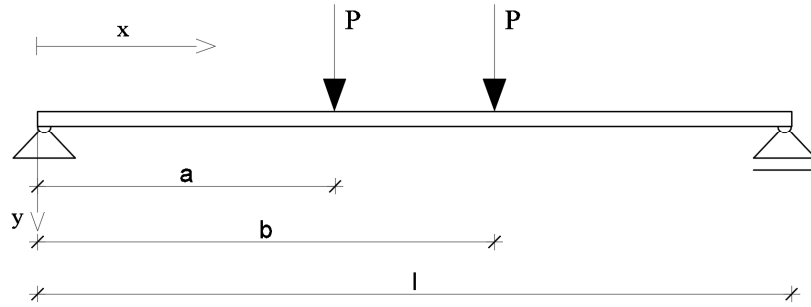


Figure 2.14. Scheme of the observed static system with the load for analytical calculation

The stress at the bottom ply is determined using the effective thickness for stress and the equation (2.6.15):

$$\sigma = \frac{M}{W_{ef,\sigma,j}} = \frac{M}{\frac{b_s * h_{ef,\sigma,j}^2}{6}} \quad (2.6.15)$$

where M is the moment in the observed cross-section (in the mid-span), b_s is the width of the cross-section, and $h_{ef,\sigma,j}$ is the effective thickness for stress determination according to each of presented approaches.

To determine the ET according to [2] and [31] for elements exposed to four-point bending, it is necessary to calculate the coupling factor Ψ for this type of boundary conditions and load shape.

According to [31] the expression to determine the coupling factor is defined with the elastic line and its derivatives related to the geometry of the observed element:

$$\Psi = \frac{\int [g''(x)]^2 dx}{\int [g'(x)]^2 dx} \quad (2.6.16)$$

For the presented geometry and load in Figure 2.14. ($a \approx 0,4l$ and $b \approx 0,6l$), the expression for the elastic line is:

$$g(x) = -\frac{P}{6} \cdot x^3 + \frac{P}{6} \cdot (x - 0,4 \cdot l)^3 + \frac{P}{6} \cdot (x - 0,6 \cdot l)^3 + \frac{3 \cdot P \cdot l^2}{25} \cdot x \quad (2.6.17)$$

where P is equal to half of the total force applied on element, and l is equal to the span of the element. By introducing the equation 2.6.17 into 2.6.16, we obtain:

$$\Psi = \frac{\int_0^{0,4l} [-P \cdot x]^2 dx + \int_{0,4l}^{0,6l} [-P \cdot x + P \cdot (x - 0,4 \cdot l)]^2 dx + \int_{0,6l}^l [-P \cdot x + P \cdot (x - 0,4 \cdot l) + P \cdot (x - 0,6 \cdot l)]^2 dx}{\int_0^{0,4l} \left[-\frac{P}{2} \cdot x^2 + \frac{3 \cdot P \cdot l^2}{25}\right]^2 dx + \int_{0,4l}^{0,6l} \left[-\frac{P}{2} \cdot x^2 + \frac{P}{2} \cdot (x - 0,4 \cdot l)^2 + \frac{3 \cdot P \cdot l^2}{25}\right]^2 dx + \int_{0,6l}^l \left[-\frac{P}{2} \cdot x^2 + \frac{P}{2} \cdot (x - 0,4 \cdot l)^2 + \frac{P}{2} \cdot (x - 0,6 \cdot l)^2 + \frac{3 \cdot P \cdot l^2}{25}\right]^2 dx} \quad (2.6.18)$$

2. Influence of temperature and load duration on the behaviour of laminated glass elements loaded out of plane

$$\psi = \frac{\frac{8 \cdot l^3 \cdot P^2}{375} + \frac{4 \cdot l^3 \cdot P^2}{125} + \frac{8 \cdot l^3 \cdot P^2}{375}}{\frac{58 \cdot l^5 \cdot P^2}{15625} + \frac{l^5 \cdot P^2}{9375} + \frac{58 \cdot l^5 \cdot P^2}{15625}} = \frac{9,915014164}{l^2} \quad (2.6.19)$$

The obtained solution closely matches to the proposal for the case of three-point bending of a simply supported beam, which is equal to:

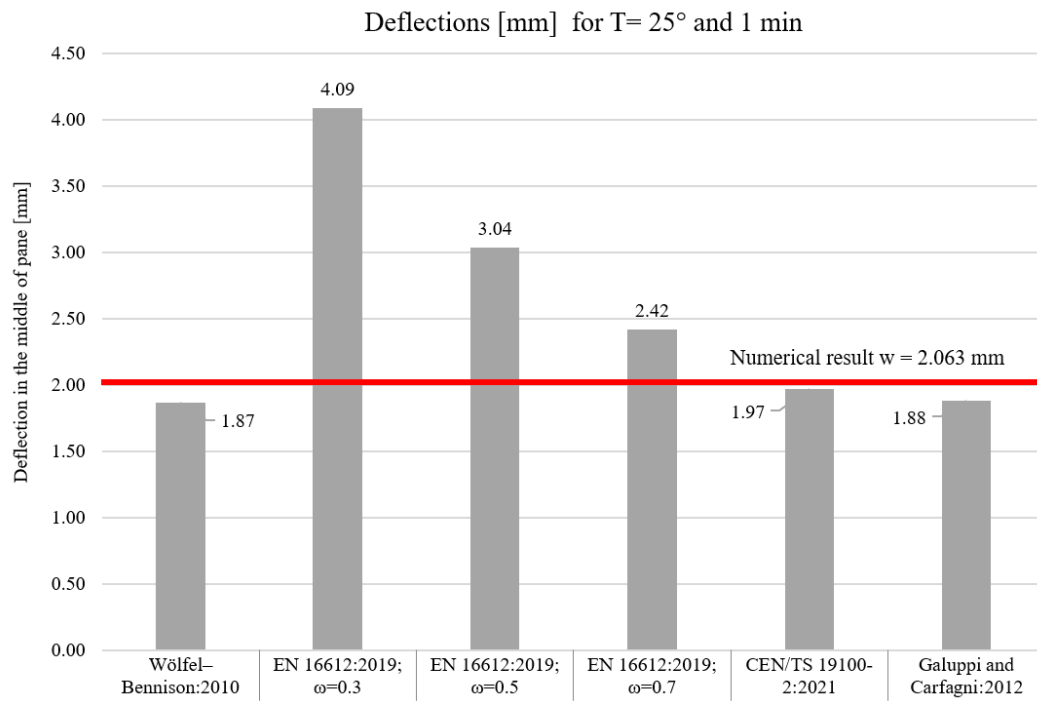
$$\psi = \frac{10}{l^2} \quad (2.6.20)$$

Furthermore, in the expression from the regulation EN 16612 [22] (Table 2.4.), the coefficient ω defines complete transfer of shear forces for $\omega = 1$ or no transfer of shear forces for $\omega = 0$. To determine the best predictability, three values of coefficient $\omega = 0.3; 0.5; 0.7$ will be used in further comparisons.

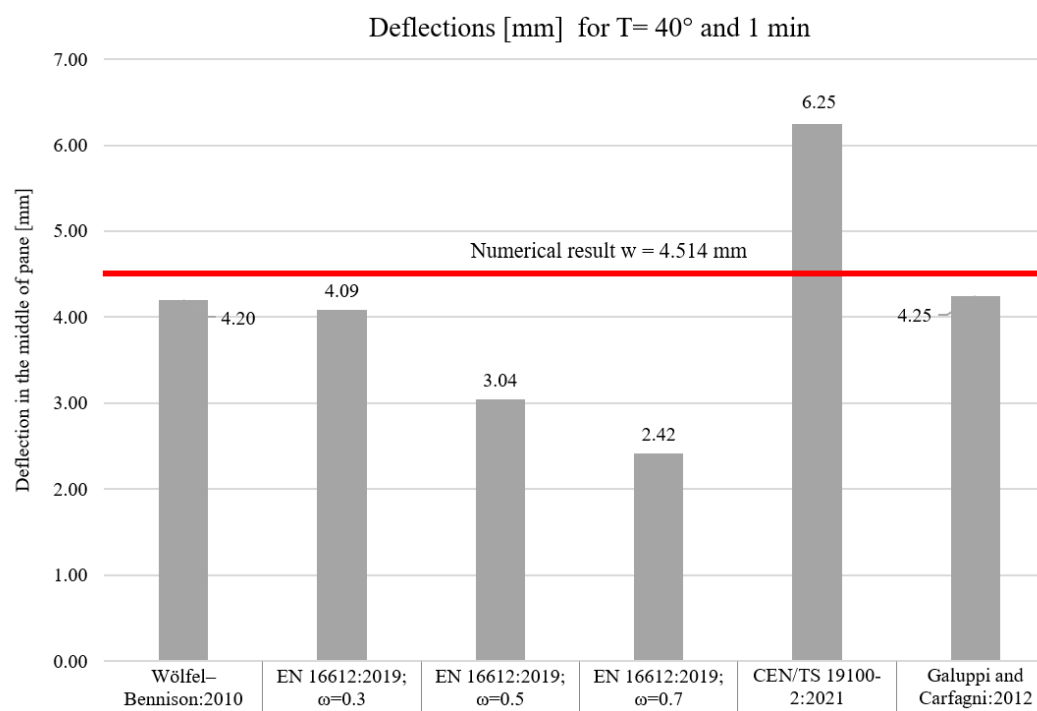
The results of the analytical calculation are shown in Figures 2.15. – 2.17., and Figures 2.19. – 2.21. Deflections for various load durations and temperatures are determined, and for each case, a numerical result is presented as a reference value. It can be observed that the results according to EN 16612 [22] (Table 2.4.) are consistent across all temperature and load durations cases. This is done to assess the best predictability regarding three proposed values of shear transfer coefficient ω . The accuracy of the approach according to EN 16612 [22] (Table 2.4.) is unsatisfactory for the most common values of coefficient ω . For instances of short load durations and room temperatures (25 °C and 1 min), the deflections are overestimated, while for longer load durations (24 h and 1 month) the deflections are significantly underestimated, which compromises safety. Specifically, for $\omega = 0.5$ the calculated deflection compared to the numerical deflection for a 1-minute load duration is 47.35% higher at 25 °C and 32.65% lower at 40 °C. For other cases of longer load durations, nearly all predictions underestimate actual deflections, indicating an overestimated stiffness of the structure. Wölfel-Bennison [58] approach provides results similar to the Galuppi and Royer-Carfagni [31] approach. Variations in the shear transfer coefficient F and the shear transfer coefficient η , dependent on the degradation of the interlayer's shear modulus, ensure lower errors with a slight tendency to underestimate the deflections. The calculations using the Wölfel-Bennison [58] approach resulted in deflections lower than the numerical model, with a discrepancy range of (3.5% - 9.36%) of the numerical deflection. Similarly, calculations using the Galuppi and Royer-Carfagni [31] effective thickness produced deflections with a discrepancy range (2.31% - 8.87%) of the numerical deflection, with a tendency to underestimate. The calculation with CEN/TS 19100-2:2021 [2] approach provides the safest results, mostly overestimating the deflections. However, the discrepancy interval is highest for a load duration of 24 h and room

2. Influence of temperature and load duration on the behaviour of laminated glass elements loaded out of plane

temperatures, reaching 56.9% of numerical prediction, which is the largest deviation observed among all predictions. The expression for effective thickness from [2] is highly sensitive to changes in the shear modulus of interlayer compared to those from [31] and [58].



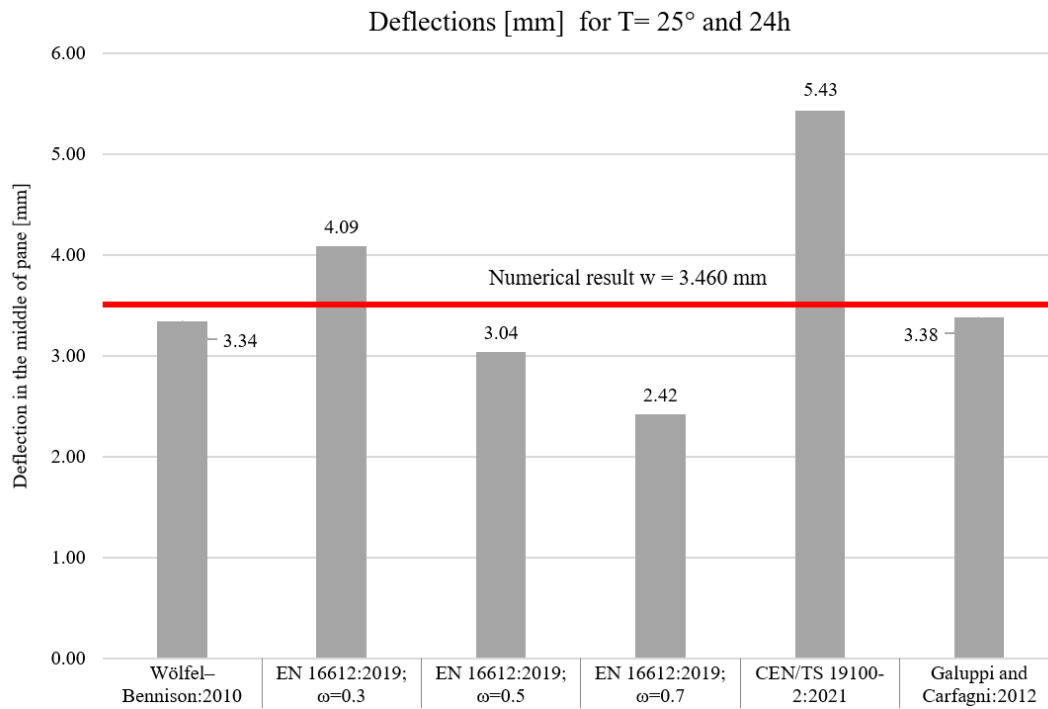
a) deflections for load duration $t = 1 \text{ min}$ and temperature $T = 25^\circ \text{C}$



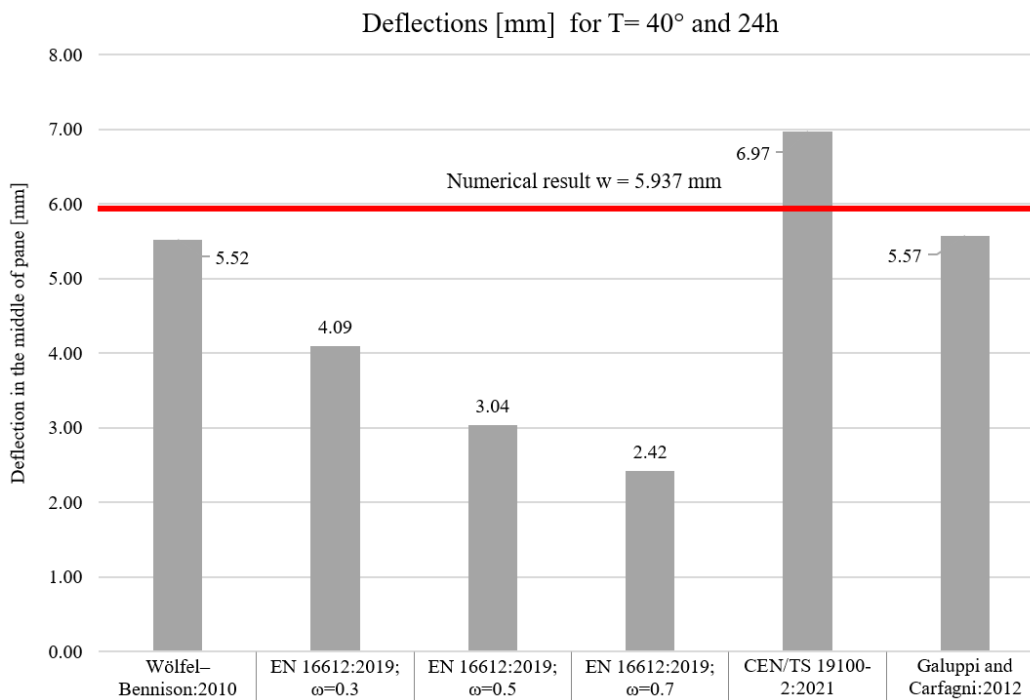
b) deflections for load duration $t = 1 \text{ min}$ and temperature $T = 40^\circ \text{C}$

Figure 2.15. Deflections according to different approaches for analytical calculation

2. Influence of temperature and load duration on the behaviour of laminated glass elements loaded out of plane



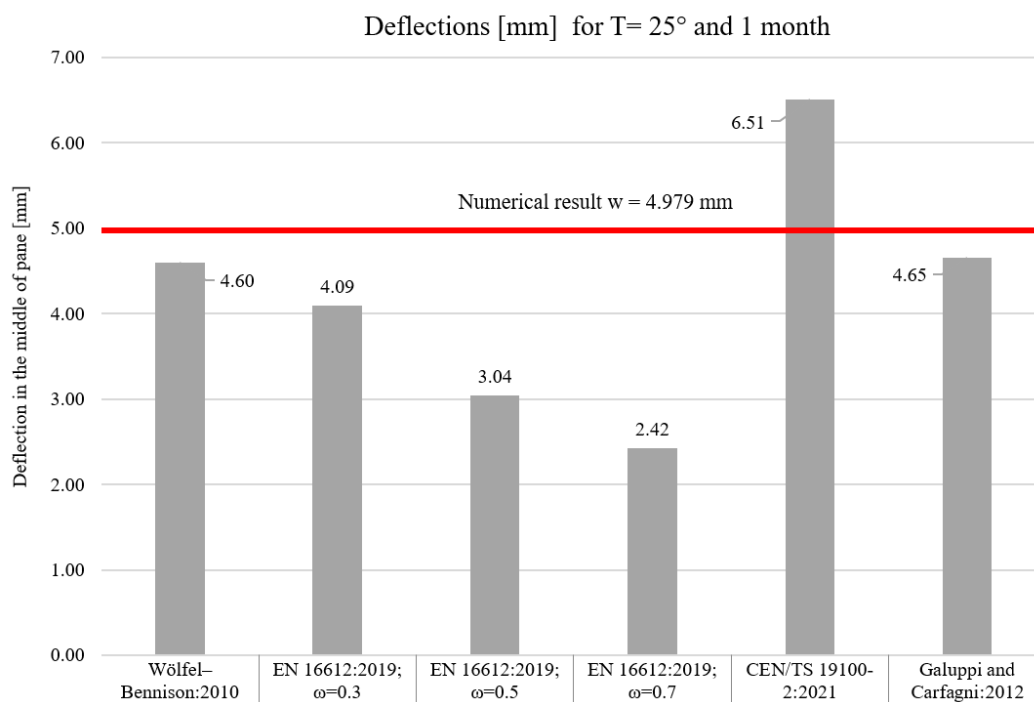
a) deflections for load duration $t = 24$ h and temperature $T = 25$ °C



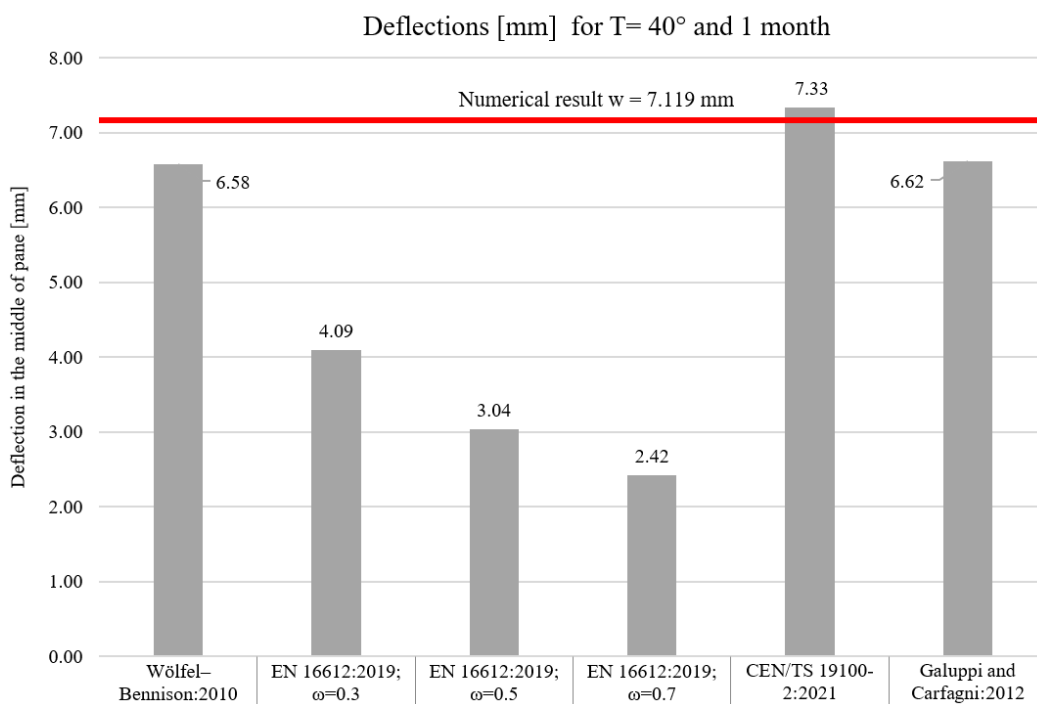
b) deflections for load duration $t = 24$ h and temperature $T = 40$ °C

Figure 2.16. Deflections according to different approaches for analytical calculation

2. Influence of temperature and load duration on the behaviour of laminated glass elements loaded out of plane



a) deflections for load duration $t = 1 \text{ month}$ and temperature $T = 25^\circ \text{C}$



b) deflections for load duration $t = 1 \text{ month}$ and temperature $T = 40^\circ \text{C}$

Figure 2.17. Deflections according to different approaches for analytical calculation

2. Influence of temperature and load duration on the behaviour of laminated glass elements loaded out of plane

To observe variation in shear transfer coefficients depending on the shear modulus of the interlayer, a comparison curve for the three values of shear transfer coefficients (with fixed geometry) is presented in Figure 2.18.

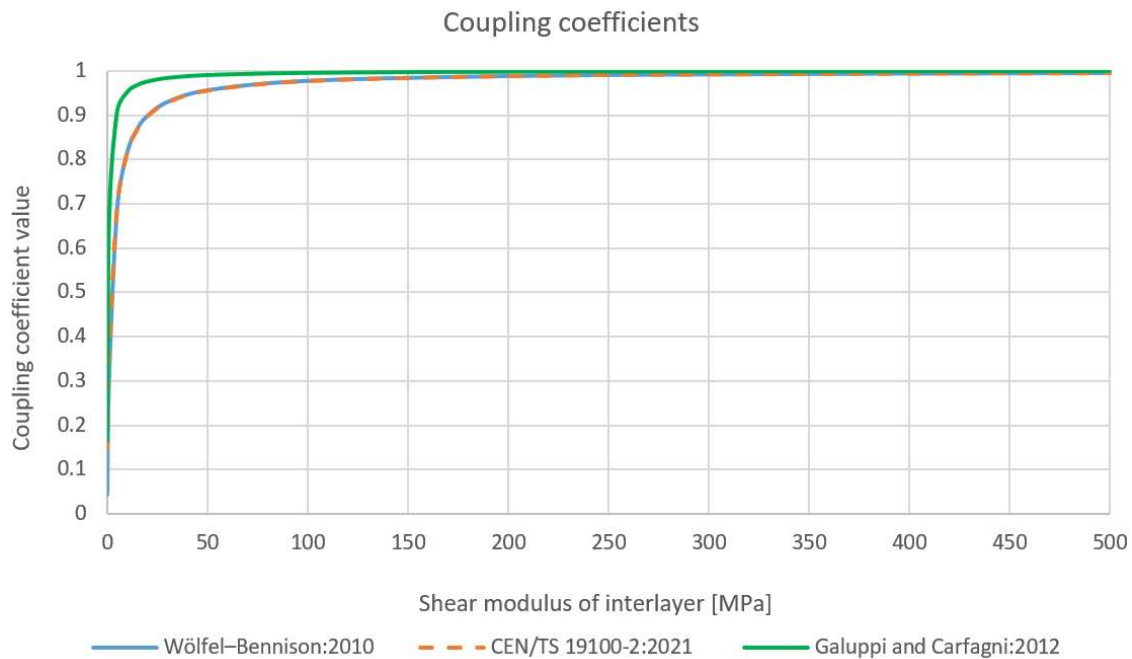
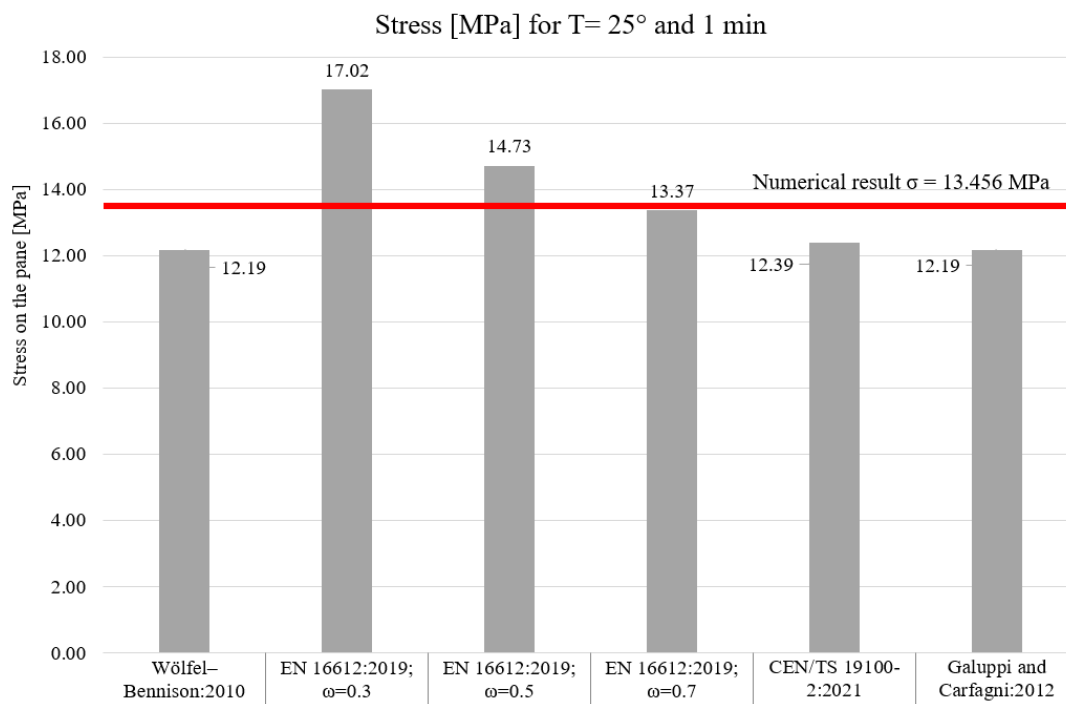


Figure 2.18. Comparison of shear transfer/coupling coefficients from different ETA [58] [31] [2]

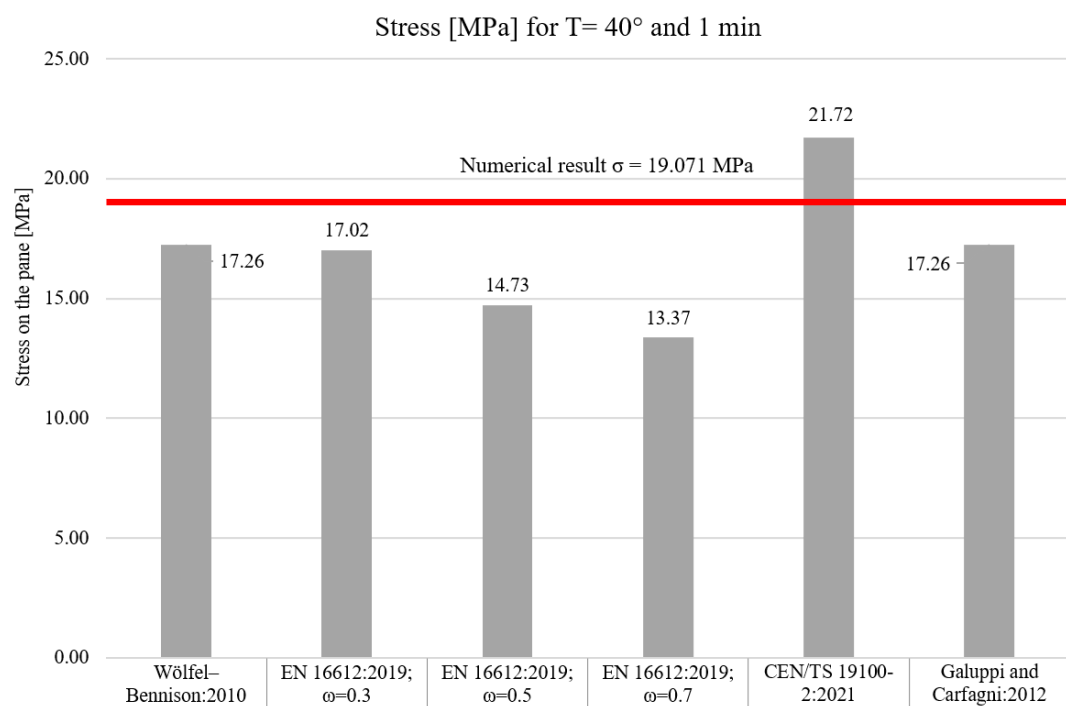
From Figure 2.18., it can be seen that the shape of the curve describing the dependence of shear transfer coefficients on the value of shear modulus is similar, and that the shape of coupling parameter η from [2] and shear transfer coefficient Γ from [31] are a perfect fit. However, due to different equations for deflections, very similar values (of deflections) occur for the approach according to Wölfel-Bennison [58] and Galuppi and Royer-Carfagni [31], while the results from CEN/TS 19100-2:2021 [2] show a different trend.

In Figures 2.19. – 2.21., the stress determined analytically using different ETA is presented and compared with the numerical value. The stress values refer to the bottom ply, which is exposed to tensile stress that leads to fracture. Again, the three values of the shear transfer coefficient ω are used for the calculations with equations from EN 16612 [22], and the other values are calculated based on the shear modulus of interlayer and geometry.

2. Influence of temperature and load duration on the behaviour of laminated glass elements loaded out of plane



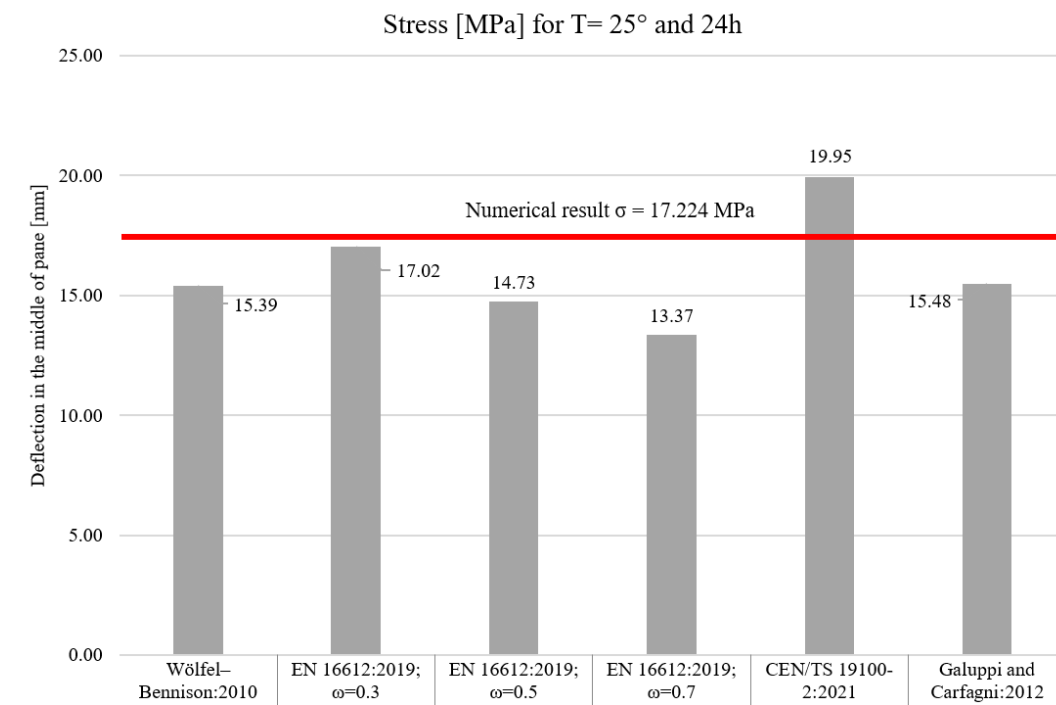
a) stress value for load duration $t = 1 \text{ min}$ and temperature $T = 25^\circ \text{C}$



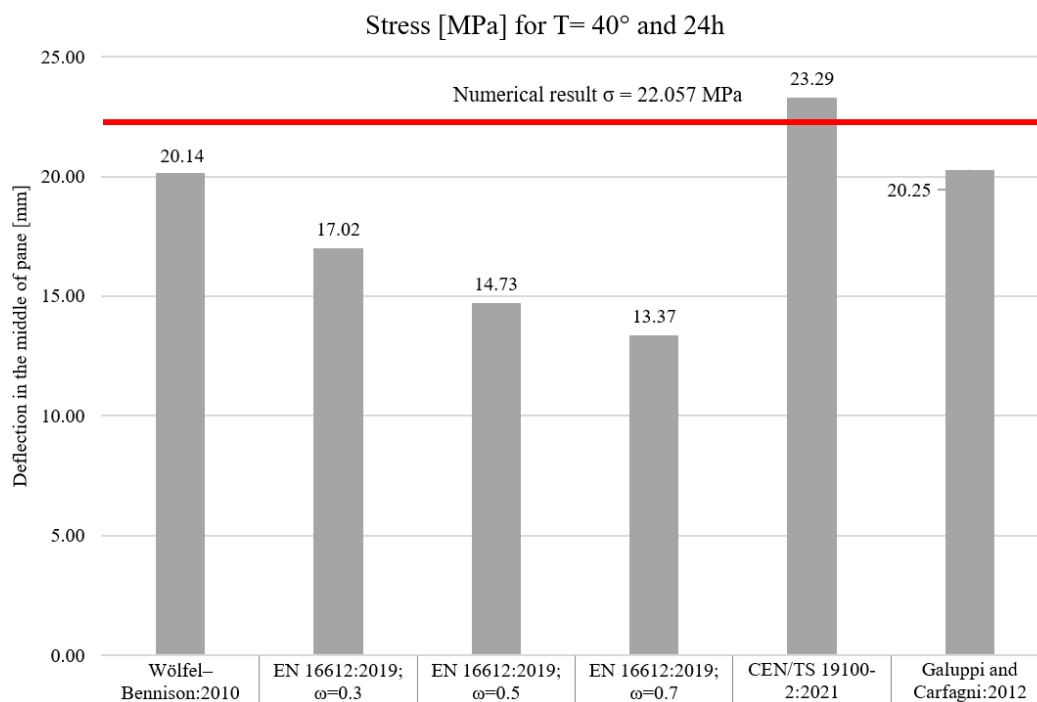
b) stress value for load duration $t = 1 \text{ min}$ and temperature $T = 40^\circ \text{C}$

Figure 2.19. Stress on elements according to different approaches for analytical calculation

2. Influence of temperature and load duration on the behaviour of laminated glass elements loaded out of plane



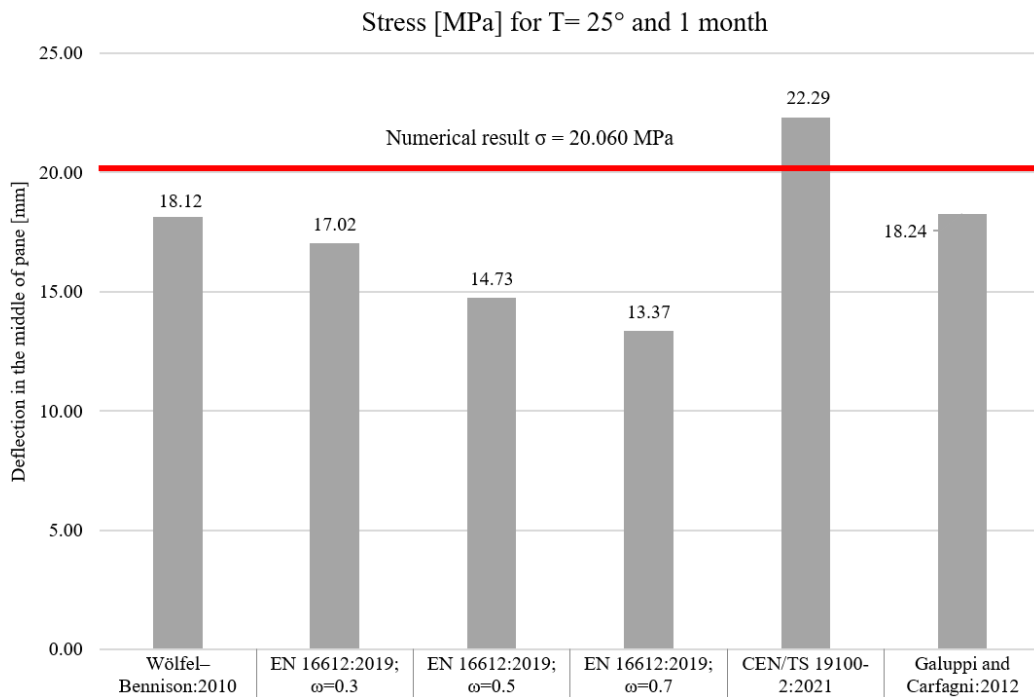
a) stress value for load duration $t = 24 h$ and temperature $T = 25^\circ C$



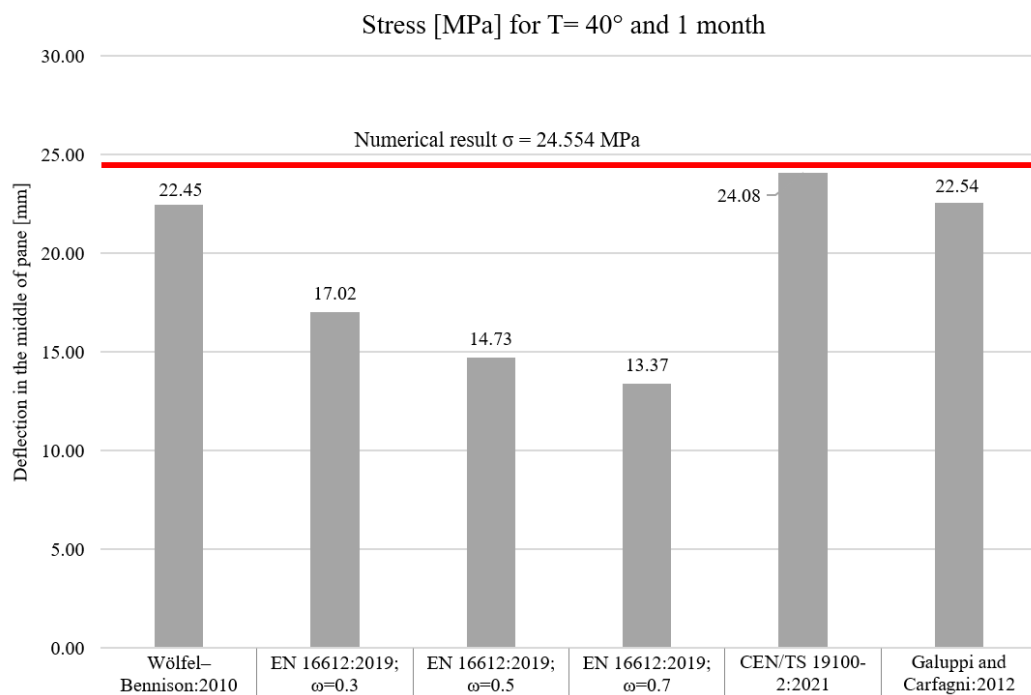
b) stress value for load duration $t = 24 h$ and temperature $T = 40^\circ C$

Figure 2.20. Stress on elements according to different approaches for analytical calculation

2. Influence of temperature and load duration on the behaviour of laminated glass elements loaded out of plane



a) stress value for load duration $t = 1 \text{ month}$ and temperature $T = 25^\circ \text{C}$



b) stress value for load duration $t = 1 \text{ month}$ and temperature $T = 40^\circ \text{C}$

Figure 2.21. Stress on elements according to different approaches for analytical calculation

The presented stress in Figures 2.19. -2.21. shows a deviation in results with a similar pattern to the deflections. The difference is in the value of the deviation, which is lower for stress

prediction compared with the deformation predictions. This leads to the conclusion that the impact of load duration and temperature change is slightly lower for stress prediction than for deformations. It can be seen that the equations from regulation [2] are on the safe side, except at 1 min loading and 25 °C temperature, and at 1 month and 40 °C, where a lower value is predicted (7.9% and 1.9% of numerical stress value, respectively). The calculation according to Wölfel–Bennison and L. Galuppi et al. provides a lower value of stress than those from numerical models, but the discrepancy is mostly within the interval of 8.2% - 10.65% of numerical stress value. The shear transfer coefficient ω from EN 16612 [22] for load durations over 1 minute should be lower than the used minimal value $\omega = 0.3$. For the expressions according to Wölfel-Bennison [58], Galuppi and Royer-Carfagni [31] and CEN/TS 19100-2:2021[2], the type of interlayer (PVB, EVA, ionoplast, etc.) is not as important as for expressions according to EN 16612 [22]. Namely, in [58][31][2], just by considering the values of material characteristics and geometry, it is possible to determine the safety interval for the observed structure. For the approach according to EN 16612 [22], it is necessary to observe what type of interlayer is used, what is the range of modulus degradations and how that (together with the size effect) affects the element's stiffness. Only with a detailed evaluation of this information can a proper value of the shear transfer coefficient ω be proposed. According to equation (2.16.13), for the liaison between regulations [22] and [2], the equivalent value of shear transfer coefficient ω for the cases of shear modulus from Table 2.7. fits in the interval $\omega_{EN\ 16612} = [0.04 - 0.92]$. This large range of the interval confirms that it is not easy to observe the behaviour of laminated glass structures through one value of the shear transfer coefficient ω for expected values of temperature and load duration changes.

2.7. Chapter Conclusions

In this chapter, the behaviour of laminated glass structures in stages before fracture is observed. This step is important because engineers need to be familiar with all aspects that can lead to higher stresses and deformations in the structure and accelerate the occurrence of breakage. Furthermore, the bearing capacity of laminated glass structures is highly affected by atmospheric conditions, load type, and load duration. It is important to reconsider all the conditions that a construction can be exposed to in its lifetime. That information is important in choosing the right type of interlayer, as well as proper structural dimensions and boundary conditions. For this type of brittle structure, we tend to create a safety offset for any critical value that could lead to failure. For engineering purposes, we tend to avoid nonlinear behaviour,

2. Influence of temperature and load duration on the behaviour of laminated glass elements loaded out of plane

at least in glass parts, because in brittle material it means to achieve failure of the observed structure. Unlike glass, interlayers are polymers, and these materials tend to enter nonlinear behaviour without catastrophic consequences. In laminated glass, the interlayers are mostly exposed to shear stress and a small amount of axial stress in ULS. Deformations in an unfractured state are small because the thickness of the interlayer is approximately 1 mm – 2 mm, but those shear deformations are of crucial importance for stress development on glass panels because they ensure coupled behaviour.

From the presented results, several conclusions can be drawn:

Laminated glass is used in construction for various purposes, where it is almost always exposed to larger or smaller temperature oscillations. Glass as a material is not subject to a significant change in properties due to amplitudes that correspond to atmospheric temperatures, but the same cannot be said for the interlayers. In the range of 0 °C up to 50 °C, the interlayers show a significant change in mechanical characteristics, as shown in previous sections. Therefore, when designing laminated glass elements, it is important to take into account the temperature changes that will occur in the structure. In addition to temperature, the durability and load-bearing capacity of interlayers also depend on ambient humidity (PVB), insolation (EVA) and load duration. In the calculation, these parameters are fixed at certain values to consider only the influence of temperature and load duration.

The simplified expressions for analytical deflection and stress prediction with ETA are tested to observe their capability to predict the behaviour of LG structures exposed to different temperatures and load durations, typical for the construction lifetime. One representative panel geometry was selected, for which the bearing capacity was tested numerically so that the reference value was familiar. The effective thicknesses were calculated according to five different expressions. From the results presented, it can be seen that only the European standards [2] provide expressions that do not overestimate the load capacity of laminated panels for static loads with durations over 1 min at room temperature and high atmospheric temperature (40°C). Expressions according to Wölfel–Bennison and L. Galuppi et al. give results very close to the numerical ones but slightly overestimate the load capacity of the panel. The expression from the European standards [2] should be improved to lower the sensitivity amplitude and thereby increase accuracy. However, the size of prediction amplitude from Wölfel–Bennison and L. Galuppi et al. is good, but the value they strive for is in all cases slightly below the expected. They would provide more confidence if it were slightly above the expected.

3. MULTISCALE MODEL WITH EMBEDDED DISCONTINUITY FOR SIMULATION OF LAMINATED GLASS ELEMENTS EXPOSED TO OUT-OF-PLANE LOADING

Contents

- 3.1. Introduction
 - 3.2. Numerical Simulations of Glass Breakage and Fragmentation – Methods Used in Literature
 - 3.3. Embedded Discontinuity Method
 - 3.4. Multiscale Model With Embedded Discontinuity
 - 3.5. Mathematical Formulations of the Fine-Scale Multilayer Model
 - 3.6. Mathematical Formulations of the Coarse-Scale Macro Model With Beam Elements
 - 3.7. Application of the Presented Mathematical Formulation in the Numerical Model
 - 3.8. Numerical Simulation Four-Point Bending Tests Using Multiscale Model
 - 3.9. Mathematical Formulations of the Coarse-Scale Macro Model With Plate Elements
 - 3.10. Chapter Conclusions
-

3.1. Introduction

Modelling the behaviour of monolithic and laminated glass structures exposed to static loading until fracture (not considering fracture itself), is available in different commercial software. An analysis regarding laminated glass behaviour is presented in the previous chapter and compared with the engineering approach for calculating the bearing capacity of laminated glass elements. The problem arises when the nonlinear behaviour of glass elements needs to be simulated. In the literature, several numerical techniques can be found for the simulation of glass fracture patterns. The methods are mostly used for dynamic loading in explicit calculations. Some of them have good graphical interpretation but lack physical explanation for certain processes (such as element deletion), and this problem is emphasized when the static load is tested. For the simulation of glass fracture under static loading, there are not many options. In the following sections, a literature overview is presented to elaborate on the achievements in the field of numerical modelling of glass nonlinear behaviour. Different methods are presented with their respective advantages and disadvantages. Afterwards, a new approach to modelling laminated glass behaviour with a multiscale model is presented. The model is based on the embedded discontinuity method, which is installed on two levels. For an introduction to the multiscale model, the embedded discontinuity method is first explained, and then a beam model is described. To validate the accuracy of the model, a comparison with experimental tests is used, and the results are presented. Furthermore, the extension of the multiscale model to the plate elements within the macro model is presented. At the end of Chapter 3, conclusions are provided and in Chapter 6 further steps are presented.

3.2. Numerical Simulations of Glass Breakage and Fragmentation – Methods Used in Literature

Simulating the fracture and fragmentation of brittle material is one of the challenges for researchers in the field of numerical modelling of glass structures. Depending on the type of glass observed (resulting in different stress conditions in the glass panel), different types of breakage patterns are achieved (Figure 1.3.). Modelling these fragmentations can be accomplished with numerical programs based on continuum or discontinuum methods. Pelfrene [60] in his thesis, described and tested different numerical methods for the simulation of glass fracture. First, the author used the Smoothed Particle Hydrodynamics (SPH) method, a mesh-free method that uses particles as a representation of a continuum, in this case, bulk glass fragments. The author concluded that SPH is a good option for simulating extreme load cases,

such as high velocity impacts where fragments achieve significant acceleration. When used at low velocity impact, a softened stiffness of the glass panel is observed. Another method presented in [60] is the Cohesive Zone Method/Model (CZM), a continuum method that enables crack propagation through elements that represent boundaries (between elements) with no need for an initial crack. The CZM models represent the fracture process zone as a line (or a surface) between elements where cohesive traction occurs. The fracture of such element appears as a gradual separation in small areas of the fracture process zone (crack tip), guided by the traction-separation law. There are two types of traction-separation laws: extrinsic and intrinsic, with differences in the behaviour before fracture. The extrinsic behaves rigidly before the defined fracture limit, while the intrinsic behaves elastically before the defined limit. These models are also used for dynamic loading, and in [60] author explained that in CZM, expected degree of fragmentation did not occur, instead, the element only behaved as softened. The intrinsic solid-shell cohesive zone model [61], and the extrinsic solid-shell cohesive zone model [62] are used for the simulation of fracture of windshield glazing exposed to impact load, where the models show increased computational efficiency compared to the solid cohesive zone model. In another analysis [63], the extrinsic shell cohesive zone models with improved contact algorithms are used to simulate the impact load on laminated glass elements, and a good prediction of fracture pattern and impact force occurred, matching the experimental results. Another method described in [60] is the Element Deletion Technique with a crack delay model based on the principle of decreasing element stiffness to zero for certain criteria. There are minor differences in approach, but the main principle is to decrease the stiffness of elements that reached the defined stress or strain criterion, and by graphically removing it, the fracture pattern is created. In most cases, criterion is that the element reaches the stress limit. In this method, the whole element is not deleted because it would result in mass instability; it is only excluded. The element deletion method is an often used method for the simulation of fracture patterns of glass elements in cases of impact loading [64][65][66] and blast loading [29][67], it occurs in finite element commercial software. The biggest drawback of this method is mesh dependence, making it unfavourable for local behaviour simulation. Osnes et al. [68] presented an explicit finite element numerical model to simulate the fragmentation of glass panels exposed to blast loading using the IMPETUS Afea Solver with high-order elements and node splitting technique. The authors describe it as suitable for large deformations and extreme loading conditions. The node splitting technique activates when integration point reaches the fracture criterion, in this case also a stress condition. This is similar to the extended finite element

method (X-FEM) where additional enrichment (jump) functions are used for describing the displacement field near the crack tips, allowing crack propagation independently of the mesh. This method is also used to simulate the behaviour of laminated glass exposed to impact load [69] and to simulate the crack development and propagation under a static load [70]. Simulation of glass and laminated glass behaviour is also conducted by discontinuity based methods such as the discrete element method (DEM) [71][72] and the combined finite discrete element method (FEM/DEM) [73][74][75]. For the DEM used in simulating glass behaviour under impact loads, a realistic fracture pattern is reported, but the authors notice a deviation in energy dissipation caused by parameter calibration [76]. The FEM/DEM has been proven to provide satisfactory results for high-velocity impacts as well as for low-velocity impacts in a comparison study between FEM, X-FEM, DEM and FEM/DEM [76]. A glass beam exposed to low-velocity hard body impact is used for a numerical test in [76] to test the accuracy of four methods (FEM, X-FEM, DEM and FEM/DEM). In FEM analysis, a smeared model is used for simulating cracking failure with a crack threshold according to Rankine's theory of maximum principal stress exceeding tensile strength. Only Mode 1 is considered for crack initiation, but both Mode 1 and Mode 2 are observed for crack propagation. For X-FEM, phantom nodes and linear elastic fracture mechanics (LEFM) theory with additional functions are used. Phantom nodes use overlapping elements to bridge discontinuities to avoid the introduction of additional unknowns and provide mesh independence. For this method (X-FEM), it is reported that the results differ most in the manner of fragmentation. The DEM domain is discretized in many elements connected with boundaries. These numerous particles act individually when force is applied, producing simulations for progressive fracturing of brittle materials. The DEM model provided a good simulation of fracturing the glass beam, but the authors point out that the demanding parameter calibration makes the method unpredictable and creates deviations in energy dissipation. FEM/DEM uses the same crack initiation criteria and critical energy release as FEM, and a stress-displacement curve is used to model Mode 1 behaviour (Fig. 3.1.). The surface under the curve represents a critical energy release rate described as 2γ (surface energy). In the strain-softening interval ($\delta_t - \delta_c$), the softening function is used to describe a decrease in bond (joints) stress. Bond stress vanishes at the point where the crack is initiated. The softening function is defined by the constants determined from the experimental results of the observed material. Shear behaviour is also calculated using a softening function and penalty function method. This method is reported as the most accurate method for predicting the real behaviour of glass under different types of low-velocity impact.[15] In [77] and [76], an overview of the

most common numerical methods for predicting the behaviour of glass elements such as DEM, FEM/DEM, CZM and the element deletion method is presented. Another overview of techniques related to failure analysis of laminated glass in FEM is presented in [78].

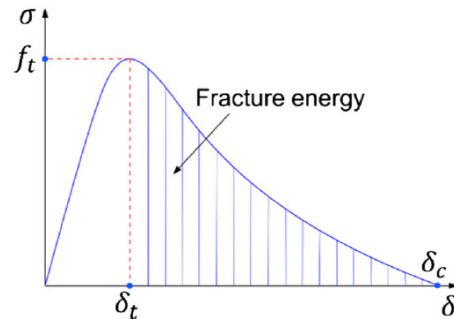


Figure 3.1. Stress - displacement curve from Wang et al. [76]

When all glass plies, or a few of them, are broken, the post-breakage capacity of LG element depends on several mechanisms that occur in this state. The behaviour of fractured LG members is primarily guided by the mechanical behaviour of the interlayer and the adhesion of the interlayer and glass fragments. In this state, a detailed simulation of interlayer behaviour in a non-homogenous stress state with a proper simulation of the adhesion of interlayer and glass fragments, as well as fragment size and position, is necessary. There are numerous pieces of research that deal with the post-breakage capacity of laminated glass for in-plane loading [79][80][81], and for out-of-plane (bending) loading [82][83]. Other influences on post-breakage capacity confirmed by research are the chemical composition of interlayers and glass surfaces [84] (peel test and through-the-crack tensile test), strain rates and temperature [85], and boundary conditions [86]. A detailed overview of approaches, techniques and their advantages and disadvantages in modelling and testing the post-breakage capacity of LG elements exposed to various loads can be found in [87]. Reliable and correct simulation of the LG mechanisms for pre- and post-breakage stages is a ubiquitous and important topic. At this current stage of development of glass regulations, it is important to define the appropriate calculation methods as well as those that are not appropriate.

3.3. Embedded Discontinuity Method

Simulation of the exact pattern of glass fragmentation is not always useful for designing glass elements. In practice, it is more important to be familiar with the strength and resistance of the observed structure than the number of fragments into which the structure is broken. Guided by this approach, a numerical model is developed, capable of simulating the fracture behaviour of laminated glass elements until the complete failure of glass plies. However, in the proposed model, the simulation of the exact fracture pattern or the number of cracks is not in the focus.

Instead, a mesh-independent finite element model is developed that can predict a structural failure threshold by using only the basic material characteristics (tensile strength, modulus of elasticity, Poisson's ratio). Since glass failure initiation is localized, and by reaching the ultimate strength at the weakest point a complete fracture occurs, it is important to predict this initial step that leads to fracture. Once the mechanism is triggered, excessive softening behaviour occurs, without a change in the modulus before fracture. To describe this phenomenon, an embedded discontinuity finite element method [88] [89] is used in a multiscale model for LG beams. The embedded discontinuity finite element method (ED-FEM) is a computationally efficient method that works on local and global levels. It simulates localized failure mechanisms by introducing a discontinuity in the deformation or displacement field for a threshold defined by material constitutive behaviour. The method is similar to X-FEM but computationally more efficient because it keeps additional unknowns at the local element level.[90] For an easier understanding of the method and the localization phenomenon, a simple tension test on generic material is illustrated in Figure 3.2. For simplification, a material that exhibits a hardening and softening regime is used. The Figure 3.2. can be observed through three columns, where the first presents the element loaded in tension with the associated strain diagrams, and the second two columns present the stress-strain diagrams of the bulk of the element and the position where an imperfection in material occurs, respectively. The three stages of loading are presented in three rows. By imposing force or displacement to one end of the element, first a uniform stress and strain represented in Figure 1a) is obtained. The element strain, at this stage, is homogeneously distributed along the element. By further increasing stress the element reaches the point where the weakest part (an imperfection in the material) enters an inelastic behaviour (Figure 3.2. b)). At this stage, the imperfection is activated, which results in a slight increase in strain in a small area (ε_2) developing heterogeneity in the strain field along the element. In the area of increased strain, inelastic deformation occurs, higher than in bulk of the material (columns two and three in Fig 3.2.b)). If the load is further increased, the specimen enters stage three, where necking appears due to the increase in a localized strain field shown in Figure 3.2.c). The localization phenomenon usually occurs in the weakest part of the element (material) and further leads to increase in strain in only one part of the element while the strain in the rest of the element decreases (see stress-strain diagrams in stage three Figure 3.2.c)).

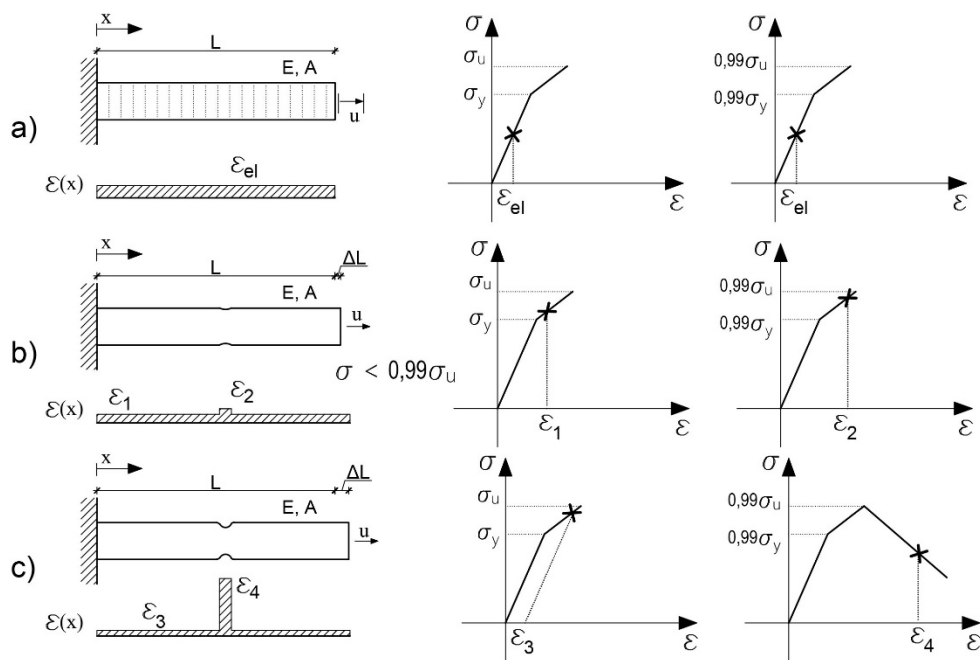


Figure 3.2. Graphical representation of stages for localization development in a simple tension test [23]

The embedded discontinuity method, with an additional kinematics enhancement in terms of a displacement jump (or strong discontinuity), is used to describe this localization phenomenon. For strong discontinuity, the jump in the displacement field can appear in the axial or transversal displacement field [91][92] or in the rotation field [93]. In finite element implementation [94], the jump is introduced as an additional degree of freedom added at the Gauss point on the finite element. This requires solving extra equations to define the energy dissipation in the softening process. [23] The jump in a displacement field is not an explicit model of crack propagation on the element level, but rather a crack simulated within the element's strain and displacement field upon reaching certain criteria, and its contribution manifests through the work of inner variables that cause energy dissipation. Depending on how the behaviour of inner variables connected with energy dissipation is defined, this approach can simulate plastic or damage type dissipation. The entire approach is based on a thermodynamics framework with two levels of calculation, known as the "operator split computational method". A more detailed description of all mechanisms is provided in the following sections.

3.4. Multiscale Model With Embedded Discontinuity

The multiscale approach consists of two models; a fine-scale multilayer and a coarse-scale macro model, based on [89]. A fine-scale multilayer model is used to define the constitutive

law parameters (of the true layered cross-section) for the beam elements in the macro model. These models can be considered as material modelling tools combined with structure modelling tools. With a combination of two models, a full simulation of laminated beam behaviour is achieved. The proposed models (micro and macro) are discretized and built using the embedded discontinuity finite element method with operator split computations. The model can represent the pre-breakage and breakage phases of laminated glass structures exposed to bending loads. In the following sections, the fine-scale multilayer model is first presented and described in detail followed by a description of a coarse-scale macro model. Subsequently, the connection between the two models is presented, along with a mesh and layer dependence test as well as numerical examples compared with experimental results.

3.5. Mathematical Formulations of the Fine-Scale Multilayer Model

This section describes the mathematical formulation of the fine-scale multilayer model, divided into three parts: kinematics, constitutive law, and equilibrium. This model serves as the basis for defining the constitutive material law for elements in the macro-scale model.

3.5.1. Kinematic Equations for Fine-Scale Multilayer Model

The fine-scale multilayer model is based on the Timoshenko beam element with a realistic cross-section of an LG beam. The cross-section is composed of n^d parts which represent glass plies and interlayers. Each of these parts is further divided into n^{lay} layers that have a uniform displacement $u^i(x, y^i)$ through the thickness of i -th layer, defined as the displacement computed along the middle axis of the observed layer. As each layer has an assigned displacement, in the case of bending these values differ through the height of the cross-section. For describing the nonlinear behaviour of each layer, an embedded discontinuity approach is used. To simulate the material failure of each layer, a corresponding displacement jump is introduced once the defined limit is exceeded. For clarification, consider an LG cantilever beam with imposed rotation, consisting of two glass plies and an interlayer in the middle, see Figure 3.3. Since the cross-section is a three-part cross-section $n^d = 3$, each of these parts is divided into layers defined by the distance y^i from the element neutral axis. The sum of these layers forms the cross-section with dimensions b/h . The layers are defined as truss bar elements with an assigned embedded axial discontinuity that can appear in the middle of the element. The appearance of the discontinuity is guided by the constitutive law. Finally, the model consists of beam elements composed of many layers through the height, which as a whole behave as the Timoshenko beam. The length of the fine-scale multilayer beam element is equal to the length

3. Multiscale model with embedded discontinuity for simulation of laminated glass elements exposed to out-of-plane loading

of the element in the macro model, to simplify the scale transition. In this manner, the scale transition is reduced to defining the macroscale constitutive model. The model used for the definition of macroscale constitutive behaviour is a simple cantilever beam with imposed displacement.

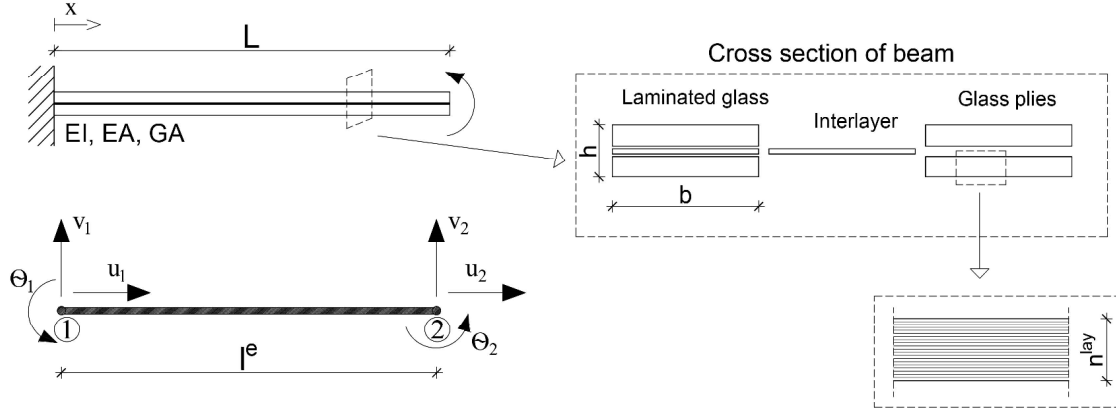


Figure 3.3. Schematic representation of the element from the fine-scale multilayer model

[23]

As already mentioned, the element in the fine-scale multilayer model is a Timoshenko beam for which the generalized strains are equal:

$$\varepsilon(x) = \frac{du(x)}{dx}; \quad \gamma(x) = \frac{dv(x)}{dx} - \theta(x); \quad \kappa(x) = \frac{d\theta(x)}{dx} \quad (3.5.1)$$

to determine the stress in each layer, it is necessary to calculate strain, which first requires defining the displacements $[u, v, \theta]$. The axial displacement of each layer, before fracture, can be described as:

$$u^i(x, y^i) = u(x) - y^i \theta(x); \quad i = 1, \dots, n^{lay} \quad (3.5.2)$$

In equation (3.5.2), y^i represents the distance of the beam neutral axis from the center of the i -th layer, and $\theta(x)$ is the rotation of the beam cross-section. As layers are modelled as truss bar elements only, the axial displacement field variation occurs. A model enhancement in the form of strong discontinuities is introduced once layers reach given limits. This enhancement represents the localized failure mechanisms in the glass layers. The discontinuity is placed at a Gauss point x_c on the layer and is treated as an additional degree of freedom. The enhanced displacement field $\tilde{u}^i(x, y^i)$ for layers with strong discontinuities is thus written as:

$$\tilde{u}^i(x, y^i) = u^i(x, y^i) + \alpha_u^i H_{x_c} \quad (3.5.3)$$

where $u^i(x, y^i)$ is the regular part of the displacement of the observed layer i , the α_u^i is the discontinuity variable defined as the axial displacement jump introduced at each layer where defined limit is exceeded, and H_{x_c} is the Heaviside function with jump in $x = x_c$ defined as:

$$H_{x_c}(x) = \begin{cases} 1, & x \geq x_c \\ 0, & x < x_c \end{cases} \quad (3.5.4)$$

By rewriting the kinematics, the enhanced axial displacement field for the i -th layer can be written as:

$$\tilde{u}^i(x, y^i) = \frac{u(x) - y^i \theta(x)}{u^i(x, y^i)} + \alpha_u^i H_{x_c} \quad (3.5.5)$$

where $u(x)$ is the axial displacement of the beam at the neutral axis, $\theta(x)$ is the beam cross-section rotation, and α_u^i is the displacement jump in the axial direction. The enhanced layer with all degrees of freedom is presented in Figure 3.4. To eliminate the influence of the discontinuity outside the layer (and element) boundary (local level), the function $\varphi(x)$ is introduced, and the previous expression (3.3.5) can be rewritten as:

$$\dot{u}^i(x, y^i) = \underbrace{\left(u^i(x, y^i) + \alpha_u^i \varphi(x) \right)}_{\bar{u}^i(x, y^i)} + \alpha_u^i \underbrace{(H_{x_c} - \varphi(x))}_{M(x)} \quad (3.5.6)$$

where $\varphi(x)$ is introduced to cancel the contribution of displacement jump α_u^i at the boundary of the layer (element) domain. By choosing the function $\varphi(x)$ to be equal negative value of shape function $-N_2(x)$, a new function $M(x)$ is created, see Figure 3.5. Equation (3.5.6) can be rewritten in the form:

$$\dot{u}^i(x, y^i) = \bar{u}^i(x, y^i) + \alpha_u^i M(x) \quad (3.5.7)$$

where $M(x)$ is a new function defined as:

$$M(x) = H(x) - N_2(x) \quad (3.5.8)$$

$$\varphi(x) = -N_2(x); \quad N_1(x) = 1 - \frac{x}{l^e}; \quad N_2(x) = \frac{x}{l^e}; \quad (3.5.9)$$

$$M(x) = \begin{cases} -\frac{x}{l^e}, & x < x_c \\ 1 - \frac{x}{l^e}, & x > x_c \end{cases} \quad (3.5.10)$$

and the $N_1(x)$ and $N_2(x)$ are the shape functions, see Figure 3.5.

This approach enables handling the discontinuity at the local level without the need for an additional degree of freedom introduced in the global phase. [94]

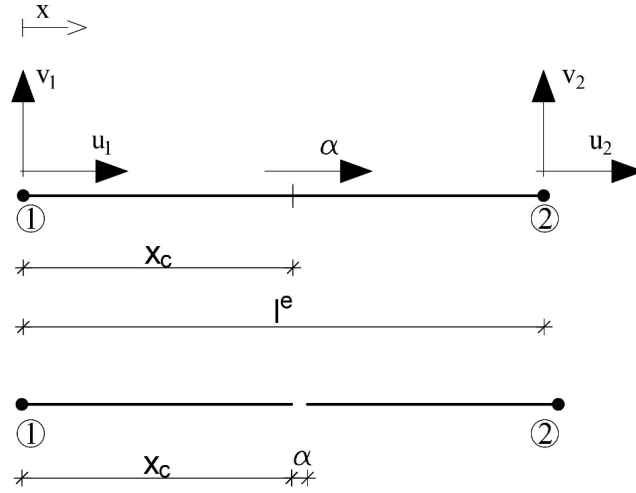


Figure 3.4. Schematic representation of one layer with all degrees of freedom and discontinuity in the middle [23]

At the local level, the discontinuity in the layer's displacement field brings the singularity further in the strain field. The equation for the layer strain field $\varepsilon^i(x)$ can be additively decomposed into:

$$\varepsilon^i(x) = \varepsilon^i(\bar{u}^i)(x) + \alpha_u^i \hat{G}(x) + \alpha_u^i \delta_{x_c}^i(x) \quad (3.5.11)$$

Where $\hat{G}(x)$ is the function created by derivation of the function $\varphi(x) = -N_2(x)$:

$$\frac{d\varphi(x)}{dx} = \hat{G} = \left(-\frac{1}{l^e}\right) \quad (3.5.12)$$

The dissipation in the form of Dirac delta function $\delta_{x_c}^i(x)$ appears only at the point $x = x_c$ while in the rest of the layer, only unloading occurs. The complete expression for axial strain in layer i can be written as:

$$\begin{cases} \varepsilon^i(x) = \frac{d\hat{u}^i}{dx} = \underbrace{\frac{u^i(x, y^i)}{l^e} + \left(-\frac{1}{l^e}\right) \alpha_u^i}_{\tilde{\varepsilon}^i} + \alpha_u^i \delta_{x_c}^i(x) & x = x_c \\ \varepsilon^i(x) = \tilde{\varepsilon}^i(x) = \frac{d\hat{u}^i}{dx} = \frac{u^i(x, y^i)}{l^e} + \left(-\frac{1}{l^e}\right) \alpha_u^i & x \neq x_c \end{cases} \quad (3.5.13)$$

$\tilde{\varepsilon}^i(x)$ denotes the regular part of the strain field, while the axial displacement jump α_u^i multiplied by the Dirac delta function $\delta_{x_c}^i(x)$ represents the singular part of the strain. For the appearance of the axial displacement jump α_u^i , at one point of the layer a dissipation occurs, while unloading occurs in the rest, represented by the second member in the equation. A

schematic representation of equation (3.5.13) is presented in Figure 3.6., where (1) is the graphical representation of the first member from both lines of equation (3.5.13) representing the classical strain on the element. The area labelled with (2) in Figure 3.6. represents the second member from both lines of equation (3.5.13) accounting for unloading (relaxation) due to the discontinuity appearance. The dissipation appears only at the point $x = x_c$, which is defined by strain multiplied by the Dirac delta function. Figure 3.6. is equivalent to Figure 3.2. which represents localization at the element. The only difference (if we compare the strains graph in Figure 3.2. c) and the one in Figure 3.6.) is in the size and representation of the softening zone (the width of the area $\varepsilon_2, \varepsilon_4$). Specifically, the issues regarding the size of the localization zone (ε_4) are avoided here by contracting it to a single point ($x = x_c$) where a localized dissipative mechanism occurs.

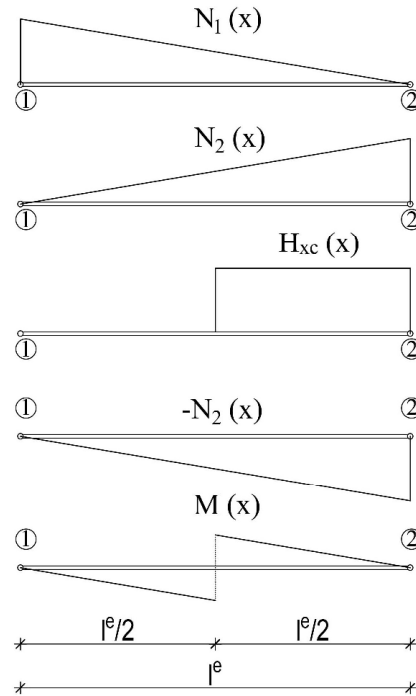


Figure 3.5 Schematic representation of base functions, Heaviside function and the construction of interpolation function for layers [23]

Strain field $\tilde{\varepsilon}^i(x)$ on the layer (the regular part) is obtained from the layer's regular displacements in the axial direction $u^i(x, y^i)$ and the belonging displacement jump, if it occurs.

$$\tilde{\varepsilon}^i(u^i, \alpha_u^i) = \sum_{a=1}^2 B_a u^i(x_a, y^i) + \left(-\frac{1}{l^{e,i}}\right) \alpha_u^i \quad (3.5.14)$$

Further, the stress at each layer can be determined incrementally:

$$\Delta\sigma^i(u^i, \alpha_u^i) = C\Delta\tilde{\varepsilon}^i(u^i, \alpha_u^i) = C \left[\sum_{a=1}^2 B_a \Delta u^i(x_a, y^i) + \left(-\frac{1}{l^{e,i}}\right) \Delta\alpha_u^i \right] \quad (3.5.15)$$

where B_a represents the derivative of the shape functions N_a , defined as:

$$B_a = \frac{dN_a}{dx} = \frac{(-1)^a}{l^e} \quad (3.5.16)$$

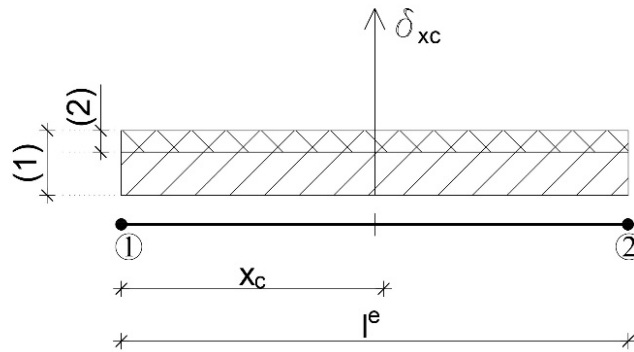


Figure 3.6 Schematic representation of strain field in one layer

3.5.2. Constitutive Laws for Glass and Polymer in Fine-Scale Multilayer Model

The constitutive model for the fine-scale multilayer model is a one-dimensional format, see [94]. It is defined independently for glass and polymer, by using their basic mechanical characteristics (elastic modulus and axial strength). Constitutive models are constructed within the framework of the thermodynamics of continuous media (e.g., see [94]).

Glass layer behaviour is defined as a linear-elastic regime with a direct transition to a softening regime for tension loading, and a linear-elastic regime with hardening and softening behaviour for compression loading. The behaviour of the interlayer layers is defined only for tension as a linear-elastic behaviour with a transition to plastic hardening. The softening (failure) mechanism for glass is described with softening laws triggered by either tensile or compressive loads. A corresponding internal variable (e.g., inelastic strain, displacement discontinuity) appears for each behaviour phase to simulate dissipative processes in materials. The stress in nonlinear behaviour for each layer is determined incrementally from the constitutive laws. Since glass has significantly lower ultimate strength in tension than in compression, the nonlinear behaviour is mostly triggered by tension. Two models of the one-dimensional

3. Multiscale model with embedded discontinuity for simulation of laminated glass elements exposed to out-of-plane loading

response of glass layers, one for tension and the other for compression, are presented in Figure 3.7.

To define the different stages of behaviour, threshold functions are introduced:

$$\Phi(\sigma_i, q) = |\sigma| - (\sigma_i - q_i) \leq 0 \quad (3.5.17)$$

In equation (3.5.17) σ_i is the stress limit defined for each stage and q_i is the stress-like variable that controls the internal variable evolution (in hardening or softening). To define the inelastic behaviour of glass, loaded in tension or in compression, different threshold functions are introduced with corresponding material parameters presented in Table 3.1.

Table 3.1. Different inputs for the threshold function and stress-strain diagram from Figure 3.7.

i = 2: tension-softening phase	$\sigma_{2,t} = f_{u,t} ; \bar{q}_{2,t} = -\bar{K}_{2,t} \bar{\xi}_{2,t}$
i = 1: compression-hardening phase	$\sigma_{1,c} = f_{c,c} ; \bar{q}_{1,c} = \bar{K}_{1,c} \bar{\xi}_{1,c}$
i = 2: compression-softening phase	$\sigma_{2,c} = f_{u,c} ; \bar{q}_{2,c} = -\bar{K}_{2,c} \bar{\xi}_{2,c}$

The hardening modulus in compression is defined as $\bar{K}_1(\bar{K}_{1,c})$, and the corresponding hardening variables are $\bar{\xi}_1(\bar{\xi}_{1,c})$. Meanwhile, $\bar{K}_2(\bar{K}_{2,t}; \bar{K}_{2,c})$ are the softening moduli, and $\bar{\xi}_2(\bar{\xi}_{2,t}; \bar{\xi}_{2,c})$ are the corresponding softening variables for tension and compression, respectively. For the first response phase, where stress is under the defined limit $\sigma_i < f_{limit} (f_{u,t}; f_{u,c})$, the model behaves linearly elastic, and the threshold function is $\Phi(\sigma_i, q) < 0$. This case implies no change in internal variables.

The hardening behaviour occurs only for glass under compressive loading, and during this phase, diffuse dissipative mechanisms in the material remain active as long as the threshold function is equal to zero.

$$\bar{\Phi}^i(\sigma_1^i, \bar{q}^i) := |\sigma^i| - (\sigma_{1,c} - \bar{q}^i) = 0 \quad (3.5.18)$$

As equation (3.5.18) is verified, the evolution of hardening variables in layer i occurs, implying that micro-damage occurs inside the fracture process zone. The stress-like hardening variable \bar{q}^i is defined in (3.5.19).

$$\bar{q}^i = -\bar{K}_1 \bar{\xi}^i \quad (3.5.19)$$

In the hardening phase, the stress-like hardening numerical variable (\bar{q}^i) describes linear hardening of the material. It is defined as the strain-like hardening variable $\bar{\xi}^i$ (with an initial value equal to zero) multiplied by \bar{K}_1 , the hardening modulus. Unloading from the hardening phase is linear and parallel with the loading line retaining the permanent deformation.

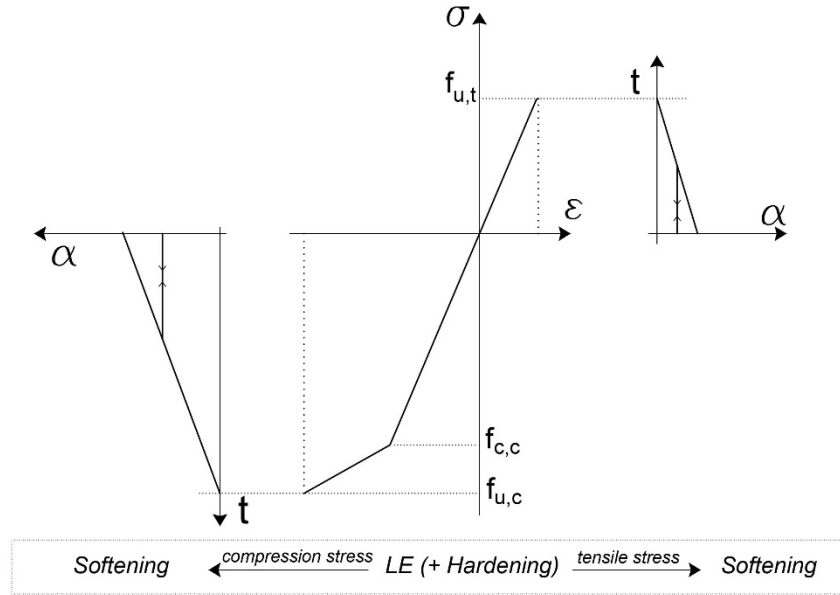


Figure 3.7 A stress-strain diagrams for glass constitutive behaviour in fine-scale model [23]

As already mentioned, glass material does not exhibit significant permanent deformation before fracture (only crushing occurs in compression), so this hardening transition is of minimal size, see Figure 3.7.

Furthermore, once the threshold function defining the ultimate limit reaches zero, the element enters a softening regime (either under tensile or compression loading):

$$\bar{\Phi}^i(t^i, \bar{q}_2^i) := |t^i| - (\sigma_{2,t} - \bar{q}_2^i) = 0 \quad (3.5.20)$$

In the softening phase, heterogeneous strain fields appear, guided by the occurrence of displacement discontinuity. The softening law is used to describe localized dissipation. The occurrence of displacement discontinuity presents a reduction in the load capacity of the observed layer. Here, the driving force of displacement at the point of discontinuity is the traction, which is equal to the bulk stress. This enables the local equilibrium inside the layer. By increasing the displacement jump (α_u^i), the driving traction at discontinuity and the bulk stress in the layer both decrease, see Figure 3.7. The displacement jump (α_u^i) represents localized inelastic deformation in softening behaviour. From this phase, the elastic reloading

follows the unloading curve, with decreasing strain and stress, leaving the internal variable unchanged.

The stress-like softening variable \bar{q}_2^i that modifies the softening threshold is defined as:

$$\bar{q}_2^i = -\bar{K}_{2,t} \bar{\xi}^i \quad (3.5.21)$$

In the softening phase, a rigid inelastic behaviour occurs and a parameter α_u^i is equal to the inelastic strain. The evolution of α_u^i can be described as:

$$\alpha_u^i = \dot{\lambda} \frac{\partial \bar{\Phi}^i}{\partial \sigma} = \dot{\lambda} \text{sign}(\sigma) \quad (3.5.22)$$

The multiplier $\dot{\lambda}$ is defined as equal to a strain-like inner variable:

$$\dot{\xi}^i = \dot{\lambda} \frac{\partial \bar{\Phi}^i}{\partial \bar{q}_2^i} = \dot{\lambda} \quad (3.5.23)$$

In the softening phase, stress reduction can be described as traction and bulk stress:

$$t^{i,trial} + \int_0^{l^e} \hat{G}^i \sigma^i dx = 0 \quad (3.5.24)$$

3.5.3. Equilibrium Equations for Fine-Scale Multilayer Model

The basic form of equilibrium of a structure can be described in a weak form, using the virtual work principle:

$$G^{int,beam} - G^{ext,beam} = 0 \quad (3.5.25)$$

The virtual work of external forces $G^{ext,beam}$ is equal to the product of the vector of virtual nodal displacements ($\mathbf{d}^{*(beam)}$) and the vector of the external forces ($\mathbf{f}^{ext,beam}$).

$$G^{ext,beam} = \mathbf{d}^{*(beam)T} \mathbf{f}^{ext,beam} = \sum_{j=1}^{n_{DOF}} d_j^{*(beam)} f_j^{ext,beam} \quad (3.5.26)$$

The virtual work of internal forces $G^{int,beam}$ is computed through assembling contributions from all finite elements.

$$G^{int,beam} = \sum_{e=1}^{n_{EL}} G^{e,int} \quad (3.5.27)$$

The internal virtual is first computed for each element by multiplying the components of the virtual strain field and the stress field and summing the product over the volume of the element (summing over the layers):

$$\begin{aligned}
 G^{e,int} &= \int_{V^e} (\varepsilon^* \sigma + \gamma^* \tau) dV = \iint_{l^e, A} (\varepsilon^* \sigma + \gamma^* \tau) dA dx \\
 &= \int_{l^e} \sum_i (\varepsilon^{i*} \sigma^i + \gamma^* \tau^i) A^i dx
 \end{aligned} \tag{3.5.28}$$

Hence, the virtual strains are equal:

$$\varepsilon^{i*} = \mathbf{B}\mathbf{u}^* - y^i \mathbf{B}\boldsymbol{\theta}^* + \hat{G}^i \alpha_u^{i*}; \quad \gamma^* = \mathbf{B}\mathbf{v}^* + \mathbf{B}^* \boldsymbol{\theta}^* \tag{3.5.29}$$

where $\mathbf{u}^* = [u_1^*, u_2^*]^T$, $\mathbf{v}^* = [v_1^*, v_2^*]^T$, and $\boldsymbol{\theta}^* = [\theta_1^*, \theta_2^*]^T$ are the virtual displacements (axial and transversal), and rotation respectively. The derivatives of the interpolation functions are $\mathbf{B} = [B_1, B_2]$, and $\mathbf{B}^* = \left[-\frac{1}{2}, -\frac{1}{2}\right]$.

After introducing equations (3.5.26) and (3.5.28) into equilibrium equation (3.5.25), we obtain two equations:

$$\mathbf{f}^{int,beam} - \mathbf{f}^{ext,beam} = 0 \tag{3.5.30}$$

$$h^{e,i} = \int_0^{l^e} \hat{G}^i \sigma^i A^i dx \tag{3.5.31}$$

The last equation is an additional equation of virtual work that needs to be solved only for layers with discontinuity. We can obtain:

$$\mathbf{t}^{i,trial} = - \int_0^{l^e} \hat{G}^i \sigma^i A^i dx \tag{3.5.32}$$

$$\bar{\Phi}_{n+1}^{i,trial} = |\mathbf{t}_{n+1}^{i,trial}| - (\sigma_{2,t} - \bar{q}_{2,n}^i) \tag{3.5.33}$$

$$\bar{\gamma}_{n+1}^i = \frac{\bar{\Phi}_{n+1}^{i,trial}}{\frac{E}{l^e} + \bar{K}_{2,t}} \tag{3.5.34}$$

$$\bar{q}_{2,n+1}^i - \bar{q}_{2,n}^i = -\bar{K}_{2,t} \cdot \bar{\gamma}_{n+1}^i \tag{3.5.35}$$

$$\mathbf{t}_{n+1}^i = \mathbf{t}_{n+1}^{i,trial} - \frac{E}{l^e} \cdot \bar{\gamma}_{n+1}^i \cdot \text{sing}(\mathbf{t}_{n+1}^i) \tag{3.5.36}$$

3.6. Mathematical Formulations of the Coarse-Scale Macro Model With Beam Elements

In this section, a geometrical and material representation of a coarse-scale macro model will be presented. The elements in this model are defined with a monolithic cross-section with material model parameters defined from a previously described fine-scale multilayer model. Since both

models use an embedded discontinuity approach, some of the already presented peculiarities will be slightly shortened here or recalled from previous equations.

3.6.1. Kinematic Equations for Coarse-Scale Macro Model (Macro Model 1)

By gathering the solution from the fine-scale multilayer model, we define a moment-rotation curve which serves as a constitutive law for the coarse-scale macro model. The macro model consists of a homogenized monolithic cross-section. The elements in the macro model are also the Timoshenko beams with two nodes and three degrees of freedom per node. Each element has enhancement in the rotation field (similar to axial enhancement in layers from the micro model) defined as embedded rotation discontinuity, see Figure 3.8.

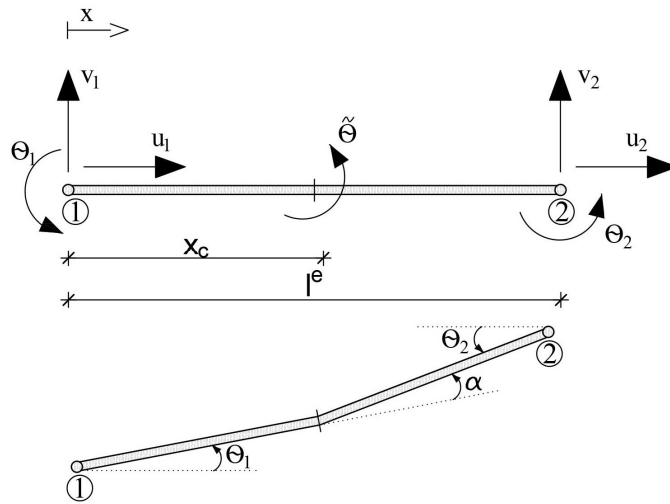


Figure 3.8 Schematic representation of a beam element with seven degrees of freedom in the macro model [23]

By using a macro coarse-scale model an enhancement in computation efficiency is achieved, concerning the option to model the entire construction within a micro model. To simulate the development of a localized failure mechanism in the macro coarse-scale model, a discontinuity in the rotation field $\theta(x)$ is adopted. The discontinuity is placed at the Gauss point on the beam neutral axis, at $x = x_c$. Hence, the rotation field of the element is composed of the sum of regular and singular parts:

$$\tilde{\theta}(x) = \theta(x) + \alpha \cdot H_{x_c} \quad (3.6.1)$$

The first part in the equation (3.6.1) is the regular part of rotational displacement, and the second singular part consists of a rotational jump α multiplied by the Heaviside function, defined in (3.5.4).

The embedded strong discontinuity in the rotation field will appear if the carrying capacity of the beam is reached. The capacity is defined in terms of the ultimate moment derived from a fine-scale multilayer model. In the rotation field, the discontinuity represents a hinge that occurs at the point $x = x_c$.

Axial and transversal displacements of the element are observed in the middle axis of the beam and those are interpolated with linear interpolation functions $N(x)$, defined as:

$$\begin{aligned} u(x) &= N_1(x)u_1 + N_2(x)u_2 = \mathbf{N}\mathbf{u} \\ v(x) &= N_1(x)v_1 + N_2(x)v_2 = \mathbf{N}\mathbf{v} \end{aligned} \quad (3.6.2)$$

The interpolation functions are defined as linear functions:

$$\mathbf{N}(x) = \{N_1, N_2\} = \left\{1 - \frac{x}{l^e}, \frac{x}{l^e}\right\} \quad (3.6.3)$$

By using the incompatible mode method [94], no additional degrees of freedom are transferred to the global phase, the discontinuity is kept at the local phase of computation. The discontinuity in the rotation field implies the corresponding singularity in the strain field. The strain field $\kappa(x)$ can be additively decomposed into regular and singular parts:

$$\kappa(x) = \hat{\kappa}(x) + \alpha \cdot \delta_{x_c}(x) \quad (3.6.4)$$

The equation (3.6.4) can be further rewritten in terms of embedded discontinuity:

$$\kappa(x) = \tilde{\kappa}(x) + \alpha \cdot \hat{G}(x) + \alpha \cdot \delta_{x_c}(x) \quad (3.6.5)$$

where $\hat{G}(x)$ is defined in (3.5.12) as the derivative of the part of function $M(x)$ that comes from the introduced additional function $\varphi(x)$ that cancels the influence of the discontinuity outside element (see equations, (3.5.8) – (3.5.12)). The deformations in the rest of the element can be written as:

$$\begin{aligned} \varepsilon(x) &= \frac{\partial u}{\partial x} = \mathbf{B}\mathbf{u} \\ \gamma(x) &= \frac{\partial v}{\partial x} - \theta = \mathbf{B}\mathbf{v} + \mathbf{B}^*\theta \\ \kappa(x) &= \mathbf{B}\theta + \hat{G}\alpha \end{aligned} \quad (3.6.6)$$

Where \mathbf{B} are derivatives of interpolation functions:

$$\mathbf{B} = \left\{-\frac{1}{l^e}, \frac{1}{l^e}\right\}; \quad \mathbf{B}^* = \left\{-\frac{1}{2}, -\frac{1}{2}\right\}; \quad (3.6.7)$$

3.6.2. Constitutive Laws For the Macro Model Elements

The constitutive law for the macro model is developed within the thermodynamics framework. For the axial and shear directions, the beam behaviour is assumed to be elastic. The nonlinear behaviour and dissipation are related only to bending. Hence, the localization results in a hinge placed at a Gauss point $x = x_c$. The physical interpretation of the hinge in the monolithic cross-section of the macro scale model defines the hinge as a part of the beam where the glass plies reach ultimate fracture strength, and the structure is held only by the interlayer, see Figure 3.9. The interlayer in the hinge enables axial connection and allows rotation. In further mathematical formulations, the hinge is observed as a plastic hinge. The choice of a plastic hinge for simulating laminated glass structure behaviour might seem strange at first, however, the fracture of the glass parts of the laminated glass beam, together with possible interlocking phenomena [16], leads to behaviour that can be well described with a plastic hinge – providing no force resistance to beam rotation once passing the threshold. [95] [23]

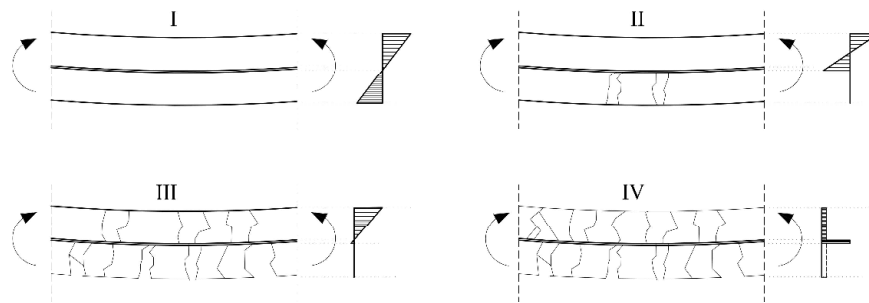


Figure 3.9. Representation of the process of hinges formation in laminated glass member

The threshold function is defined with ultimate bending moments, derived from the microscale model:

$$\Phi(M, q) = |M| - (M_n - q) \leq 0 \quad (3.6.8)$$

In equation (3.6.8), q is the stress-like variable that controls the evolution of the plasticity threshold. It depends linearly on the inner (bending) strain variable (ξ), and M_n is the moment corresponding to the limits of each regime (defined from the microscale mode curve). Constitutive behaviour consists of a linear part, a small hardening transition, and a linear softening part. The procedure for determining constitutive limits and factors through the representative beam element is presented further in the chapter. By using the second principle of thermodynamics for the elastic process, the state equations for the linear hardening part are determined:

$$M = EI(\kappa^{tot} - \kappa^{pl}) = EI\kappa^{el} \quad (3.6.9)$$

$$q = -K\xi \quad (3.6.10)$$

In equation (3.6.10), the K is the modulus derived from the fine-scale multilayer model, and ξ is strain variable. By using the principle of maximum dissipation, the evolution law and constitutive equations are derived as:

$$\dot{\kappa}^{pl} = \dot{\lambda} \frac{\partial \Phi}{\partial M} = \dot{\lambda} \text{sign}(M) \quad (3.6.11)$$

$$\dot{\xi} = \dot{\lambda} \frac{\partial \Phi}{\partial q} = \dot{\lambda} \quad (3.6.12)$$

Depending on the current value of the plastic multiplier ($\dot{\lambda}$), plastic loading or elastic unloading appears, which allows defining the bending rate equation:

$$\dot{M} = \begin{cases} EI\dot{\kappa} & \dot{\lambda} = 0 \\ \frac{EIK}{EI + K}\dot{\kappa} & \dot{\lambda} > 0 \end{cases} \quad (3.6.13)$$

The loading/unloading conditions define the plastic admissibility of bending moments:

$$\dot{\lambda}\Phi = 0; \quad \dot{\lambda} \geq 0, \Phi \leq 0 \quad (3.6.14)$$

The dissipation, defined according to the second principle of thermodynamics, will be zero [23]:

$$\begin{aligned} 0 \leq D^{pl} &= M\dot{\kappa} - \frac{d}{dt}\psi(\kappa^{el}, \xi) \\ &= M\dot{\kappa}^{pl} + q\dot{\xi} = M_y\dot{\xi} \end{aligned} \quad (3.6.15)$$

The first activation of dissipative mechanisms, triggered by zero value of the threshold function, occurs when the element briefly enters the hardening behaviour in the bulk.

$$\bar{\Phi}_y(M, \bar{q}_y) := |M| - (M_y - \bar{q}_y) = 0 \quad (3.6.16)$$

The hardening evolution, is again controlled by a stress-like variable, is equal to:

$$\bar{q}_y = -\bar{K}_1\bar{\xi} \quad (3.6.17)$$

where $\bar{\xi}$ is the equivalent variable to the bending strain. Furthermore, the second dissipative mechanism is triggered again by the zero value of the threshold function that represents the softening behaviour:

$$\bar{\Phi}_u(M_{x_c}, \bar{q}) = |M_{x_c}| - (M_u - \bar{q}) \leq 0 \quad (3.6.18)$$

M_{x_c} is the bending moment on the rotation discontinuity at $x = x_c$, and M_u is the ultimate moment limit value that can be modified with \bar{q} , a stress- like variable that controls softening:

$$\bar{q} = -\bar{K}_2 \bar{\xi}; \quad \bar{K}_2 < 0 \quad (3.6.19)$$

During the softening phase, a change of internal variable $\bar{\xi}$ occurs. This variable is equal to the localized plastic strain. According to its evolution, the equation can be defined as:

$$\dot{\bar{\xi}} = \dot{\lambda} \frac{\partial \bar{\Phi}}{\partial \bar{q}} = \dot{\lambda} \quad (3.6.20)$$

The associated value of parameter α is then defined as:

$$\dot{\alpha} = \dot{\lambda} \frac{\partial \bar{\Phi}}{\partial M} = \dot{\lambda} \text{sign}(M) \quad (3.6.21)$$

Thus, defining the constitutive equation for the plastic hinge:

$$\dot{M}_{x_c} = \bar{K} \dot{\alpha} \quad (3.6.22)$$

3.7. Application of the Presented Mathematical Formulation in the Numerical Model

All further computations presented are carried out using a research version of the computer program FEAP, developed by Prof. R.L. Taylor at UC Berkeley [96]. The presented model is intended to simulate the behaviour of laminated glass elements exposed to out-of-plane loading. To be able to connect the two-scale model, the first step is to develop a real laminated glass cross-section in a multilayer model with basic material parameters. The multilayer model is designed as a source of parameters for the coarse-scale macro model. The scale transition is done through the chosen length of the elements in the multilayer model and the macro model and the determination of the corresponding parameters. The elements on which we first establish a connection between the two models are defined as representative beam elements (RBE), and these have the same length, load and boundary conditions. Hence, the chosen RBE is a cantilever beam loaded with imposed rotation, which is distributed uniformly along the beam, creating strain in each layer.

In all examples, the chosen cross-section consists of glass plies of tempered or float glass connected with a 0.76/1.52 mm thick layer of PVB (poly-vinyl-butylal) interlayer. These cross-sections are chosen so that results can be compared with experimental results from [12] [54] [83]. The used material characteristics for the glass elements and the interlayers are presented in Table 3.2. The cross-section in the fine-scale multilayer model is a composition of $n^d \cdot n^{lay}$ layers for n^d parts of the cross-section. As already presented, each of the layers behaves as a truss bar undergoing a uniaxial stress field, so it is only necessary to define the tension and compression axial strength of the material. For glass material, it is common that bending tests

3. Multiscale model with embedded discontinuity for simulation of laminated glass elements exposed to out-of-plane loading

are used to determine the strength of glass specimens, and pure axial tensile strength is not a common value when it comes to brittle materials. The defined strength of glass is usually taken as a flexural strength due to the rare appearance of pure tensile loading on these types of elements. The value of pure tensile strength is naturally lower than the bending strength in brittle heterogeneous materials. This happens as a consequence of the greater area exposed to maximum tensile stresses in pure tension. If the same size specimens are observed, the specimen loaded in uniaxial tension develops the maximum stress throughout its entire volume, while the specimen exposed to bending experiences maximum tensile stress only on one surface/small part of the volume. When it comes to brittle materials, which are highly sensitive to imperfections, this change in sampling volume means that there is a higher statistical probability of finding a larger imperfection. Hence, the strength and fracture properties measured in tensile tests will typically be lower than the corresponding properties measured in bending. Since in a fine-scale numerical model the element is defined through a composition of truss bars, it is necessary to introduce a pure tensile strength of glass. Here, 80% of the bending strength is taken to be equal to the pure tensile strength. The interlayer characteristics are taken from the literature, according to the experimental conditions, such as test temperature and load duration.

Table 3.2. Used material properties for glass and interlayer material

Properties	Label	Tempered glass	Float glass	PVB interlayer 1	PVB interlayer 2
Young modulus	E	70 000 MPa	70 000 MPa	387 MPa	24 MPa
Poisson's ratio	ν	0.23	0.23	0.46	0.46
Compressive hardening strength	$\sigma_{1,c} = f_{c,c}$	999 MPa	99 MPa	-	-
Hardening modulus, tension	$K_{1,t}$	70 000 MPa	70 000 MPa	1 MPa	1 MPa
Hardening modulus, compression	$K_{1,c}$	70 000 MPa	70 000 MPa	-	-
Tensile ultimate strength	$\sigma_{2,t} = f_{u,t}$	95 MPa	30 MPa	10 MPa	20 MPa
Compressive ultimate strength	$\sigma_{2,c} = f_{u,c}$	1000 MPa	100 MPa	-	-
Softening modulus, tension	$\overline{\overline{K}}_{2,t}$	- 700 0000 MPa	- 700 0000 MPa	-	-
Softening modulus, compression	$\overline{\overline{K}}_{2,c}$	- 700 0000 MPa	- 700 0000 MPa	-	-

3.7.1. Layer Optimization for a Fine-Scale Multilayer Numerical Model

To determine the optimal number of layers (n^{lay}) for each part of the cross-section (n^d), several setups with differences in the number of layers are tested. The results are presented in Figure 3.10. From the graph, it can be seen that the optimal number of layers that ensures convergent results starts from the number of layers $n^{lay} = 10$. Further, an increase in the number of layers doesn't provide more accurate results but only increases the computation time. To obtain optimal and precise results, a slightly higher number of layers is chosen for further analysis $n^{lay} = 20$.

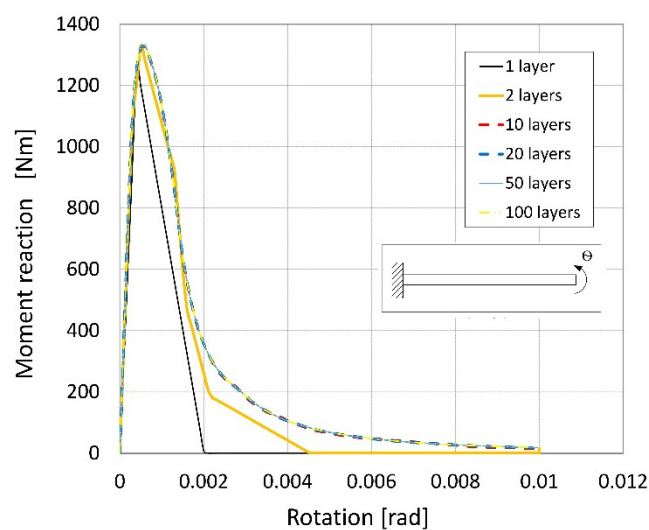


Figure 3.10. Layer calibration test for a cantilever beam using imposed end rotation [23]

3.7.2. Mesh Objectivity Test for the Macro Numerical Model

A test on mesh objectivity is conducted on a simple static system. For this test, a model of a cantilever beam with imposed rotation is introduced. The length of the entire beam is fixed, and the results are obtained for several elements $n^{elem} = 1, 2, 4, 8$ and 10 and presented in Figure 3.11. To avoid a diffuse structural response [93], one element in the mesh is introduced as slightly weaker than the others, so that the unfavourable effect is eliminated. The obtained results in Figure 3.11. show a mesh-independent convergence. The slightly weaker elements enter softening first, causing elastic unloading in the other elements before entering the softening, which allows proper failure simulation. [23]

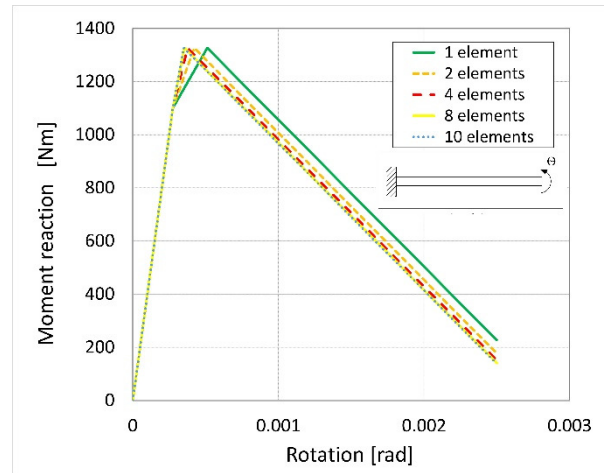


Figure 3.11. Mesh dependence test on a cantilever beam with imposed end rotation [23]

3.7.3. Determination of Input Parameters for Coarse-Scale Macro Models

With the defined fine-scale model elements and by using a simple cantilever beam static system loaded in free-end rotation, a moment-rotation diagram is derived. This diagram serves as input for defining the behaviour of elements in the macro model. Several critical points are considered that define the transition from linear behaviour to a short hardening regime and further to softening. The determination of parameters (limits and modulus for each regime) for the macro model is achieved by an iterative procedure of determining the first derivative of the function that describes the behaviour of the micro model (the moment-curvature curve) to determine coefficients that describe the behaviour of the macro model. [23]

The macro parameters are identified on a representative beam element (RBE), again chosen as a cantilever beam loaded in pure bending with imposed end rotation. By obtaining coefficients for use from the multilayer model, these are implemented in the RBE in the macro model and compared with the results. The RBE in the macro model is the same size, loaded in pure bending but with a monolithic cross-section, and enhancement in the rotational field. The multilayer model graph is divided into three characteristic parts (linear, hardening and softening) using characteristic points. The first point occurs as a significant deflection from the initial tangent line (linear line) on the curve. The second point is the local maximum of the curve, and the third is the intersection of the original (multilayer) curve and the linear local fit of the multilayer curve from the maximum locus up to the point where a significant deflection of the curve occurs. After defining these points, a local linear function is fitted between the points defining the initial values of modulus and limit moments for the macro model. The obtained local linear functions are evaluated with the appropriate parts of the original curve, and the goodness-of-fit

3. Multiscale model with embedded discontinuity for simulation of laminated glass elements exposed to out-of-plane loading

parameters (SSE, RMSE, and R2) are obtained and analysed for each linear element. These processes are iterated (shifting from the first to the third point) until the best goodness-of-fit overall is obtained. The overlapped diagrams of the macro and micro models for chosen parameters in the RBE in the macro model (for Test 1), are presented in Figure 3.12.

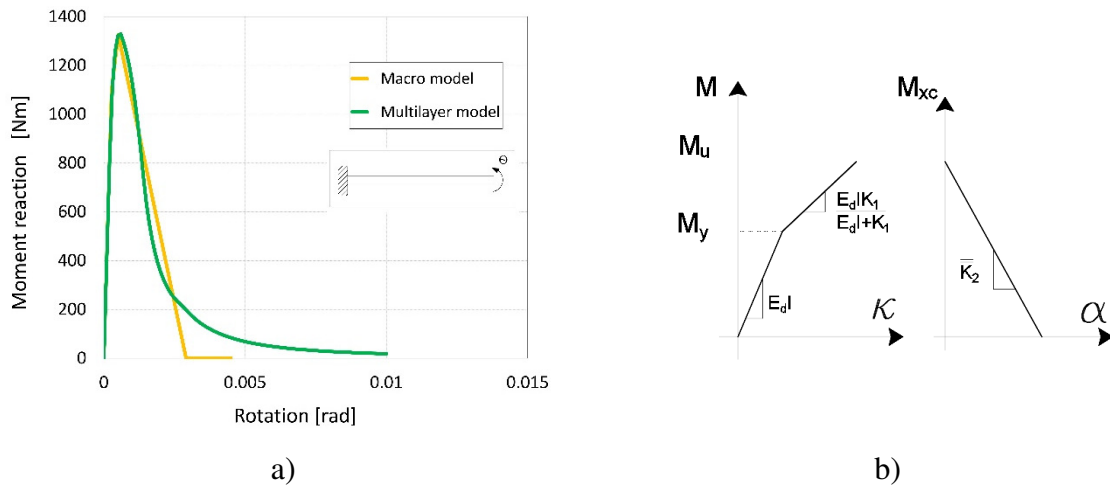


Figure 3.12. Graphical representation of the steps for determination coefficients for the macro model: a) approximation of multilayer model results with macro parameters b) parameters of the macro model

The obtained parameters of the macro model for four full-height cross-sections and two reduced heights (ETA) are presented in Table 3.3. and Table 3.4. Using these parameters, a structure in the macro model will be tested and compared with the experimental tests. In first column of Table 3.3, the parameters for the macro model of the full-height cross section 12.76 mm, and width 330 mm are presented. In second and third columns of Table 3.3, the parameters for macro model with the height equal to the effective thickness according to EN 16612 [22] and Galuppi and Royer-Carfagni [31] (again with the width of 330 mm) are presented. All these parameters are determined from the multilayer model 6+0.76+6 mm with tempered glass and PVB interlayer 1 from Table 3.2. In Table 3.4, the parameters of macro models for comparison with the experimental results from [54] [83] are presented. In first two columns of Table 3.4, the parameters for cross-section of total height 8.76 mm / 9.52 mm, and width 360 mm are determined, consisting of float glass and PVB interlayer 2 from Table 3.2. Third column of Table 3.4. presents the material characteristics of the macro model with a total-height of 17.52 mm, and width of 1000 mm, consisting of tempered glass and PVB interlayer 1 from Table 3.2.

3. Multiscale model with embedded discontinuity for simulation of laminated glass elements exposed to out-of-plane loading

Table 3.3. Parameters for the macro models for Test 1 (T1), Test 2 (T2) and Test 3 (T3)

Macro model parameters for Test 1 (T1)	Macro model parameters for Test 2 (T2)	Macro model parameters for Test 3 (T3)
$6 + 0.76 + 6 \text{ mm}$	$6 + 0.76 + 6 \text{ mm}$	$6 + 0.76 + 6 \text{ mm}$
$h = 12.76 \text{ mm}$	$h_{eff} = 11.656 \text{ mm}$	$h_{eff} = 12.714 \text{ mm}$
$E_d = 70 \text{ GPa}$	$E_d = 76 \text{ GPa}$	$E_d = 60 \text{ GPa}$
$M_y = 1100 \text{ Nm}$	$M_y = 1230 \text{ Nm}$	$M_y = 1200 \text{ Nm}$
$K_1 = 2.20 \cdot 10^{10}$	$K_1 = 2.20 \cdot 10^{10}$	$K_1 = 1.8 \cdot 10^{10}$
$M_u = 1327 \text{ Nm}$	$M_u = 1327 \text{ Nm}$	$M_u = 1330 \text{ Nm}$
$\bar{K}_2 = -8.5 \cdot 10^{12}$	$\bar{K}_2 = -8.5 \cdot 10^{12}$	$\bar{K}_2 = -8.50 \cdot 10^{12}$

Table 3.4. Parameters for the macro models for Test 4 (T4), Test 5 (T5) and Test 6 (T6)

Macro model parameters for Test 4 (T4)	Macro model parameters for Test 5 (T5)	Macro model parameters for Test 6 (T6)
$4 + 0.76 + 4 \text{ mm}$	$4 + 1.52 + 4 \text{ mm}$	$8 + 1.52 + 8 \text{ mm}$
$h = 8.76 \text{ mm}$	$h = 9.52 \text{ mm}$	$h = 17.52 \text{ mm}$
$E_d = 70 \text{ GPa}$	$E_d = 70 \text{ GPa}$	$E_d = 70 \text{ GPa}$
$M_y = 215 \text{ Nm}$	$M_y = 250 \text{ Nm}$	$M_y = 6000 \text{ Nm}$
$K_1 = 2.2 \cdot 10^{10}$	$K_1 = 2.2 \cdot 10^{10}$	$K_1 = 2.2 \cdot 10^{10}$
$M_u = 227 \text{ Nm}$	$M_u = 255 \text{ Nm}$	$M_u = 7500 \text{ Nm}$
$\bar{K}_2 = -8.5 \cdot 10^{12}$	$\bar{K}_2 = -8.5 \cdot 10^{12}$	$\bar{K}_2 = -8.80 \cdot 10^{12}$

3.8. Numerical Simulation Four-Point Bending Tests in Multiscale Model

After obtaining all the ingredients necessary to define the macro model, different static systems can be tested in bending tests. The numerical examples are created based on the experimental four-point and three-point bending tests. The thickness of the cross-sections in the macro model is equal to the sum of all parts of the cross-section in the multilayer models or to effective thickness, depending on tests. As explained, the macro model contains elements with a unique cross-section that can develop discontinuity in the rotation field. The discontinuity is described with a plastic hinge that enables dissipative mechanisms. Dissipation is a simulation of a fracture of glass plies combined with visco-plastic deformation of the polymeric interlayer. This visco-brittle combination of two materials results, in laminated glass, results in a breakage shape similar to a composition of plastic hinges, for tempered glass plies known as a “wet blanket effect”. In tests, the load is applied in lines (across the width of the cross-section) as a

vertical displacement, which is increased linearly until complete failure. The load is placed at a distance from the middle of the beam according to the experimental tests. The model contains elements, some of which are slightly weakened to properly simulate material heterogeneity. Three different setups are used to simulate material fracture as a defect-sensitive phenomenon for four-point bending tests. They are divided based on the number of elements that first develop dissipation mechanisms. In Figure 3.13., the setups are presented with an emphasis on the initiation element. The first setup (Type 1) is created so that only one weakened element occurs on the beam, not necessarily exactly in the centre. In the second setup (Type 2), two initiation elements are positioned around the end of the constant moment span. The third type is defined with randomly placed initiation elements inside the load span, creating an initiation area. The third type is tested several times by introducing slight changes in random fields.

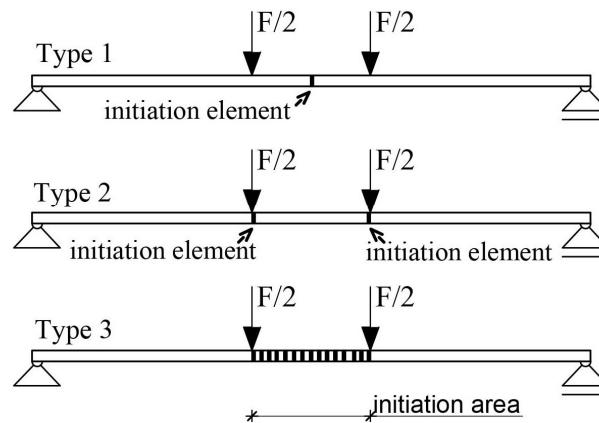


Figure 3.13. The scheme of different setups for numerical simulations

The results obtained for several setups (Types) are plotted as force F versus deflection (at the middle of the beam). On the same graph, the results from experimental tests of laminated glass with the same geometry are presented. The setup for Type 3 is carried out three times (R1, R2, and R3), with small perturbations in the positions of the initiation elements inside the defined (load) span. This approach enables a representation of heterogeneity in glass caused by a network of initial imperfections. To be able to determine the real material characteristics of brittle material such as glass and overcome inappropriately prepared samples, it is recommended to use a four-point bending test (instead of three-point bending) due to the uniform distribution of moments in the fracture zone. Namely, it is more accurate to determine the strength of the laminated glass panel when the bending moment is constant and with no shear force influence, enabling a uniform stress state. By considering these five different setups, specimen heterogeneity is emphasized, and it plays an important role in the obtained bearing

capacity, as it does in real tests. Additionally, in cases of fracture initiation outside the force span in experimental tests, the results are not usually taken into account. This mostly happens due to specimen inadequacy or a dominant initial imperfection in the fracture region. For this reason, the initiation elements are only placed in the area of maximal moment (load span). Hence, this numerical model is capable of accurately simulating the possible results dispersion regarding the position of the initiation crack. [23]

3.8.1. Numerical Simulation of Tests 1, 2 and 3 in the Macro Model 1

The first numerical examples are created based on the experimental four-point bending test from [12], with a 950 mm span and the width of the cross-section equal to 330 mm. The height of the cross-section, for Test 1 is equal to the sum of all parts of the cross-section in the multilayer model $h=12.76$ mm. In the cases of Test 2 and Test 3, the height of the cross-sections is equal to the effective thicknesses according to EN 16612 [22] and Galuppi and Royer-Carfagni [31]. The values of macro model parameters for three tests are presented in Table 3.3. The load is placed symmetrically from the middle of the beam at a distance of 200 mm between forces. The model consists of 95 elements, some of which are slightly weakened to properly simulate material heterogeneity. The results of Test 1, Test 2 and Test 3 are presented in Figures 3.14. (3.15.), Figure 3.17., and Figure 3.18., respectively.

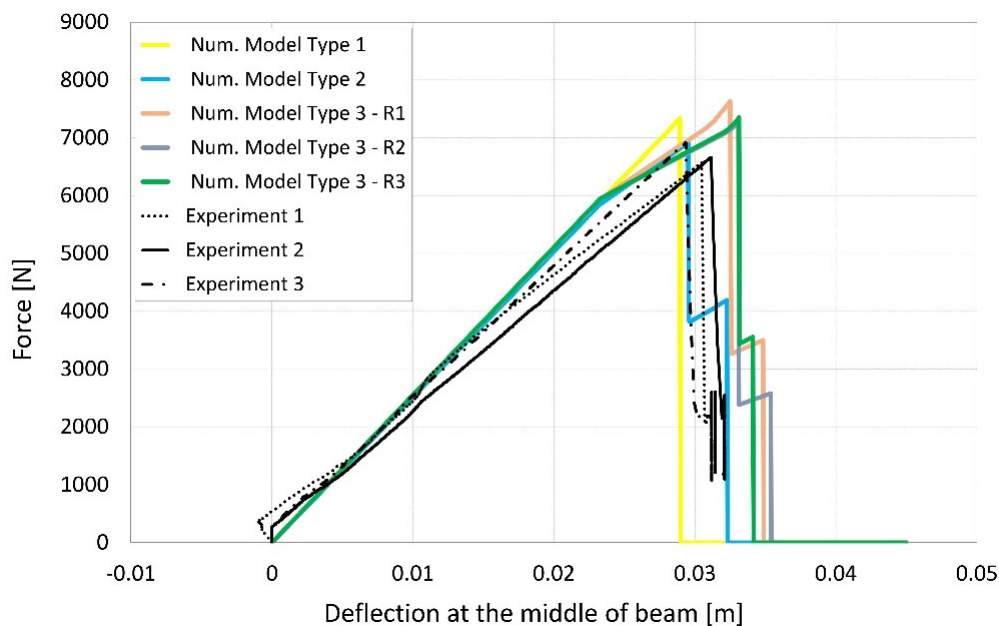


Figure 3.14. Force-displacement diagrams from numerical simulations and experiments

For Test 1, the results obtained from numerical models show very good agreement compared with experimental results. In Figure 3.14., despite a small difference in the final stage, both approaches (numerical and experimental) provide good insight into the realistic behaviour of laminated glass panes. The ultimate load for some of the setups (Type 3 – R1, Type 3 – R3) is slightly higher, while the results for Type 2 match the Experiment 3 curve. Since specimens in these experiments were not tested until complete failure, we can allow this small difference in the last stage. The deviation between the average ultimate force from the experiments ($F = 6711$ N) and the force from numerical models ($F = 7300$ N) is approximately 8 %, and the difference in ultimate deflection is 3.5 %. Regarding the ultimate force, a slight deviation appears in the final results within computed diagrams. Hence, if we compare the mean value of the experimental results with the models in Figure 3.15., it can be seen that the prediction of the model is satisfactory.

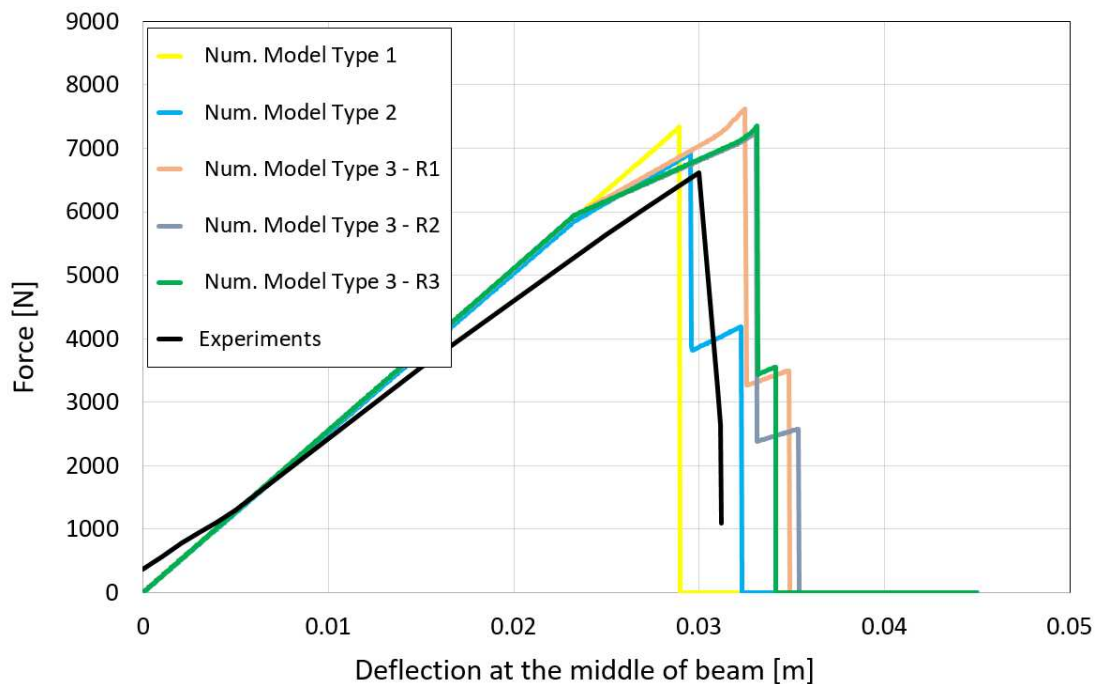
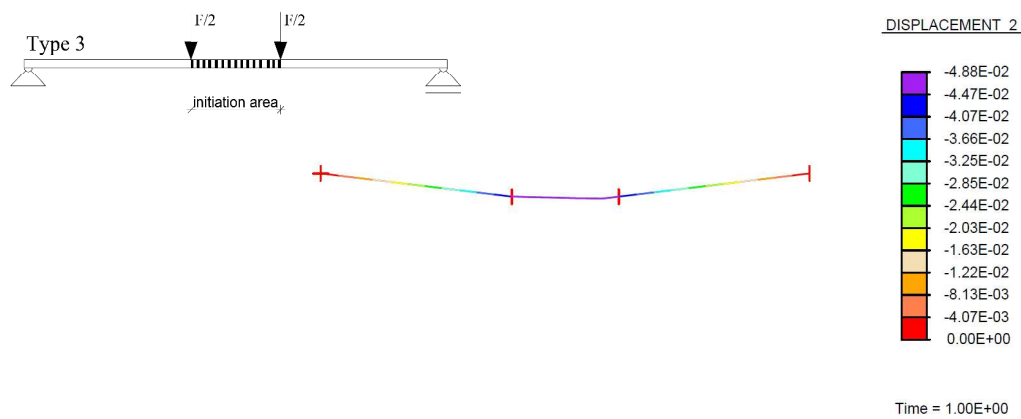


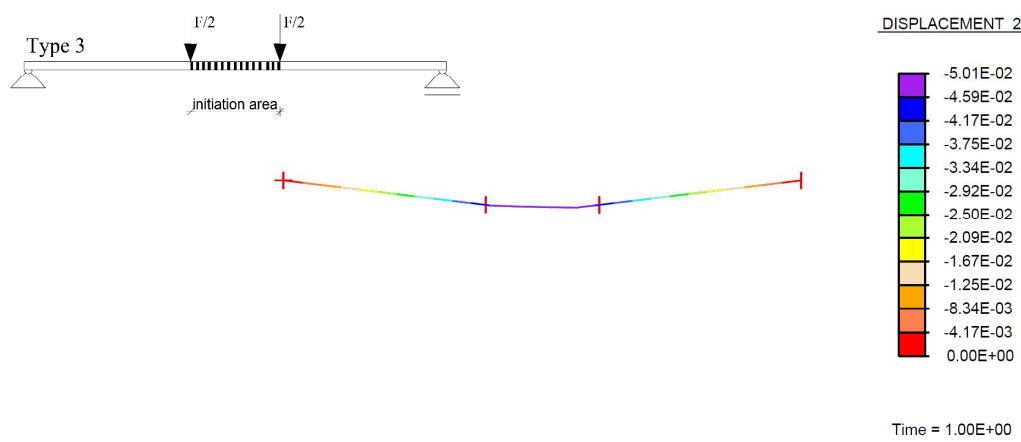
Figure 3.15. Force-displacement diagrams from numerical simulations and mean value from the experiments

The deformed structure after the breakage occurs is presented in Figure 3.16. for the Type 3 scheme (R1, R2, and R3).

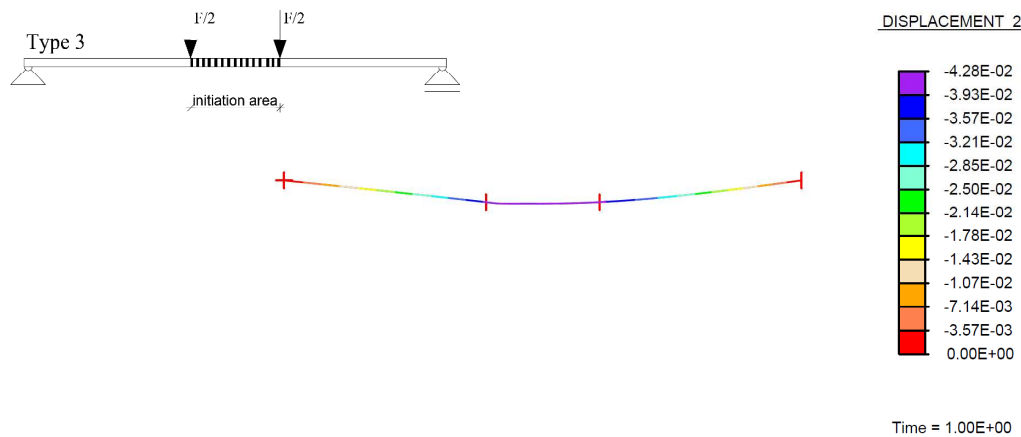
3. Multiscale model with embedded discontinuity for simulation of laminated glass elements exposed to out-of-plane loading



a) R1



b) R2



c) R3

Figure 3.16. Representation of deformed structures after the breakage for Type 3 setups

In Test 2 and Test 3, the results from the numerical model with monolithic glass height according to the effective thickness approach are obtained and presented in Figure 3.17. and Figure 3.18. In the analysis, the same setups with the same geometry (except height) and

3. Multiscale model with embedded discontinuity for simulation of laminated glass elements exposed to out-of-plane loading

loading, as shown in Figure 3.13., are used, but with parameters for elements that correspond to the calculated effective thickness approach given in Table 3.3. Effective thickness is determined according to the expression for deflection prediction from EN 16612:2019 [22], which is previously presented in Chapter 2, equation (2.6.4). The shear transfer parameter is chosen as the highest of the proposed values, $\omega = 0.7$. The obtained results are presented in Figure 3.17. It can be seen that for all setups, the deflection is significantly overestimated. The highest difference is for Type 3 – R2 (37.8 mm), where the difference between the lowest ultimate deflections of the experiment (29.4 mm) is $\Delta=8.4$ mm. The difference between the averaged ultimate deflection for experiments (30.3 mm) and the averaged ultimate deflection from the numerical model with a simplified approach (36.48 mm) is 16.9%. To determine the cross-section height according to [22], the highest proposed value of shear transfer coefficient ω is used, which means that for any smaller value of the shear transfer coefficient ($\omega = 0.5$; $\omega = 0.3$), the difference in results will be even greater.

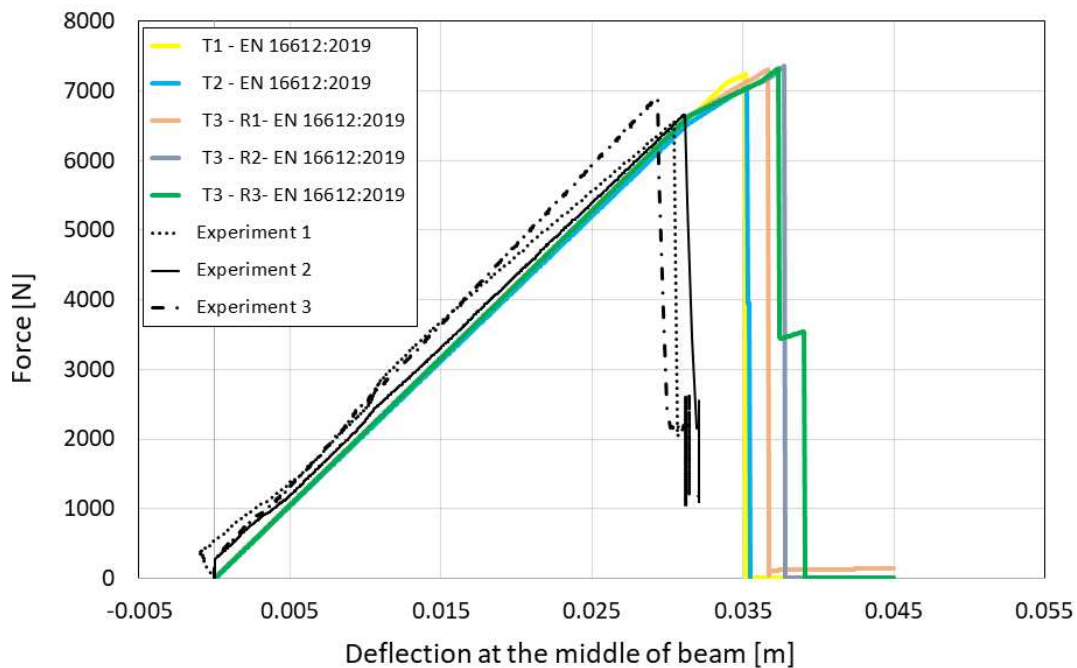


Figure 3.17. Comparison of force-displacement diagrams obtained with numerical simulations using effective thickness height according to [22] and the experimental results

The results obtained with another simplified engineering approach according to [31] are presented in Figure 3.18. To determine effective thickness according to [31], an equation presented in Chapter 2 (2.6.9) is used, together with the material parameters presented in Table 3.2. for PVB interlayer 1. This approach shows a slightly better prediction of deflection in the

middle of the beam but is still overestimated. The difference between the average ultimate deflection for experiments (30.3 mm) and the average ultimate deflection for the numerical model (35.9 mm) is 15.6%. For both used expressions for the effective thickness approach, we can conclude that results are on the safety side regarding deflection prediction. The expression (2.6.4) from regulation EN 16612:2019 [22] provides more conservative results than the proposed expression (2.6.9). This comparison is created for room temperature conditions according to experiments. In cases of higher temperatures or different load durations, coefficient ω for (2.6.4) and coefficient η for (2.6.9) need to be adequately changed. The combination of the effective thickness method with this multi-scale model did not show any advantages; the behaviour prediction is much better when using the macro model with a full-height cross-section. In a certain way, this multiscale approach is also an effective approach, but instead of reducing the height, it proposes the “effective” material characteristics. The combination of effective thickness geometry with this multiscale model offers only a cancelling effect of advantages from both approaches. The multi scale model provides more accurate results when a full height of laminated glass is considered in the macro model. The effective thickness in combination with the multiscale model will not be considered in future work.

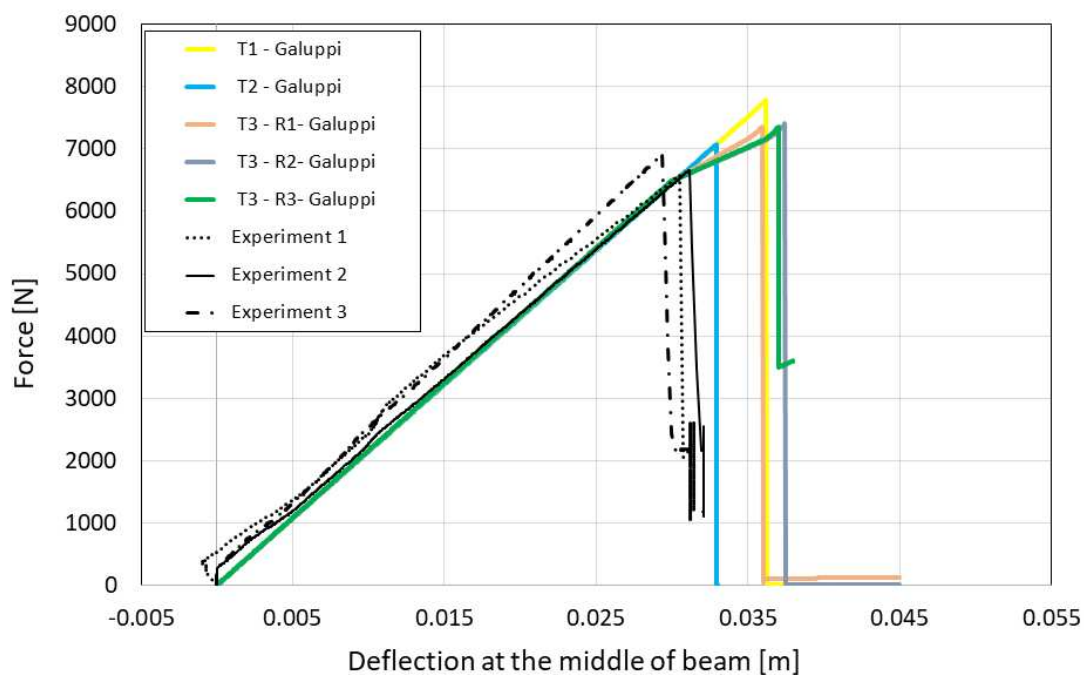


Figure 3.18. Comparison of force-displacement diagrams obtained for numerical simulations using effective thickness height according to [31] and the experimental results

3.8.2. Numerical Simulation of Tests 4 and 5 in Macro Model 1

In the work of Castori and Speranzini [54] seven specimens with PVB interlayer are tested in four-point bending according to regulation EN 1288-3 [24]. Specimens are made of float annealed glass with dimensions 1100 mm x 360 mm. Two groups of thickness are used, both consisting of two glass plies of 4 mm + 4 mm. First group (Test 4) had three specimens with height $h = 8.76 \text{ mm}$ consisting of glass and one ply of PVB interlayer. The second group (Test 5) had four specimens with height $h = 9.52 \text{ mm}$ made of glass and two plies of PVB interlayer. Specimens are tested in four-point bending with a span $l = 1000 \text{ mm}$ and forces at a distance of 200 mm placed symmetrically.

For multiscale numerical tests, mechanical characteristics for specimens are adopted as described in [54] and presented in Table 3.2. (float glass and PVB interlayer 2). Furthermore, the parameters for macro models are determined in a multilayer model for both cross-sections and presented in Table 3.4. Five different setups are used, as presented in Figure 3.13., to emphasize the heterogeneity of glass specimens. The comparison of numerical and experimental results is presented in Figure 3.19. and Figure 3.20.

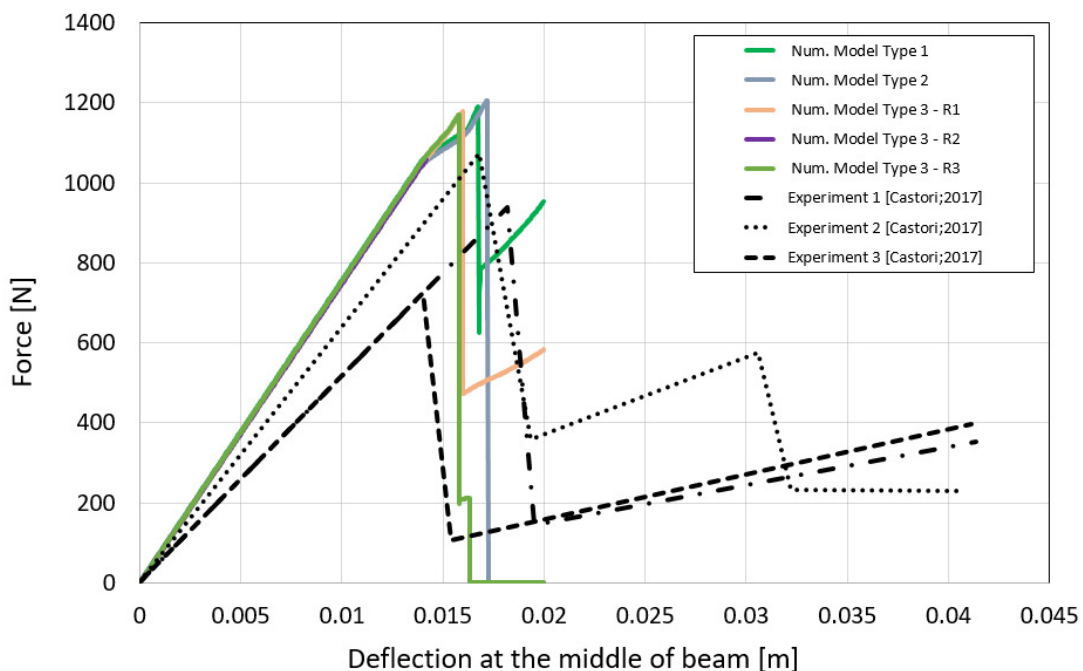


Figure 3.19. Force-displacement diagrams from numerical simulations and experiments from [54] for the case of laminated glass with PVB interlayer thickness 0.76 mm (Test 4)

In Figure 3.19., Test 4 is presented. The five different setups in the numerical model did not offer the deflection range within the fractures that occurred in the experimental test. However,

3. Multiscale model with embedded discontinuity for simulation of laminated glass elements exposed to out-of-plane loading

the mean value of fracture initiation deflection in the numerical model is $w_{num} = 16.24 \text{ mm}$, and the mean value of deflection at the break point is $w_{break} = 16.373 \text{ mm}$, which shows a good prediction of the behaviour. The mean value of force prediction in the numerical model is $F_{num} = 1178 \text{ N}$, and the mean value of force at fracture from experimental tests $F_{break} = 927 \text{ N}$. The difference that occurs in force prediction is inevitable (similar as in Test 1) due to the complete fracture that occurs in numerical tests, where the whole cross section fractures at once, while in the experimental tests, when the fracture of the bottom ply occurs, unloading occurs and the second ply fractures further. This predicted force from the numerical model represents the ultimate force for the breakage of whole cross-section, not just the bottom ply. The different physics behind these values (force and deflection) result in different stiffness, and leading to an apparently stiffer behaviour of the numerical model compared to the experiment.

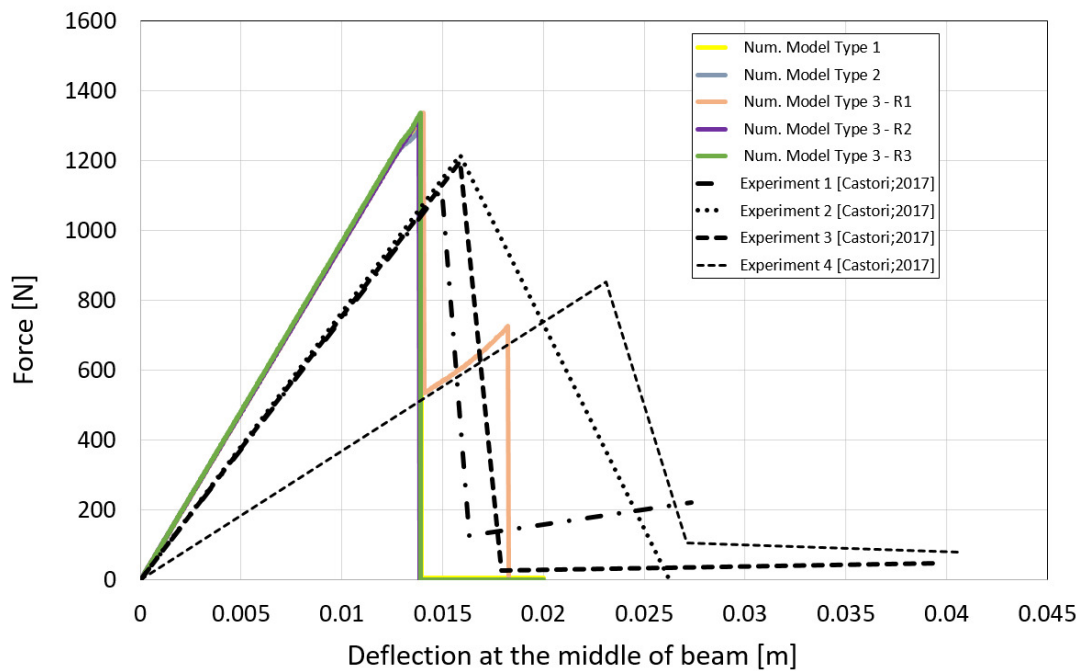


Figure 3.20. Force-displacement diagrams from numerical simulations and experiments from [54] for the case of laminated glass with PVB interlayer thickness 1.52 mm (Test 5)

In Figure 3.20., Test 5 is presented. This test has the same geometry as Test 4, with the only difference being height of the cross-section due to the double ply of the PVB interlayer. Again, five different setups in the numerical model are used. Experimental results show significant dispersion, while the numerical results are grouped around the same value for all setups. The mean value of fracture initiation deflection in the numerical model is $w_{num} = 14.28 \text{ mm}$, and the mean value of deflection at the break point is $w_{break} = 17.996 \text{ mm}$, which shows a $\approx 20\%$

deviation from the mean value of realized deflection. However, due to the great dispersion of experimental results, the confidence interval is defined with $w_{break} = 17.996 \text{ mm} \pm 4.738$, where a deviation of $\approx 26\%$ from the mean value appears in experimental results. This means that the result from the numerical model fits within the interval. The mean value of force prediction in the numerical model is $F_{num} = 1374 \text{ N}$, and the mean value of force at breakage from experimental tests is $F_{break} = 1104 \text{ N}$. This difference is expected due to the mentioned fracture behaviour, where a complete fracture occurs in numerical tests while in the experiments it develops gradually.

3.8.3. Numerical Simulation of Test 6 in the Macro Model 1

The next simulation is a three-point bending test from [83] conducted on plate-like geometry. The experimental tests are conducted on an $8 + 1.52 + 8 \text{ mm}$ cross-section, made of tempered glass and PVB DG 41 interlayer. The same interlayer is used in experimental tests from Test 1, and the belonging material characteristics are presented in Table 3.2. (tempered glass and PVB interlayer 1). The dimensions of the specimens are $1100 \text{ mm} \times 1000 \text{ mm}$, the span is 1100 mm and the load is placed in midline across the width of the specimen. The material characteristics are determined based on the multilayer model and presented in Table 3.4, in the third column. With these inputs, a geometry is created in the macro model and tested. Since here a three-point test is simulated, only one setup is used with initiation elements placed in the vicinity of the midline of the specimen. This setup is considered because the fracture initiation is expected in the vicinity of the midline. The comparison of results in terms of the force-displacement graph is presented in Figure 3.21.

As mentioned, only one numerical prediction is considered, and the prediction of deflection and force is satisfactory. The value of fracture initiation deflection in the multiscale numerical model is $w_{num} = 25.155 \text{ mm}$, which is slightly lower than the deflection at the break point in the experiment $w_{break} = 25.67 \text{ mm}$. The force prediction in the numerical model is $F_{num} = 29487 \text{ N}$, and the value of force at breakage from experimental tests $F_{break} = 27500 \text{ N}$. The results from the numerical model presented by Biolzi and Simoncelli [83] are also close to the experimental, with a force value at breakage $F_{num,BS} = 27890 \text{ N}$ and the corresponding deflection $w_{num,BS} = 26.607 \text{ mm}$. This numerical model is created in ABAQUS, conducted as linear analyses where the glass and the interlayers were considered as linear materials. The model does not simulate fracture, and the analysis is manually interrupted when the

experimental failure loads are reached. Hence, this force and displacement prediction cannot be observed as fracture prediction, and the only good agreement from this model is the one in terms of global stiffness of the specimen.

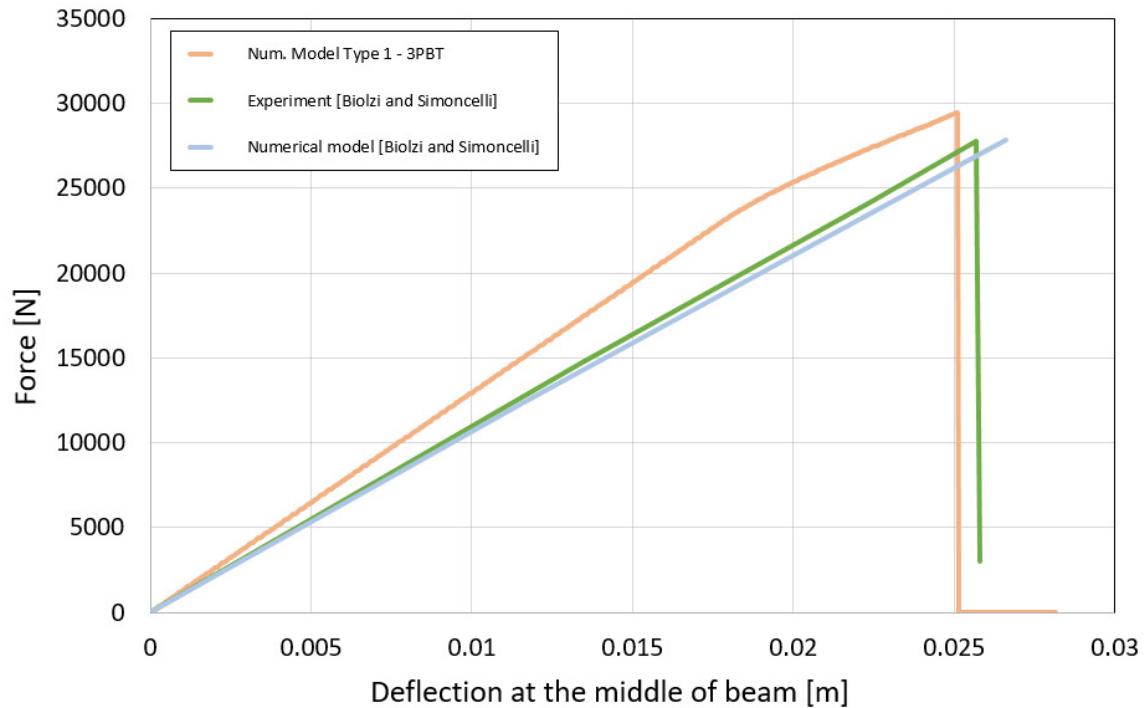


Figure 3.21. Force-displacement diagrams from numerical simulations and experiments from [83]

3.9. Mathematical Formulations for the Coarse-Scale Macro Model 2 With Plate Elements

Since a many laminated glass structures have thin plate-like geometry or boundary conditions that enforce plate effects, it is often more appropriate to simulate LG structure with a plate element rather than with a beam element. For this reason, a macro model is further extended into a model with plate elements featuring a monolithic cross-section and a constitutive law defined from a micro (multilayer) model in terms of a moment-curvature graph. The used plate theory is the Kirchhoff -Love theory, which can be considered as an extended version of the Euler-Bernoulli beam theory. The macro model element is presented in Figure 3.22., along with the coordinate system and the corresponding displacements. This model will be referred to as “macro model 2” to distinguish it from the previously presented macro model with beam elements (macro model 1). Unlike macro model 1 with beam elements, macro model 2 does not use an embedded discontinuity approach to simulate fractures. Instead, the stiffness reduction

due to fracture is simulated using a specific form of non-linear elasticity, which allows stress redistribution to other elements that have not reached the limit. The load on the elements is increases monotonically until redistribution through elements is possible. Once all elements are fractured in a certain zone, redistribution is disabled, indicating structural collapse. One needs to point out that under a monotonically increasing loading, it is very likely that local unloading will occur due to redistribution of stiffness, and the effects associated with unloading are considered elastic. In this phase, the model doesn't cover post-breakage behaviour but only pre-fracture and fracture behaviour.

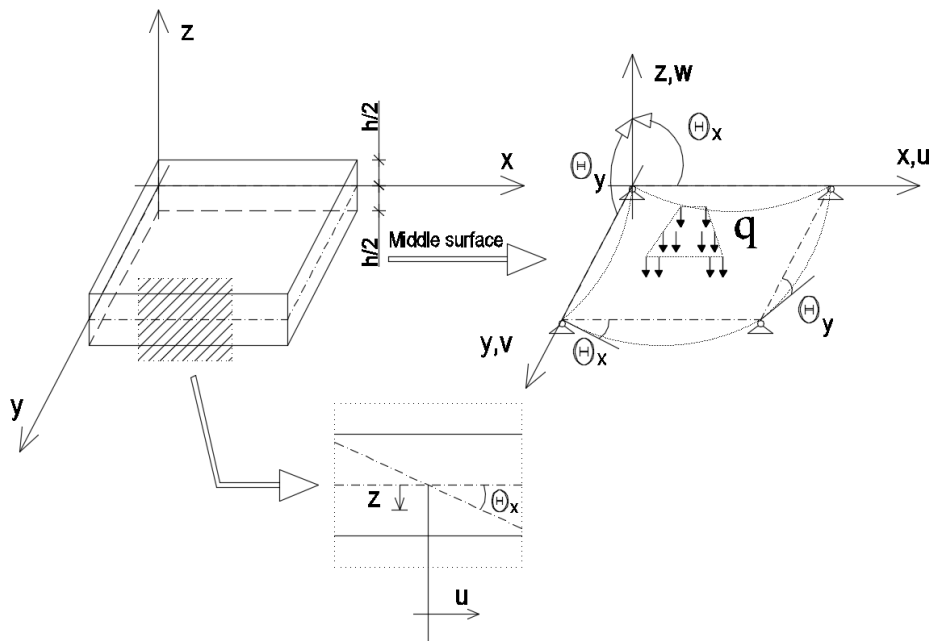


Figure 3.22. Schematic representation of plate element with the degrees of freedom and deformations in macro model 2

3.9.1. Kinematic Equations for Macro Model 2

As previously mentioned, the model is based on Kirchhoff -Love plate theory and it features a monolithic cross-section. The field variables are two rotations (θ_x and θ_y) and the transverse displacement $w(x, y)$. If one plate element is observed with vertical deflection $w(x, y)$ on the middle surface, the rotations in deformed shape for two directions (θ_x and θ_y) can be described as:

$$\theta_x = \frac{\partial w}{\partial x}; \quad \theta_y = \frac{\partial w}{\partial y} \quad (3.9.1)$$

The axial displacements of the plate (u and v) through its height are equal:

$$\begin{aligned} u &= -z \cdot \theta_x = -z \cdot \frac{\partial w}{\partial x} \\ v &= -z \cdot \theta_y = -z \cdot \frac{\partial w}{\partial y} \end{aligned} \quad (3.9.2)$$

These axial displacements result from bending action, without taking into consideration the axial forces. Furthermore, this leads to strain in each direction which is defined as:

$$\begin{aligned} \varepsilon_x &= \frac{\partial u}{\partial x} = -z \cdot \frac{\partial^2 w}{\partial x^2} \\ \varepsilon_y &= \frac{\partial v}{\partial y} = -z \cdot \frac{\partial^2 w}{\partial y^2} \end{aligned} \quad (3.9.3)$$

The shear strain is defined as:

$$\gamma_{xy} = \frac{\partial u}{\partial y} + \frac{\partial v}{\partial x} = -2z \cdot \frac{\partial^2 w}{\partial x \partial y} \quad (3.9.4)$$

Since the normal to the undeformed surface remains perpendicular to the deformed surface, the length of the normal does not change. The stress in the direction of normal (z direction) and the associated shear stresses are zero. This is justified for the LG cross-section (simulated here with a monolithic cross-section) due to the high stiffness of glass plies, which do not undergo any significant deformation perpendicular to the surface, and the polymeric interlayer's geometry ensures negligible deformation for the uses thickness.

3.9.2. Constitutive Equations for Macro Model 2

The constitutive model is set directly in terms of stress resultants [97][98]. By multiplying the strains with the material modulus, we obtain in-plane stresses. Further, by integrating these stresses through the plate's thickness, we obtain resultants such as moments in x - z plain M_x (3.9.5), y - z plain M_y (3.9.6) and twisting moment M_{xy} (3.9.7).

$$\begin{aligned}
 M_x &= \int_{-\frac{h}{2}}^{\frac{h}{2}} \sigma_{xz} (dzx1) = -\frac{E}{1-\nu^2} \int_{-\frac{h}{2}}^{\frac{h}{2}} [\varepsilon_x + \nu\varepsilon_y] z \, dz \\
 &= -\frac{E}{1-\nu^2} \int_{-\frac{h}{2}}^{\frac{h}{2}} \left[\frac{\partial^2 w}{\partial x^2} + \nu \frac{\partial^2 w}{\partial y^2} \right] z^2 \, dz = -\frac{Eh^3}{12(1-\nu^2)} \cdot \left[\frac{\partial^2 w}{\partial x^2} + \nu \frac{\partial^2 w}{\partial y^2} \right]
 \end{aligned} \tag{3.9.5}$$

Similar to the x direction, we define moment M_y :

$$\begin{aligned}
 M_y &= \int_{-\frac{h}{2}}^{\frac{h}{2}} \sigma_{yz} (dzx1) = -\frac{E}{1-\nu^2} \int_{-\frac{h}{2}}^{\frac{h}{2}} [\varepsilon_y + \nu\varepsilon_x] z \, dz \\
 &= -\frac{E}{1-\nu^2} \int_{-\frac{h}{2}}^{\frac{h}{2}} \left[\frac{\partial^2 w}{\partial y^2} + \nu \frac{\partial^2 w}{\partial x^2} \right] z^2 \, dz = -\frac{Eh^3}{12(1-\nu^2)} \cdot \left[\frac{\partial^2 w}{\partial y^2} + \nu \frac{\partial^2 w}{\partial x^2} \right]
 \end{aligned} \tag{3.9.6}$$

For twisting moment we have:

$$M_{xy} = \int_{-\frac{h}{2}}^{\frac{h}{2}} \tau_{xyz} (dzx1) = -\frac{E}{1+\nu} \int_{-\frac{h}{2}}^{\frac{h}{2}} z^2 \cdot \frac{\partial^2 w}{\partial x \partial y} \, dz = -\frac{Eh^3}{12(1-\nu^2)} \cdot (1-\nu) \frac{\partial^2 w}{\partial x \partial y} \tag{3.9.7}$$

By denoting material and geometric constants as D , we can write:

$$\begin{aligned}
 M_x &= -D \cdot \left[\frac{\partial^2 w}{\partial x^2} + \nu \frac{\partial^2 w}{\partial y^2} \right] \\
 M_y &= -D \cdot \left[\frac{\partial^2 w}{\partial y^2} + \nu \frac{\partial^2 w}{\partial x^2} \right] \\
 M_{xy} &= -D \cdot (1-\nu) \frac{\partial^2 w}{\partial x \partial y}
 \end{aligned} \tag{3.9.8}$$

The defined moment-curvature relationship from the multilayer model is used in the space of principal directions of plate bending moments, eliminating the need of defining the constitutive law for plate twisting moment.

The presented moment components from the global coordinate system $[M_x, M_y, M_{xy}]$ are used to determine the moment components in the principal directions $[M_1, M_2]$ via an orthogonality similarity transformation:

$$\begin{aligned} \mathbf{M} &= \mathbf{T}\widehat{\mathbf{M}} \\ \mathbf{M} &= \langle M_x, M_y, M_{xy} \rangle^T \\ \widehat{\mathbf{M}} &= \langle M_1, M_2 \rangle^T \end{aligned} \quad (3.9.9)$$

where the transformation matrix is defined as:

$$\mathbf{T} = \begin{bmatrix} \cos^2\phi & \sin^2\phi \\ \sin^2\phi & \cos^2\phi \\ \sin\phi \cos\phi & -\sin\phi \cos\phi \end{bmatrix} \quad (3.9.10)$$

and ϕ is the angle of the principal axes of moments determined with:

$$\phi = \tan^{-1} \frac{2M_{xy}}{M_x - M_y} \quad (3.9.11)$$

The primary goal is to evaluate the limit load for laminated glass planar elements and to determine initial crack directions and critical stress areas. The limit moments are controlled in the space of principal moments. When the limit moment is exceeded, the corresponding strain and the reduced (limit) moment are used to define the reduced stiffness of the observed element. This stiffness is then transformed into the space of moments $[M_x, M_y, M_{xy}]$, as new value of material and geometric constant D . To establish a connection between the multilayer model and macro model 2, a representative planar element (RPE) is used. The RPE's geometry is equal to the dimensions of one element in macro model 2. Thus, the width of RPE is equal to the width of one element and not the whole structure, as was the case in the macro model with beam elements. With the presented geometries, this element is a beam element in the multilayer model and a plate element in the macro model. The scheme for determining initial parameters for macro model 2 is presented in Figure 3.23.

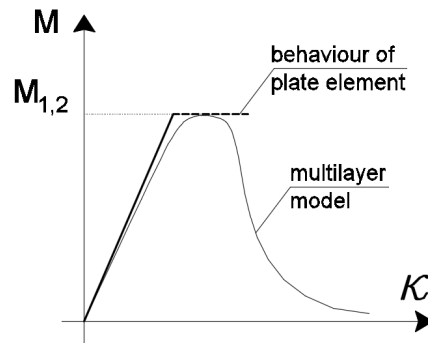


Figure 3.23. Results from the micro model and for chosen macro model 2 parameters
The limit moment is determined as the global maximum of the multilayer curve, and the corresponding modulus is a tangent on the first part of the multilayer curve leading to this

maximum. The determined parameters are used for both directions of principal moments. Once the limit is achieved in one direction it affects the stress (moments) in the other perpendicular direction, on the same element, as well as the stress distribution on the nearest elements. The load transfers through the elements until the complete development of the critical zone. As of the writing of this dissertation, macro model 2 is still in the development phase, and only basic model inputs are presented. In the following part of the chapter, the preliminary results are presented. These results demonstrate the advantages of macro model 2 compared to macro model 1. In Figure 3.24., three setups are presented with geometry equal to those from experiments described in Chapter 2, section 2.3. The length is 950 mm, the width is 330 mm, and the thickness of the plate is 12.76 mm with a monolithic cross-section. The loading conditions of the first setup match the loading from Chapter 2, Section 2.3., and are also tested in the multilayer model in Section 3.8 in Test 1, Test 2, and Test 3. The displacement is introduced through the width of the cross-section at a distance of 100 mm from the midline on both sides of the specimen. Only this first type of loading, uniform through the width of the cross-section, is possible to test in the beam multiscale model (micro model + macro model 1). The second and the third setup exhibit pronounced plate effects due to the load shape, which doesn't ensure uniform uniaxial stress distribution. These setups can only be tested in macro model 2. The gradual development of the critical zone for each of these setups is demonstrated in Figure 3.25, Figure 3.26, and Figure 3.27.

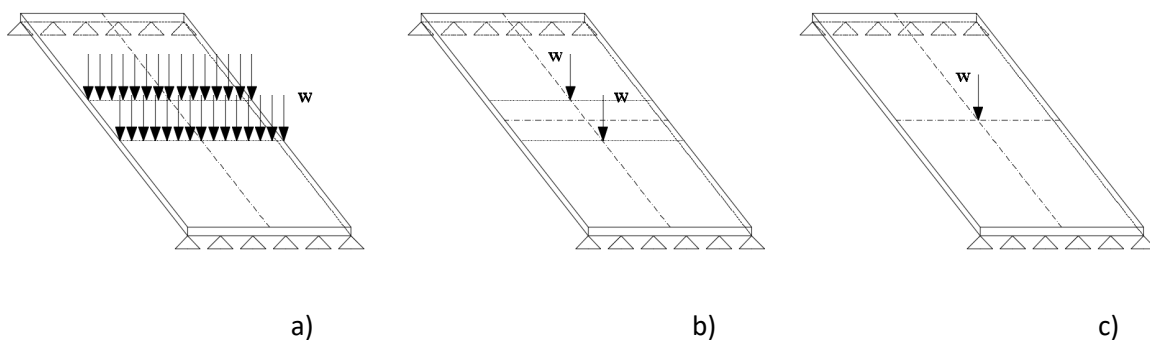


Figure 3.24. Three setups for preliminary tests in macro model 2

In Figure 3.25., the results for the first test setup are presented. The load is introduced as displacement in two lines which is monotonically increasing until a critical area is created. Once the critical value is accomplished, by further increasing the load, the critical area spreads through the zone between the load-lines. Inside the critical area, stress (moments) is constant, and with further increasing load, it redistributes through the elements. The angle of the principal

axes for this type of loading is small due to stress distribution that follows the geometry of the elements, and it can be considered as uniaxial bending.

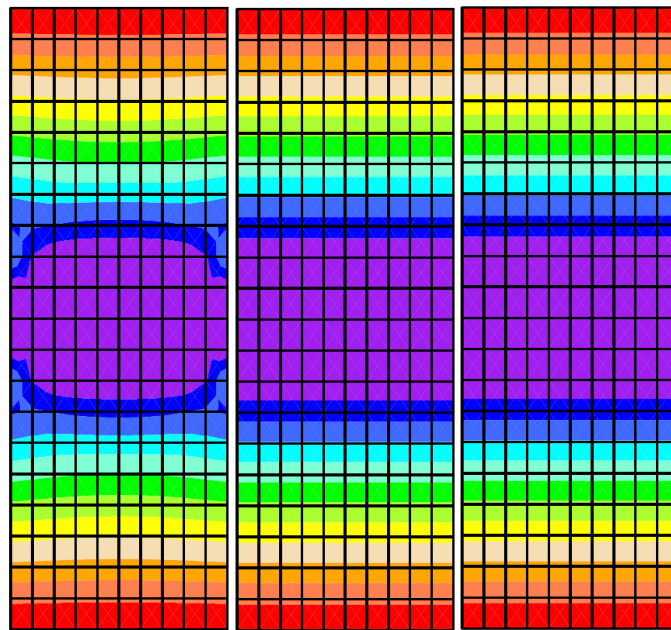


Figure 3.25. The critical area development from macro model 2 for setup a) Fig. 3.24.

In Figure 3.26., the development of the critical area for the second test setup is presented. Here, it can be seen that the shape of the observed area culminates differently from the first setup. The plate effects are pronounced, and the development of critical zone is achieved non-uniformly in both directions.

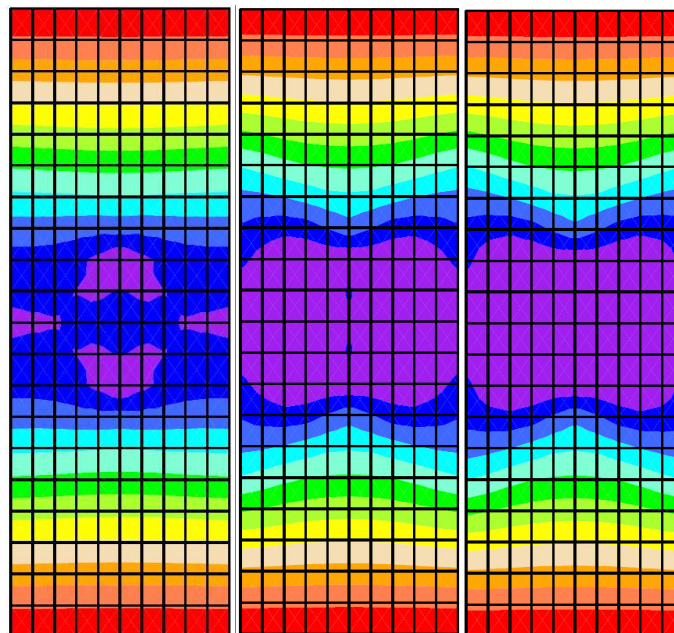


Figure 3.26. The critical area development from macro model 2 for setup b) Fig. 3.24.

The graphical representation of critical zone development for the third load type from Figure 3.24. again shows pronounced plate effects and the development of the critical zone through the width of the structure, as seen in Figure 3.27. This distribution can be simulated only with a 2D macro model but it is determined based on laminated glass beam behaviour (constitutive law derived from the multilayer model).

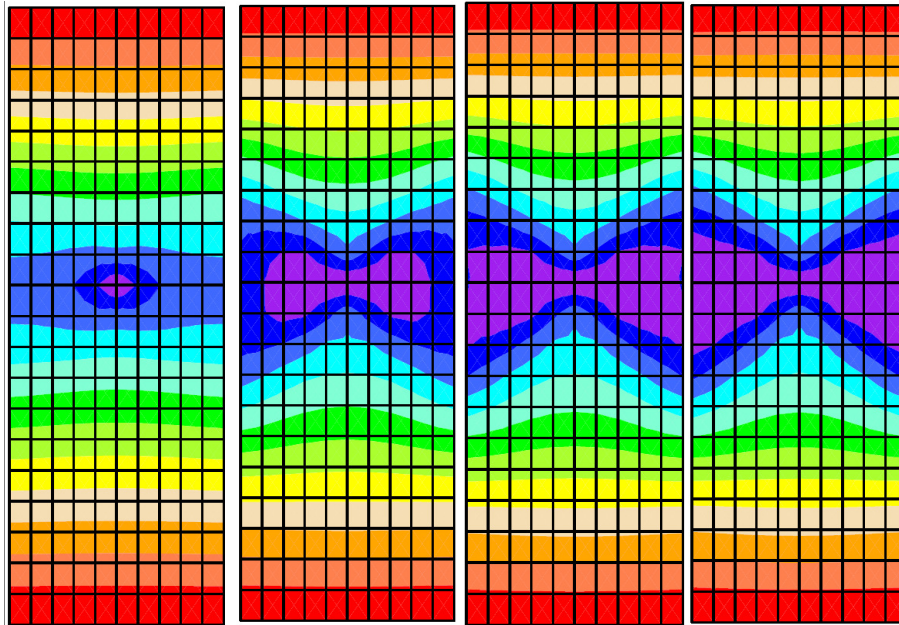


Figure 3.27. The critical area development from macro model 2 for setup c) Fig. 3.24.

3.10. Chapter Conclusions

A novel numerical model for the prediction of the behaviour of laminated glass structures is presented in this chapter. The numerical model consists of two connected models, creating a unique multiscale approach capable of simulating the fracture of LG members. In this approach, a fine-scale multilayer model is combined with a coarse-scale macro model to achieve accuracy and high computational efficiency. The fine-scale multilayer beam model simulates the real LG cross-section and provides the parameters for the macro model. Detailed simulation is achieved by dividing the cross-section geometry into layers defined solely by their axial properties. Each layer is modelled with predefined behaviour in dependence on the axial stress state, and by reaching fracture at a defined limit, this model accurately describes the gradual development of fracture through the cross-section. The fracture of one layer represents a degradation of part of the cross-section and it further influences the stress state of other layers. This transfer is carried out (for loaded element) until the complete failure of the element.

3. Multiscale model with embedded discontinuity for simulation of laminated glass elements exposed to out-of-plane loading

The macro model has a monolithic cross-section and behaves according to the constitutive curve derived from the fine-scale multilayer model. The model represents the fracture of LG structures through a composition of hinges that occur in elements at defined load limits.

To determine the constitutive law of both models, a thermodynamics framework is used for simulation of irreversible processes of damage occurrence. Five different model setups are used to simulate the heterogeneity of glass elements (regarding initial imperfections).

The model predictions are tested by comparing with experimental tests, achieving a very good agreement. The proposed approach for heterogeneity achieved a good representation of imperfections in the glass material.

In addition to these comparisons, simplified engineering approaches for deflection prediction are also tested in the numerical model and compared with the experimental results. It is proven that the use of an effective thickness approach in combination with a multiscale model doesn't provide any benefits, instead, it provides deteriorated results regarding deflection prediction. The most accurate results are achieved by using the full height of the cross-section in the macro model (including all material nonlinear effects obtained by the microscale model). The heterogeneity covers the dispersion of experimental results and provides an interval for the expected behaviour of the structure. Comparison with four groups of experiments confirms the accuracy of the interval and the good predictability of the multiscale model. To overcome the limitations of beam elements in the multiscale model, a new macro model 2 is presented. This model is improved in the aspect of overcoming limitations in load shape and different boundary conditions. Besides, it offers a simplification in the aspect of failure prediction and simulation of the element softening phase which is here reduced to critical zone detection. For this model, only preliminary results are presented to introduce the expected advantages regarding different load shapes and boundary conditions.

Since the model is not completed at the time of writing this dissertation, it remains one of the future tasks to be discussed in Chapter 6. In addition to completing and testing the presented new part of the model, the next step is to simulate the behaviour of elements after failure and predict their post-fracture capacity.

4. STABILITY OF LAMINATED GLASS ELEMENTS EXPOSED TO IN-PLANE LOADING

Contents

- 4.1. Introduction
 - 4.2. Overview of the Research Area
 - 4.3. Brief Model Description
 - 4.4. Numerical Prediction of Critical Buckling Load for Laminated Glass Elements
 - 4.5. Chapter Conclusions
-

4.1. Introduction

The stability of laminated glass structures is the topic of the third part of the glass regulations. It is one of the main design requirements for the load-carrying laminated glass elements subjected to in-plane loads. The coupling effect provided by interlayers is important for ensuring the integrity of the LG elements in case of damage to one or more glass plies. Similar to the case with out-of-plane load, the polymeric interlayer exhibits time and temperature-dependent behaviour that can't be determined by a single limit value of force or stress. The rules for designing in-plane loaded LG members are defined in regulations [3], and simplified calculations in the manner of effective thickness are proposed, but the limits of the method are not determined. To properly consider the contributions of load duration and temperature on the behaviour of interlayers, it is necessary to define more precisely all factors that should be considered when using the method.

In this chapter, the accuracy of the simplified approach (effective thickness approach) is tested. This approach is used for predicting the critical buckling load for laminated glass elements. By comparing results from different experimental tests [99][100][101] with numerical results from two simplified numerical models, the accuracy of obtained numerical results is tested. Two numerical models are used, one with beam elements and the other with shell elements. The models, developed by Hajdo et. al. [102][103][104], are here used for the numerical simulation of structural stability tests of LG structures. These models are capable of simulating elements with monolithic (uniform) cross-sections and are used with assigned equivalent thickness determined through effective thickness approaches. With this setup, the critical buckling load is determined and compared with experimental test results from the literature. The comparisons of realized critical force prediction for different LG cross-sections and different element slenderness provide insights into differences and the necessary level of structure modelling. Additionally, the difference between cross-sections with different interlayers is visible, as well as the influence of boundary conditions.

4.2. Overview of the Research Area

Laminated glass (LG) members have coupled types of cross-sections, where glass plies provide rigidity, and the interlayers ensure joint action of the plies. The polymeric interlayers ensure a certain capacity after the fracture of one or several glass plies, which overcomes the brittle nature of glass for a certain critical period. Post-fracture capacity occurs under static and impact loads applied perpendicular to the element plane if the structural stability is not endangered. This property is not equally emphasized in the case of LG members subjected to in-plane

compressive loads if structural stability is endangered. In the case of breakage of one or several plies of slender, in-plane loaded LG member, the interlayer retains fragments bonded [18] and ensures additional capacity. Once the critical buckling load is reached for the LG member, the interlayer is not capable of ensuring any additional capacity. [99] However, the influence of the interlayer type on the critical load and the behaviour before failure is not negligible. As already mentioned, the viscoelastic material properties of interlayers bring time and temperature dependent values of critical buckling load. This critical buckling load is divided into two categories: “rubbery” and “glassy” critical loads described in [105][106] [107]. For the rubbery critical load, the influence of the interlayer is emphasized, and this critical load is the value that can be used for elements exposed to long-term loading where the viscous nature of the interlayer is emphasized. The glassy critical buckling force is used for LG members exposed to short-term loading where buckling occurs in a short period and the interlayer provides very stiff behaviour. The two presented values are limits, and most buckling occurs in between these two limits. For a realized buckling load that fits into these boundaries, it can be said that creep buckling occurred either due to certain load duration or temperature change. LG structural members loaded in-plane are mostly columns or walls with different cross-sections or supported by lateral restraints made also of glass or other materials. Glass lateral restraints are mostly used due to the retention of transparency of vertical elements accompanied by increased stability. The additional glass members are usually positioned perpendicular to the cross-section of the LG structural member to provide stabilization without transferring the axial force. Besides restraints, T-shaped, X-shaped and H-shaped cross-sections created as whole cross-sections or with lateral supports can be found in the literature [108][109][110][111]. A closed square hollow cross-section [108] and a bundled type of glass columns [109] are also in use. In [108], authors tested glued glass columns with closed square hollow cross-sections exposed to axial compressive force. This type of cross-section showed resistance to global buckling, and the fracture initiation occurred from the bottom of the column, proving local instability, which is more pronounced for this type of cross-section. The analytical calculation for critical buckling force for a closed square hollow cross-section provided an overestimated result. The authors developed two numerical models to achieve better prediction of the results. The 3D solid model showed better prediction of the critical buckling force compared to the shell model. Similar closed cross-sections, only with tubular geometry, exposed to compression load, are tested in [111]. Again, local fracture initiation occurred starting from the bottom of the column. The slenderness of the first described hollow section columns from [108] is around $\lambda \approx 20$, and the second tubular cross-section from [111] is $\lambda \approx 40$, which places these elements in the group of non-slender elements that are not

eligible for flexural buckling. The inaccurate analytical prediction is due to small slenderness, and for this type of members, it is expected that failure will occur due to local stress peaks. In [111], authors developed a numerical model of a tubular cross-section using shell elements. The model predicted the failure behaviour of the tubular columns, but the prediction of critical force was not accurate when compared to the experimental tests. A buckling curve is proposed in these studies. In [110], authors experimentally tested glass columns with T-shape and X-shape cross-sections and proposed simplified expressions for determining their capacity. For these types of cross-sections, the results show that the failure is governed by torsional buckling combined with glue failure between connected components. Compared to flat-shaped laminated glass, the cross-sections with T, X, square hollow, and tubular shape are less sensitive to flexural buckling, and their failure is generally caused by local buckling (for closed cross-sections) and torsional buckling effects (for open cross-sections). The cross-section with lateral glass restraints is studied in [112]. The shape of the cross-section reminds of a T-shaped section, but here the restraints do not transfer the axial force. Experimental and analytical analyses of these columns showed that these types of restraints increase the value of the critical buckling force and change the buckling shape by providing multiple half-sine waves. The authors defined design recommendations for restrained LG columns based on their study. In [113], the authors measured initial curvatures for 312 specimens made of different types of glass (laminated and monolithic) and different interlayers. These specimens were produced by four different manufacturers, which is also considered to compare the influence of production technique on the imperfections in specimens. The authors concluded that the imperfections for heat-strengthen glass (HSG) and tempered glass (TG) are of similar values, but higher than those on annealed glass. Furthermore, it is concluded that the interlayer type does not influence the imperfections, but the lamination process contributes to imperfections, and the influence varies depending on the manufacturer. Thus, the imperfections in LG members are influenced by production lines and machines. These measured values present the true value of initial flexural imperfection for different conditions and those can be used for defining buckling curves for LG columns. These imperfections have an even greater impact on members loaded in eccentric compression.

In [114], the authors tested the behaviour of LG members under combined in-plane and out-of-plane loads, defined as eccentric compression. Further, an analytical interaction curve is proposed for an imperfection factor $\alpha = 0.70$. A similar combination of compression and bending load influence is tested experimentally and compared with analytical results in [115]. For glass elements, the expressions for a buckling reduction factor and a normalized slenderness

ratio used to determine buckling curves are similar to those of steel elements where the expression for limit buckling force ($N_{b,Rd}$) is equal:

$$N_{b,Rd} = \chi \cdot A \cdot \sigma_{Rd} \quad (4.2.1)$$

From equation (4.2.1), χ is a buckling reduction factor which, for the case $\chi \leq 1$, is equal to:

$$\chi = \frac{1}{\phi + \sqrt{\phi^2 - \bar{\lambda}^2}} \quad (4.2.2)$$

where ϕ is equal to:

$$\phi = 0,5 \cdot [1 + \alpha_{imp} \cdot (\bar{\lambda} - \alpha_0) + \bar{\lambda}^2]. \quad (4.2.3)$$

In equations (4.2.2.) and (4.1.3), $\bar{\lambda}$ represents the normal slenderness ratio, that is defined as:

$$\bar{\lambda} = \sqrt{\frac{A \cdot \sigma_{Rk}}{N_{cr}}} \quad (4.2.4)$$

from where N_{cr} is the Euler critical buckling load and σ_{Rk} is the characteristic strength.

$$\sigma_{Rd} = \frac{\sigma_{Rk}}{\gamma_M} \quad (4.2.5)$$

The difference from calculations of steel elements occurs in the proposed imperfection factors α_{imp} , α_0 and used partial safety factors γ_M . Several levels of detailing for designing elements exposed to in-plane loading are described in regulations [3]. All consider the geometrical and material imperfections defined through the equivalent imperfection. This imperfection should be considered for ULS (ultimate limit state), FLS (fracture limit state), and PFLS (post-fracture limit state). The imperfection for ULS depends on the type of buckling and it doesn't include any fracture effect on increasing the value of imperfection. This value is defined by the length of the specimen and load introduction eccentricity. The imperfections related to FLS and PFLS can be considered only in case of fracture of one or several plies because the additional shift appears due to fragmentation of plies, as described in regulations [3]. For LG elements, interlayer modelling is proposed in three levels according to the table for interlayer modelling from the first part of the regulations [1]. As already described in the first chapter, the levels start from the most radical approach, which proposes neglecting the interlayer in case of positive effects on bearing capacity. The second level of interlayer modelling proposes the effective thickness approach, and the third level of interlayer modelling defines modelling by using a detailed numerical model. For the determination of critical buckling load, the effective moment of inertia is proposed in an expression which can be used for symmetric LG (two and three-ply) cross-sections with sinusoidal lateral deflection shape.

Numerical calculations with exact imperfections and real LG cross-sections are costly but provide accurate results. The combination of measured imperfection with a robust numerical

model is not always easy to obtain for structural elements. In everyday engineering practice, it is more common to use reliable simplified methods that are time-saving and ensure productivity. The effective thickness can be considered a simplified method that can be used in combination with standard numerical models to overcome the detailed modelling of layered cross-sections.

4.2.1. Effective Thickness Approach in Buckling Analysis

The effective thickness approach (ETA) is presented in Chapter 1 and Chapter 2 of this work. It can be said that ETA is a simplified engineering approach that provides simplification through the homogenization of layered cross-sections. By using this method, the LG cross-section is replaced with a monolithic cross-section with reduced thickness, which under the same boundary and load conditions can predict the behaviour of the LG member. The reduction is dependent on the shear coupling provided by interlayer shear stiffness, geometry, type of loading, etc. To use this method for the determination of the buckling critical load, the primary focus will be on expressions for deflection prediction. There are several approaches for effective thickness methods, and most of them are developed for out-of-plane loading. The basic methods with the expressions and additional explanations are presented in Table 2.3. for the method by Wolfel [57] described in the research of Calderone et al. [58] where it was tested on elements exposed to out-of-plane loading. Another expression, based on the previous (Wolfel [57]/ Calderone et al. [58]) but with certain modifications, is described in Table 2.4. It originates from the previous version of standards [22]. In literature [116], a criticism can be found on this way of defining the effective thickness (only by adopting coefficient ω) without taking into account aspects such as boundary condition, size effect, and load type. Galuppi and Royer-Carfagni developed an enhanced expression (Enhanced Effective Thickness) using a variational approach primarily for out-of-plane loading [31], presented in Table 2.6. This approach is further defined for in-plane load [117] presented in Table 4.1., expression (4.2.6). This expression (4.2.6) for buckling laminated glass structures is proposed in [117] based on the assumptions from the previous EET model for the out-of-plane load. The shape function used in EET is adopted as a co-sinusoidal buckling shape for in-plane load, and the values of the coupling factor Ψ are determined for the most common static schemes. The evaluation is done analytically and confirmed by using eigenvalue buckling analysis in commercial software. The authors determined critical buckling force based on the numerical model of the LG cross-section and determined h_{eff} and I_{eff} from the result. Thus, the expression for h_{eff} was tested and validated for different boundary conditions. The authors commented that the greater the

constraints of the beam, the lower the coupling of the interlayer, and consequently, the effective thickness for the same cross-section should be lower. [117] There are other studies in the literature related to the determination of effective thickness or effective stiffness. López-Aenlle et al. [105] proposed an expression for effective stiffness as a simplified method for the calculation of critical buckling load using the Euler theory. The expression for the effective stiffness is presented in Table 4.1. in equation (4.2.7), and for simply supported structures (both sides hinged), it provides the same results as the expression (4.2.6) from [117]. In [118], the same group of authors presented the expression for the determination of critical buckling load of three-ply LG members, also based on the work form [119]. Another expression for effective moment of inertia (4.2.8) can be found in regulation [3]. The expression is adopted from the research carried out by Langosch and Feldmann [120] and is based on Newmark's theory. All presented expressions (4.2.6 - 4.2.8) provide the same results in the case of simply supported elements (both sides hinged) made of LG with two glass plies. The difference appears in the case of other boundary conditions and for multiple glass plies. An overview of effective methods can be found in [100] together with direct methods for the determination of critical load.

Table 4.1. Different equations for the effective thickness approach (ETA) from the literature [117][105][120]

<p>b – width of cross-section E – modulus of elasticity of glass G – shear modulus of interlayer h_1 and h_2 – height of glass plies t – thickness of interlayer I_L – moment of inertia for layered case I_M – moment of inertia for monolithic case Ψ – coupling factor (4.2.9)</p>	$h_{eff} = \left[\frac{b}{12} \cdot \left(\frac{\eta}{I_M} + \frac{1-\eta}{I_L} \right) \right]^{-\frac{1}{3}}$ $\eta = \frac{1}{1 + \frac{E \cdot t}{G} \cdot \frac{h_1 \cdot h_2}{h_1 + h_2} \cdot \frac{I_L}{I_M} \cdot \Psi}$ $I_L = \frac{b}{12} \sum_{i=1}^N h_i^3; I_M = \frac{b}{12} \sum_{i=1}^N (h_i^3 + 12d_i^3 h_i)$	<p>(4.2.6)</p>
<p>E – modulus of elasticity of glass plies (1 and 3) $I(t, T)_S$ – moment of inertia (time and temperature) H_1 and H_3 – height of glass plies H_2 – thickness of interlayer $G_2(t, T)$ – shear modulus of interlayer β – buckling shape coefficient L – length of the member</p>	$EI(t, T)_S = EI_T \left[1 + \frac{Y}{1 + \frac{E_1 H_1 H_2 E_3 H_3}{G_2(t, T) \cdot (E_1 H_1 + E_3 H_3)} \cdot \frac{\pi^2}{(\beta L)^2}} \right]$ $Y = \frac{h_s^2 H_1 H_3}{(I_1 + I_3)(H_1 + H_3)}$ $h_s = 0.5(H_1 + H_3) + H_2$	<p>(4.2.7)</p>
<p>E – modulus of elasticity of glass plies I_i – the moment of inertia of i-th glass ply A_i – area of i-th glass ply $\Psi_s = h_s$ $K_s = \frac{G}{t} B$ slip stiffness L – length of the member</p>	$I_{z,eff} = \frac{\sum I_i}{1 - \frac{\Psi_s \cdot \beta \cdot K_s}{\left(\frac{\pi}{L}\right)^2 + \alpha^2}}$ $\beta = \frac{h_s}{E(I_1 + I_2)}$ $\alpha = \frac{K_s}{E} \left(\frac{h_s^2}{(I_1 + I_2)} + \frac{1}{A_1} + \frac{1}{A_2} \right)$	<p>(4.2.8)</p>

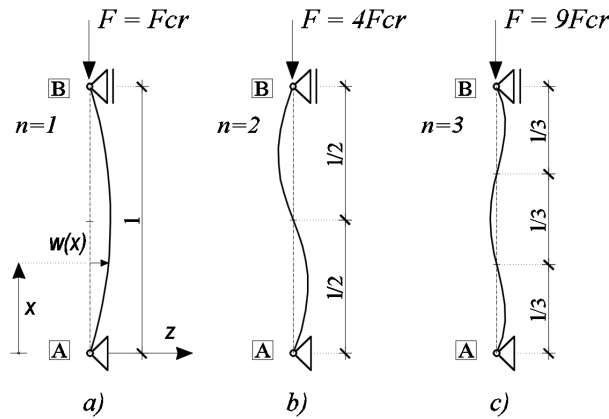


Figure 4.1. Buckling shapes for simply supported member

In equation (4.2.6) from [117], the value of factor Ψ is defined using the equation from [31]:

$$\Psi = \frac{\int [g''(x)]^2 dx}{\int [g'(x)]^2 dx}; 0 \leq x \leq l \quad (4.2.9)$$

From [31] $g(x)$ is the proposed shape function of the displacement, that depends on the external load $p(x)$ and the boundary conditions. To define the coupling factor Ψ , a simply supported element with both sides hinged is considered. By solving a second-order homogeneous differential equation with constant coefficients, the general solution is determined as:

$$g(x) = A \cdot \sin ax + B \cdot \cos ax \quad (4.2.10)$$

For chosen boundary conditions with a known deflection at $x = 0$ and $x = l$ we obtain:

$$g(x) = \sin \frac{n\pi}{l} x \quad (4.2.11)$$

In expression (4.2.11), n denotes the number of half-waves of the sinusoid over the length of the element. For the lowest value of critical force from Figure 4.1., the chosen value is $n = 1$ (for $n = 0$, a trivial solution occurs).

$$g(x) = \sin \frac{\pi}{l} x \quad (4.2.12)$$

Further, by introducing (4.2.12) into (4.2.9), the coupling factor for a simply supported element is as follows in [117]:

$$\Psi = \frac{\pi^2}{l^2} \quad (4.2.13)$$

In the case of both sides fixed boundary conditions, the shape function is equal to two half-waves of the sinusoid:

$$g(x) = -B(1 - \cos \frac{2\pi}{l} x) \quad (4.2.14)$$

where B is a constant, and the obtained coupling factor Ψ is equal:

$$\Psi = \frac{4\pi^2}{l^2} \quad (4.2.15)$$

4.3. Brief Model Description

In previous works by Hajdo et. al. [102][103][104], a linear instability problem is solved using finite elements by introducing the von Karman deformation measure. This deformation measure can be used in cases when rotations are moderate and deformations are small. Models with beam and shell finite elements are defined for determining the critical buckling load. These elements were validated in previous works by a comparison to the analytical solutions for the critical buckling load. Furthermore, it is shown that the elements can be used for complex structures to determine critical buckling load, for structures with small prebuckling displacements [102][103]. Here, only a brief description of the model is provided, as it is not developed by the author. All further computations are carried out a research version of the computer program FEAP, developed by Prof. R.L. Taylor at UC Berkeley [96].

A set of algebraic equations defined in (4.3.1) is the final product of the finite element discretization for the geometrical instability problem:

$$\mathbf{w}^{eT} \mathbf{f} = \sum_{e=1}^n \mathbf{w}^{eT} \underbrace{[\mathbf{K}_m^e + \mathbf{K}_g^e]}_{\mathbf{K}_t} \mathbf{d} \quad (4.3.1)$$

With \mathbf{K}_t a tangent stiffness matrix is defined, which consists of the material stiffness matrix \mathbf{K}_m and the geometric stiffness matrix \mathbf{K}_g . Equation (4.3.1) describes a nonlinear problem, where the geometric stiffness matrix depends on the internal force that leads to displacement at the critical point. By using a unique geometric stiffness form, which exhibits concerning applied loads, the geometric stiffness matrix can be expressed as the product of the reference value of the geometric stiffness matrix $\overline{\mathbf{K}}_g$ and the load multiplier λ_p :

$$\mathbf{K}_t = \mathbf{K}_m + \lambda_p \overline{\mathbf{K}}_g \quad (4.3.2)$$

For a linear elastic material, the material stiffness matrix \mathbf{K}_m remains constant, while the geometric stiffness changes linearly with the applied load. The reference value of geometric stiffness $\overline{\mathbf{K}}_g$ is determined regarding the reference load value $\overline{\mathbf{f}}$. Once the applied load reaches the critical value $\mathbf{f}_{cr} = \lambda_{cr} \overline{\mathbf{f}}$, the system falls into a state where the stiffness matrix becomes singular, and its determinant is equal to zero (critical equilibrium).

$$\det(\mathbf{K}_m + \lambda_{cr} \overline{\mathbf{K}}_g) = 0 \quad (4.3.3)$$

To obtain the critical load value, an eigenvalue problem is used. For the critical equilibrium state $\mathbf{K}_t \boldsymbol{\psi}_{cr} = 0$, it implies that for the critical mode $\boldsymbol{\psi}_{cr}$, the tangent stiffness matrix \mathbf{K}_t will have a zero eigenvalue. [104]

$$(\mathbf{K}_m + \lambda_{cr} \overline{\mathbf{K}}_g) \boldsymbol{\psi}_{cr} = 0 \quad (4.3.4)$$

In the numerical analysis, beam and shell finite elements are used with von Karman deformation measures. A more detailed description of models is provided in [102][103][104].

4.4. Numerical Prediction of Critical Buckling Load for Laminated Glass Elements

The simplified approach used in numerical prediction combines a numerical model (without considering imperfections) with the monolithic cross-section derived from the analytical expressions for homogenization of the LG cross-section (ETA). This approach is used in the prediction of the critical buckling force for several different geometries. For easier validation, the geometries are adopted from the literature [99][100][101] where experimental buckling tests were conducted on laminated glass columns (specimens). As mentioned, two numerical models are used: one with shell elements and another with beam elements. The predictions from both models are compared with the forces obtained from experimental results. By using the presented expressions for the effective thickness approach [105][117][120]([3]), the thickness of the homogenized cross-section is determined and used to simulate the LG tests in the beam and shell model. All information about specimens (geometry, boundary conditions, temperature, load duration, material characteristics of interlayer) is taken from the experimental tests in [99][100][101].

4.4.1. Test 1 – Laminated Glass Elements (2-Ply and 3-Ply Cross-Section)

In the first comparison with results from [99], four types of specimens are simulated. All specimens have the same length and width, with differences is in the number of plies and interlayers. Laminated glass specimens are made of annealed float glass ($f_{u,bending} = 45N/mm^2$) with SGP and PVB interlayers. The values of the Poisson's ratio coefficient and Young's modulus of interlayers for the case of load duration $t = 3$ sec and $t = 10$ years, and for temperatures of 20 °C and 50 °C, are determined from the literature. These values are considered as limit values of realistic interval in normal loading conditions and are used to determine the glassy and rubbery buckling force. The material characteristics for exact load duration and temperature conditions from experiments (≈ 10 min and ≈ 20 °C) are not specified in the literature, and those are interpolated from known material characteristics. The length of the specimens is 2700 mm, and the width of the cross-section is 300 mm. The boundary

conditions of the specimens are presented in Figure 4.2. A total of 21 tests are conducted in [99] at a temperature of ≈ 20 °C with a load duration of ≈ 10 min. The photography of test setup is taken from the literature and presented in Figure 4.3. With all the information from the literature, the first step was to determine the effective thickness for each specimen considering three cases of load duration and temperatures (the limit values and experimental values). After determining the effective thickness, elements are further simulated in numerical models with homogenized cross-sections, see Figure 4.2.

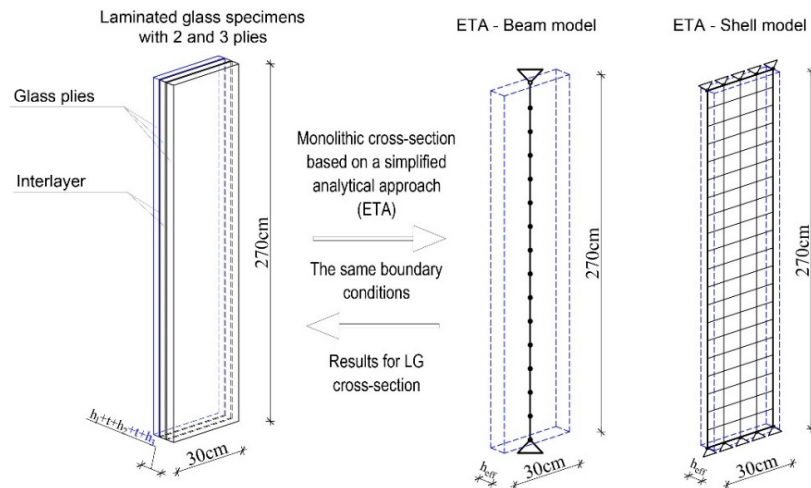


Figure 4.2. Numerical models of Test 1- implementation of analytical solution into beam and shell numerical model

Two effective thicknesses are determined for each geometry/interlayer type: one according to [117] (G. D'Ambrosio and L. Galuppi) and the other according to [3]/[120] (regulation/ Langosch and Feldmann). In the case of two-ply laminated glass cross-sections, the expressions provide equal thickness values for the same specimen (Table 4.2.), while for three-ply cross-sections, the results are slightly different (Table 4.3.). All specimens are hinged on both sides.

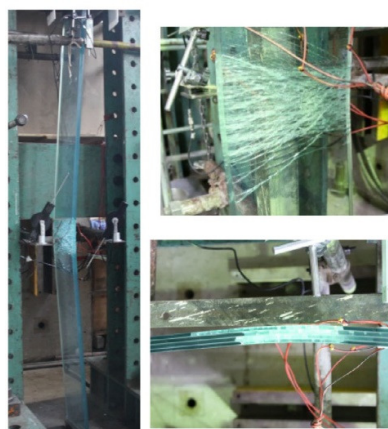


Figure 4.3. Photography of experimental test 1 from [99]

4. Stability of laminated glass elements exposed to in-plane loading

Table 4.2. Effective thickness for specimens with two-ply laminated glass cross-sections

SGP interlayer (2700mmx300mm) [99]			PVB interlayer (2700mmx300mm) [99]				
Glass panel thickness	12+12mm; 16+16 mm		Glass panel thickness	12+12mm			
Specimen name	C-1SG-24/C-1SG-32		Specimen name	C-1PVB-24			
Interlayer thickness	1.78mm		Interlayer thickness	1.52mm			
Tested specimens	2x/1x		Tested specimens	2x			
Material characteristics	h_{eff} (12+12mm)	h_{eff} (16+16mm)	Material characteristics	h_{eff} (12+12mm)	h_{eff} (16+16mm)		
$E_{3s, 20^\circ C}$	612 MPa	25.744	33.722	$E_{3s, 20^\circ C}$	24.15 MPa	24.989	32.457
$\nu_{3s, 20^\circ C}$	0.449			$\nu_{3s, 20^\circ C}$	0.498		
$E_{3s, 50^\circ C}$	78.8 MPa	25.519	33.337	$E_{3s, 50^\circ C}$	1.44 MPa	19.880	25.282
$\nu_{3s, 50^\circ C}$	0.493			$\nu_{3s, 50^\circ C}$	0.4999		
$E_{10min, 20^\circ C}$	530 MPa	25.739	33.713	$E_{10min, 20^\circ C}$	≈3,95 MPa	22.370	28.520
$\nu_{10min, 20^\circ C}$	0,453			$\nu_{10min, 20^\circ C}$	0.498		
$E_{10y, 20^\circ C}$	256 MPa	25.698	33.642	$E_{10y, 20^\circ C}$	0.80 MPa	18.478	23.636
$\nu_{10y, 20^\circ C}$	0.479			$\nu_{10y, 20^\circ C}$	0.4999		
$E_{10y, 50^\circ C}$	6.00 MPa	23.231	29.746	$E_{10y, 50^\circ C}$	0.156 MPa	16.037	21.044
$\nu_{10y, 50^\circ C}$	0.50			$\nu_{10y, 50^\circ C}$	0.50		

Table 4.3. Effective thickness for specimens with three-ply laminated glass cross-sections ([3]/[120] - first result; [117] - second result)

SGP interlayer (2700mmx300mm) [99]				PVB interlayer (2700mmx300mm) [99]			
Glass panel thickness	12+16+12mm;10+12+10;8+8+8 mm			Glass panel thickness	12+16+12mm		
Specimen name	C-2SG-40/-32/-24			Specimen name	C-2PVB-40		
Interlayer thickness	1.78mm			Interlayer thickness	1.52mm		
Tested specimens	2x/2x/2x			Tested specimens	1x		
Material characteristics	h_{eff} (12+16+12)	h_{eff} (10+12+10)	h_{eff} (8+8+8)	Material characteristics	h_{eff} (12+16+12)		
$E_{3s, 20^\circ C}$	612 MPa	42.833	34.930	27.046	$E_{3s, 20^\circ C}$	24.15 MPa	40.142
$\nu_{3s, 20^\circ C}$	0.449				$\nu_{3s, 20^\circ C}$	0.498	
$E_{3s, 50^\circ C}$	78.8 MPa	42.014	34.362	26.688	$E_{3s, 50^\circ C}$	1.44 MPa	28.290
$\nu_{3s, 50^\circ C}$	0.493				$\nu_{3s, 50^\circ C}$	0.4999	
$E_{10min, 20^\circ C}$	530 MPa	42.814	34.916	27.038	$E_{10min, 20^\circ C}$	≈3,95 MPa	33.497
$\nu_{10min, 20^\circ C}$	0.453				$\nu_{10min, 20^\circ C}$	0.498	
$E_{10y, 20^\circ C}$	256 MPa	42.659	34.809	26.971	$E_{10y, 20^\circ C}$	0.80 MPa	25.630
$\nu_{10y, 20^\circ C}$	0.479				$\nu_{10y, 20^\circ C}$	0.4999	
$E_{10y, 50^\circ C}$	6.00 MPa	35.091	29.241	23.212	$E_{10y, 50^\circ C}$	0.156 MPa	21.238
$\nu_{10y, 50^\circ C}$	0.50				$\nu_{10y, 50^\circ C}$	0.50	

For a three-ply LG cross-section, a critical buckling force is determined for two effective thicknesses. Due to a small difference that is not noticeable in the interval graph, in the further analysis of critical load, only one value of effective thickness [120] is used.

The comparison of results from two numerical models and experimental tests from [99] are presented in Table 4.4. for two-ply LG cross-sections and in Table 4.5. for three-ply LG cross-sections (all with PVB or SGP interlayer). The glassy and rubbery critical buckling loads are obtained in the beam and shell models. For these values, there are no experimental results, but

they serve as limits of interval in which buckling should occur. The value of the reported buckling load from the experiments [99] fits inside the critical interval, higher than the rubbery critical buckling load and under the glassy critical buckling load. By using interpolated values of material characteristics for the interlayer, the prediction of the exact force from the experiment conditions is also determined. Thus, it can be seen that the numerical prediction values fit within the intervals in which the experimental results are scattered.

Table 4.4. The experimental results from [99] and obtained numerical results for specimens with two-ply cross-sections

Time	Temp.	Glass thickness [mm]	Interlayer	Effective thickness [mm]	λ	Shell model	Beam model	Experiments from [99]
						Force (kN)	Force (kN)	Force (kN)
3 s	20°C	12+12	SGP	25.744		40.05	40.5	x
3 s	20°C	12+12	PVB	24.989		37.05	37.06	x
3 s	50°C	12+12	SGP	25.519		39.47	39.47	x
3 s	50°C	12+12	PVB	19.880		18.65	18.66	x
10min	20°C	12+12	SGP	25.739	363.38	40.48	40.50	48.5; 48.3
10min	20°C	12+12	PVB	22.370	418.11	26.58	26.59	26.5; 26.5
10 y	20°C	12+12	SGP	25.698		40.3	40.3	x
10 y	20°C	12+12	PVB	18.478		14.98	14.99	x
10 y	50°C	12+12	SGP	23.231		29.78	29.78	x
10 y	50°C	12+12	PVB	16.037		9.8	9.8	x
3 s	20°C	16+16	SGP	33.722		91.04	91.07	x
3 s	20°C	16+16	PVB	32.457		81.2	81.2	x
3 s	50°C	16+16	SGP	33.337		87.96	87.98	x
3 s	50°C	16+16	PVB	25.282		38.4	38.4	x
10min	20°C	16+16	SGP	33.713	277.43	90.97	90.99	96.7
10min	20°C	16+16	PVB	28.520		55.07	55.09	x
10 y	20°C	16+16	SGP	33.642		90.39	90.42	x
10 y	20°C	16+16	PVB	23.636		31.35	31.36	x
10 y	50°C	16+16	SGP	29.746		62.48	62.48	x
10 y	50°C	16+16	PVB	21.044		22.12	22.14	x

The authors noticed in experimental tests [99] that an increase in the number of glass plies provides increased buckling resistance for the SGP interlayer; they also commented that in the case of specimens with PVB, the opposite effect occurs. However, once stability is compromised, neither of the interlayers (PVB or SGP) is capable of providing any additional post-buckling capacity.

Table 4.5. The experimental results from [99] and obtained numerical results for specimens with three-ply cross-sections

Time	Temp.	Glass thickness [mm]	Interlayer	Effective thickness [mm]	λ	Shell model	Beam model	Experiments from [99]
						Force (kN)	Force (kN)	Force (kN)
3 s	20°C	12+16+12	SGP	42.833		186.56	186.58	x
3 s	20°C	12+16+12	SGP	42.745		185.41	185.44	x
3 s	20°C	12+16+12	PVB	40.142		153.56	153.59	x
3 s	20°C	12+16+12	PVB	38.847		139.17	139.20	x
10min	20°C	12+16+12	SGP	42.814	218.54	186.31	186.34	176.5; 208.7
10min	20°C	12+16+12	SGP	42.711		184.97	184.99	176.5; 208.7
10min	20°C	12+16+12	PVB	33.497	279.43	89.23	89.26	94.4
10min	20°C	12+16+12	PVB	30.826		69.54	69.56	94.4
10 y	50°C	12+16+12	SGP	35.091		102.58	102.61	x
10 y	50°C	12+16+12	SGP	32.283		79.87	79.90	x
10 y	50°C	12+16+12	PVB	21.238		22.74	22.75	x
10 y	50°C	12+16+12	PVB	20.629		20.84	20.85	x
3 s	20°C	10+12+10	SGP	34.930		101.18	101.21	x
3 s	20°C	10+12+10	SGP	34.876		100.71	100.74	x
10min	20°C	10+12+10	SGP	34.916	268.17	101.05	101.08	99.2; 101.7
10min	20°C	10+12+10	SGP	34.855		100.53	100.56	99.2; 101.7
10 y	50°C	10+12+10	SGP	29.241		59.36	59.38	x
10 y	50°C	10+12+10	SGP	27.245		48.01	48.03	x
3 s	20°C	8+8+8	SGP	27.046		46.97	46.99	x
3 s	20°C	8+8+8	SGP	27.020		46.83	46.85	x
10min	20°C	8+8+8	SGP	27.038	346.44	46.92	46.94	55.5; 53.5
10min	20°C	8+8+8	SGP	27.008		46.77	46.79	55.5; 53.5
10 y	50°C	8+8+8	SGP	23.212		29.69	29.70	x
10 y	50°C	8+8+8	SGP	22.025		25.36	25.38	x

The results from Tables 4.4. and 4.5., are graphically presented in Figure 4.4. It can be seen that the position of experimental results inside the rubbery and glassy critical load confirms conclusions about the SGP interlayer. Namely, the results for specimens with SGP interlayer are on the upper boundary or exceeding the interval of expected critical buckling load. This confirms that the realized stiffness of the SGP interlayer in test conditions is higher than expected. The buckling force for specimens with PVB interlayer fits inside intervals, mostly around the middle of the interval and slightly closer to the glassy limit. This behaviour is expected due to the short load duration of the experimental test (10 min) and the same temperature as used for determination of the glassy critical load. The middle value of the critical buckling force interval for the two-ply LG - PVB (12+12mm) specimens is $F_{mean,2GL} = 23.43kN$ and the mean value of the experimental force is $F_{exp,10min,20^\circ} = 26.50kN$. In the case of three-ply LG - PVB (12+16+12mm) specimens, $F_{mean,3GL} = 88.15kN$ and the obtained experimental force is $F_{exp,10min,20^\circ} = 94.40kN$. This shows that for an increase in load duration from 3sec to 10min at the same temperature of 20°C, the buckling force for PVB

4. Stability of laminated glass elements exposed to in-plane loading

specimens is closer to the interval middle value than the glassy limit. The difference between the accomplished buckling force from experiments and the numerical prediction of the glassy limit for PVB specimens is $\Delta F_{num-exp,2GL} = 10.55kN$ for two-ply LG-PVB specimens and $\Delta F_{num-exp,3GL} = 59.16kN$ for three-ply LG specimens. These deviations are in total 45.2% and 37.7% of the entire critical interval for two and three-ply LG - PVB specimens, respectively, and occur only for increasing load duration from 3 sec to 10 min.

The size of the critical interval varies and increases with increasing the number and the thickness of glass plies. This trend occurs for specimens with both SGP and PVB interlayers. It can be concluded that with increasing buckling resistance of the specimens, the difference between glassy and rubbery critical load is higher, which means that the influence of the interlayer on the critical buckling force is increased.

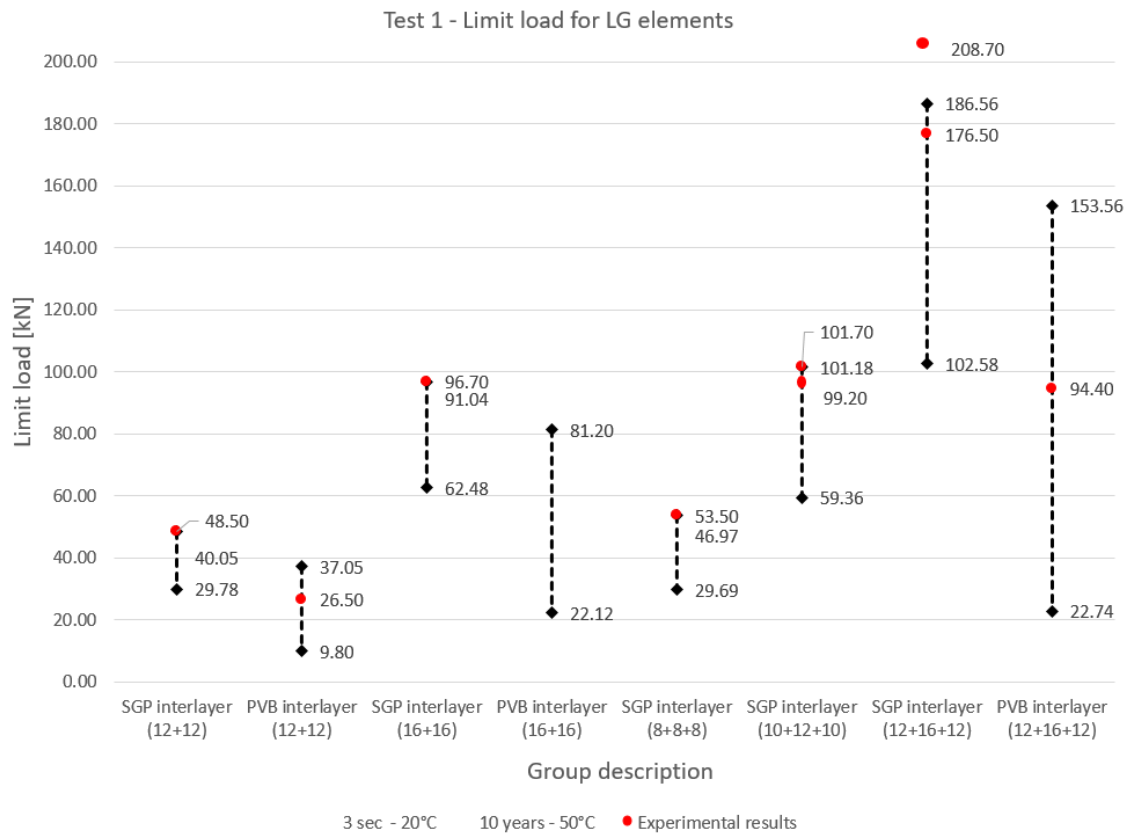


Figure 4.4. Graphical presentation of numerically predicted critical intervals and the experimental result for Test 1

The graphical representation of the relationship between the numerically predicted critical buckling forces and the experimental results is shown in Figure 4.5. The values are presented in dependence on the effective slenderness of specimen λ , which is determined using effective

thickness. Regarding the results from two models (beam and shell models), it can be seen that the results from the beam and shell models show deviations mostly within 1% of total force. The numerical results (along with the effective thickness approach) provide a slightly overestimated critical force when compared to experimental results. The mean value of realised errors for seven different geometries is $\Delta(F_{numerical}/F_{experimental}) = 1.07$. Thus, this combination of the shell/beam numerical model with the analytical expressions for effective thickness provides a critical force prediction with the discrepancy of $\approx 7\%$ of realised experimental buckling forces.

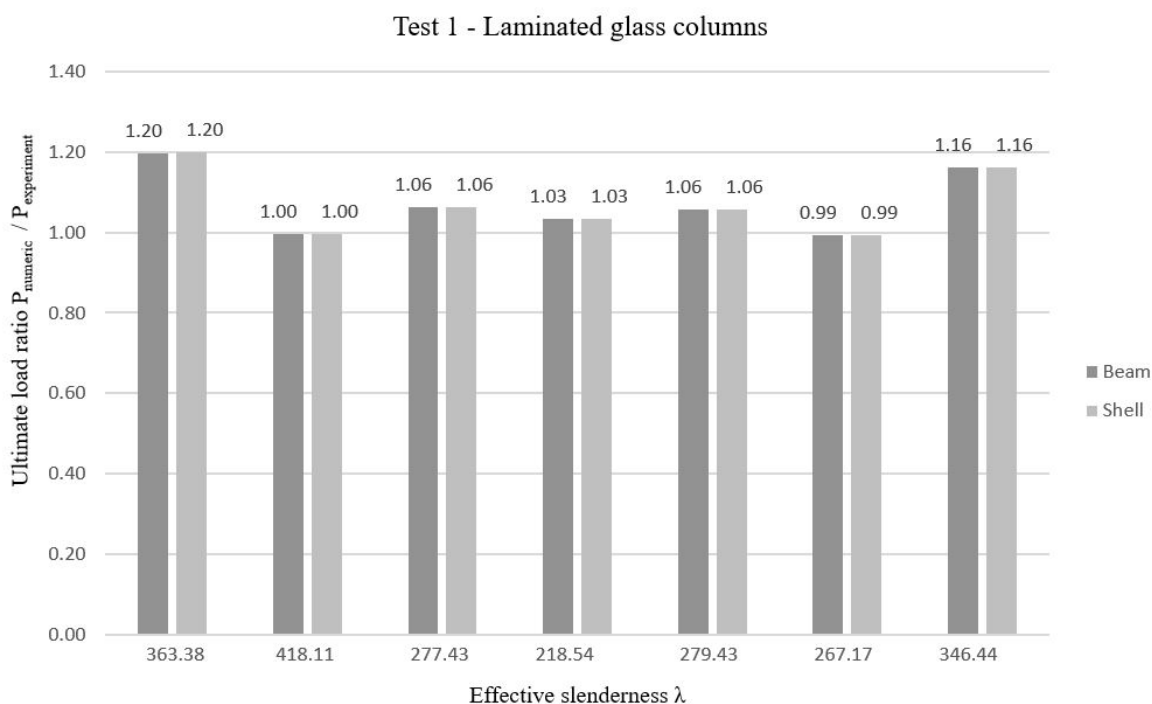


Figure 4.5. Graphical presentation of the ratio between the numerically predicted critical force and the experimental results ($F_{numerical}/F_{experimental}$) for Test 1

4.4.2. Test 2 – Laminated Glass Elements With Different Geometry

In the second test, laminated glass specimens with different slenderness are tested, and the geometry and material characteristics are defined according to experimental tests from [100], see Table 4.6. All specimens are composed of three-ply cross-sections bonded with two interlayers (SGP and PVB). The thickness of the interlayers for all specimens is $t = 0.76$ mm. The width of specimens is 150 mm and the heights of specimens are 600 mm, 1000 mm, and

1300 mm, all made of annealed float glass ($f_{u,bending} = 45N/mm^2$). Boundary conditions are shown in Figures 4.6. and 4.7. Two types of interlayers are used: DuPont (Butacite® PVB) PVB interlayer, and the SG interlayer from Kuraray. For the PVB interlayer, the material properties are determined based on the work of Hooper et al. [121], and for SGP, from [122]. The duration of the test is not defined, and the effective thickness for only two boundaries (rubbery and glassy) is determined. The limits are determined by varying only load duration at a known temperature $T_0 = 30^\circ C$. The material properties of the interlayer that match these two limits are determined from the master curves from [121][122], as was presented and explained in [100]. The used shift factor for temperature of $T_0 = 30^\circ C$ is $\log \alpha_T = -0.354$ for PVB, and $\log \alpha_T = -3.67$ for SGP.

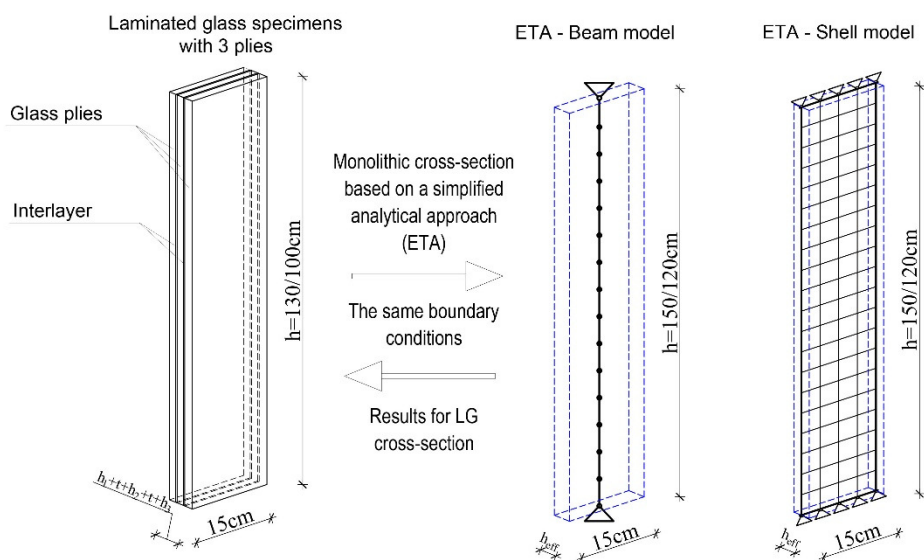


Figure 4.6 Numerical models of Test 2- implementation of analytical solution into beam and shell numerical model

With all the information from the experiments, effective thickness is determined for two cases of load duration and fixed temperature for each specimen geometry. In the case of three glass plies, a slight difference occurs in effective thickness calculated according to [120] and [117] respectively; the results are presented in Table 4.6. The buckling length of specimens is magnified for 200 mm due to the length of a steel sleeve that is used as support. By using this homogenized cross-section geometry and specimen geometry, critical buckling forces are determined in two numerical models (beam model and shell model).



Figure 4.7. Photography of experimental test 2 from [100]

Table 4.6. Effective thickness for specimens with three-ply laminated glass cross-sections ([3]/[120] - first result; [117] - second result)

SGP interlayer (1000mmx150mm)[100]				PVB interlayer (1000mmx150mm)[100]			
Glass panel thickness		4+4+4mm		Glass panel thickness		4+4+4mm; 8+8+8mm	
Specimen name		PVB-3_4-1000		Specimen name		SG-3_4-1000/SG-3_8-1000	
Interlayer thickness		0.76mm		Interlayer thickness		0.76mm	
Tested specimens		3x		Tested specimens		3x/3x	
Material characteristics		h_{eff} (4+4+4)	h_{eff} (8+8+8)	Material characteristics		h_{eff} (4+4+4)	h_{eff} (8+8+8)
$G_{short, 30^{\circ}C}$	237.137 MPa	13.291 13.277	25.205 25.179	$G_{short, 30^{\circ}C}$	177.6 MPa	13.279 13.260	25.161 25.127
$G_{long, 30^{\circ}C}$	0.706 MPa	9.167 8.596	15.599 15.139	$G_{long, 30^{\circ}C}$	0.112MPa	6.712 6.472	12.428 12.292
SGP interlayer (1300mmx150mm) [100]				PVB interlayer (1300mmx150mm) [100]			
Glass panel thickness		4+4+4mm; 8+8+8mm		Glass panel thickness		4+4+4mm; 8+8+8mm	
Specimen name		PVB-3_4-1300/-3_8-1300		Specimen name		SG-3_4-1300/SG-3_8-1300	
Interlayer thickness		0.76mm		Interlayer thickness		0.76mm	
Tested specimens		3x/3x		Tested specimens		3x/3x	
Material characteristics		h_{eff} (4+4+4)	h_{eff} (8+8+8)	Material characteristics		h_{eff} (4+4+4)	h_{eff} (8+8+8)
$G_{short, 30^{\circ}C}$	237.137 MPa	13.306 13.297	25.260 25.244	$G_{short, 30^{\circ}C}$	177.6 MPa	13.300 13.287	25.233 25.212
$G_{long, 30^{\circ}C}$	0.706 MPa	9.935 9.342	16.866 16.337	$G_{long, 30^{\circ}C}$	0.1122 MPa	7.194 6.858	12.952 12.747

In Table 4.7. all the specimen information and the forces from experiments and numerical models are presented. As can be seen, the small difference in effective thickness between the two methods does not impact the limits of the buckling force intervals. Therefore, in the further analysis, only the effective thickness according to [3]/[120] (regulation/Langosch and Feldmann) is considered.

Table 4.7. The experimental results from [100] and obtained numerical results for specimens with three-ply cross-sections

Time	Temp.	Glass thickness [mm]	Specimen info. [mm]	Buckling length [mm]	Effe. thickness [mm]	Shell model	Beam model	Experiments from [100]
						Force (kN)	Force (kN)	Force (kN)
3 s	30°C	4+4+4	1000x150 SGP	1200	13.291	14.11	14.11	12.28; 11.32; 12.38;
					13.277	14.05	14.05	
10 y	30°C	4+4+4	1000x150 SGP	1200	9.167	4.63	4.63	
					8.596	3.82	3.82	
3 s	30°C	4+4+4	1000x150 PVB	1200	13.279	14.07	14.07	5.41; 5.57; 5.76
					13.26	14.01	14.01	
10 y	30°C	4+4+4	1000x150 PVB	1200	6.712	1.82	1.82	
					6.472	1.63	1.63	
3 s	30°C	8+8+8	1000x150 SGP	1200	25.205	96.23	96.20	x
					25.179	95.93	95.90	
10 y	30°C	8+8+8	1000x150 SGP	1200	15.599	22.81	22.82	
					15.139	20.85	20.86	
3 s	30°C	8+8+8	1000x150 PVB	1200	25.161	95.72	95.70	28.01; 26.61; 24.94
					25.127	95.34	95.31	
10 y	30°C	8+8+8	1000x150 PVB	1200	12.428	11.54	11.54	
					12.292	11.16	11.16	
3 s	30°C	4+4+4	1300x150 SGP	1500	13.306	9.06	9.06	8.97; 8.84; 8.94
					13.297	9.04	9.04	
10 y	30°C	4+4+4	1300x150 SGP	1500	9.935	3.77	3.77	
					9.342	3.13	3.13	
3 s	30°C	4+4+4	1300x150 PVB	1500	13.3	9.05	9.05	3.82; 3.88; 3.75
					13.287	9.02	9.02	
10y	30°C	4+4+4	1300x150 PVB	1500	7.194	1.43	1.43	
					6.858	1.24	1.24	
3 s	30°C	8+8+8	1300x150 SGP	1500	25.26	61.97	61.99	52.7; 54.35; 57.23
					25.244	61.86	61.87	
10 y	30°C	8+8+8	1300x150 SGP	1500	16.866	18.45	18.46	
					16.337	16.76	16.76	
3 s	30°C	8+8+8	1300x150 PVB	1500	25.233	61.77	61.79	23.09; 19.49; 18.74
					25.212	61.62	61.64	
10 y	30°C	8+8+8	1300x150 PVB	1500	12.952	8.35	8.36	
					12.747	7.96	7.96	

The position of the experimental results within the interval defined by the glassy and rubbery critical load can be seen in the graph in Figure 4.8. For easier comparison, only shell model results are presented because the difference is imperceptible. All values of critical buckling forces from the experiments fit within the limits of the rubbery critical load and glassy critical load, but due to the wide range of the interval and the lack of detailed information on

experimental conditions, the accuracy of the results cannot be fully analysed. However, the behaviour pattern regarding the type of interlayer is similar, the critical buckling force for LG-SGP specimens is closer to the upper limit (i.e. maximal critical buckling force), while the buckling force values for LG - PVB specimens are closer to the mean value of the buckling force interval, this time leaning towards the lower, rubbery limit. For specimens with thinner glass plies (4+4+4), the predicted buckling force is lower, and the size of the critical interval is smaller than for 8+8+8mm plies, which confirms that the interlayer's contribution to the behaviour of the specimen is lower. This results appears for both types of specimens with SGP and PVB interlayers. When increasing the thickness of each glass ply (from 4 mm to 8 mm), the size of the critical interval increases 7.7 times for SGP L1 and 8.6 times for SGP L2 specimens, and 6.9 times for PVB L1 and 7.1 times fro PVB L2 specimens. This enlargement is directly related to the increase of the mean value of the critical buckling interval; the ratio is not linear but is correlated. The presented intervals within which creep buckling can occur are quite large. If the design value of the in-plane load of a structure is set below the lower limit, the structures could be oversized. To reduce the size of the interval, it would be useful to distinguish between the values of long-duration loads and short-duration loads.

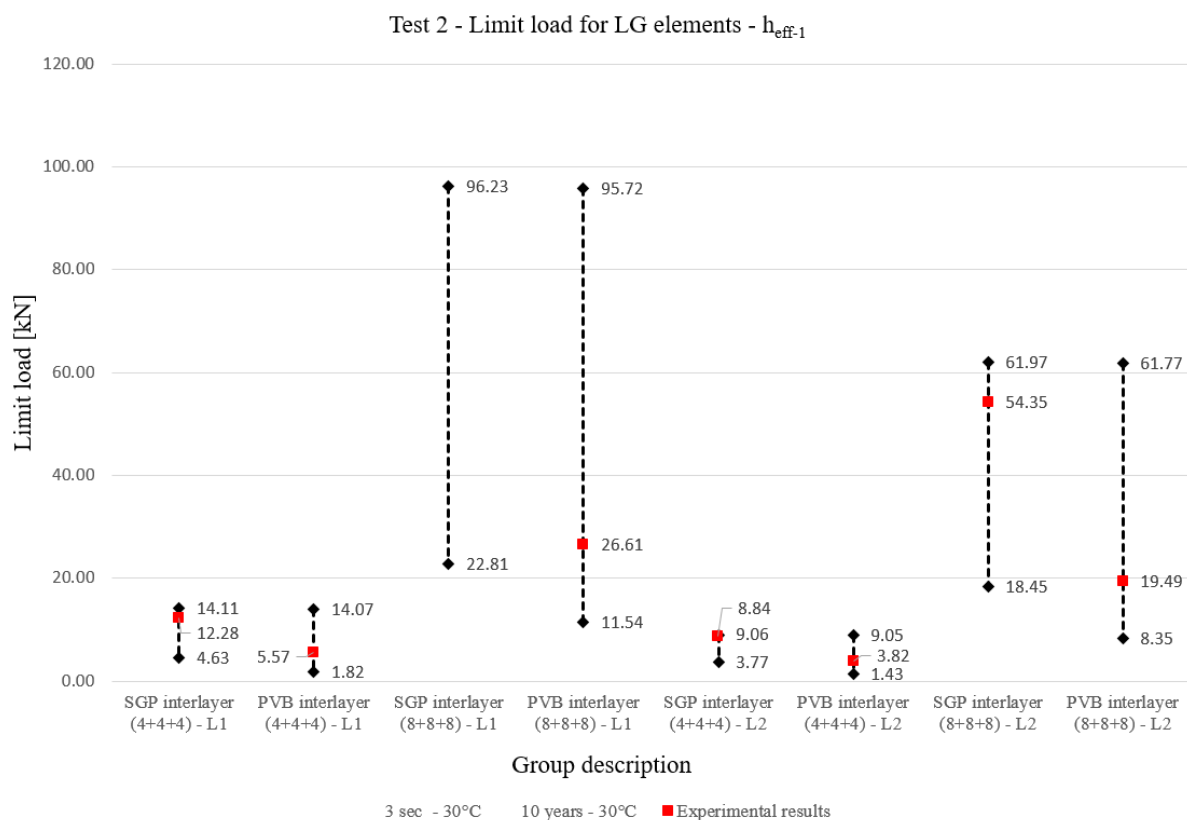


Figure 4.8. Graphical presentation of numerically predicted critical intervals and the experimental result for Test 2

4.4.3. Test 3 – Laminated Glass Elements With Different Boundary Conditions

The third test is related to elements with different boundary conditions (and geometries). For comparison and validation of results, the experimental tests from Foraboschi [123] are simulated. In [123], a total of 52 experimental tests were conducted on annealed laminated glass specimens with three different geometries and boundary conditions (Figure 4.9.).

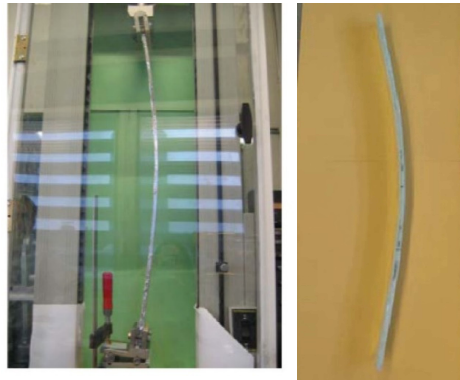


Figure 4.9. Photography of experimental test 3 from [123]

The height and width of the tested specimens are: 1100mm/70mm, 800mm/60mm and 750mm/50mm. The specimens' cross-section is two-ply laminated glass with a PVB interlayer. The thickness of cross-sections is 5mm/4mm + 0,38mm/1,52mm + 5mm/4mm. Experimental tests were conducted at three different loading rates to emphasize the contribution of the visco-elastic nature of the interlayer.

Test durations and loading rates are not explicitly specified for each experimental test, but the authors assign a shear modulus (G_{PVB}) for each specimen. Those shear moduli are used to determine the effective thickness of each specimen and to group them for easier comparison. The specimens are divided into three time groups: Time group 1 corresponds to $G_{PVB} = 0.12MPa$; Time group 2 to $G_{PVB} = 0.87MPa$; and Time group 3 to $G_{PVB} = 1.25MPa$. With this data, the effective thickness is determined, and the values are presented in Tables 4.8. and 4.9. The homogenized cross-section geometry and the specimen geometry (with two boundary conditions) are used to simulate tests in numerical models as presented in Figure 4.10.

The effective thickness determined according to [117] (G. D'Ambrosio and L. Galuppi) and [3]/[120] (regulation / Langosch and Feldmann) provides the same results due to the two-ply laminated glass cross-section for both types of boundary conditions.

4. Stability of laminated glass elements exposed to in-plane loading

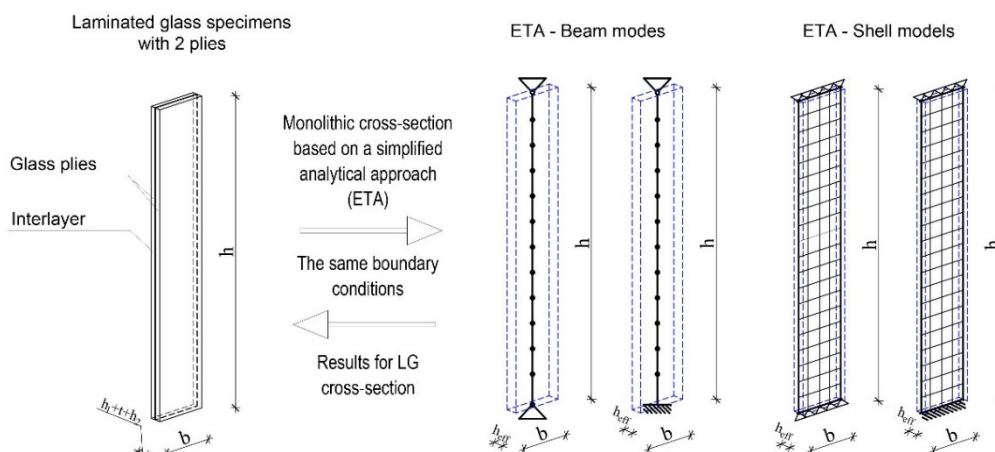


Figure 4.10. Numerical models of Test 3 - implementation of analytical solution into beam and shell numerical model

Table 4.8. Effective thickness for specimens with two-ply LG cross-sections – both sides hinged

PVB interlayer (1100mmx70mm)[123]				PVB interlayer (800mmx60mm) [123]			
Glass panel thickness		5+5mm		Glass panel thickness		5+5mm	
Interlayer thickness		0.38mm/1.52mm		Interlayer thickness		0.38mm/1.52mm	
Type of support				Type of support			
Roller- hinged support				Roller- hinged support			
Material characteristics		h_{eff} (0.38mm)	h_{eff} (1.52mm)	Material characteristics		h_{eff} (0.38mm)	h_{eff} (1.52mm)
G_{PVB}	0.12 MPa	7.413mm	/	G_{PVB}	0.12 MPa	6.987mm	6.591mm
G_{PVB}	0.87 MPa	/	8.505mm	G_{PVB}	0.87/1.25 MPa	8.657/-	-/8.184
PVB interlayer (750mmx50mm) [123]							
Glass panel thickness		4+4mm					
Interlyer thickness		0.38mm/1.52mm					
Type of support				Type of support			
Roller- hinged support							
Material characteristics		h_{eff} (0.38mm)	h_{eff} (1.52mm)				
G_{PVB}	0.12 MPa	5.651mm	5.323mm				
G_{PVB}	0.87/1.25 MPa	7.049/-	-/6.779				

Table 4.9. Effective thickness for specimens with two-ply LG cross-sections – hinged + fixed

PVB interlayer (1100mmx70mm)[123]				PVB interlayer (800mmx60mm) [123]			
Glass panel thickness		5+5mm		Glass panel thickness		5+5mm	
Interlayer thickness		0.38mm/1.52mm		Interlayer thickness		0.38mm/1.52mm	
Type of support				Type of support			
Roller- fixed support				Roller- fixed support			
Material characteristics		h_{eff} (0.38mm)	h_{eff} (1.52mm)	Material characteristics		h_{eff} (0.38mm)	h_{eff} (1.52mm)
G_{PVB}	0.12 MPa	6,945mm	/	G_{PVB}	0.12 MPa	6.673mm	6.448mm
G_{PVB}	0.87 MPa	/	7.717mm	G_{PVB}	0.87/1.25 MPa	7.964/-	-/7.464
PVB interlayer (750mmx50mm) [123]							
Glass panel thickness		4+4mm					
Interlyer thickness		0.38mm/1.52mm					
Type of support				Type of support			
Roller- fixed support							
Material characteristics		h_{eff} (0.38mm)	h_{eff} (1.52mm)				
G_{PVB}	0.12 MPa	5.375mm	5.184mm				
G_{PVB}	0.87/1.25 MPa	6.483/-	-/6.137				

4. Stability of laminated glass elements exposed to in-plane loading

The prediction of the critical buckling force is obtained by using the effective thickness. The values of critical buckling forces are determined for the beam and shell models, and the results are presented in Table 4.10.

Table 4.10 Comparison of experimental results [123] and numerical results for beam and shell models

Time group	Glass plies [mm]	Dimension [mm]	Inter. tick. [mm]	Interl.	λ	h_{eff} [mm]	Shell model	Beam model	Experiments from [123]
							Force (kN)	Force (kN)	Force (kN)
Hinged boundary condition									
1	5+5	1100x70	0.38	PVB	514.03	7.413	1.36	1.36	1.32; 1.3
2	5+5	1100x70	1.52	PVB	448.03	8.505	2.05	2.05	1.58; 1.74
1	5+5	800x60	0.38	PVB	396.63	6.987	1.84	1.85	1.84; 1.86; 2.0
2	5+5	800x60		PVB	320.12	8.657	3.51	3.51	3.01; 3.26; 3.38; 3.48
1	5+5	800x60	1.52	PVB	420.46	6.591	1.55	1.55	1.53; 1.73
3	5+5	800x60		PVB	338.62	8.184	2.96	2.97	2.44; 2.47
1	4+4	750x50	0.38	PVB	459.76	5.651	0.925	0.926	0.93; 0.91; 0.97
2	4+4	750x50		PVB	368.57	7.049	1.795	1.797	1.52; 1.68; 1.71; 1.72
1	4+4	750x50	1.52	PVB	488.08	5.323	0.773	0.774	0.77; 0.83
3	4+4	750x50		PVB	383.25	6.779	1.597	1.598	1.15; 1.30
Hinged + fixed boundary condition									
1	5+5	1100x70	0.38	PVB	384.07	6.945	2.294	2.295	1.89; 1.10
2	5+5	1100x70	1.52	PVB	345.65	7.717	3.15	3.15	2.29; 2.56
1	5+5	800x60	0.38	PVB	290.71	6.673	3.3	3.3	2.47; 2.65; 2.86
2	5+5	800x60		PVB	243.58	7.964	5.61	5.61	4.07; 4.47; 5.05; 5.16
1	5+5	800x60	1.52	PVB	300.85	6.448	2.98	2.98	2.19; 2.40
3	5+5	800x60		PVB	259.90	7.464	4.62	4.62	3.34; 3.63
1	4+4	750x50	0.38	PVB	338.35	5.375	1.63	1.63	1.30; 1.28; 1.33
2	4+4	750x50		PVB	280.53	6.483	2.87	2.88	2.24; 2.39; 2.43; 2.34
1	4+4	750x50	1.52	PVB	350.82	5.184	1.47	1.46	1.06; 1.19
3	4+4	750x50		PVB	296.34	6.137	2.43	2.43	1.43; 1.88

The results for the beam and shell models are almost equal, and compared to the experimental results, a good coincidence can be observed. The relationship between the numerically predicted buckling force and the experimental value from [123] ($F_{numerical}/F_{experimental}$) for different slenderness of the specimen is shown in Figure 4.10. for the hinged boundary conditions, and in Figure 4.11. for the hinged-fixed boundary conditions. The effective slenderness of the specimen λ is calculated using the effective thickness. The mean value of the

buckling forces obtained from the experimental tests (for the same specimens and loading conditions) is used for comparison. Hence, the standard deviation interval (σ) from the experimental forces $\sigma_{L1} = 0.04822$ for buckling length L_1 and $\sigma_{L2} = 0.1616$ for buckling length L_2 is added in the graph so that the discrepancy can be observed through the obtained experimental deviation. This interval of standard deviation serves to acknowledge the accuracy of the buckling force prediction.

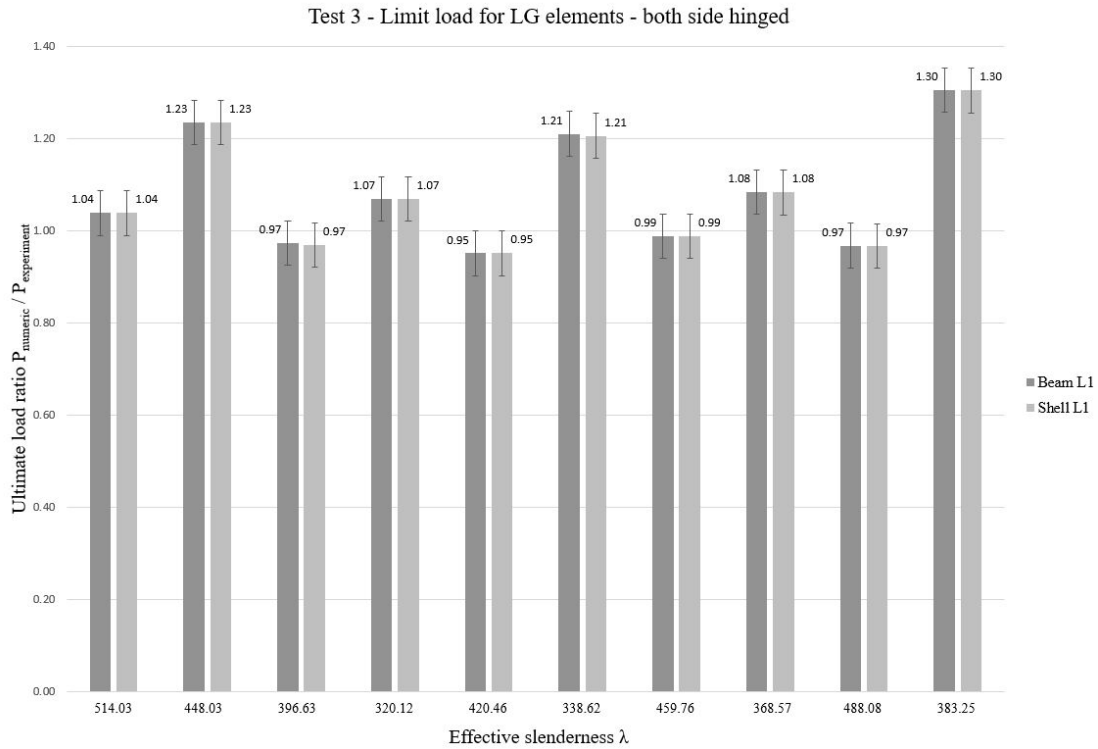


Figure 4.11. Graphical presentation of the ratio between the numerically predicted critical force and the experimental results ($F_{numerical}/F_{experimental}$) for hinged element– Test 3

The analysis in Figure 4.11. presents the ratio for the case of hinged specimens (buckling length L_1), and it can be seen that half of the results cover the ratio value of 1.0 within the expected interval. For all specimens, the mean value of realized errors between numerically predicted forces and the experimental results is $\Delta(F_{numerical}/F_{experimental}) = 1.081$, which is equal to an 8.1% error with a standard deviation of $\sigma_{L1, F_{nu}/F_{exp}} = 0.1178$. The 95% confidence interval of the prediction is [0.85-1.32]. For the case of fixed-hinged boundary conditions (buckling length L_2), presented in Figure 4.12., the discrepancy is higher. However, the value of the experimental force's standard deviation (σ) is also higher than that for the first case $\sigma_{L2} = 0.1616$. Still, it is not enough to cover the expected ratio of 1.0. In the case of buckling length L_2 , the mean value of realized errors between numerically predicted forces and the

experimental results is equal to $\Delta(F_{numerical}/F_{experimental}) = 1.316$ with a standard deviation of $\sigma_{L2,F_{nu}/F_{exp}} = 0.18295$. From this, the 95% confidence interval is [0.95-1.68], which is not a good predictability of critical buckling force.

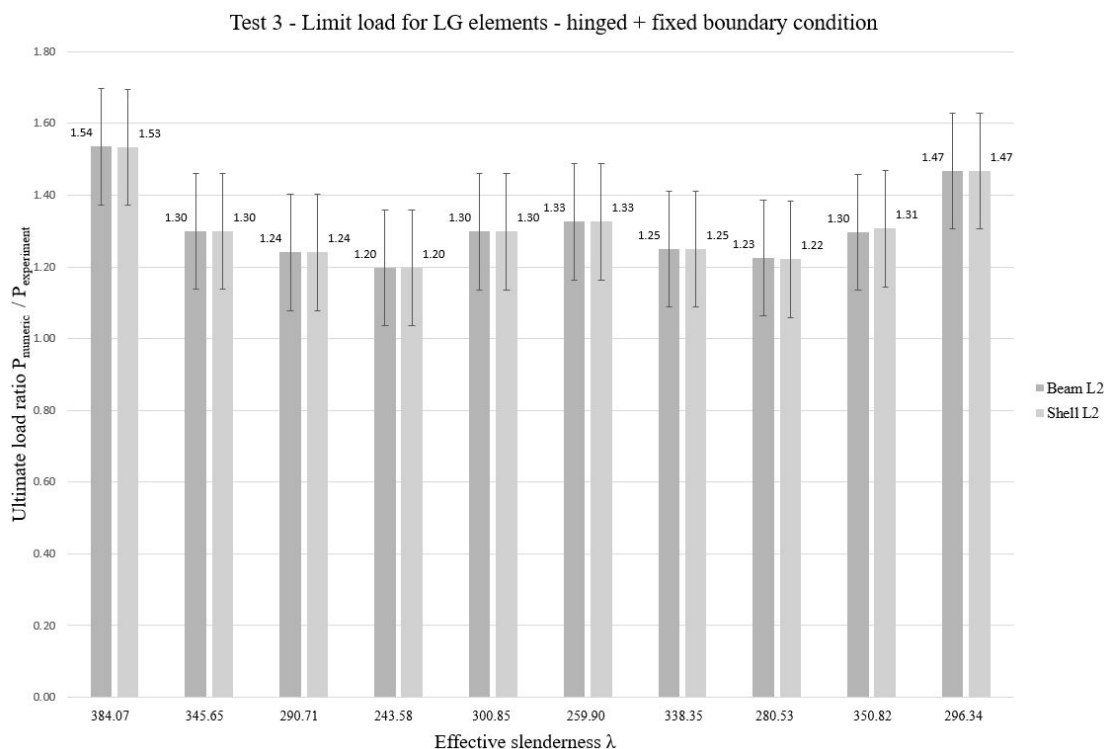


Figure 4.12. Graphical presentation of the ratio between the numerically predicted critical force and the experimental results ($F_{numerical}/F_{experimental}$) for hinged + fixed element – Test 3

When the predictability is observed through the effective slenderness of the specimen λ , there is no correlation between results either in Figure 4.11. or in Figure 4.12. From this test, it can be seen that the force prediction for the hinged boundary condition is slightly overestimated but the error is acceptable (1.081), while in the case of hinge-fixed boundary conditions, the accuracy is much lower, and the confidence interval is wide and does not lead to a ratio of 1.0.

4.5. Chapter Conclusions

In this chapter, the effective thickness approach is tested to define the limits of usage of the method in combination with numerical models that do not consider initial imperfections in LG elements. This approach adopts two simplifications: one by neglecting the influence imperfections, and another by reducing the level of interlayer modelling to Level 2 from [1] by

using the effective thickness approach. This analysis aims to evaluate the potential risks of using this simplified approach and to identify cases where maybe it may not be appropriate.

The analysis was performed for several different geometries of LG specimens, with different types of interlayers and boundary conditions. The load duration and temperature from experimental tests are considered alongside the limit values of load duration (expected for structures) and atmospheric temperatures, which define critical intervals. The observed critical interval is defined by rubbery and glassy critical loads, determined based on interlayer material characteristics. Two numerical models are used in the analysis: one with beam elements and the other with shell elements. As mentioned, the models do not account for initial imperfections. The methods for determining the effective thickness are used according to the literature.

By combining the numerical models with the effective thickness approach, the critical buckling load was determined for glassy and rubbery limits, as well as for experimental conditions, and the results were compared. The predicted critical buckling force from this simplified approach is within the range of expected values, confirmed by assigning the confidence interval obtained from the experimental results (in cases where there are several experimental tests for the same specimen geometry) to the numerically determined value of critical buckling force.

The analyses showed different values of buckling forces for glass elements with different types of interlayers (and the same geometry and boundary conditions) or different numbers of glass plies. The results for the SGP interlayer show better buckling resistance, consistent with experimental tests, while for the PVB interlayer, the results fit within the critical interval of buckling load.

The difference between the results from the numerical models with beam and shell elements is almost negligible. This is expected due to the simplicity of boundary conditions and the geometrical ratio, where the width is approximately 1/10 of the length for the tested specimens. There is no noticeable difference in the accuracy of the predicted buckling force concerning the different slenderness of the elements, but this is valid only for the tested slenderness that fits in intervals of $\lambda \sim [220 \rightarrow 500]$. Regarding boundary conditions, there is slightly less accurate predictability for the case of fixed+hinged support compared with hinged+hinged support boundary conditions.

It can be concluded that, considering the number of simplifications regarding the homogenization of cross-sections and neglecting the initial imperfections, the obtained results are quite accurate and provide a reliable estimate of the structural resistance of laminated glass elements to the in-plane loading. One advantage of this numerical modeling with an effective thickness approach is the possibility of testing different combinations of parameters such as the

number of glass and interlayer plies, type of interlayer, and boundary condition with minimal computational cost. This analysis is useful for evaluating the potential risks of using the simplified approach and for precisely defining its limits for daily engineering practice.

The next step in our analysis is to include the initial imperfections and test the improvement of predictability by using the effective thickness approach. Also, not all simplified approaches offered by regulations are tested, and other combinations should be considered to test the accuracy and limits of usage.

5. OVERVIEW OF RESEARCH RESULTS

Contents

- 5.1. Summary of all Conducted Research
 - 5.2. Overview of Research Results
-

5.1. Summary of all Conducted Research

This thesis addresses three fields which are currently a topic of interest in the field of laminated glass structures. Each of these topics has resulted in published papers [12][23][15], and some parts are still in development and will be completed and published later.

The research begins with Chapter 2, where the influence of atmospheric temperatures and load duration on laminated glass structures is tested. The focus of this research is to analyse the stiffness degradation of LG members exposed to higher temperatures within the range of atmospheric temperatures and various load durations. Numerical models, previously validated with experimental results, are used to obtain the results. In the experiments, specimens are tested until fracture, while in numerical analysis, fracture is not simulated due to the lack of methods that could reliably describe the nonlinear behaviour of the glass part of the elements. The chosen test is defined according to regulation EN 1288-3 [24] so that the results can be comparable with the other results from the literature. The analysis is further extended to a simplified engineering approach (ETA), where the accuracy of predicting stress and deflection under assigned loads is tested within the range of atmospheric temperatures. Simplified expressions for the analytical determination of deflection are tested to assess their capability to predict deflections for LG members regarding expected temperature and load duration over the construction lifetime. One representative panel geometry was selected, for which the bearing capacity was tested numerically, and effective thicknesses were calculated according to five different expressions.

In Chapter 3 a model for simulation of non-linear behaviour of laminated glass members exposed to static load is presented. The shortcomings in the simulation of fracture in laminated glass members identified in the previous analysis (with commercial software) are solved here. The simulation of laminated glass fracture for structures exposed to static loads is achieved using the embedded discontinuity method on two scales. For static loading, there are not many numerical methods that can accurately predict the nonlinear behaviour of brittle materials, and those capable of it usually require defining an initial crack. Simulating the initial crack is not consistent with the nature of glass material because this type of analysis primarily observes crack propagation, and an initial crack in glass elements typically means the failure of the whole element (especially in tempered glass). The solution is found using the embedded discontinuity method, which can simulate crack appearance in solids without the need for initial cracks. By using the embedded discontinuity method, a multiscale model is developed, capable of simulating the ultimate load for laminated glass elements without simulation of detailed fracture

pattern. The model consists of a micro model that simulates a real laminated glass cross-section and a macro model that is a monolithic cross-section with assigned material behaviour according to the micro model. This model is further extended for plate structures using discrete Kirchhoff plate theory and a constitutive model for principal directions of internal forces / stresses. The basic micro model is used to define the constitutive behaviour, but this time for the principal directions of macro plate elements.

In Chapter 4, research related to in-plane loaded laminated glass elements and the combination of a simple numerical model with Level 2 of interlayer modelling is conducted. The simplified engineering approach (ETA) from regulations and literature is analysed regarding the predictability of buckling forces for in-plane loaded laminated glass members. Two numerical models are used: one with beam elements and the other with shell elements. Both models are not developed in this work, but are used as tools. The analysis was performed for several different geometries of LG specimens, with different types of interlayers and different boundary conditions. The buckling force prediction is validated by comparing the results with experimental data from the literature for different cases of geometry, interlayers and boundary conditions.

5.2. Overview of Research Results

Since the work is divided into three parts (Chapters 2, 3 and 4) and each chapter includes its own conclusions, this section will only provide an overview of all results. For detailed insight, the reader should refer to the relevant chapter.

Fracture is an undesirable event in the lifetime of a structure, so it is necessary to establish a safety margin from critical stress values under normal conditions. By considering the material characteristics of the interlayer and applying those to numerical models, it has been proven that the bearing capacity of laminated glass structures is significantly affected by atmospheric temperature fluctuations, load type, and load duration. This impact depends on the type and thickness of the interlayer.

For tested the structural PVB (Saflex DG41) it is proven that for the thickness of $t=0.76$ mm, fixed loading, and a temperature increase of only 5 °C (from 25 °C to 30 °C) the decrease in moment of inertia is approximately $\Delta I_{eff} = 2.072cm^4$ ($I_{eff,25^\circ C} = 6.919cm^4$; $I_{eff,30^\circ C} = 4.847cm^4$), resulting in a deflection increase $\Delta_w = 1.479$ mm and a stress increase in the bottom tensile ply of $\Delta_\sigma = 2.747MPa$. For the same interlayer (PVB Saflex DG41), temperature interval, and loading conditions, but with a thickness of $t=1.52$ mm, the increase

in deflection is equal to $\Delta_w = 1.562 \text{ mm}$ and the increase in stress in the bottom tensile ply is $\Delta_\sigma = 2.747 \text{ MPa}$. For the highest considered value of PVB interlayer thickness of $t=2.28 \text{ mm}$ (6 layers) under a fixed load, and a temperature increase of only $5 \text{ }^\circ\text{C}$, the decrease in moment of inertia (or stiffness for multiplied with fixed E) is approximately $\Delta_{I_{eff}} = 1.36 \text{ cm}^4$ ($I_{eff,25^\circ\text{C}} = 5.181 \text{ cm}^4$; $I_{eff,30^\circ\text{C}} = 3.821 \text{ cm}^4$), resulting in a deflections increase of $\Delta_w = 1.645 \text{ mm}$ and a stress increase in the bottom tensile ply of $\Delta_\sigma = 3.665 \text{ MPa}$. These values, although they may seem small, are significant given that the total load was only 1 kN , much lower than the ultimate load of approximately 8.8 kN . Hence, the stiffness degradation is approximately 30% of $I_{eff,25^\circ\text{C}}$ for thickness $t = 0.76 \text{ mm}$, and 27% of $I_{eff,25^\circ\text{C}}$ for $t = 2.28 \text{ mm}$. These values were calculated for a load duration of 24 hours, and temperature (from $25 \text{ }^\circ\text{C}$ to $30 \text{ }^\circ\text{C}$) indicating that the increased thickness of the interlayer still has a slightly positive effect for LG members with PVB interlayer.

For structure with an ionoplast interlayer, under a fixed load, and a temperature increase of $5 \text{ }^\circ\text{C}$ (from $25 \text{ }^\circ\text{C}$ to $30 \text{ }^\circ\text{C}$) the decrease in moment of inertia is approximately $\Delta_{I_{eff}} = 0.244 \text{ cm}^4$ ($I_{eff,25^\circ\text{C}} = 11.781 \text{ cm}^4$; $I_{eff,30^\circ\text{C}} = 11.537 \text{ cm}^4$) for a thickness of $t=0.89 \text{ mm}$, resulting in a deflection increase of $\Delta_w = 0.043 \text{ mm}$ and a stress increase in the bottom tensile ply of $\Delta_\sigma = 0.17 \text{ MPa}$. For the same interlayer, temperature interval, and loading conditions, but with a thickness of $t=1.52 \text{ mm}$, the deflection increase is to $\Delta_w = 0.066 \text{ mm}$ and the stress increase in the bottom tensile ply is $\Delta_\sigma = 0.238 \text{ MPa}$. For the highest value of SGP interlayer thickness of $t=2.28 \text{ mm}$, under a fixed load and a temperature increase of only $5 \text{ }^\circ\text{C}$, the decrease in moment of inertia is approximately $\Delta_{I_{eff}} = 1.36 \text{ cm}^4$ ($I_{eff,25^\circ\text{C}} = 13.146 \text{ cm}^4$; $I_{eff,30^\circ\text{C}} = 12.482 \text{ cm}^4$), resulting in a deflections increase of $\Delta_w = 0.097 \text{ mm}$ and a stress increase in the bottom tensile ply of $\Delta_\sigma = 0.24 \text{ MPa}$. The results for LG members with ionoplast interlayer show significantly stiffer behaviour compared to those with PVB interlayer. The stiffness decrease for LG members with ionoplast interlayer is approximately 2% of $I_{eff,25^\circ\text{C}}$ for $t = 0.89 \text{ mm}$, and 1% of $I_{eff,25^\circ\text{C}}$ for $t = 2.28 \text{ mm}$.

Increasing the thickness of the ionoplast interlayer makes the LG structure stiffer, even at high atmospheric temperatures. These observations, presented in detail in Chapter 2, are crucial for selecting the appropriate interlayer type, as well as proper structural dimensions and boundary conditions. It is proven that within the range of $0 \text{ }^\circ\text{C}$ to $50 \text{ }^\circ\text{C}$, interlayers undergo significant change in mechanical characteristics, decreasing structural stiffness (at higher temperatures). When designing laminated glass structures, it is essential to consider temperature changes

specific to geographic and other conditions (heating regime, influence of radiation). In addition to temperature, the load-bearing capacity of interlayers also depends on load duration.

Simplified expressions for the analytical determination of deflection and stress prediction are tested to assess their capability to predict deflections for LG members considering expected temperatures during the construction lifetime. From the results, it is concluded that the most reliable predictions come from the expressions in Table 2.5., defined in the draft version of European regulation CEN/TS 19100-2:2021 [2]. This prediction reliably accounts for increases and decreases in element stiffness (deflection) due to temperature changes. Expressions according to Wölfel–Bennison [57] and L. Galuppi et al. [31] provide more accurate results, closely matching numerical ones, but slightly overestimate the stiffness of the panel.

Furthermore, the simulation of laminated glass fracture behaviour is accurately predicted with the proposed multiscale model. Compared to various experimental results, it is shown that the model provides reliable predictions. The multiscale model combines a fine-scale multilayer model with a coarse-scale macro model to achieve accuracy and high computational efficiency. The presented model is complex due to the two scales used for detailed simulation, but its biggest advantage is the minimal amount of required inputs. Only the pure tensile strength, pure compressive strength, and modulus of elasticity (together with the geometry of structure and load type) are necessary to establish a robust model with excellent predictability of the structural response of laminated glass structures. Unlike other methods used for fracture simulation of laminated glass (such as XFEM, FEM-DEM, cohesive zone, DEM, etc.), this model simulates behaviour under static load without the need to introduce an initial crack. By comparing the numerical results with four different experimental test results, the model's good predictability is proven with minimal input information. The limits of the multiscale model are defined by the limits of the beam element. This type of element doesn't support the possibility of boundary conditions in other directions or different load shapes that change through the width of the element. To overcome the limits of beam elements in the multiscale model, a new macro model 2 is presented. This model is an upgrade in the aspect of overcoming limits in load shape and different boundary conditions. It also simplifies failure prediction and the simulation of the element softening phase, reducing it to critical zone detection. Only preliminary results for this model are presented to introduce its expected advantages regarding different load shapes and boundary conditions.

Furthermore, the effective thickness approach is tested for laminated glass members loaded in-plane. The predictability of this approach, which adopts two simplifications, is tested. The first simplification neglects imperfections in the numerical model, and the second reduces the level

of interlayer modelling to Level 2 from [1] by using the effective thickness approach. This analysis evaluates the potential risks of using the simplified approach and tests cases where it may not be appropriate. Two numerical models are used in the analysis, one with beam elements and the other one with shell elements, to observe differences in results for different types of elements. The results show that for tested elements with high slenderness ($\lambda \sim [220 \rightarrow 500]$), the predictions slightly overestimate the buckling force. In cases where the predicted buckling force is most overestimated (such as Test 3 for fixed-hinged boundary conditions) the mean error was 31.6% of the achieved buckling force when comparing the predicted numerical force and the mean experimental results. However, when the discrepancy interval of experimental results is included, this error decreases to 15.5% of the achieved buckling force. The mean error in other tests is 8.1% for Test 3 with hinged-hinged boundary conditions and 7% of accomplished buckling force for Test 1. The models with beam and shell elements provide similar results, with less than 1.5% difference, and the results remain consistent across different mesh sizes. Besides exact prediction, a critical interval was observed with the upper and lower values defined by interlayer material characteristics for limit values of temperature and load duration in the regular usage regime. The limits of this observed critical interval are defined as “rubbery” and “glassy” critical load. The numerical predictions and experimental results from literature for laminated glass specimens with PVB interlayers fit within critical interval, while the numerical and experimental results for specimens with SGP (ionoplast) interlayers exceeded the interval (on the safety side) and showed greater stiffness than calculated. These results indicate that the interlayer significantly influences the bearing capacity of slender laminated glass specimens, and the critical interval spans covers a wide range of critical buckling forces. The results also show that the number of plies increases the buckling resistance and that in the case of boundary condition fixed + hinged (each on one side) the predictability of critical buckling force is slightly less accurate. The mean value of ratios of numerical to experimental forces ($F_{numerical}/F_{experimental}$) for both-side hinged boundary conditions is 1.081, while the mean ratio for fixed-hinged conditions is 1.316. Overall, the results for the SGP interlayer show better buckling resistance, consistent with experimental tests, while the PVB interlayer, results fit within the critical interval of buckling load. When the accuracy of predicted forces is observed through the slenderness of tested specimens, no specific dependence or rule is noticed. This observation is valid only for the slenderness interval of observed elements that are equal $\lambda \sim [220 \rightarrow 500]$. Regarding the number of simplifications adopted in this test, the obtained results are quite accurate and provide a reliable estimate of the structural resistance of laminated glass members exposed to in-plane loading. The advantage of this approach is the possibility

of testing different combinations of parameters such as the number of glass and interlayer plies, type of interlayer, and boundary condition, all with minimal computational cost. This analysis proves that the potential risks of the simplified approach are low and that it can be considered for daily engineering practice with safety factors included.

6. CONCLUSION AND FURTHER PERSPECTIVES

Contents

6.1. Conclusions Based on the Obtained Results

6.2. Future Perspectives

6.1. Conclusions Based on the Obtained Results

Based on the results of conducted research, there are several proposals related to improvements in the current method of calculating laminated glass structures. For the design of laminated glass structures, it is important to pay attention to the choice of the interlayer. In cases where the expected useful load duration is short (less than 24h, such as a pedestrian bridge in a closed space or with a canopy), and no significant amount of permanent load is expected, and the boundary conditions do not provide stress concentrations, structural interlayers based on polyvinyl butyral would satisfy the demands and provide enough stiffness. For this case, if a small amount of dynamic load occurs, this type of interlayer will provide a favourable damping effect due to its “softer” behaviour compared to ionoplast structural interlayers. To determine the value of critical stress that can appear in this type of structure, it is necessary to consider the highest value of the expected temperature and the highest load duration. However, in cases where most of the design load is a permanent load or where structures are exposed to climatic loads such as snow or insolation, ionoplast interlayers are a better choice due to their stiff behaviour under high load durations, even when temperatures increase up to 40 °C. Simplified engineering approaches offered by regulations should be used with caution. The values of effective thickness should also be determined by considering the temperature regime, load durations, boundary conditions, and load type. For properly determining the boundary condition from joints in glass structures, it is necessary to be familiar with the deformability of sleeve bearings and additional protective rubber (in clamped joints) to establish if the connection is closer to a fixed boundary condition or if some rotation is enabled. The most reliable results, when temperature changes are analysed (for > 24h load duration), are ensured by the expression from the draft version of the new European regulation CEN/TS 19100-2:2021 [2], which mostly appears on the side of safety with a tendency to slightly underestimate the capacity of the structure.

The lack of numerical methods for predicting the fracture of laminated glass elements under static load is solved by using the embedded discontinuity method within a multi-scale approach. This model enables accurate prediction of fracture load for layered cross-sections. The micro model provides a specific type of constitutive law defined with the moment-curvature relationship derived from a true LG cross-section using only basic material properties, defined solely for the axial direction (tensile strength, compressive strength, and modulus of elasticity). The determined constitutive law is used as input information for the macro model, which has a homogenized cross-section and material characteristics defined by the micro model. The main

idea of this approach is similar to the effective thickness approach. The difference is that in the effective thickness approach, the stiffness of the element is reduced by reducing the height, while in this micro-macro relationship from the multiscale model, material characteristics are changed and applied to the homogenized cross-section of the same height as the observed LG cross-section. The combination of this multiscale model with an effective thickness approach was tested, but the results were not satisfactory, which is somewhat expected. By applying reduced height (determined by ETA) in the macro model, the element appears too softened because two reductions are applied: one from ETA and another by deriving substitutive material behaviour.

The effective thickness approach has proved to be a good choice when determining the in-plane resistance of laminated glass elements. Again, it is necessary to reconsider the observed structure and determine the critical interval regarding expected temperature and load duration in regular usage.

The basic features and scientific contributions of this dissertation are:

- presentation of the influence of external factors (temperature and load duration) on the load capacity of laminated glass structures and the influence of the thickness and type of interlayer in combination with temperature and different load durations
- a new multiscale model that simulates the fracture of laminated glass structures within the finite element method without the need for an initial crack
- a new multiscale model for the determination of material-constructive connections in laminated glass construction
- parametric analysis of the simplified engineering calculation "Effective thickness approach" for predicting deflection in structures loaded out of the plane
- parametric analysis of the simplified engineering calculation "Effective thickness approach" for predicting the loss of stability of in-plane loaded structures

6.2. Future Perspectives

Each of the presented topics opens several directions for future research, the focus is on two directions. The first is related to extending the multiscale model to the plate element. This model is presented in Chapter 2, and the beam elements provide satisfactory results compared to experimental tests from different authors. However, to overcome limits in aspects of load, geometry, and boundary conditions, the next step is to extend this model to the plate elements. This model uses the same micro model as the presented multiscale model but has a macro model

with plate elements. For the first step, a simplification in simulating fracture in the macro model is introduced, where the embedded discontinuity method is replaced with the redistribution of internal forces through the elements without entering the softening zone. This approach enables the determination of critical zones. The greatest challenge in establishing this model so far is ensuring a proper connection between the beam micro model elements and the plate macro model elements. In the previous multiscale model, this was done through a representative beam element, and the connection provided satisfactory results. However, for the new macro model, the connection needs to be established on the beam–plate level, more precisely on the beam – principal axes of the plate level. This task is still in the development phase, and once it is solved, it will open the path to testing various geometries with complex load shapes and boundary conditions.

The second direction of future research is related to in-plane loaded elements. This analysis is currently in its early phases, with only the most simplified method tested so far. The next step in analysis is to include the initial imperfection and test the improvement of predictability by using the effective thickness approach. Additionally, other simplified approaches offered by literature will be tested and compared with planned experimental tests. The experimental tests are planned for several load durations for both side fixed boundary conditions at room temperatures. The influence of boundary conditions on increasing the impact of imperfections needs to be tested in this field because analysis has shown that introducing the imperfection is not a crucial factor for the accuracy of buckling forces prediction. Since in analysis, most boundary conditions were hinged specimens (at least on one side), there is a possibility that for both sides fixed, the results would not be as accurate.

7. BIBLIOGRAPHY

Contents

- 7.1. Bibliography
 - 7.2. List of Figures
 - 7.3. List of Tables
 - 7.4. List of Published Papers
 - 7.5. List of Attended Conferences
-

7.1. Bibliography

- [1] CEN/TS 19100-1, *Design of glass structures - Part 1: Basis of design and materials Conception*. 2021.
- [2] CEN/TS 19100-2, *Design of glass structures - Part 2: Design of out-of-plane loaded glass components*. 2021.
- [3] CEN/TS 19100-3, *Design of glass structures - Part 3: Design of in-plane loaded glass components and their mechanical joints*. 2021.
- [4] A. Berenjjan and G. Whittleston, "History and Manufacturing of Glass," *American Journal of Materials Science*, vol. 7, no. 1, pp. 18–24, 2017, doi: 10.5923/j.materials.20170701.03.
- [5] M. Hasanuzzaman, A. Rafferty, M. Sajjia, and A. G. Olabi, *Properties of Glass Materials*. Elsevier Ltd., 2016.
- [6] P. Amal, *Chemistry of glasses*. Springer, 1990.
- [7] L. F. Francis, *Materials Processing: A Unified Approach to Processing of Metals, Ceramics and Polymers*. Elsevier, 2016.
- [8] M. Lindqvist, "Structural Glass Strength Prediction Based on Edge Flaw Characterization," *École Polytechnique Fédérale de Lausanne*, 2013.
- [9] A. A. Griffith, "The Phenomena of Rupture and Flow in Solids," *Philosophical Transactions of the Royal Society of London. Series A, Containing Papers of a Mathematical or Physical Character*, vol. 221, pp. 163–198, 1921, doi: 10.1098/rsta.1921.0006.
- [10] G. R. Irwin and D. C. Washington, "Analysis of stresses and strains near the end of a crack traversing a plate," *J. Applied Mechanics*, vol. 24, pp. 361–364, 1957.
- [11] D. Kinsella, "Modelling of annealed glass fracture," *Lund university*, 2018.
- [12] M. Galic, G. Grozdanic, V. Divic, and P. Marovic, "Parametric Analyses of the Influence of Temperature, Load Duration, and Interlayer Thickness on a Laminated Glass Structure Exposed to Out-of-Plane Loading," *Crystals*, 2022, doi: <https://doi.org/10.3390/cryst12060838>.
- [13] CEN, *prEN 13474-3 - Glass in building - Determination of the strength of glass panes - Part 3: General method of calculation and determination of strength of glass by testing*. 2009.
- [14] CEN European Committee for Standardization, *Guidance for European Structural Design of Glass Components*. 2014.
- [15] G. Grozdanic, M. Galic, and P. Marovic, "Some aspects of the analyses of glass structures exposed to impact load," *Coupled Systems Mechanics*, vol. 10, no. 6, pp. 475–490, 2021, doi: 10.12989/csm.2021.10.6.475.
- [16] X. Wang, J. Yang, X. Huang, F. Wang, and Y. Zhu, "Voronoi-FDEM concept for modelling post-fracture response of progressively damaged structural glass," *Engineering with Computers*, no. 0123456789, 2021, doi: 10.1007/s00366-021-01318-6.
- [17] I. Stelzer and M. Singh Rooprai, "Post breakage strength testing for overhead laminated glass," *Challenging Glass Conference Proceedings - Challenging Glass 5: Conference on Architectural and Structural Applications of Glass*, no. June, pp. 391–398, 2016.
- [18] L. Biolzi, S. Cattaneo, and M. Simoncelli, "Post-failure behavior of 2-ply laminated glass plates with different interlayers," *Engineering Fracture Mechanics*, vol. 268, p. 108496, 2022, doi: 10.1016/j.engfracmech.2022.108496.
- [19] L. Biolzi, E. Cagnacci, M. Orlando, L. Piscitelli, and G. Rosati, "Long term response of glass-PVB double-lap joints," *Composites Part B: Engineering*, vol. 63, pp. 41–49, 2014, doi: 10.1016/j.compositesb.2014.03.016.
- [20] T. Hána, M. Vokáč, M. Eliášová, and K. V. Machalická, "Experimental investigation of temperature and loading rate effects on the initial shear stiffness of polymeric interlayers," *Engineering Structures*, vol. 223, 2020, doi: 10.1016/j.engstruct.2020.110728.

- [21] CEN EN 16613, “EN 16613 - Glass in building - Laminated glass and laminated safety glass - Determination of interlayer viscoelastic properties,” 2019.
- [22] CEN EN 16612, *EN 16612 - Glass in building — Determination of the lateral load resistance of glass panes by calculation*. 2019.
- [23] G. Grozdanic, A. Ibrahimbegovic, M. Galic, and V. Divic, “Multiscale beam model for simulating fracture in laminated glass structures,” *Engineering Fracture Mechanics*, vol. 292, 2023, doi: 10.1016/j.engfracmech.2023.109606.
- [24] EN 1288-3, *EN 1288-3 - Glass in building — Determination of the bending strength of glass — Part 3: Test with specimen supported at two points (four point bending)*. 2016.
- [25] J. Schmidt, A. Zemanová, J. Zeman, and M. Šejnoha, “Phase-Field Fracture Modelling of Thin Monolithic and Laminated Glass Plates under Quasi-Static Bending,” *Materials*, vol. 13, pp. 1–29, 2020, doi: 10.3390/ma13225153.
- [26] X. Zhang *et al.*, “Impact Response of Laminated Glass with Varying Interlayer Materials,” *International Journal of Impact Engineering*, 2020, doi: <https://doi.org/10.1016/j.ijimpeng.2020.103505>.
- [27] T. Serafinavičius, A. K. Kvedaras, and G. Sauciuvenas, “Bending Behavior of Structural Glass Laminated With Different Interlayers,” *Mechanics of Composite Material*, vol. 49, no. 4, pp. 437–446, 2013.
- [28] M. Timmel, S. Kolling, P. Osterrieder, and P. A. Du Bois, “A finite element model for impact simulation with laminated glass,” *International Journal of Impact Engineering*, vol. 34, pp. 1465–1478, 2007, doi: 10.1016/j.ijimpeng.2006.07.008.
- [29] J. Pelfrene, J. Kuntsche, S. Van Dam, W. Van Paepegem, and J. Schneider, “Critical assessment of the post-breakage performance of blast loaded laminated glazing : Experiments and simulations,” *International Journal of Impact Engineering*, vol. 88, pp. 61–71, 2016, doi: 10.1016/j.ijimpeng.2015.09.008.
- [30] K. Pankhardt and G. L. Balázs, “Temperature dependent load bearing capacity of laminated glass panes,” *Periodica Polytechnica Civil Engineering*, vol. 1, pp. 11–22, 2010.
- [31] L. Galuppi and G. F. Royer-Carfagni, “Effective thickness of laminated glass beams: New expression via a variational approach,” *Engineering Structures*, vol. 38, pp. 53–67, 2012, doi: 10.1016/j.engstruct.2011.12.039.
- [32] A. Van Duser, A. Jagota, and S. J. Bennison, “Analysis of Glass/Polyvinyl Butyral Laminates Subjected to Uniform Pressure,” *JOURNAL OF ENGINEERING MECHANICS*, no. April, pp. 435–442, 1999.
- [33] T. Serafinavičius, J. Lebet, C. Louter, T. Lenkimas, and A. Kuranovas, “Long-term laminated glass four point bending test with PVB , EVA and SG interlayers at different temperatures,” *Procedia Engineering*, vol. 57, pp. 996–1004, 2013, doi: 10.1016/j.proeng.2013.04.126.
- [34] C. Louter, J. Belis, F. Veer, and J. P. Lebet, “Durability of SG-laminated reinforced glass beams: Effects of temperature, thermal cycling, humidity and load-duration,” *Construction and Building Materials*, vol. 27, no. 1, pp. 280–292, 2012, doi: 10.1016/j.conbuildmat.2011.07.046.
- [35] T. Hána *et al.*, “Experimental and Numerical Study of Viscoelastic Properties of Polymeric Interlayers Used for Laminated Glass : Determination of Material Parameters,” *Materials*, vol. 12, 2019, doi: 10.3390/ma12142241.
- [36] T. Hána, M. Eliášová, K. Machalická, and M. Vokáč, “Determination of PVB interlayer’s shear modulus and its effect on normal stress distribution in laminated glass panels,” 2017, doi: 10.1088/1757-899X/251/1/012076.
- [37] L. Biolzi, S. Cattaneo, M. Orlando, L. Ruggiero, and P. Spinelli, “Constitutive relationships of different interlayer materials for laminated glass,” *Composite Structures*, vol. 244, no. March, 2020, doi: 10.1016/j.compstruct.2020.112221.
- [38] G. Grozdanic, A. Ibrahimbegovic, and M. Galic, “Different Approaches in Analyses and Modelling Laminated Glass Elements Exposed to Static Load,” in *PROCEEDINGS 6 th International Conference on Computational Methods for Solids and Fluids*, 2023, pp. 90–92.

- [39] R. Iwasaki, C. Sato, J. L. Latailladeand, and P. Viot, “Experimental study on the interface fracture toughness of PVB (polyvinyl butyral)/ glass at high strain rates,” *International Journal of Crashworthiness*, vol. 12, pp. 293–298, 2013, doi: 10.1080/13588260701442249.
- [40] G. Molnár, L. G. Vigh, G. Stocker, and L. Dunai, “Finite element analysis of laminated structural glass plates with polyvinyl butyral (PVB) interlayer,” *Periodica Polytechnica Civil Engineering*, vol. 1, pp. 35–42, 2012.
- [41] “Mechanical Properties of Laminated Glass : FEM Study About Saflex.”
- [42] Kuraray, “SentryGlas ® Ionoplast Interlayer-Elastic Properties (SG5000),” Available online: https://www.trosifol.com/fileadmin/user_upload/technical_information/downloads/sentryglas/150129_Kuraray_TM_Datenblatt_SG.pdf (accessed on 29 January 2022). .
- [43] M. Novotný and B. Poot, “Influence of Temperature on Laminated Glass Performances Assembled with Various Interlayers,” in *Challenging Glass Conference Proceedings - Challenging Glass 5: Conference on Architectural and Structural Applications of Glass*, 2016, no. June, pp. 219–232.
- [44] X. Centelles, M. Martín, A. Solé, J. R. Castro, and L. F. Cabeza, “Tensile test on interlayer materials for laminated glass under diverse ageing conditions and strain rates,” *Construction and Building Materials*, vol. 243, 2020, doi: 10.1016/j.conbuildmat.2020.118230.
- [45] P. A. Hooper, B. R. K. Blackman, and J. P. Dear, “The mechanical behaviour of poly (vinyl butyral) at different strain magnitudes and strain rates,” *Journal of Materials Science*, vol. 47, pp. 3564–3576, 2012.
- [46] X. Zhang, H. Hao, Y. Shi, and J. Cui, “The Mechanical Properties of Polyvinyl Butyral (PVB) at High Strain Rates,” *Construction and Building Materials*, vol. 93, pp. 404–415, 2015, doi: <https://doi.org/10.1016/j.conbuildmat.2015.04.057>.
- [47] M. L. Aenlle, A. Noriega, and F. Pelayo, “Mechanical characterization of polyvinyl butyral from static and modal tests on laminated glass beams,” *Composites Part B*, 2019, doi: 10.1016/j.compositesb.2019.03.077.
- [48] M. Schuster, M. Kraus, J. Schneider, and G. Siebert, “Investigations on the thermorheologically complex material behaviour of the laminated safety glass interlayer ethylene-vinyl-acetate,” *Glass Structures and Engineering*, vol. 3, no. 2, pp. 373–388, 2018, doi: 10.1007/s40940-018-0074-9.
- [49] M. Baric, M. Galic, N. Stipanelov, and G. Siebert, “Determination of the relationship between the chemical properties of different interlayers and their mechanical resistance in laminated glass structures exposed to different loads,” in *Glass Performance Days*, vol. 119, Tampere, 2023, p. 2023.
- [50] L. Sable, D. Kinsella, and M. Kozłowski, “Influence of EVA , PVB and Ionoplast Interlayers on the Structural Behaviour and Fracture Pattern of Laminated Glass,” *International Journal of Structural Glass and Advanced Materials Research*, vol. 3, 2019, doi: 10.3844/sgamrsp.2019.62.78.
- [51] M. Kraus, M. Schuster, J. Kuntsche, G. Siebert, and J. Schneider, “Parameter identification methods for visco- and hyperelastic material models,” *Glass Structures and Engineering*, vol. 2, no. 2, pp. 147–167, 2017, doi: 10.1007/s40940-017-0042-9.
- [52] L. Andreozzi, S. Briccoli Bati, M. Fagone, G. Ranocchiai, and F. Zulli, “Dynamic torsion tests to characterize the thermo-viscoelastic properties of polymeric interlayers for laminated glass,” *Construction and Building Materials*, vol. 65, pp. 1–13, 2014, doi: 10.1016/j.conbuildmat.2014.04.003.
- [53] S. Chen, Y. Lu, Y. Zhang, and X. Shao, “Experimental and analytical study on uniaxial tensile property of ionomer interlayer at different temperatures and strain rates,” *Construction and Building Materials*, vol. 262, p. 120058, 2020, doi: 10.1016/j.conbuildmat.2020.120058.
- [54] G. Castori and E. Speranzini, “Structural analysis of failure behavior of laminated glass,” *Composites Part B: Engineering*, vol. 125, 2017, doi: 10.1016/j.compositesb.2017.05.062.
- [55] M. T. M. Inc., “MatLab.” 2018.
- [56] G. A. F. . Seber and C. J. . Wild, “Nonlinear Regression,” no. ISBN 0-471-47135-6, Hoboken, Ed. John Wiley & Sons, 2003.
- [57] E. Wölfel, “Nachgiebiger Verbund Eine Näherungslösung und deren Anwendungsmöglichkeiten.”

- Stahlbau*, vol. 6, pp. 173–180, 1987.
- [58] I. Calderone, P. S. Davies, S. J. Bennison, H. Xiaokun, and L. Gang, “Effective laminate thickness for the design of laminated glass,” *Glass Processing Days*, pp. 1–3, 2009.
- [59] Buildings Department, “Code of Practice for Structural Use of Glass,” no. 1, 2018, [Online]. Available: <http://www.hfea.gov.uk/docs/CodeOfPracticeold.pdf%0Awww.tsoshop.co.uk>.
- [60] J. Pelfrene, “Numerical Analysis of the Post-Fracture Response of Laminated Glass under Impact and Blast Loading,” Ghent University, 2016.
- [61] X. Xu, D. Wang, M. Zang, and S. Chen, “Development of an intrinsic solid-shell cohesive zone model for impact fracture of windshield laminated glass,” *International Journal of Impact Engineering*, vol. 163, no. April 2021, 2022, doi: 10.1016/j.ijimpeng.2022.104187.
- [62] X. Xu, S. Chen, D. Wang, and M. Zang, “An efficient solid-shell cohesive zone model for impact fracture analysis of laminated glass,” *Theoretical and Applied Fracture Mechanics*, vol. 108, no. January, p. 102660, 2020, doi: 10.1016/j.tafmec.2020.102660.
- [63] D. Wang, S. Chen, W. Xu, M. Zang, and S. Yoshimura, “A computational framework for impact fracture analysis of laminated glass: An extrinsic cohesive shell approach,” *Computers and Structures*, vol. 233, p. 106238, 2020, doi: 10.1016/j.compstruc.2020.106238.
- [64] C. Alter, S. Kolling, and J. Schneider, “An enhanced non-local failure criterion for laminated glass under low velocity impact,” *International Journal of Impact Engineering*, vol. 109, pp. 342–353, 2017, doi: 10.1016/j.ijimpeng.2017.07.014.
- [65] G. Yu *et al.*, “Computation modeling of laminated crack glass windshields subjected to headform impact,” *Computers and Structures*, vol. 193, pp. 139–154, 2017, doi: 10.1016/j.compstruc.2017.08.011.
- [66] Y. Peng, W. Ma, S. Wang, K. Wang, and G. Gao, “Investigation of the fracture behaviors of windshield laminated glass used in high-speed trains,” *Composite Structures*, vol. 207, no. August 2018, pp. 29–40, 2019, doi: 10.1016/j.compstruct.2018.09.009.
- [67] X. Zhang and H. Hao, “Experimental and numerical study of boundary and anchorage effect on laminated glass windows under blast loading,” *Engineering Structures*, vol. 90, pp. 96–116, 2015, doi: 10.1016/j.engstruct.2015.02.022.
- [68] K. Osnes, J. K. Holmen, O. S. Hopperstad, and T. Børvik, “Fracture and fragmentation of blast-loaded laminated glass: An experimental and numerical study,” *International Journal of Impact Engineering*, vol. 132, no. 7491, p. 103334, 2019, doi: 10.1016/j.ijimpeng.2019.103334.
- [69] X. Xu, J. Xu, J. Chen, P. Li, B. Liu, and Y. Li, “Investigation of dynamic multi-cracking behavior in PVB laminated glass plates,” *International Journal of Impact Engineering*, vol. 100, pp. 62–74, 2017, doi: 10.1016/j.ijimpeng.2016.10.013.
- [70] K. Rodacki and K. Furtak, “Numerical analysis of crack development of timber-glass composite I-beams in the extended finite element method (XFEM),” *Composite Structures*, vol. 209, pp. 349–361, 2019, doi: 10.1016/j.compstruct.2018.01.111.
- [71] X. Wang, J. Yang, S. Peng, Y. Wang, and X. Hou, “Microscale Discrete Element Model for Simulating Bridging Behavior of Fractured Glass Laminates,” in *Challenging Glass Conference Proceedings—Volume 8 – 2022*, 2022, vol. 8, no. June, pp. 1–12, doi: 10.47982/cgc.8.451.
- [72] W. Gao and M. Zang, “Engineering Analysis with Boundary Elements The simulation of laminated glass beam impact problem by developing fracture model of spherical DEM,” *Engineering Analysis With Boundary Elements*, vol. 42, pp. 2–7, 2014, doi: 10.1016/j.enganabound.2013.11.011.
- [73] X. Chen, A. H. C. Chan, and J. Yang, “Simulating the breakage of glass under hard body impact using the combined finite-discrete element method,” *Computers and Structures*, vol. 177, pp. 56–68, 2016, doi: 10.1016/j.compstruc.2016.08.010.
- [74] X. Wang, J. Yang, F. Wang, Q. Liu, and H. Xu, “Simulating the impact damage of laminated glass considering mixed mode delamination using FEM / DEM,” *Composite Structures*, vol. 202, no. May, pp. 1239–1252, 2018, doi: 10.1016/j.compstruct.2018.05.127.

- [75] X. Chen and A. H. C. Chan, “International Journal of Impact Engineering Modelling impact fracture and fragmentation of laminated glass using the combined finite-discrete element method,” *International Journal of Impact Engineering*, vol. 112, no. April 2017, pp. 15–29, 2018, doi: 10.1016/j.ijimpeng.2017.10.007.
- [76] X. Wang, J. Yang, Q. Liu, Y. Zhang, and C. Zhao, “A comparative study of numerical modelling techniques for the fracture of brittle materials with specific reference to glass,” *Engineering Structures*, vol. 152, pp. 493–505, 2017, doi: 10.1016/j.engstruct.2017.08.050.
- [77] S. Chen, M. Zang, D. Wang, S. Yoshimura, and T. Yamada, “Numerical analysis of impact failure of automotive laminated glass: A review,” *Composites Part B: Engineering*, vol. 122, pp. 47–60, 2017, doi: 10.1016/j.compositesb.2017.04.007.
- [78] M. Teotia and R. K. Soni, “Applications of finite element modelling in failure analysis of laminated glass composites: A review,” *Engineering Failure Analysis*, vol. 94, no. July, pp. 412–437, 2018, doi: 10.1016/j.engfailanal.2018.08.016.
- [79] S. Muralidhar, A. Jagota, S. J. Bennison, and S. Saigal, “Mechanical behaviour in tension of cracked glass bridged by an elastomeric ligament,” *Acta Materialia*, vol. 48, no. 18–19, pp. 4577–4588, 2000, doi: 10.1016/S1359-6454(00)00244-5.
- [80] L. Galuppi and G. Royer-Carfagni, “A homogenized model for the post-breakage tensile behavior of laminated glass,” *Composite Structures*, vol. 154, pp. 600–615, 2016, doi: 10.1016/j.compstruct.2016.07.052.
- [81] F. Freddi and L. Mingazzi, “Phase field simulation of laminated glass beam,” *Materials*, vol. 13, no. 14, 2020, doi: 10.3390/ma13143218.
- [82] D. Baraldi, A. Cecchi, and P. Foraboschi, “Broken tempered laminated glass: Non-linear discrete element modeling,” *Composite Structures*, vol. 140, pp. 278–295, 2016, doi: 10.1016/j.compstruct.2015.12.050.
- [83] L. Biolzi and M. Simoncelli, “Overall response of 2-ply laminated glass plates under out-of-plane loading,” *Engineering Structures*, vol. 256, no. October 2021, p. 113967, 2022, doi: 10.1016/j.engstruct.2022.113967.
- [84] P. Fourton, K. Piroird, M. Ciccotti, and E. Barthel, “Adhesion rupture in laminated glass: influence of adhesion on the energy dissipation mechanisms,” *Glass Structures and Engineering*, vol. 5, no. 3, pp. 397–410, 2020, doi: 10.1007/s40940-020-00136-4.
- [85] P. Elzière, C. Dalle-Ferrier, C. Creton, É. Barthel, and M. Ciccotti, “Large strain viscoelastic dissipation during interfacial rupture in laminated glass,” *Soft Matter*, vol. 13, no. 8, pp. 1624–1633, 2017, doi: 10.1039/c6sm02785g.
- [86] F. Freddi, G. Royer-Carfagni, and M. Silvestri, “Full-Scale Experiments for Point-Fixing Frameless Laminated Glass,” *International Journal of Applied Glass Science*, vol. 1, no. 3, pp. 257–272, 2010, doi: 10.1111/j.2041-1294.2010.00028.x.
- [87] L. Galuppi and G. Royer-Carfagni, “The post-breakage response of laminated heat-treated glass under in plane and out of plane loading,” *Composites Part B: Engineering*, vol. 147, no. August 2017, pp. 227–239, 2018, doi: 10.1016/j.compositesb.2018.04.005.
- [88] A. Ibrahimbegovic and D. Brancherie, “Combined hardening and softening constitutive model of plasticity: Precursor to shear slip line failure,” *Computational Mechanics*, vol. 31, no. 1-2 SPEC., pp. 88–100, 2003, doi: 10.1007/s00466-002-0396-x.
- [89] B. H. Pham, D. Brancherie, L. Davenne, and A. Ibrahimbegovic, “Stress-resultant models for ultimate load design of reinforced concrete frames and multi-scale parameter estimates,” *Computational Mechanics*, vol. 51, no. 3, pp. 347–360, 2013, doi: 10.1007/s00466-012-0734-6.
- [90] A. Ibrahimbegovic and S. Melnyk, “Embedded discontinuity finite element method for modeling of localized failure in heterogeneous materials with structured mesh: An alternative to extended finite element method,” *Computational Mechanics*, vol. 40, no. 1, pp. 149–155, 2007, doi: 10.1007/s00466-006-0091-4.

- [91] N. N. Bui, M. Ngo, M. Nikolic, D. Brancherie, and A. Ibrahimbegovic, "Enriched Timoshenko beam finite element for modeling bending and shear failure of reinforced concrete frames," *Computers and Structures*, vol. 143, pp. 9–18, 2014, doi: 10.1016/j.compstruc.2014.06.004.
- [92] J. Čarija, M. Nikolić, A. Ibrahimbegovic, and Ž. Nikolić, "Discrete softening-damage model for fracture process representation with embedded strong discontinuities," *Engineering Fracture Mechanics*, vol. 236, pp. 1–15, 2020, doi: 10.1016/j.engfracmech.2020.107211.
- [93] M. Jukic, B. Brank, and A. Ibrahimbegovic, "Embedded discontinuity finite element formulation for failure analysis of planar reinforced concrete beams and frames," *Engineering Structures*, vol. 50, pp. 115–125, 2013, doi: 10.1016/j.engstruct.2012.07.028.
- [94] A. Ibrahimbegovic, *Nonlinear solid mechanics: Theoretical Formulations and Finite Element Solution Methods*. Springer, 2009.
- [95] S. C. Angelides, J. P. Talbot, and M. Overend, "The influence of fracture pattern on the residual resistance of laminated glass at high strain-rates: an experimental investigation of the post-fracture bending moment capacity based on time-temperature mapping of interlayer yield stress," *Glass Structures and Engineering*, 2022, doi: 10.1007/s40940-022-00168-y.
- [96] R. L. Taylor, "FEAP Finite Element Analysis Program. University of California, Berkeley," [Online]. Available: <http://projects.ce.berkeley.edu/feap/>.
- [97] A. Ibrahimbegovic and F. Frey, "Stress resultant finite element analysis of reinforced concrete plates," *Engineering Computations*, vol. 10, no. 1, pp. 15–30, 1993, doi: 10.1108/eb023892.
- [98] A. Ibrahimbegovic and F. Frey, "An Efficient Implementation of Stress Resultant Plasticity in Analysis of Reissner-Mindlin Plates," *International Journal for Numerical Methods in Engineering*, vol. 36, no. 1993, pp. 303–320, 1993.
- [99] Q. Liu, X. Huang, G. Liu, Z. Zhou, and G. Li, "Investigation on flexural buckling of laminated glass columns under axial compression," *Engineering Structures*, vol. 133, pp. 14–23, 2017, doi: 10.1016/j.engstruct.2016.12.006.
- [100] Y. Lu, S. Zhao, and S. Chen, "Compressive buckling performance of multilayer laminated glass columns with different interlayers," *Engineering Structures*, vol. 281, no. February, 2023.
- [101] M. Feldmann and K. Langosch, "Buckling resistance and buckling curves of pane-like glass columns with monolithic sections of heat strengthened and tempered glass," *Challenging Glass 2 – Conference on Architectural and Structural Applications of Glass*, no. May, 2010.
- [102] I. Imamovic, A. Ibrahimbegovic, and E. Hajdo, "Geometrically exact initially curved Kirchhoff's planar elasto-plastic beam," *Coupled Systems Mechanics*, vol. 8, no. 6, pp. 537–553, 2019, doi: 10.12989/csm.2019.8.6.537.
- [103] E. Hajdo, A. Ibrahimbegovic, and S. Dolarevic1, "Buckling analysis of complex structures with refined model built of frame and shell finite elements," *Coupled Systems Mechanics*, vol. 9, no. 1, pp. 29–46, 2020, doi: 10.12989/csm.2020.9.1.029.
- [104] E. Hajdo, E. Hadzalic, and A. Ibrahimbegovic, "Linear Buckling Analysis of Structures on the Elastic Support," in *Proceedings of the International Symposium on Innovative and Interdisciplinary Applications of Advanced Technologies (IAT)*, 2022, vol. 1, pp. 92–102.
- [105] M. López-Aenlle, F. Pelayo, G. Ismael, M. A. G. Prieto, A. Martín Rodríguez, and A. Fernández-Canteli, "Buckling of laminated-glass beams using the effective-thickness concept," *Composite Structures*, vol. 137, pp. 44–55, 2016, doi: 10.1016/j.compstruct.2015.11.014.
- [106] L. Galuppi and G. Royer-carfagni, "Buckling of three-layered composite beams with viscoelastic interaction," *Composite Structures*, vol. 107, pp. 512–521, 2014, doi: 10.1016/j.compstruct.2013.08.006.
- [107] T. M. Minahen and W. G. Knauss, "CREEP BUCKLING OF VISCOELASTIC STRUCTURES," *International Journal of Solids and Structures*, vol. 30, no. 8, pp. 1075–1092, 1993, doi: 10.1016/0020-7683(93)90004-Q.
- [108] R. Kalamar, C. Bedon, and M. Eliášová, "Experimental investigation for the structural performance assessment of square hollow glass columns," *Engineering Structures*, vol. 113, pp. 1–15, 2016, doi:

- 10.1016/j.engstruct.2016.01.028.
- [109] F. Oikonomopoulou, E. A. M. van den Broek, T. Bristogianni, F. A. Veer, and R. Nijse, “Design and experimental testing of the bundled glass column,” *Glass Structures and Engineering*, vol. 2, no. 2, pp. 183–200, 2017, doi: 10.1007/s40940-017-0041-x.
- [110] G. Campione and V. Rondello, “Effects of shape of transverse cross-section on the load carrying capacity of laminated glass columns,” *Construction and Building Materials*, vol. 61, pp. 349–359, 2014, doi: 10.1016/j.conbuildmat.2014.02.053.
- [111] M. K. Kamarudin, M. M. Yusoff, P. Disney, and G. A. R. Parke, “Experimental and Numerical Investigation of the Buckling Performance of Tubular Glass Columns under Compression,” *Structures*, vol. 15, no. July, pp. 355–369, 2018, doi: 10.1016/j.istruc.2018.08.002.
- [112] X. Huang, S. Duan, Q. Liu, J. Nie, and W. Han, “Investigation on buckling behavior of laminated glass columns with elastic lateral restraint under axial compression,” *Composite Structures*, vol. 279, no. July 2021, 2022, doi: 10.1016/j.compstruct.2021.114810.
- [113] J. Belis, D. Mocibob, A. Luible, and M. Vandebroek, “On the size and shape of initial out-of-plane curvatures in structural glass components,” *Construction and Building Materials*, vol. 25, no. 5, pp. 2700–2712, 2011, doi: 10.1016/j.conbuildmat.2010.12.021.
- [114] C. Amadio and C. Bedon, “A buckling verification approach for monolithic and laminated glass elements under combined in plane compression and bending,” *Engineering Structures*, vol. 57, p. 393, 2013, doi: 10.1016/j.engstruct.2013.10.002.
- [115] P. Foraboschi, “Experimental characterization of non-linear behavior of monolithic glass,” *International Journal of Non-Linear Mechanics*, vol. 67, pp. 352–370, 2014, doi: 10.1016/j.ijnonlinmec.2014.09.016.
- [116] L. Galuppi and G. Royer-Carfagni, “The effective thickness of laminated glass: Inconsistency of the formulation in a proposal of EN-standards,” *Composites Part B: Engineering*, vol. 55, pp. 109–118, 2013, doi: 10.1016/j.compositesb.2013.05.025.
- [117] G. D’Ambrosio and L. Galuppi, “Enhanced effective thickness model for buckling of LG beams with different boundary conditions,” *Glass Structures and Engineering*, vol. 5, no. 2, pp. 205–210, 2020, doi: 10.1007/s40940-019-00116-3.
- [118] F. Pelayo, M. López-Aenlle, G. Ismael, and A. Fernández-Canteli, “Buckling of multilayered laminated glass beams: Validation of the effective thickness concept,” *Composite Structures*, vol. 169, pp. 2–9, 2017, doi: 10.1016/j.compstruct.2017.01.040.
- [119] L. Galuppi and G. Royer-carfagni, “Enhanced Effective Thickness of multi-layered laminated glass,” *Composites Part B*, vol. 64, pp. 202–213, 2014, doi: 10.1016/j.compositesb.2014.04.018.
- [120] K. Langosch and M. Feldmann, “Design of pane-like laminated glass columns,” vol. 169, pp. 403–415, 2016.
- [121] P. A. Hooper, B. R. K. Blackman, and J. P. Dear, “The mechanical behaviour of poly(vinyl butyral) at different strain magnitudes and strain rates,” *Journal of Materials Science*, vol. 47, no. 8, pp. 3564–3576, 2012, doi: 10.1007/s10853-011-6202-4.
- [122] Y. Lu, S. Chen, and X. Shao, “Shear modulus of ionomer interlayer: Effects of time, temperature and strain rate,” *Construction and Building Materials*, vol. 302, no. July, p. 124224, 2021, doi: 10.1016/j.conbuildmat.2021.124224.
- [123] P. Foraboschi, “Buckling of a laminated glass column under test,” *Structural Engineer*, vol. 87, no. 1, pp. 2–8, 2009.

7.2. List of Figures

Figure 1.1. Float process scheme	4
Figure 1.2. Stress-strain diagrams for structural materials.....	5
Figure 1.3. Breakage pattern for different types of glass	6
Figure 2.1. Representation of two limit states of the load capacity of LG.....	15
Figure 2.2. Comparison of degradation of Young modulus E (MPa), for the ionoplast and PVB interlayers due to load duration log (t(s)) at different temperatures T (°C)	16
Figure 2.3. Schematic representation of test setup and loading [12].....	20
Figure 2.4. Photo of test setup:a) before loading;b) when breakage of bottom ply occurred ..	20
Figure 2.5. Photography of fracture patterns of specimens: (a) S1; (b) S3; and (c) side view on centre of LG pane [12]	21
Figure 2.6. Results of four-point bending test compared with other similar tests [30] [27] from the literature [12].....	22
Figure 2.7. Force-displacement graph – comparison of the results of experimental test and numerical model [12]	24
Figure 2.8. The deflection graph for disposition D1: (a) PVB interlayers; (b) ionoplast interlayers [12]	27
Figure 2.9. The deflection graph for disposition D2: (a) PVB interlayers; (b) ionoplast interlayers [12]	28
Figure 2.10. The deflection graph for disposition D3: (a) PVB interlayers; (b) ionoplast interlayers [12]	29
Figure 2.11. The stress graph for a disposition D1: (a) PVB interlayers; (b) ionoplast interlayers [12].....	30
Figure 2.12. The stress graph for a disposition D2: (a) PVB interlayers; (b) ionoplast interlayers [12].....	31
Figure 2.13. The stress graph for a disposition D3: (a) PVB interlayers; (b) ionoplast interlayers [12].....	32
Figure 2.14. Scheme of the observed static system with the load for analytical calculation ..	40
Figure 2.15. Deflections according to different approaches for analytical calculation.....	42
Figure 2.16. Deflections according to different approaches for analytical calculation.....	43
Figure 2.17. Deflections according to different approaches for analytical calculation.....	44
Figure 2.18. Comparison of shear transfer/coupling coefficients from different ETA [58] [31] [2].....	45

Figure 2.19. Stress on elements according to different approaches for analytical calculation	46
Figure 2.20. Stress on elements according to different approaches for analytical calculation	47
Figure 2.21. Stress on elements according to different approaches for analytical calculation	48
Figure 3.1. Stress - displacement curve from Wang et al. [76]	55
Figure 3.2. Graphical representation of stages for localization development in a simple tension test [23]	57
Figure 3.3. Schematic representation of the element from the fine-scale multilayer model [23]	59
Figure 3.4. Schematic representation of one layer with all degrees of freedom and discontinuity in the middle [23]	61
Figure 3.5. Schematic representation of base functions, Heaviside function and the construction of interpolation function for layers [23]	62
Figure 3.6. Schematic representation of strain field in one layer	63
Figure 3.7. A stress-strain diagrams for glass constitutive behaviour in fine-scale model [23]	65
Figure 3.8. Schematic representation of beam element with seven degrees of freedom in the macro model [23]	68
Figure 3.9. Representation of the process of hinges formation in laminated glass member	70
Figure 3.9. Representation of the process of hinges formation in laminated glass member	70
Figure 3.10. Layer calibration test for a cantilever beam using imposed end rotation [23]	74
Figure 3.11. Mesh dependence test on a cantilever beam with imposed end rotation [23]	75
Figure 3.12. Graphical representation of the steps for determination coefficients for the macro model: a) approximation of multilayer model results with macro parameters b) parameters of the macro model	76
Figure 3.13. The scheme of different setups for numerical simulations	78
Figure 3.14. Force-displacement diagrams from numerical simulations and experiments	79
Figure 3.15. Force-displacement diagrams from numerical simulations and mean value from the experiments	80
Figure 3.16. Representation of deformed structures after the breakage for Type 3 setups	81

Figure 3.17. Comparison of force-displacement diagrams obtained with numerical simulations using effective thickness height according to [22] and the experimental results	82
Figure 3.18. Comparison of force-displacement diagrams obtained for numerical simulations using effective thickness height according to [31] and the experimental results	83
Figure 3.19. Force-displacement diagrams from numerical simulations and experiments from [54] for the case of laminated glass with PVB interlayer thickness 0.76 mm (Test 4)	84
Figure 3.20. Force-displacement diagrams from numerical simulations and experiments from [54] for the case of laminated glass with PVB interlayer thickness 1.52 mm (Test 5)	85
Figure 3.21. Force-displacement diagrams from numerical simulations and experiments from [83]	87
Figure 3.22. Schematic representation of plate element with the degrees of freedom and deformations in macro model 2	88
Figure 3.23. Results from the micro model and for chosen macro model 2 parameters	91
Figure 3.24. Three setups for preliminary tests in macro model 2	92
Figure 3.25. The critical area development from the macro model 2 for setup a) Fig. 3.24. ...	93
Figure 3.26. The critical area development from the macro model 2 for setup b) Fig. 3.24. ...	93
Figure 3.27. The critical area development from the macro model 2 for setup c) Fig. 3.24. ...	94
Figure 4.1. Buckling shapes for simply supported member.	103
Figure 4.2. Numerical models of Test 1- implementation of analytical solution into beam and shell numerical model.	106
Figure 4.3. Photography of experimental test 1 from [99].	106
Figure 4.4. Graphical presentation of numerically predicted critical intervals and the experimental result for Test 1	110
Figure 4.5. Graphical presentation of the ratio between the numerically predicted critical force and the experimental results ($F_{numerical}/F_{experimental}$) for Test 1	111
Figure 4.6. Numerical models of Test 2- implementation of analytical solution into beam and shell numerical model	112
Figure 4.7. Photography of experimental test 2 from [100]	113
Figure 4.8. Graphical presentation of numerically predicted critical intervals and the experimental result for Test 2	115

Figure 4.9. Photography of experimental test 2 from [100] 116

Figure 4.10. Numerical models of Test 3 - implementation of analytical solution into beam and shell numerical model 117

Figure 4.11. Graphical presentation of ratio between the numerically predicted critical force and the experimental results ($F_{numerical}/F_{experimental}$) for hinged element– Test 3..... 119

Figure 4.12. Graphical presentation of ratio between the numerically predicted critical force and the experimental results ($F_{numerical}/F_{experimental}$) for hinged + fixed element – Test 3..... 120

7.3. List of Tables

Table 1.1. Physical properties of glass	5
Table 1.2. Characteristic bending strength of each type of glass according to prEN 13474:2009 and degree of surface prestressing	5
Table 2.1. Basic mechanical properties of the interlayers from [41][42][43][12]	17
Table 2.2. The dispositions: title and the associated geometries.....	25
Table 2.2. The dispositions: title and the associated geometries.....	25
Table 2.3. The expressions for the effective thickness approach according to Wölfel Bennison.....	35
Table 2.4. The expressions for the effective thickness approach according to EN 16612 [22]	36
Table 2.5. The expressions for the effective thickness approach according to CEN/TS 19100-2:2021 [2].....	37
Table 2.6. The expressions for the effective thickness approach according to Galuppi and Royer-Carfagni [31]	38
Table 2.7. The values of shear modulus (G_{int}) of PVB interlayer [41].....	39
Table 3.1. Different inputs for threshold function and stress-strain diagram from Figure 3.7.	64
Table 3.2. Used material properties for glass and interlayer material.....	73
Table 3.3. Parameters for the macro models for Test 1 (T1), Test 2 (T2) and Test 3 (T3).....	77
Table 3.4. Parameters for the macro models for Test 4 (T4), Test 5 (T5) and Test 6 (T6).....	77
Table 4.1. Different equations for the effective thickness approach (ETA) from the literature [117][105][120].....	102
Table 4.2. Effective thickness for specimens with two-ply laminated glass cross-sections ..	107
Table 4.3. Effective thickness for specimens with three-ply laminated glass cross-sections ([3]/[120] - first result; [117] - second result).....	107
Table 4.4. The experimental results from [99] and obtained numerical results for specimens with two-ply cross-sections.....	108
Table 4.5. The experimental results from [99] and obtained numerical results for specimens with three-ply cross-sections.....	109
Table 4.6. Effective thickness for specimens with three-ply laminated glass cross-sections ([3]/[120] - first result; [117] - second result).....	113

Table 4.7. The experimental results from [100] and obtained numerical results for specimens with three-ply cross-sections..... 114

Table 4.8. Effective thickness for specimens with two-ply LG cross-sections – both sides hinged 117

Table 4.9. Effective thickness for specimens with two-ply LG cross-sections – hinged + fixed..... 117

Table 4.10. Comparison of experimental results [123] and numerical results for beam and shell models 118

7.4. List of Published Papers

- Paper 1. Grozdanić, Gabrijela; Ibrahimbegović, Adnan; Galić, Mirela; Divić, Vladimir;
Multiscale beam model for simulating fracture in laminated glass structures //
Engineering fracture mechanics, 292 (2023), 109606, 23. doi:
<https://doi.org/10.1016/j.engfracmech.2023.109606>
- Paper 2. Galić, Mirela ; Grozdanić, Gabrijela ; Divić, Vladimir ; Marović, Pavao
Parametric Analyses of the Influence of Temperature, Load Duration, and Interlayer
Thickness on a Laminated Glass Structure Exposed to Out-of-Plane Loading //
Crystals, 12 (2022), 6; 10.3390/cryst12060838, 28. doi: 10.3390/cryst12060838
- Paper 3. Grozdanić, Gabrijela ; Galić, Mirela ; Marović, Pavao
Some aspects of the analyses of glass structures exposed to impact load // Coupled
Systems Mechanics, 10 (2021), 6; 475-490. doi:
doi.org/10.12989/csm.2021.10.6.475

7.5. List of Attended Conferences

Conf. 1 . Grozdanić, Gabrijela; Ibrahimbegović, Adnan; Galić, Mirela

Different Approaches in Analyses and Modelling Laminated Glass Elements Exposed to Static Load // 6th International Conference on Multi-scale Computational Methods for Solids and Fluids, June 25-27, 2023, Sarajevo PROCEEDINGS. Sarajevo: University of Sarajevo, 2023. str. 90-92

Conf. 2. Grozdanić, Gabrijela ; Galić, Mirela ; Marović, Pavao

Some aspects of the glass structures analyses exposed to impact load // Proceedings - ECCOMAS MSF 2021 - 5th International Conference on Multi-scale Computational Methods for Solids and Fluids / Ibrahimbegović, Adnan ; Nikolić, Mijo (ur.). Sarajevo: Građevinski fakultet Univerziteta u Sarajevu, 2021. str. 140-143

APPEDIX A

Contents

A.1. Appedix A

Table A.1. Dataset for plate-thickness disposition 10 + d + 6 (mm)

Deflection 10+2.28+6 (mm)								
Temp (°C)	PVB				IONOPLAST			
	1min	24h	1 month	10 years	1 min	24h	1 month	10 years
10	1.642	1.960	4.185	5.737	1.645	1.652	1.657	1.660
25	1.673	4.255	5.586	6.141	1.660	1.690	1.739	1.820
30	1.920	5.580	6.048	6.753	1.684	1.770	2.232	2.081
40	5.200	6.320	6.996	7.421	1.865	2.964	3.329	3.467
Bottom panel - stress - 10+2.28+6 (MPa)								
Temp (°C)	PVB				IONOPLAST			
	1min	24h	1 month	10 years	1 min	24h	1 month	10 years
10	11.820	12.273	14.893	21.577	11.809	11.821	11.834	11.840
25	11.865	15.169	20.949	23.349	11.834	11.885	11.963	12.090
30	12.218	20.897	22.930	25.903	11.874	12.012	12.605	13.226
40	19.276	24.102	26.977	28.790	12.150	13.382	13.739	13.882
Deflection 10+1.52+6 (mm)								
Temp (°C)	PVB				IONOPLAST			
	1min	24h	1 month	10 years	1 min	24h	1 month	10 years
10	1.835	2.077	3.909	5.403	1.837	1.843	1.847	1.852
25	1.858	3.963	5.245	5.827	1.848	1.872	1.907	1.971
30	2.040	5.234	5.724	6.500	1.866	1.931	2.279	2.732
40	4.860	6.015	6.778	7.279	2.000	2.858	3.158	3.274
Bottom panel - stress - 10+1.52+6 (MPa)								
Temp (°C)	PVB				IONOPLAST			
	1min	24h	1 month	10 years	1 min	24h	1 month	10 years
10	12.614	12.910	14.676	19.998	12.605	12.612	12.621	12.624
25	12.641	14.731	19.339	21.891	12.620	12.652	12.703	12.783
30	12.886	19.266	21.429	24.810	12.646	12.732	13.159	13.615
40	17.619	22.710	26.000	28.180	12.822	13.733	14.000	14.113
Deflection 10+0.76+6 (mm)					Deflection 10+0.89+6 (mm)			
Temp (°C)	PVB				IONOPLAST			
	1min	24h	1 month	10 years	1 min	24h	1 month	10 years
10	2.064	2.210	3.457	4.736	1.978	1.981	1.984	1.988
25	2.077	3.447	4.561	5.157	1.984	2.000	2.023	2.065
30	2.181	4.525	5.031	5.907	1.996	2.038	2.266	2.576
40	4.177	5.323	6.241	6.922	2.083	2.664	2.881	2.967
Bottom panel - stress - 10+0.76+6 (MPa)					Bottom panel - stress - 10+0.89+6 (MPa)			
Temp (°C)	PVB				IONOPLAST			
	1min	24h	1 month	10 years	1 min	24h	1 month	10 years
10	13.508	13.630	14.740	16.885	13.133	13.138	13.140	13.145
25	13.516	14.725	16.105	18.756	13.142	13.161	13.185	13.232
30	13.605	15.964	18.195	22.075	13.157	13.203	13.481	13.813
40	15.320	19.515	23.544	26.557	13.256	13.898	14.103	14.182

Table A.2. Dataset for plate-thickness disposition 6 + d + 10 (mm)

Deflection 6+2.28+10 (mm)								
Temp (°C)	PVB				IONOPLAST			
	1min	24h	1 month	10 years	1 min	24h	1 month	10 years
10	1.640	1.960	4.183	5.733	1.645	1.652	1.657	1.660
25	1.670	4.253	5.582	6.135	1.660	1.690	1.739	1.825
30	1.919	5.575	6.042	6.742	1.680	1.770	2.232	2.810
40	5.201	6.312	6.982	7.395	1.865	2.964	3.329	3.467
Bottom panel - stress - 6+2.28+10 (MPa)								
Temp (°C)	PVB				IONOPLAST			
	1min	24h	1 month	10 years	1 min	24h	1 month	10 years
10	11.440	12.784	19.698	24.349	11.444	11.490	11.522	11.559
25	11.619	19.910	23.896	25.557	11.536	11.710	11.940	12.301
30	12.631	23.876	25.274	27.401	11.674	12.083	13.761	15.617
40	22.746	26.094	28.146	29.511	12.461	16.096	17.201	17.612
Deflection 6+1.52+10 (mm)								
Temp (°C)	PVB				IONOPLAST			
	1min	24h	1 month	10 years	1 min	24h	1 month	10 years
10	1.835	2.077	3.907	5.402	1.837	1.843	1.847	1.852
25	1.858	3.962	5.242	5.824	1.848	1.872	1.907	1.971
30	2.042	5.231	5.720	6.493	1.866	1.931	2.279	2.732
40	4.855	6.010	6.768	7.260	2.001	2.857	3.158	3.274
Bottom panel - stress - 6+1.52+10 (MPa)								
Temp (°C)	PVB				IONOPLAST			
	1min	24h	1 month	10 years	1 min	24h	1 month	10 years
10	12.362	13.416	19.086	23.483	12.365	12.403	12.429	12.459
25	12.506	19.249	23.014	24.730	12.439	12.579	12.761	13.044
30	13.292	22.984	24.426	26.707	12.549	12.873	14.176	15.649
40	21.833	25.279	27.528	29.051	13.166	16.037	16.947	17.291
Deflection 6+0.76+10 (mm)					Deflection 6+0.89+10 (mm)			
Temp (°C)	PVB				IONOPLAST			
	1min	24h	1 month	10 years	1 min	24h	1 month	10 years
10	2.063	2.203	3.421	4.707	2.022	2.026	2.029	2.032
25	2.076	3.440	4.540	5.133	2.029	2.045	2.068	2.110
30	2.180	4.520	5.013	5.888	2.041	2.083	2.312	2.624
40	4.174	5.317	6.230	6.907	2.129	2.713	2.931	3.018
Bottom panel - stress - 6+0.76+10 (MPa)					Bottom panel - stress - 6+0.89+10 (MPa)			
Temp (°C)	PVB				IONOPLAST			
	1min	24h	1 month	10 years	1 min	24h	1 month	10 years
10	13.400	14.093	17.921	21.643	13.218	13.247	13.267	13.290
25	13.498	17.992	21.160	22.867	13.273	13.376	13.509	13.712
30	14.006	21.102	22.528	25.042	13.354	13.589	14.504	15.552
40	20.108	23.399	26.025	27.994		15.833	16.507	16.767

Table A.3. Dataset for plate-thickness disposition 8 + d + 8 (mm)

Deflection 8+2.28+8 (mm)								
Temp (°C)	PVB				IONOPLAST			
	1min	24h	1 month	10 years	1 min	24h	1 month	10 years
10	1.614	1.971	4.223	6.060	1.815	1.821	1.825	1.831
25	1.647	4.621	5.851	6.597	1.827	1.852	1.892	1.963
30	1.918	6.266	6.460	7.800	1.846	1.918	2.308	2.823
40	5.790	7.224	7.834	8.691	1.996	2.966	3.314	3.450
Bottom panel - stress - 8+2.28+8 (MPa)								
Temp (°C)	PVB				IONOPLAST			
	1min	24h	1 month	10 years	1 min	24h	1 month	10 years
10	11.458	12.591	18.121	22.108	12.360	12.388	12.409	12.434
25	11.600	18.718	21.654	23.277	12.417	12.527	12.675	12.907
30	12.449	22.383	22.975	25.827	12.504	12.767	13.872	15.103
40	21.317	24.517	25.973	27.980	13.010	15.424	16.212	16.514
Deflection 8+1.52+8 (mm)								
Temp (°C)	PVB				IONOPLAST			
	1min	24h	1 month	10 years	1 min	24h	1 month	10 years
10	1.812	2.084	4.223	6.061	1.815	1.821	1.258	1.831
25	1.837	4.265	5.851	6.597	1.827	1.852	1.892	1.963
30	2.040	5.827	6.458	7.470	1.846	1.918	2.308	2.822
40	5.356	6.826	7.834	8.501	1.996	2.966	3.314	3.449
Bottom panel - stress - 8+1.52+8 (MPa)								
Temp (°C)	PVB				IONOPLAST			
	1min	24h	1 month	10 years	1 min	24h	1 month	10 years
10	12.361	13.225	18.121	22.108	12.360	12.390	12.409	12.435
25	12.471	18.217	21.654	23.227	12.417	12.528	12.675	12.907
30	13.111	21.603	22.975	25.171	12.504	12.767	13.872	15.103
40	20.580	23.776	25.973	27.534	13.010	15.424	16.212	16.514
Deflection 8+0.76+8 (mm)					Deflection 8+0.89+8 (mm)			
Temp (°C)	PVB				IONOPLAST			
	1min	24h	1 month	10 years	1 min	24h	1 month	10 years
10	2.049	2.211	3.644	5.197	2.007	2.011	2.014	2.019
25	2.063	3.460	4.979	5.721	2.015	2.032	2.058	2.105
30	2.018	4.939	5.564	6.681	2.028	2.075	2.333	2.688
40	4.514	5.937	7.119	8.027	2.125	2.789	3.042	3.142
Bottom panel - stress - 8+0.76+8 (MPa)					Bottom panel - stress - 8+0.89+8 (MPa)			
Temp (°C)	PVB				IONOPLAST			
	1min	24h	1 month	10 years	1 min	24h	1 month	10 years
10	13.385	13.931	17.225	20.514	13.200	13.222	13.236	13.258
25	13.456	17.224	20.060	21.615	13.241	13.321	13.425	13.590
30	13.850	19.971	21.285	23.633	13.303	13.490	14.244	15.131
40	19.071	22.057	24.554	26.474	13.659	15.365	15.926	16.147

Curriculum vitae

Gabrijela Grozdanić was born in march 18, 1992 in Šibenik. After graduating from the Technical School in Šibenik, she enrolled at the University of Split Faculty of Civil Engineering, Architecture and Geodesy (FGAG) in the academic year 2010/2011. She obtained a master's degree in civil engineering in September 2016, in the field of Structures. During the last semester of graduate studies, in February 2016, she started working as an associate structural designer in Kuzmanić&Šimunović projekt d.o.o. where she worked for two years. In March 2018, she started working as an assistant at the Department of Metal and Timber Structures, where she was enrolled for one year as a teaching assistant. At the end of the contract, she was employed as a senior associate at the Department of Theory of Structures at the Interreg project PMO-GATE. In October 2019, at the end of her previous contract, she enrolled as a teaching assistant at the Department of Strength of Materials and Structural Testings. During this period at the Faculty of Civil Engineering, Architecture, and Geodesy she enrolled in postgraduate studies in the scientific field of technical science, and at the University of Technology Compiegne as a double doctorate between the two universities. During PhD, and in accordance with the Cotutelle contract, she spent eight months at the University of Split, where a mentor, Professor Mirela Galic, guides one part of her research, and then four months a year at the Roberval Laboratory for Mechanics, Electricity, and Acoustics, where she worked under the guidance of mentor, professor Adan Ibrahimbegovic. She has been actively participating in classes since 2018 as an assistant, in different subjects, according to the departments. Currently, she is enrolled as an assistant in the subjects Strength of Materials I and II, Basis of structures II, and Installations. During postgraduate studies, and under the guidance of both mentors, she published three scientific papers in the Web of Science Core Collection database, and the fourth is in the process of review. Also, she participated in four international conferences, two of which were oral presentations.